

University of St Andrews



Full metadata for this thesis is available in
St Andrews Research Repository
at:

<http://research-repository.st-andrews.ac.uk/>

This thesis is protected by original copyright

Dynamical Optical Nonlinearities in Semiconductor Optical Amplifiers and Quantum Cascade Lasers

Thesis submitted to the University of St Andrews
in application for the degree of Doctor of Philosophy

Alvaro Gomez-Iglesias



School of Physics and Astronomy

University of St Andrews

Fife, Scotland

July 2005



Th
F70

Declaration

I, Alvaro Gomez-Iglesias, hereby certify that this thesis, which is approximately 45000 words in length, has been written by me, that it is the record of work carried out by me and that it has not been submitted in any previous application for a higher degree.

Date

Signature of candidate

I was admitted as a research student in October, 2001 and as a candidate for the degree of Doctor of Philosophy in June, 2002; the higher study for which this is a record was carried out in the University of St. Andrews between 2001 and 2005.

Date

Signature of candidate

I hereby certify that the candidate has fulfilled the conditions of the Resolution and Regulations appropriate for the degree of Doctor of Philosophy in the University of St. Andrews and that the candidate is qualified to submit this thesis in application for that degree.

Date

Signature of supervisor

Unrestricted

In submitting this thesis to the University of St. Andrews I understand that I am giving permission for it to be made available for use in accordance with the regulations of the University Library for the time being in force, subject to any copyright vested in the work not being affected thereby. I also understand that the title and abstract will be published, and that a copy of the work may be made and supplied to any bona fide library or research worker.

Date

Signature of candidate

A mis padres

*"Era como si Dios hubiera resuelto poner a prueba toda capacidad de asombro, y mantuviera a los habitantes de Macondo en un permanente vaivén entre el alborozo y el desencanto, la duda y la revelación, hasta el extremo de que ya nadie podía saber a ciencia cierta dónde estaban los límites de la realidad. Era un intrincado frangollo de verdades y espejismos, que convulsionó de impaciencia al espectro de José Arcadio Buendía bajo el castaño y lo obligó a caminar por toda la casa aun a pleno día."*¹

Gabriel García Marquez. *Cien Años de Soledad*.

¹"It was as if God had decided to put to the test every capacity for surprise and was keeping the inhabitants of Macondo in a permanent alternation between excitement and disappointment, doubt and revelation, to such an extreme that no one knew for certain where the limits of reality lay. It was an intricate stew of truths and mirages that convulsed the ghost of José Arcadio Buendía with impatience and made him wander all through the house even in broad daylight."

Abstract

The ultrafast dynamics in semiconductor optical amplifiers (SOAs) relevant to all-optical switching have been studied by means of time-resolved spectroscopic experiments on a multiple quantum well InGaAs amplifier. The nonlinear light generation in Quantum Cascade (QC) lasers has also been a subject of research.

The switching windows of a TOAD-like three-beam interferometric set-up, measured using 700 *fs* pulses in the 1.5 μm wavelength region, revealed an ultrafast feature (~ 2 *ps*) dependent on the pulse energy of the pump beam. These dynamics, and the subsequent reshaping of the switching window edge, are attributed to refractive index changes in the SOA caused by ultrafast carrier heating, consistent with the predictions of a sliced propagation model based on rate equations.

Counter-propagating sub-picosecond pulses were used to monitor gain saturation along the SOA waveguide at different wavelengths around the peak gain. The functional form of the spatial dependence of gain saturation is found to depend on pulse energy. These observations are interpreted by combining the optical nonlinearities associated with inter-band carrier dynamics and carrier heating together and their respective time constants. Aided by the rate-equation model, we show that the amplification of the pump as it propagates along the amplifier may lead to the saturation of a portion of the device and to an effective narrowing of the switching windows of a TOAD (even for pulse energies below 1 pJ). Particular attention is devoted to discussing the limit of full saturation across the entire SOA waveguide.

Observation of stimulated electronic Anti-Stokes Raman emission in QC lasers is reported. We present four distinct designs of active regions with enhanced Anti-Stokes Raman nonlinearity. In all four, the pump laser is monolithically integrated with the nonlinear region in a two-stack active core within the same waveguide. Stimulated electronic Raman emission was observed in samples of three of these designs. Additionally, for the designs with positive detuning, an incoherent up-conversion signal resulting from optical pumping is detected.

Contents

1	Introduction	1
1.1	Semiconductor optical amplifiers for all-optical switching	2
1.1.1	All optical switching	3
1.1.2	SOAs in optical switching	6
1.1.3	Current status and challenges for SOA-based all-optical switches . .	12
1.2	Quantum Cascade lasers	14
1.2.1	Introduction	14
1.2.2	Background and present challenges	15
1.3	Light propagation in active media	17
1.3.1	Linear propagation	18
1.3.2	Nonlinear phenomena	21
1.4	Summary	23
	References for Chapter 1	24
2	Physics of the semiconductor gain materials	28
2.1	Band structure of bulk III-V compound semiconductors	28
2.1.1	Crystalline and electronic properties	28
2.1.2	Dispersion relations and density of states	30
2.2	Quantum wells and superlattices	34
2.2.1	A single quantum well	35
2.2.2	Multiple quantum well structures and superlattices	39
2.2.3	Optical transitions in quantum wells	40
2.3	Semiconductor optical amplifiers	45
2.3.1	Principles of SOA operation	45

2.3.2	Heterostructures	46
2.3.3	Optical gain and absorption	48
2.3.4	Optical nonlinearities	51
2.3.5	Nonlinear refraction	56
2.3.6	Nonlinear effects on pulse propagation	57
2.4	Quantum Cascade lasers	58
2.4.1	Gain and loss in QC lasers	60
2.4.2	Carrier transport	62
2.4.3	Intersubband optical nonlinearities in QC lasers	63
2.5	Summary	64
	References for Chapter 2	65
3	Device structure and experimental techniques	67
3.1	SOA structure and mounting of the device	67
3.1.1	Device characterisation	69
3.1.2	Coupling of light into the SOA waveguide	72
3.2	Resolving the SOA ultrafast dynamics	73
3.2.1	The pump-probe technique	73
3.2.2	Optical source: Optical Parametric Oscillator	77
3.3	Wafer processing and mounting of the QC lasers	85
3.4	QC laser characterisation	87
3.4.1	Spectral measurements	87
3.4.2	Electrical measurements	91
3.5	Summary	92
	References for Chapter 3	93
4	Ultrafast nonlinearities in semiconductor optical amplifiers	94
4.1	Introduction	94
4.2	Modelling the SOA dynamics	95
4.2.1	Our approach: a sliced propagation model	98
4.3	Ultrafast dynamics in SOA-based interferometric switches	104
4.3.1	Three beam pump-probe set-up	104

4.3.2	Resolving the onset of all-optical switching	108
4.3.3	Modelling of results and analysis	110
4.4	Spatial dependence of optical nonlinearities	114
4.4.1	Experimental results	116
4.4.2	Analysis and modelling results	118
4.4.3	Implications for all-optical switching	121
4.5	Summary	124
	References for Chapter 4	126
5	Stimulated electronic Anti-Stokes Raman emission in QC lasers	128
5.1	Nonlinear generation of light in QC lasers	128
5.1.1	Stimulated Raman scattering	129
5.2	Laser design	135
5.2.1	Different designs of active regions	135
5.2.2	Mid-IR Waveguides	144
5.3	Experimental results	149
5.3.1	Wafer D2924	150
5.3.2	Wafers D3008 and D3036	154
5.3.3	Wafers D3015 and D3037	159
5.3.4	Wafer D3018	164
5.4	Comparative analysis	167
5.5	Summary	168
	References for Chapter 5	170
6	Summary and Conclusions	172
6.1	Summary of thesis	172
6.2	Further work	175
	References for Chapter 6	178

Chapter 1

Introduction

Since W. Pauli stated in 1931, somewhat hopelessly...

*“One shouldn’t work on semiconductors, that is a filthy mess;
who knows whether they really exist”,*

the field of semiconductor physics has undergone tremendous progress, both in terms of theory and applications. Transistors, semiconductor lasers and a plethora of other devices have changed the face of modern technology. Progress in epitaxial growth techniques over the past decades has allowed the creation of heterostructures with physical dimensions on the order of or smaller than the DeBroglie wavelength of the electrons, leading to the observation of quantum phenomena on a device level.

Parallel to the developments in purely electronic technology, the interaction between the carriers in semiconductors and light has led to extensive research, launching a field in itself, with the application in devices often referred to as photonics. This research has been driven by the needs of lightwave communication systems, amongst other applications, and optical or optoelectronics alternatives to electronic switching and logic elements. In this context, the quantum confinement of carriers leads to drastically different semiconductor optical properties and allows for band-structure engineering and the implementation of novel components.

The response of semiconductors to an optical field is dictated by the material band-structure and the carrier dynamics, to which a rich variety of interband and intraband

mechanisms contribute. In this thesis, two different aspects of the interaction of light with electrons in semiconductor heterostructures will be covered.

In the first section of this chapter, we give an overview addressing the role of semiconductor optical amplifiers in the context of all-optical communications. This explains the motivation for our study of the ultrafast gain/refractive index dynamics in SOAs, particularly the interplay of the interband dynamics and the much faster intraband scattering processes in switching applications involving subpicosecond pulses.

The second part of the thesis is related to nonlinear light generation in Quantum Cascade (QC) lasers, and presents the work carried out as a visiting student at Princeton University. In the present chapter, the evolution time-line of these novel injection semiconductor lasers, based on electronic and optical intersubband transitions in multiple quantum well structures, is reviewed. Additionally, the potential of QC lasers as compact high-power optical sources in the mid- to far-IR wavelength range is discussed in the context of applications such as trace gas sensing.

The final section in this chapter is devoted to reviewing the basics of light propagation, linear and nonlinear, in active media, as this is a fundamental issue to both SOAs and QC lasers.

1.1 Semiconductor optical amplifiers for all-optical switching

Since the early 1980's, optical technology has proven to be enormously successful in boosting the speed at which information is transmitted. Nowadays, single fibre capacities in the range of hundreds of Gbits/s are commercially available. Combining such high-rate time division multiplexing (TDM) systems with wavelength division multiplexing (WDM) systems, aggregate rates close to 1 Tb/s can be demonstrated. Despite this amazing success, tasks such as switching or routing are still performed by electronic means, requiring conversion of the signal from the optical to the electronic domain and vice versa, limiting the processing speeds to below 10 Gb/s and thus not taking full advantage of the high optical transmission rates. It is hardly surprising, regarding the latter, that the idea of all optical networks was so appealing to many researchers. To overcome the limitations

of electronics, implementation of switching, routing or signal regeneration in all optical systems (optical TDM) is expected to be the key to ultra-high capacity communication networks.

The most basic function to be performed in a high-speed optical system is switching, needed for demultiplexing, signal regeneration, routing and other essential applications. We will from now on concentrate in all optical fast gating devices and their underlying physics, keeping in mind the requirements for practical all-optical switches, which include ultrafast response, high repetition rate (fast recovery), low switching energy, a high contrast ratio and low insertion loss.

As intensive research is being undertaken worldwide in all-optical switching at communication wavelengths (especially $1.5\ \mu\text{m}$), it is a vast field to cover. Our aim here is to give a broad view of the topic on a chronological basis that may help to understand the important role that SOAs play at present and their promising future.

1.1.1 All optical switching

For the last twenty five years efforts on photonic switching have been based on nonlinear optical phenomena. The idea is to take advantage of the fact that a propagating optical beam can change the refractive index of a material depending on its intensity. As a result of the intensity dependent wave vector, if any of the powers (or both) of two coherent optical beams are changed, their interference is modified. This way, the output of the optical gate is set by the intensity either of the input pulse (self-switching) or a second beam (control pulse induced switching). From a historical point of view, the first important efforts in optical switching date from the late 1970's and dealt with bistable etalons [1]. These devices consisted of a Fabry-Perot cavity filled with an optically nonlinear material, typically a semiconductor operated at frequencies near the bandgap to achieve strong nonlinearities. The device is designed in such a way that a low intensity input pulse will be far from any of the cavity resonant frequencies and will thus be reflected. Nevertheless, a high intensity input pulse will induce a change in the refractive index of the filling material, shifting the cavity resonant modes to match the pulse carrier frequency and therefore achieving high transmission. The cavity feedback can create conditions for regenerative switching. The main drawbacks of these devices are the high losses and their slow recovery

times, which make them better suited for parallel processing. A more successful approach to optical switching appeared in the 1980's with the use of waveguide devices. Within this category, a plethora of different solutions have been proposed [2] and experimentally tested, although two main groups may be distinguished: *integrated* and *fibre* switches.

On the one hand, integrated devices have the a priori advantage of the availability of large nonlinearities, the semiconductor two-channel Non Linear Directional Coupler (NLDC) being the most important device within this category. The input pulse is switched between two possible outputs either by changing the intensity of the input beam or by the action of a control pulse injected in to the second channel. The main drawback in this system is the difficulty of achieving multiple π phase shifts within the attenuation length. One reason for this is the massive absorption when using the resonant nonlinearity of charge carrier generation, i.e., on absorption of a photon an electron moves to the conduction band and changes the refractive index. To overcome these limitations, two different proposals were considered:

- (i). To use near-resonant nonlinearities, requiring a trade off between optical nonlinearity and absorption.
- (ii). To work at frequencies below half the bandgap [3].

In principle, optical fibres do not seem to be good candidates for switching because of the weak Kerr type non linearity in fused silica ($n_2 \approx 3 \times 10^{-16} \text{ cm}^2/\text{W}$). Nevertheless, due to the non resonant nature of the non linearity involved, attenuation is very low and the required phase shift can be achieved by employing a long length of fibre. Additionally, from the point of view of recovery times, the instantaneous nature of the Kerr nonlinearity is very advantageous.

Despite the great variety of fibre switches, we will limit our discussion to the intensively studied Nonlinear-optical Loop Mirror (NOLM) [4], which represented a key development towards the application of SOAs in optical switching, as will later be pointed out.

As shown in figure 1.1, the input pulse is split by the coupler with a splitting ratio r . Two replicas of the pulse then counter propagate in the fibre. If the power of the input pulse is low enough to neglect any nonlinear effects, both replicas will recombine in phase at the coupler, giving an output $P_{out} = P_{in} [1 - 2r(1 - r)]$. When the input pulse power

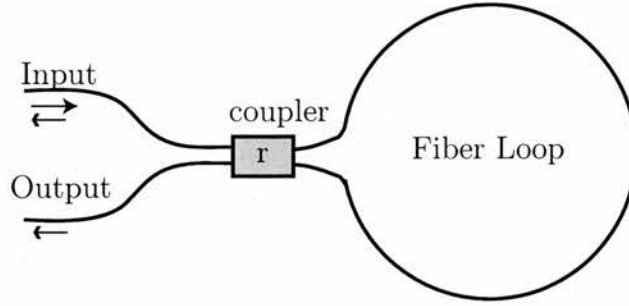


Figure 1.1: Schematics of a NOLM.

is high and $r \neq 0.5$, the replicas will experience a nonlinear refractive index, and thus accumulate different phases in the loop. In this case

$$P_{out} = P_{in} [1 - 2r(1 - r) \{1 + \cos [(1 - 2r)\Delta\beta P_{in}L]\}], \quad (1.1)$$

where $\Delta\beta$ is the change in the propagation constant in the fibre due to the non linear refractive index, and L is the length of the loop. Therefore, we see that the input pulse is capable of self-switching depending on its power.

Figures of merit

Regarding all the different approaches to optical switching discussed so far, all based on passive components, we clearly see that the key factor is to achieve the required nonlinear phase shift $p\pi$ within the attenuation length of the material, α^{-1} (where α is the absorption coefficient). p is a parameter whose value depends on the type of device and typically lies within the range $1 < p < 4$. For example, while in the case of a Mach-Zehnder interferometer $p = 1$, a NLDC generally requires at least a net phase change of 4π [5].

The search for materials other than glass meeting simultaneously high nonlinearity and low absorption turned out to be non trivial and had not been satisfactorily overcome by the early 1990's. Stegeman and Miller [2] developed a criteria to systematically evaluate materials as candidates for switching.

According to reference [2], let $\Delta\Phi_{NL} = 2\pi\Delta n_{NL}L/\lambda_0$ be the nonlinear phase shift, with L the length of the device, Δn_{NL} the nonlinear contribution to the refractive index and λ_0 the wavelength in vacuum. In addition, we must consider the attenuation coefficient $\alpha = \alpha_0 + \beta_2 I$, where α_0 represents the linear absorption and $\beta_2 I$ accounts for two photon

absorption (TPA).

In the case of a semiconductor, when operating near the band edge, $\alpha_0 \gg \beta_2 I$. In this case a saturating nonlinearity (band filling) is involved, and $\Delta n_{NL} = \Delta n_{sat}$. To quantify the nonlinear optical efficiency/transparency ratio, it is useful to define the figure of merit $W = \Delta\Phi_{NL}/2\pi\alpha L$, thus obtaining

$$W = \Delta n_{sat}/\alpha_0\lambda_0. \quad (1.2)$$

On the other hand, working well below the conduction band edge but above half bandgap, TPA dominates the picture ($\beta_2 I \gg \alpha_0$), $\Delta n_{NL} = n_2 I$ and a different FOM applies, $T = 2\pi\alpha L/\Delta\Phi_{NL}$, which yields

$$T = \lambda_0\beta_2/n_2. \quad (1.3)$$

It can be clearly seen that, for successful switching, both conditions $W > p/2$ and $T < 2/p$ must be met simultaneously¹. In addition, if ultrafast switching is to be achieved, it was thought that the relaxation time of the material should be less than 10 ps to allow for recovery between two pulses. This, in principle, ruled out semiconductors as realistic candidates operating near the bandgap because of the slow recovery rate associated with band filling nonlinearities (typically ~ 1 ns, unless carrier sweep-out was employed or trapping centers introduced). On the other hand, below half bandgap operation is faster due to virtually instantaneous Kerr nonlinearities, but at the unaffordable cost of high switching powers [3].

1.1.2 SOAs in optical switching

A SOA, otherwise known as Semiconductor Laser Amplifier (SLA) or Travelling Wave Amplifier (TWA), is simply a semiconductor diode laser whose facets have been antireflection coated or angled to minimise the feedback and thus prevent the device from lasing. Despite being promising candidates for high speed optical communications in the 1980's, they were soon displaced when Erbium Doped Fibre Amplifiers (EDFAs) became com-

¹*SiO*₂, for example, has an excellent figure of merit ($T \ll 1$) at wavelengths longer than 1.06 μ m due to the very low absorption coefficient ($\sim 10^{-6}$ cm⁻¹). On the negative side, however, using multikilometer lengths of fibre causes long latency times between input and output. Figures of merit for other materials can be found in references [2, 5].

mercially available. The latter proved to have superior performance in terms of linearity, absence of crosstalk in wavelength division multiplexing applications and polarisation independence near $1.55\ \mu\text{m}$, thus replacing SOAs as in-line repeaters. It is precisely the strong nonlinearities inherent to SOAs that makes them interesting for switching. In fact, it turned out that a SOA biased for gain automatically meets Stegeman's criteria, since the pulse is amplified as it propagates through the device. This has resulted in extensive research being conducted on SOA-based switches over the last decade. Below, we focus on the Terahertz Asymmetric demultiplexer (TOAD), as it raises issues common to many other interferometric switching configurations and corresponds to the experimental set-up used in our work. Other alternative switches employing SOAs are also discussed.

The Terahertz Optical Asymmetric Demultiplexer (TOAD)

One of the earliest switching configurations to employ SOAs followed previous work on fibre-based nonlinear optical mirrors. This was the implementation of a Semiconductor Laser Amplifier in a Loop Mirror configuration (SLALOM) [6] experimentally performing contrast enhancement and optical correlation. In the same year, Sokoloff *et al.* [7] first reported the Terahertz Optical Asymmetric Demultiplexer (TOAD).

The TOAD is basically a NOLM in which kilometres of fibre are substituted by a SOA placed asymmetrically within the loop with an offset Δx (see figure 1.2). It relies on the gain saturation nonlinearity of the SOA induced by an intense control pulse to introduce the required phase shift between the counter-propagating pulse replicas.

The role of the control pulse is to saturate the gain and thus cause a change in refractive index. If the control pulse arrives at the SOA well after the replicas, both replicas will be more than Δx from the SOA and traveling away without having experienced any nonlinear refractive index change. No signal emerges from the output port after the pulses recombine in the coupler, according to the reflectivity formula of the loop mirror.

$$R = \frac{1}{2} [1 + \cos(\Delta\phi)] \quad (1.4)$$

where $\Delta\phi$ is the phase difference between the two replicas. Let us assume now that the control pulse arrives at the SOA well before the pulse entering the loop from the coupler.

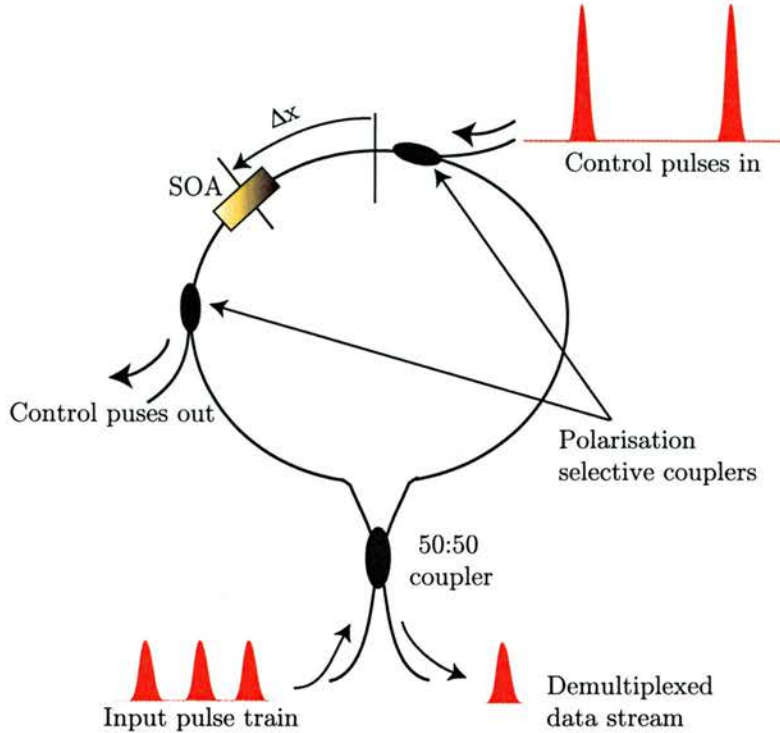


Figure 1.2: Sketch of a TOAD. The control pulses are introduced in the loop via polarisation couplers (this would not be necessary if, for example, different wavelengths are used for pump and probe). Note that the clockwise propagating (CW) replica reaches the SOA $2\Delta x/c$ seconds before its counter clockwise (CCW) twin.

Now, the gain is already saturated when both replicas head towards the SOA. Being a time $2\Delta x/c$ apart, when they reach the SOA, they will experience a slow recovering gain and accumulate roughly the same phase (provided that $\tau_{recovery} \gg 2\Delta x/c$), again interfering in the coupler without producing an output pulse.

Finally, consider the case when the signal pulse enters the loop at about the same time as the control pulse. By the time the latter arrives at the SOA, the clockwise propagating (CW) replica has already crossed the device and is traveling back to the coupler. However, the counter clockwise (CCW) pulse arrives after the SOA gain has been saturated and experiences a non linear refractive index change. Because of the phase difference between both replicas, they will interfere in the coupler to give an output pulse. Figure 1.3 depicts the evolution of the carrier density in the amplifier when the control stream is formed by a regular train of pulses (as it is the case in a demultiplexer). Note that the arrival of the control pulse in between clockwise and anticlockwise replicas causes the depletion of the carrier density and, concomitantly, a change in the refractive index.

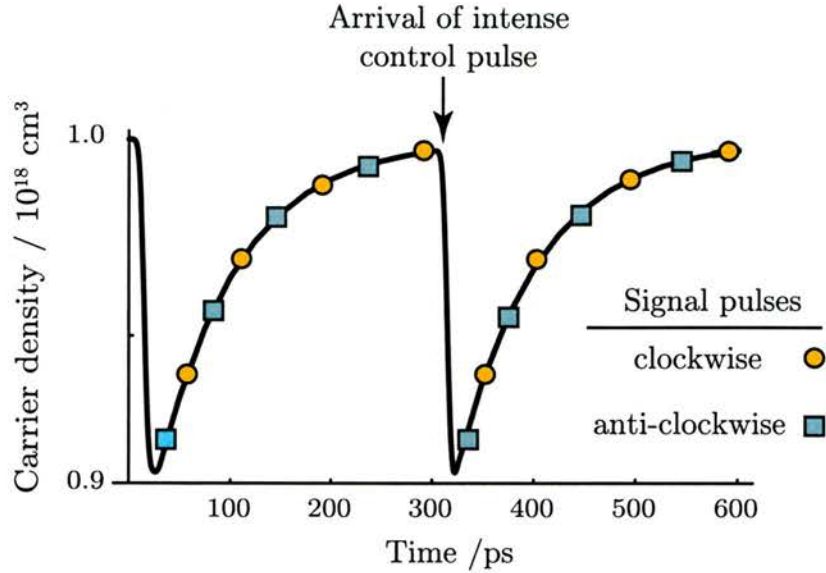


Figure 1.3: Sketch of the temporal evolution of the SOA carrier density in a TOAD. Circles and squares indicate, respectively, the arrival at the amplifier of clockwise and anticlockwise signal pulses. The role of the control pulses is to deplete some of the available carrier density and induce a differential phase shift between a pair of counter-propagating data pulse replicas. After the perturbation caused by the control pulse, the carrier density recovers.

In conclusion, the offset Δx creates a switching window $2\Delta x/c$ seconds long, meaning that any pulse whose replicas lay within a Δx range of the SOA when its gain is saturated, will exit from the output channel. Switching will be possible providing that the temporal window is smaller than the bit period in the channel to be demultiplexed. It was thought that the SOA should be allowed to fully recover before the next bit was demultiplexed. (Sokoloff *et al.* reported demultiplexing of a 50 Gb/s channel down to a 1.25 Gb/s data stream). Therefore, the slow recovering (~ 1 ns) nonlinearity of the SOA still imposed a limit to the demultiplexing rate.

The small size of SOAs, typically in the order of $500 \mu m$ long, makes them more stable than optical fibre, avoids long latency times, and is suitable for on-chip integration. Despite the latter, the definitive breakthrough came with the experimental demonstration by Ellis and Spirit [8] that the TOAD could be operated faster than the rate imposed by the device recovery time. A 40 Gbits/s data stream was demultiplexed into a 10 Gbits/s pulse train. This is possible because, for typical devices, the carrier density change required for a π phase shift can be replenished on a timescale as short as tens of picoseconds. To numerically illustrate this, assume a $500 \mu m$ long SOA operating at $1.5 \mu m$. An index change of 1.5×10^{-3} corresponds to a π phase shift. Taking the rate of

change of the refractive index with carrier density to be $dn/dN = -2 \times 10^{-20} \text{ cm}^3$ [9], a population change of $\sim 10^{17} \text{ cm}^{-3}$ is thus required. Regarding the typical inversions available ($\sim 10^{18} \text{ cm}^{-3}$), it is clear that multiple π phase shifts can be achieved under normal conditions. In conclusion, when operating the TOAD at high switching rates, the SOA is not allowed to fully recover between control pulses.

Although the switching window width of the TOAD is in principle determined by the offset Δx of the amplifier in the loop, the finite device length will impose extra limitations. This is a common feature of switches in which data and control pulses counter-propagate [10], and will be discussed thoroughly in chapter 4, in connection with the spatial dependence of optical nonlinearities in SOAs.

Other SOA-based switches

In parallel with the TOAD, other switches employing SOAs have been developed. One remarkable example is the symmetric Mach Zehnder interferometer (SMZ)(see figure 1.4(a)), first implemented by Tajima and coworkers in 1993 [11]. Its operation is based on the band-filling effect in conventional semiconductor materials (SOAs or passive nonlinear waveguides, NLW), combined with differential phase modulation of the nonlinear elements.

In these switches, the data pulse is split into two identical replicas, each traveling along one of the arms of the interferometer. In the absence of any perturbation, the MZ is balanced to send the data pulse to the 'reject' port. To achieve switching, two control pulses are injected each into one arm of the interferometer, with a relative delay Δt_c between them. The photon energy of the control pulses is chosen to be larger than the semiconductor bandgap to induce interband transitions and cause the saturation of gain/absorption (depending on whether an SOA or a passive NLW is used). However, the wavelength of the data pulses is longer than the wavelength at the bandgap so that these only experience the subsequent changes in the refractive index and none of the gain compression. This is sometimes referred to as gain-transparent configuration [12, 13].

When the timing is such that the data pulse travels in between the two control pulses, one of its replicas will experience a depleted NLW, while the other replica propagates through an unperturbed nonlinear waveguide. The subsequent phase shift between the replicas will give a transmitted pulse in the output port. If the data pulse arrives at the

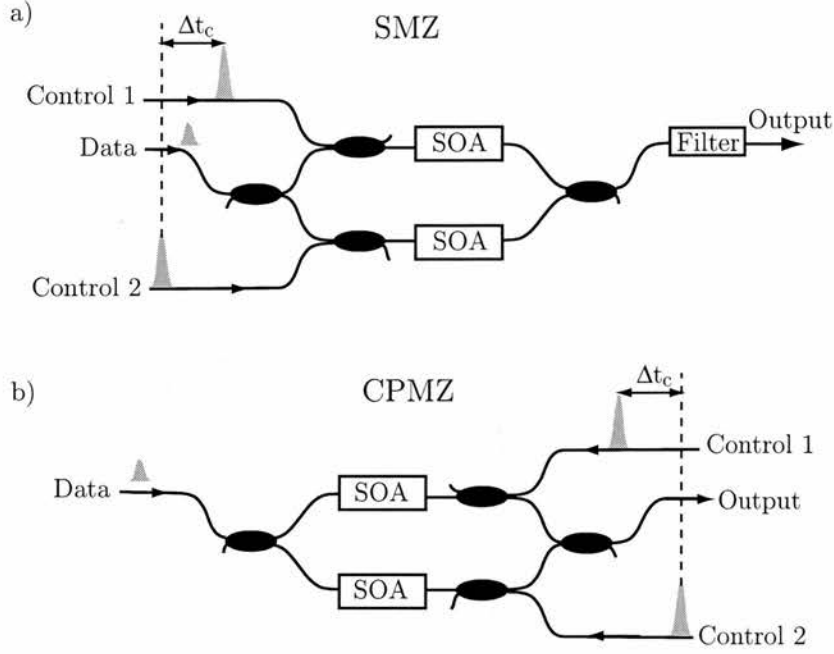


Figure 1.4: Sketch of (a) Symmetric Mach-Zehnder Interferometer (SMZ) and (b) Colliding Pulse Mach-Zehnder Interferometer (CPMZ).

amplifiers later than the control pulses, both replicas will experience the slowly recovering gain and accumulate a similar phase, thus sending the data pulse to the 'reject' port. Therefore, the width of the switching window in a MZ is determined by the delay between the two control pulses, Δt_c .

In the SMZ, control and data pulses co-propagate and a filter is needed in the output port to discriminate between them. The colliding pulse MZ (CPMZ) (see figure 1.4(b)) avoids this problem by using counter-propagating control and data pulses, which in turn imposes extra limitations on the window width, as we will discuss in detail in section 4.4. Both configurations present the 'a priori' disadvantage of using two nonlinear elements, thus requiring an accurate balance between them. On the other hand, compared with the TOAD, the SMZ exhibits shorter switching windows due to the co-propagating nature of control and data pulses.

An interesting variant of the original SMZ, using only one nonlinear element, is the polarisation discriminating SMZ (PD-SMZ) [14], also known as ultrafast nonlinear interferometer (UNI) [15] when employing a SOA as the nonlinear element. The linearly polarised signal pulse is split into TE and TM components, one of which is delayed with

respect to the other before reaching the nonlinear waveguide (or the SOA). If a control pulse is injected into the NLW after the leading pulse component but before the trailing one, the latter acquires a nonlinear phase shift as a result of the long-lived change in the refractive index induced by the control pulse. The delay between the components of the data pulse is then recovered by means of some birefringent medium. The acquired differential phase shift will dictate the polarisation of the output signal and, by using a polariser, the output of the switch.

To date, the PD-SMZ has yielded the shortest switching windows (~ 200 fs [16]) obtained via the band-filling nonlinearity in semiconductor based switches. However, large control pulse energies (a few picojoules) are required to induced the necessary differential phase shift in passive nonlinear waveguides. The use of SOAs in MZ switches has lowered considerably the power requirements, as the band-filling nonlinearity is enhanced by stimulated emission [17, 18]. In this case, nevertheless, the gating speed is affected by the intraband phenomena in the amplifier, as it will be discussed in chapters 2 and 4.

Although the work presented in this thesis is mostly concerned with switching, it must be noted that other key functions of all-optical networks such as 3R regeneration (reamplifying, reshaping, and retiming) [19] can also be implemented by means of the SOA nonlinearities. Another remarkable example which has attracted considerable attention is wavelength conversion [20], crucial for WDM applications. Several types of SOA-based wavelength convertors have been reported, making use of four wave mixing, cross-gain or cross-phase modulation. In the case of cross-gain and cross-phase modulation, the control sequence is the data stream itself, which patterns a regular clock or CW beam at a different wavelength. Cross-phase modulation is usually employed within an interferometric arrangement similar to those described previously.

1.1.3 Current status and challenges for SOA-based all-optical switches

The successful integration of interferometric switches [21, 22], providing stable operation and minimising the switching power requirements, has been a significant boost for the competitiveness of SOAs as nonlinear elements for all optical switching. However, such integration is at an early stage, and there are still major challenges ahead both in terms of response speed and power consumption.

Beyond size and potential for integration, SOAs offer several other advantages in the context of interferometric all optical switching. These include signal amplification and large resonant nonlinearities (enhanced by stimulated emission), which ultimately allow for switching powers well below 1 pJ, smaller by almost two orders of magnitude compared to those required with passive elements. On the downside, the interband dynamics in SOAs exhibit a slow recovery, the nonlinearities may cause channel cross-talk, and the amplified spontaneous emission (ASE) contributes to the noise in communication channels.

The switching window widths of interferometric configurations such as the TOAD or MZ interferometers are not limited by the slow recovery time associated with the band filling nonlinearity. However, the finite device length imposes restrictions in the form of degradation of the bit error rate (BER) in those switches, e.g. the TOAD, with counter-propagating control and data pulses. Configurations like the SMZ avoid this problem at the expense of using two SOAs, with the subsequent balancing issues. In terms of switching ratio and reduction of noise due to ASE, the use of non degenerate signal and control wavelengths [11, 13] seems advantageous.

When it comes to achieving high repetition rates, the slow band-filling nonlinearity in SOAs is a drawback. In demultiplexing, as previously discussed, full recovery is not strictly necessary for switching operation and ongoing research efforts have been devoted to speeding up the recovery by means of larger applied bias or optical holding beams. In this respect, the work with Quantum Dot (QD) SOAs is also promising, as recovery times of a few picoseconds have been reported [23, 24]. Also, the potential improvements resulting from the optimisation of SOAs as phase shifters instead of amplifiers have not been yet fully explored.

Apart from demultiplexing, more complex processing functions have been implemented to date based on architectures like the TOAD. These include loop mirrors with feedback working as shift registers and spontaneous clock division [25, 26], clock recovery [27, 28] and all optical memory [29]. Some of these applications, such as clock recovery, and others (e.g. wavelength conversion or 3R-regeneration) require driving the SOA with a modulated train of pulses, as opposed to using regular sequence of control pulses. This complicates the picture, the reason being that when several zeros occur consecutively, the SOA is allowed to further recover and the quasi-equilibrium in phase/carrier density

evolution is perturbed, leading to data patterning effects. This issue stresses the need for faster recovery times mentioned in the paragraph above.

In the quest for higher switching speeds, pulse durations are progressively shortened making jitter levels more of a problem. In the subpicosecond regime, the SOA intraband dynamics such as carrier heating and spectral hole burning become important in dictating the device behaviour, as discussed in the next chapter. In principle, these ultrafast nonlinearities have been found to reduce the gating speed [18], although there is still much to be understood in this respect. Additionally, the use of pulse durations below 100 fs is expected to raise issues related to dispersion and coherent effects.

Presently, research on all-optical switching by means other than SOAs has attracted considerable attention (see, for example, [30] and references therein). Ongoing work is devoted to investigating new ultrafast nonlinearities in material families that have been used traditionally for optoelectronic devices, such as GaAs and InP. Spin relaxation in QW structures, for example, has been used to implement all-optical spin polarisation switches [31]. The ultrafast dynamics of intersubband transitions in quantum wells, crucial to the operation of QC lasers as we will soon discuss, are also appealing for all-optical switching applications. To achieve operation wavelengths in the $1.3 - 1.5 \mu m$ range, material systems with large band offsets such as InGaAs/AlAsSb [32] or GaN/AlGaN have been investigated.

1.2 Quantum Cascade lasers

1.2.1 Introduction

In the previous section, we have discussed the potential of semiconductor amplifiers for optical processing in communication systems. Such applications require operating in the near-infrared wavelength range, mostly at around 1.5 or $1.3 \mu m$ wavelength, for which conventional semiconductor device technology is well suited and widely established.

The mid-IR range of the spectrum also attracts considerable attention, amongst other reasons because it comprises both the molecular fingerprint region ($3 - 20 \mu m$) and the atmospheric windows for free-space optical communications ($3 - 5 \mu m$ and $8 - 13 \mu m$). Practical applications such as trace gas sensing require compact tunable optical sources.

Despite the fact that the band structure of semiconductors can be tailored to some extent [33], by virtue of quantum confinement of the carriers in one or more dimensions or via strain engineering, the emission characteristics of conventional diode lasers are still drastically limited by material properties, notably, the energy bandgap. For this reason, until recently, the choices for semiconductor-based tunable optical sources in the mid-IR wavelength range have been limited almost exclusively to lead-salt lasers.

Quantum Cascade (QC) lasers are novel semiconductor injector lasers based on optical and electronic intersubband transitions (ISTs) in multiple quantum well heterostructures. Light emission from these devices can be controlled via the well and barrier thicknesses and the external applied electric field. This allows for great design flexibility and true band-structure engineering [34]. In addition, the unipolar nature of QC lasers allows electrons to remain in the conduction band and undergo several ISTs, resulting in large output powers. In this section, the origins and the evolution of QC lasers will be reviewed, along with their most remarkable characteristics. Finally, in connection with the work to be presented in this thesis, the current research trends and challenges will be identified.

1.2.2 Background and present challenges

Soon after the seminal paper by Esaki and Tsu introducing the concept of the superlattice [35], Kazarinov and Suris postulated in 1971 that light amplification was possible in intersubband transitions [36]. This proposal covered both the required population inversion and the cascading of the carriers across many stages. In practice, however, the structure could not achieve a uniform electric field or stable current flow due to space charge injection.

It took over twenty years until a device based on such a gain mechanism, the Quantum Cascade laser, was successfully implemented [37, 38]. This accomplishment owed to previous progress in the understanding of tunneling and scattering phenomena (see, for example, the review in reference [39]), and to high quality growth by state-of-the-art Molecular Beam Epitaxy (MBE).

The first QC laser to be implemented back in 1994 was operated in pulsed mode at cryogenic temperatures. The laser transition was diagonal in real space, i.e., upper and lower laser states were mostly localised in different wells. This scheme was soon replaced

with the so called 'three well vertical' design and, within the year that followed, CW operation at cryogenic temperatures [40] and, in pulsed mode, up to room temperature (RT) [41] were demonstrated. Since then, the performance of QC lasers has greatly improved [39, 42], both in terms of operating temperature, available wavelength range and output power.

In 1996, QC-DFB lasers were introduced, providing continuously tunable single mode laser output [43] and thus very well suited for trace gas sensing applications, as demonstrated for the first time two years later [44]. The quest for improved performance led to novel design concepts. One remarkable example is the superlattice active region [45], in which the laser transition occurs between broad minibands rather than between discrete subbands. This scheme allows for larger current flow, being thus ideal for obtaining higher powers or emission at longer wavelengths, as they experience more absorption loss.

In 1998, the 'bow-tie' laser, a variant of previously researched QC micro-disc and micro-cylinder lasers, was implemented [46]. These QC-based micro-lasers presented distinct directionality and an output power increase of several orders of magnitude. Up to this point, QC lasers had been successfully grown only in the InGaAs/AlInAs on InP material system. Sirtori and coworkers [47] were the first to demonstrate a QC laser in the GaAs/AlGaAs on GaAs material system, currently subject of ongoing research.

A unique feature of QC lasers is the ultrafast carrier relaxation time, mostly determined by electron-optical phonon scattering, making them ideal for high-speed operation. This aspect has also been explored [48], including ultrashort pulse generation via mode-locking [49], or high-speed data transmission [50]. More recently, the flexibility in the design of QC structures has allowed the implementation of new functionalities, such as multiple-wavelength [51] or ultrabroadband [52, 53, 54] QC lasers.

At present, ongoing research is devoted to increasing the maximum CW operating temperature. This is crucial for trace gas sensing and other applications.

Considerable effort is also being devoted to expand the range of wavelengths available with QC lasers, both towards the near-IR region and into the Terahertz regime. In this context, for the last couple of years, nonlinear light generation in QC-lasers has been one subject of research. To date, various types of nonlinearities based on intersubband transitions have been successfully integrated with QC lasers [55, 56, 57, 58]. In this

thesis, we report the observation of stimulated electronic Anti-Stokes Raman emission in QC lasers (see chapter 5). This is the first step towards AS Raman lasing, which holds promise to extend straightforward operation of unstrained InP QC lasers to wavelengths below $4\ \mu\text{m}$.

Parallel to the developments in QC laser technology, other novel semiconductor-based sources in the mid-infrared wavelength range have been demonstrated. The 'quantum-fountain' laser [59, 60] relies on optically-pumped intersubband transitions in asymmetric quantum wells, but does not include the cascade effect. Another remarkable example are the so called type-II cascade lasers, proposed by Yang [61, 62] and also researched by other groups [63]. These devices are based on diagonal inter-well interband transitions occurring when an electron recombines with a hole in the valence band. Due to the type-II band alignment, electrons can efficiently re-tunnel into the conduction band and thus undergo several transitions.

1.3 Light propagation in active media

To analyse the interaction of light with the carriers in the semiconductor devices studied in this thesis, it is useful to give a brief introduction to the propagation of light in active media in the framework of Maxwell's equations.

Assuming that the electric field varies little in the direction of propagation ($\nabla\mathbf{E} \approx 0$) and a non-magnetic medium ($\mu = \mu_0$), the wave equation reads

$$\nabla^2\mathbf{E}(\mathbf{r}, t) = \mu_0 \frac{\partial^2\mathbf{D}(\mathbf{r}, t)}{\partial t^2}. \quad (1.5)$$

Here, the light-matter interaction is represented by the displacement electric field \mathbf{D} . When it comes to semiconductor active media, it is useful to define \mathbf{D} as

$$\mathbf{D} = \epsilon_b\mathbf{E} + \mathbf{P}, \quad (1.6)$$

distinguishing the background permeability of the host medium (the lattice) ϵ_b and the induced polarisation corresponding to the carriers. By using equation 1.6, the wave equation can be rewritten as

$$\nabla^2 \mathbf{E} - \frac{n_b^2}{c^2} \frac{\partial^2 \mathbf{E}}{\partial t^2} = \mu_0 \frac{\partial^2 \mathbf{P}}{\partial t^2}. \quad (1.7)$$

where $n_b^2 = \epsilon_b/\epsilon_0$ is the background refractive index, typically around 3.5, and $c = 1/\sqrt{\epsilon_0\mu_0}$ is the speed of light in the vacuum.

1.3.1 Linear propagation

For optical beams with not too high intensities, the polarisation induced in the medium can be taken to depend linearly on the optical field. Using scalar notation for the sake of simplicity, this dependence for a non-polar medium can be expressed as

$$P = \epsilon_0 \chi E, \quad (1.8)$$

χ being the complex susceptibility of the medium. Under these assumptions, one of the simplest solutions to the wave equation (1.7) is a plane wave-like optical field of the form

$$E(z, t) = E(z) \exp \{i [k_b z - \omega_0 t + \varphi(z)]\} + \text{c.c.}, \quad (1.9)$$

taken to be propagating in the z direction and with an angular frequency ω_0 . k_b is the wavevector associated with the background refractive index ($k_b = \omega_0 n_b/c$) and $\varphi(z)$ is a phase term resulting from the interaction of light and carriers. Substituting equations 1.8 and 1.9 in the wave equation (1.7), in the slowly varying envelope approximation -neglecting terms containing $d^2 E/dz^2$, $d^2 \varphi/dt^2$ and $(dE/dz)(d\varphi/dt)$ -, we find

$$\frac{dE}{dz} = -\frac{k_b}{2} \chi''(z) E(z), \quad (1.10a)$$

$$\frac{d\varphi}{dz} = -\frac{k_b}{2} \chi'(z), \quad (1.10b)$$

Here, χ' and χ'' are the real and imaginary parts of the complex susceptibility ($\chi = \chi' + i\chi''$), whose functional form is material dependent. However, in general terms, the intensity of the optical field will change as

$$I(z) = I_0 \exp(gz), \quad (1.11)$$

where $g = -k_b\chi''$ is the so called gain coefficient. Note that light will be absorbed if $g < 0$, as it occurs in passive semiconductor materials. On the other hand, the effective contribution to the refractive index due to the carriers via the term $\varphi(z)$ is

$$\Delta n = \frac{k_b c}{2\omega_0} \chi', \quad (1.12)$$

and therefore the optical field propagates with a total wavevector $k = k_b(1 + \chi'/2)$ and a phase velocity given by ω_0/k . It must be stressed that both the background refractive index and the complex susceptibility caused by the carriers are strongly dependent on frequency. This dependence is usually referred to as material dispersion.

In the linear regime, the frequency dependent background refractive index $n_b(\omega)$ can be modelled in the framework of a simple Lorentz oscillator model and expressed by an empirical Sellmeier equation of the form

$$n_b(\omega) - 1 = \sum_j \frac{A_j}{\omega_j^2 - \omega^2}, \quad (1.13)$$

where the parameters A_j and ω_j depend on the material and must be obtained experimentally. Equation 1.13 also applies to passive semiconductors or dielectrics. However, the expression of $\chi(\omega)$ for active gain materials is not so simple and depends of the particulars of the system to be described (the optical gain in SOAs, for example, is discussed in chapter 2).

For the time being, let us assume that the total refractive index experienced by the propagating optical field in the linear regime is $n(\omega)$, including the contributions of carriers and background refractive index. Then, the phase accumulated after propagating along a distance L is

$$\phi(\omega) = \frac{\omega n(\omega)}{c} L. \quad (1.14)$$

$\phi(\omega)$ in equation 1.14 is sometimes referred to as the phase transfer function, and will be very useful in analysing the implications of material dispersion on the linear propagation of optical pulses, discussed next.

Optical pulses and dispersion

In the previous section, we assumed a monochromatic optical field with angular frequency ω_0 . However, our measurements on semiconductor optical amplifiers are carried out by using subpicosecond pulses and dispersion becomes significant. In the time domain, optical pulses can be expressed as the product of a slow varying envelope and a fast oscillating exponential term at the carrier frequency ω_0

$$E(t) = A(t) \exp(-i\omega_0 t), \quad (1.15)$$

which, on the frequency domain, corresponds to

$$\tilde{E}(\omega) = \tilde{A}(\omega - \omega_0) \quad (1.16)$$

In the linear regime, the phase accumulated by the pulse upon propagation is given by the phase transfer function of equation 1.14. The dispersive properties of the system can be extracted by expanding this transfer function around the carrier frequency [64]

$$\phi(\omega) = \sum_n \frac{1}{n!} \phi^{(n)}(\omega_0) (\omega - \omega_0)^n \quad (1.17)$$

where $\phi^{(n)}(\omega_0)$ is the n^{th} -order derivative of ψ with respect to ω , evaluated at the carrier frequency. The zero-order term of the expansion is the phase accumulated at the frequency of the optical carrier. $\phi^{(1)}$, usually expressed in units of femtoseconds, gives the velocity at which the center of the pulse envelope propagates in the medium (group velocity).

$$v_g = \frac{d\omega}{dk} = L \frac{d\omega}{d\phi} \quad (1.18)$$

The coefficient $\phi^{(2)}$, called group delay dispersion (GDD) and measured in units of fs^2 , is of the outmost importance. GDD, roughly, measures the rate at which a pulse centered at the reference frequency will increase in duration upon propagation through the system. It is also responsible for the variations in the instantaneous frequency of the optical pulses, defined as $\partial \arg[E(t)]/\partial t$, known as chirping. Dispersion is said to be negative or positive depending on the sign of the GDD. The distortion introduced by higher order terms is

more difficult to interpret.

Pulse distortion can be managed by virtue of the dispersive properties of some materials. One relevant example is the introduction of glass prisms in optical cavities, such as those in the Optical Parametric Oscillator of our pump-probe setup (see section 3.2.2).

Typically, light in semiconductor devices is confined to a waveguide in which the optical mode experiences an effective refractive index n_{eff} . The nature of the frequency dependence of n_{eff} is twofold, originating both from the inherent material dispersion and the geometry of the optical confinement (waveguide dispersion) [64].

1.3.2 Nonlinear phenomena

When interacting with high-intensity optical beams, the material response deviates from a linear behaviour. A more general expression for the polarisation in the medium is required, including higher order terms [65]

$$P_i = \epsilon_0 \chi_{ij}^{(1)} E_j + \epsilon_0 \chi_{ijk}^{(2)} E_j E_k + \epsilon_0 \chi_{ijkl}^{(3)} E_j E_k E_l + \dots \quad (1.19)$$

where P_i is the i component of the polarisation vector. $\chi^{(1)}$ is the first order susceptibility, used in the previous discussion of the material linear properties. $\chi^{(n)}$ are the higher (n^{th}) order complex susceptibility tensors, whose values are smaller for increasing order, hence the need for large optical powers to observe nonlinear phenomena.

Second and higher order terms in equation 1.19 include the product of two or more components of the electric field. This may result in frequency mixing and, as the polarisation is the source of optical field in the wave equation (1.7), lead to the generation of light at new wavelengths. As nonlinear optics is a broad field in itself, with a wide spectrum of applications, this section is limited to introducing briefly some of the optical nonlinearities most relevant to our work.

Second order processes can be observed in noncentrosymmetric crystalline materials [66], provided high optical intensities. Of these, non-resonant second harmonic generation (SHG) and difference frequency generation (DFG) must be highlighted. They are used in our setup, respectively, to estimate the duration of the optical pulses (autocorrelation technique) and to produce pulses in the near-IR wavelength range (further details in

chapter 3).

In the context of this work, $\chi^{(3)}$ and related processes are of the outmost importance. Concerning SOAs, the third order processes manifest mostly in the form of self- or cross-modulation of the propagating pulses, both in amplitude and in phase.

As discussed previously in this chapter, many SOA-based interferometric switches rely on the cross-phase modulation associated with the long lived band-filling resonant nonlinearity. Additionally, as a result of the limited states available for stimulated transitions, the gain/refractive index experienced by an optical pulse may saturate for high pulse intensities. In the low saturation regime, this dependence on the intensity can be regarded as a third order contribution to the susceptibility [33, 65, 66].

The propagation of optical pulses across the amplifier may also be influenced by additional third order nonlinear processes such as Two Photon Absorption (TPA) or the optical Kerr effect, especially for high pulse peak powers. The loss associated with TPA can be expressed via the absorption coefficient $\alpha_{TPA} = \beta_2 I(t)$, dependent on the intensity profile of the pulse $I(t)$, where β_2 is the two-photon coefficient. When occurring in the active region, TPA may contribute to the heating of the carriers, causing a further decrease of the available gain. The reduction in gain caused by TPA is accompanied by an instantaneous change in the refractive index which follows the temporal intensity profile of the pulse.

The optical Kerr effect is a nonresonant third order nonlinearity which contributes exclusively to the real part of $\chi^{(3)}$ and hence to the self-modulation of the optical pulses via the nonlinear refractive index. Similarly to TPA, the change in the refractive index caused by the Kerr effect is proportional to the pulse intensity. Mathematically

$$\Delta n_{Kerr} = \frac{3\text{Re}[\chi^{(3)}]}{4\epsilon_0 n_0^2 c} I(t) = n_2 I(t). \quad (1.20)$$

The Kerr coefficient n_2 is typically small, but this effect may still be significant due to the high peak powers of ultrashort pulses (remember, for example, the operation of the fibre nonlinear optical mirror switch described in section 1.1.1).

The work presented on chapter 5 deals with the study of nonlinear generation of light in QC lasers via a third order process, stimulated Raman scattering. In this case,

the $\chi^{(3)}$ nonlinearity is based on real electronic intersubband transitions. The nonlinear susceptibility is greatly enhanced by optical pumping near resonance of the ISTs.

1.4 Summary

In the present chapter, we have analysed the role of SOAs in all-optical processing applications, reviewing current research efforts and identifying key areas for improvement. The carrier ultrafast dynamics in SOAs relevant to interferometric switching, both interband and intraband, will be described in chapter 2.

QC lasers have also been introduced as novel optical sources for applications in the mid to far-IR wavelength range, reviewing past and present research trends. In this context, the integration of nonlinearities based on intersubband transitions and QC lasers has been addressed. The operation of these lasers will be described in detail in chapter 2, with emphasis on crucial issues such as resonant tunneling and intersubband LO-phonon scattering.

Finally, the basics of light propagation in active media have been reviewed. This provides a background on which understand and model the amplification of light and nonlinear phenomena in devices with optical gain such as SOAs and QC lasers.

References for Chapter 1

- [1] H M Gibbs. *Optical bistability: controlling light with light*. Academic Press, Orlando, 1985.
- [2] G I Stegeman and A Miller. *Photonics in Switching*, volume 1, chapter Physics of all-optical switching devices, pages 81–145. Academic Press, London, 1993.
- [3] J S Atchinson, A H Kean, C N Ironside, A Villeneuve, and G I Stegeman. Ultrafast all-optical switching in $Al_{0.18}Ga_{0.82}As$ directional coupler in $1.55\ \mu\text{m}$ region. *Electron. Lett.*, 27(19):1709–1710, 1991.
- [4] N J Doran and D Wood. Nonlinear-optical loop mirror. *Opt. Lett.*, 13(1):56–58, 1988.
- [5] G I Stegeman, E M Wright, N Finlayson, R Zanoni, and C T Seaton. Third Order Nonlinear Integrated Optics. *IEEE/OSA J. Lightwave Technol.*, 6(6):953–970, 1988.
- [6] M Eiselt, W Pieper, and H G Weber. SLALOM: Semiconductor laser amplifier in a loop mirror. *IEEE J. Lightwave Technol.*, 13(10):2099, 1995.
- [7] J P Sokoloff, P R Prucnal, I Glesk, and M Kane. A terahertz optical asymmetric demultiplexer (TOAD). *IEEE Photon. Technol. Lett.*, 5(7):787, 1993.
- [8] A D Ellis and D M Spirit. Compact 40 gbit/s optical demultiplexer using a GaInAsP optical amplifier. *Electron. Lett.*, 29(24):2115, 1993.
- [9] D Cotter, R J Manning, K J Blow, A D Ellis, A E Kelly, D Nisset, I D Phillips, A J Poustie, and D C Rogers. Nonlinear optics for high-speed digital information processing. *Science*, 286(5444):1523–1528, 1999.
- [10] P Toliver, T Runser, I Glesk, and P R Prucnal. Comparison of three nonlinear interferometric optical switch geometries. *Opt. Commun.*, 175:365–373, 2000.
- [11] K Tajima. All-optical switch with switch-off time unrestricted by carrier lifetime. *Jpn. J. Appl. Phys.*, 32 Part 2(12A):L1746–L1749, 1993.
- [12] G Toptchiyski, S Randel, K Petermann, S Diez, E Hilliger, C Schimidt, C Schubert, R Ludwig, and H G Weber. Analysis of switching windows in a gain-transparent-SLALOM configuration. *IEEE/OSA J. Lightwave Technol.*, 18(12):2188–2195, 2000.
- [13] C Schubert, J Berger, S Diez, H J Ehrke, R Ludwig, U Feiste, C Schmidt, H G Weber, G Toptchiyski and S Randel, and K Petermann. Comparison of interferometric all-optical switches for demultiplexing applications in high-speed OTDM systems. *IEEE/OSA J. Lightwave Technol.*, 20(4):618–624, 2002.
- [14] K Tajima, S Nakamura, and Y Sugimoto. Ultrafast polarization-discriminating Mach-Zehnder all-optical switch. *Appl. Phys. Lett.*, 67(25):3709–3711, 1995.
- [15] N A Patel, K A Rauschenbach, and K L Hall. 40-GB/S demultiplexing using an ultrafast nonlinear interferometer (UNI). *IEEE Photon. Technol. Lett.*, 8(12):1695, 1996.
- [16] S Nakamura, Y Ueno, and K Tajima. Ultrafast (200fs switching, 150-Tb/s demultiplexing) and high-repetition (10 GHz) operation of a polarisation-discriminating symmetric Mach-Zehnder all-optical switch. *IEEE Photon. Technol. Lett.*, 10(11):1575–1577, 1998.
- [17] K Tajima, S Nakamura, and Y Ueno. Ultrafast all-optical signal processing with symmetric Mach-Zehnder type all-optical switches. *Opt. Quant. Electron.*, 33:875–897, 2001.
- [18] K Tajima, S Nakamura, and Y Ueno. Semiconductor nonlinearities for ultrafast all-optical gating. *Meas. Sci. Technol.*, 13:16921697, 2002.
- [19] Y Ueno, S Nakamura, and K Tajima. Pulse Regeneration at 84 Gb/s by Using a Symmetric-MachZehnder-Type Semiconductor Regenerator. *IEEE Photon. Technol. Lett.*, 13(5):469–471, 2001.
- [20] M J Adams, D A O Davies, M C Tatham, and M A Fisher. Non-linearities in semiconductor laser amplifiers. *Opt. Quant. Electron.*, 27:1–13, 1995.

- [21] V M Menon, W Tong, C Li, F Xia, I Glesk, P R Prucnal, and S F Forrest. All optical wavelength conversion using a regrowth free monolithically integrated Sagnac interferometer. *IEEE Photon. Technol. Lett.*, 15(2):254–256, 2003.
- [22] K Tajima, S Nakamura, Y Ueno, J Sasaki, T Sugimoto, T Kato, T Shimoda, M Itoh, H Hatakeyama, T Tamanuki, and T Sasaki. Hybrid integrated symmetric Mach-Zehnder all-optical switch with ultrafast, high extinction switching. *Electron. Lett.*, 35(23), 1999.
- [23] T Akiyama, H Kuwatsuka, T Simoyama, Y Nakata, K Mukai, M Sugawara, O Wada, and H Ishikawa. Nonlinear Gain Dynamics in Quantum-Dot Optical Amplifiers and Its Application to Optical Communication Devices. *IEEE J. Quantum Electron.*, 37(8):1059–1065, 2001.
- [24] P Borri, W Langbein, J M Hvam, F Heinrichsdorff, M H Mao, and D Bimberg. Spectral hole-burning and carrier-heating dynamics in quantum-dot amplifiers: comparison with bulk amplifiers. *Phys. Stat. Sol. B*, 224(2):419–423, 2001.
- [25] K J Blow, R J Manning, and A J Poustie. Nonlinear optical loop mirrors with feedback and a slow nonlinearity. *Opt. Commun.*, 134:43–48, 1997.
- [26] R J Manning, A E Kelley, K J Blow, A J Poustie, and D Nasset. Semiconductor optical amplifier based nonlinear optical loop mirror with feedback: Two modes of operation at high switching rates. *Opt. Commun.*, 157:45–51, 1998.
- [27] D M Patrick and R J Manning. 20 Gb/s all optical clock recovery using semiconductor nonlinearity. *Electron. Lett.*, 36:151–152, 1994.
- [28] R J Manning, A D Ellis, A J Poustie, and K J Blow. Semiconductor laser amplifiers for ultrafast all-optical signal processing. *J. Opt. Soc. Am. B*, 14(11):3204–3216, 1997.
- [29] A J Poustie, K J Blow, and R J Manning. All-optical regenerative memory for long term data storage. *Opt. Commun.*, 140:184–186, 1997.
- [30] O Wada. Femtosecond all-optical devices for ultrafast communication and signal processing. *New Journal of Physics*, 6:183, 2004.
- [31] Y Nishikawa, A Tackeuchi, M Yamaguchi, S Muto, and Osamu Wada. Ultrafast All-Optical Spin Polarization Switch Using Quantum-Well Etalon. *IEEE J. Sel. Top. Quantum Electron.*, 2(3):661–667, 1996.
- [32] T Akiyama, N Georgiev, T Mozume, H Yoshida, A Venu Gopal, and O Wada. 1.55 – μm picosecond all-optical switching by using intersubband absorption in InGaAs-AlAs-Sb coupled quantum wells. *IEEE Photon. Technol. Lett.*, 14(4):495–497, 2002.
- [33] W W Chow and S W Koch. *Semiconductor-laser fundamentals: physics of the gain materials*. Springer-Verlag, Berlin, 1999.
- [34] F Capasso. Band-gap engineering: From physics and materials to new semiconductor devices. *Science*, 35:172–176, 1987.
- [35] L Esaki and R Tsu. Superlattice and negative differential conductivity in semiconductors. *IBM J. Res. Develop.*, 14:61–65, 1970.
- [36] R Kazarinov and R A Suris. Amplification of electromagnetic waves in a semiconductor superlattice. *Sov. Phys. Semicond.*, 5:707709, 1971.
- [37] J Faist, F Capasso, D L Sivco, C Sirtori, A Hutchinson, and A Y Cho. Quantum cascade laser. *Science*, 264(5158):553–556, 1994.
- [38] F Capasso, J Faist, C Sirtori, and A Y Cho. Infrared (4–11 μm) quantum cascade lasers. *Solid Stat. Comm.*, 102(2-3):231–236, 1994.
- [39] F Capasso, R Paiella, R Martini, R Colombelli, C Gmachl, T L Myers, M S Taubman, R M Williams, C G Bethea, K Unterrainer, H Y Hwang, D L Sivco, A Y Cho, A M Sergent, H C Liu, and E A Whittaker. Quantum Cascade Lasers: Ultrahigh-Speed Operation, Optical Wireless Communication, Narrow Linewidth, and Far-Infrared Emission. *IEEE J. Quantum Electron.*, 38(6):512–532, 2002.

- [40] J Faist, F Capasso, C Sirtori, D L Sivco, A L Hutchinson, and A Y Cho. Vertical transition quantum cascade laser with Bragg confined excited state. *App. Phys. Lett.*, 66:538–540, 1994.
- [41] J Faist, F Capasso, C Sirtori, D L Sivco, J N Baillargeon, A L Hutchinson, S-N G Chu, and A Y Cho. High power mid-infrared ($\lambda \sim 5 \mu\text{m}$) quantum cascade lasers operating above room temperature. *App. Phys. Lett.*, 68(26):3680–3682, 1996.
- [42] C Gmachl, F Capasso, D L Sivco, and A Y Cho. Recent progress in quantum cascade lasers and applications. *Rep. Prog. Phys.*, 64(11):1533–1601, 2001.
- [43] J Faist, C Gmachl, F Capasso, C Sirtori, D L Sivco, J N Baillargeon, and A Y Cho. Distributed feedback quantum cascade lasers. *App. Phys. Lett.*, 70(20):2670–2672, 1997.
- [44] K Namjou, S Cai, E A Whittaker, J Faist, C Gmachl, F Capasso, D L Sivco, and A Y Cho. Sensitive absorption spectroscopy with a room-temperature distributed-feedback quantum-cascade laser. *Opt. Lett.*, 23(3), 1998.
- [45] G Scamarcio, F Capasso, C Sirtori, J Faist, A L Hutchinson, D L Sivco, and A Y Cho. High-power infrared (8-micrometer wavelength) superlattice lasers. *Science*, 276:773–776, 1997.
- [46] C Gmachl, F Capasso, E E Narimanov, J U Nöckel, A Douglas Stone, J Faist, D L Sivco, and A Y Cho. High-Power Directional Emission from Microlasers with Chaotic Resonators. *Science*, 280:1556–1564, 1998.
- [47] C Sirtori, P Kruck, S Barbieri, P Collot, J Nagle, M Beck, J Faist, and U Oesterle. $\text{GaAs}/\text{Al}_x\text{Ga}_{1-x}\text{As}$ quantum cascade lasers. *App. Phys. Lett.*, 73(24):3486–3488, 1998.
- [48] R Paiella, F Capasso, C Gmachl, C G Bethea, D L Sivco, J N Baillargeon, A L Hutchinson, A Y Cho, and H C Liu. Generation and Detection of High-Speed Pulses of Mid-Infrared Radiation with Intersubband Semiconductor Lasers and Detectors. *IEEE Photon. Technol. Lett.*, 12(7):780–782, 2000.
- [49] R Paiella, F Capasso, C Gmachl, D L Sivco, J N Baillargeon, A L Hutchinson, Alfred Cho, and H C Liu. Self-mode-locking of quantum cascade lasers with giant ultrafast optical nonlinearities. *Science*, 290:1739–1742, 2000.
- [50] R Martini, R Paiella, C Gmachl, F Capasso, E A Whittaker, H C Liu, H Y Hwang, D L Sivco, J N Baillargeon, and A Y Cho. High-speed digital data transmission using mid-infrared quantum cascade lasers. *Electron. Lett.*, 37(21):1290–1292, 2001.
- [51] C Gmachl, D L Sivco, J N Baillargeon, A L Hutchinson, F Capasso, and A Y Cho. Quantum cascade lasers with a heterogeneous cascade: Two-wavelength operation. *App. Phys. Lett.*, 79(5):572–574, 2001.
- [52] C Gmachl, D L Sivco, R Colombelli, F Capasso, and A Y Cho. Ultra-broadband semiconductor laser. *Nature*, 415:883–887, 2002.
- [53] C Gmachl, A Soibel, R Colombelli, D L Sivco, F Capasso, and A Y Cho. Minimal Group Refractive Index Dispersion and Gain Evolution in Ultra-Broad-Band Quantum Cascade Lasers. *IEEE Photon. Technol. Lett.*, 14(12):1671–1673, 2002.
- [54] A Soibel, C Gmachl, D L Sivco, M L Peabody, A M Sergent, A Y Cho, and F Capasso. Optimization of broadband quantum cascade lasers for continuous wave operation. *App. Phys. Lett.*, 83(1):24–26, 2003.
- [55] N Owschimikow, C Gmachl, A Belyanin, V Kocharovskiy, D L Sivco, R Colombelli, F Capasso, and A Y Cho. Resonant second-order nonlinear optical processes in quantum cascade lasers. *Phys. Rev. Lett.*, 90(4):043902, 2003.
- [56] O Malis, A Belyanin, C Gmachl, D L Sivco, M L Peabody, A M Sergent, and A Y Cho. Improvement of second-harmonic generation in quantum-cascade lasers with true phase matching. *App. Phys. Lett.*, 84(15):2721–2723, 2004.
- [57] T S Mosely, A Belyanin, C Gmachl, D L Sivco, M L Peabody, and A Y Cho. Third harmonic generation in a Quantum Cascade laser with monolithically integrated resonant optical nonlinearity. *Opt. Express*, 12(13):2972–2976, 2004.

- [58] M Troccoli, A Belyanin, F Capasso E Cubukcu, D L Sivco, and A Cho. Raman Injection Laser. *Nature*, 433:845–848, 2005.
- [59] F H Julien, A Sa'ar J Wang, and J-P Leburton. Optically pumped intersub-band emission in quantum wells. *Electron. Lett.*, 31(10):838 – 839, 1995.
- [60] O Gauthier-Lafaye, F H Julien, S Cabaret, J M Lourtioz, G Strasser, E Gornik, M Helm, and P Bois. High-power GaAs/AlGaAs quantum fountain unipolar laser emitting at $14.5\ \mu\text{m}$ with 2.5% tunability. *App. Phys. Lett.*, 74(11):1537–1539, 1999.
- [61] R Q Yang. Infrared laser based on intersubband transitions in quantum wells. In *7th Int. Conf. Superlattices, Microstructures and Microdevices, Banff, Canada*, 1994.
- [62] R Q Yang, J L Bradshaw, J D Bruno, J T Pham, and D E Wortman. Power, Efficiency, and Thermal Characteristics of Type-II Interband Cascade Lasers. *IEEE J. Quantum Electron.*, 37(2):282–289, 2001.
- [63] C L Felix, W W Bewley, I Vurgaftman, J R Meyer, D Zhang, C-H Lin, R Q Yang, and S S Pei. Interband Cascade Laser Emitting >1 Photon per Injected Electron. *IEEE Photon. Technol. Lett.*, 9(11):1433–1435, 1997.
- [64] I Walmsley, L Waxer, and C Dorrer. The role of dispersion in ultrafast optics. *Rev. Sci. Instr.*, 72(1):1–29, 2001.
- [65] Y R Shen. *The Principles of Nonlinear Optics*. Wiley, New York, 1984.
- [66] R W Boyd. *Nonlinear Optics*. Academic Press, New York, 1992.

Chapter 2

Physics of the semiconductor gain materials

The present chapter serves as an introduction to the semiconductor devices studied in this thesis. Emphasis is placed on the optical properties of quantum well (QW) heterostructures, associated with both interband and intersubband transitions.

After reviewing fundamental concepts of semiconductor physics, the relation between optical gain and refractive index in SOAs is analysed in depth. Understanding the interplay between the slow interband dynamics and the ultrafast nonlinearities associated with intraband processes is essential to assess the potential of SOAs for ultrafast switching applications.

The last section is devoted to describing the operation of QC lasers. The gain mechanism, based on intersubband transitions, and the sources of loss in these devices are thoroughly discussed. This provides a background for chapter 5, in which the nonlinear light generation in QC lasers is addressed.

2.1 Band structure of bulk III-V compound semiconductors

2.1.1 Crystalline and electronic properties

Compound semiconductors comprising elements from groups III and V, such as GaAs or InP, crystallise in the zinc-blende structure. This consists of two interleaved face centered cubic (f.c.c.) lattices displaced from one another by one quarter of one the cube's main

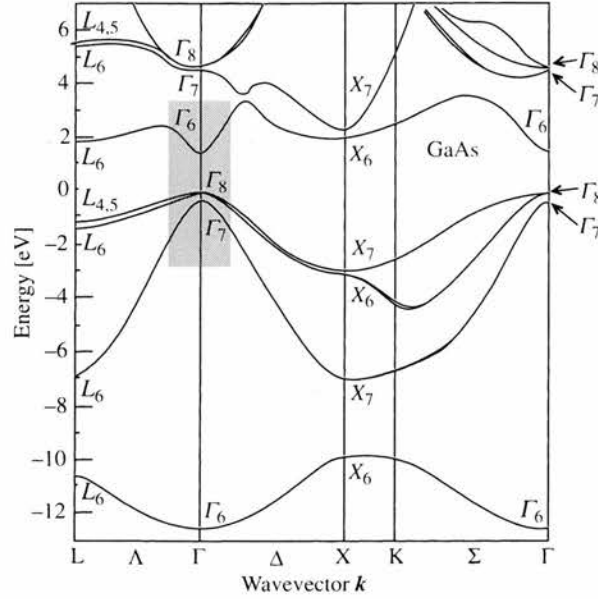


Figure 2.1: Electronic band structure of GaAs calculated using the pseudopotential technique. The gray shaded area encloses the region around the direct bandgap at $k = 0$ (Γ point). Reproduced from reference [1].

diagonals. In the zinc-blende lattice, the elementary cell contains two atoms, which we will refer to as A (group III) and B (group V). Setting the origin arbitrarily at the position of one of them, the other would be located at $(a/4, a/4, a/4)$, where a is the cube side.

In III-V binary compounds, eight outer electrons per primitive unit cell are available for chemical bonding. The remaining electrons are highly bound to the nuclei and form a 'frozen' shell which does not contribute to the electronic properties relevant to our work, namely, electronic transport and near bandgap optical properties.

The wavefunctions of those eight outer electrons (3 from A and 5 from B) hybridise forming tetrahedral bonds between an atom and the neighboring four atoms of the other species. The hybridisation of two orbitals (s -like or p -like) produces two levels, one bonding and one antibonding, and the large number of unit cells causes the broadening of such levels into bands.

The lowest energy corresponds to the s bonding levels, which are always occupied by a pair of electrons. The remaining 6 electrons are distributed amongst the 3 p -type bonding levels, which lie at higher energies, and form the three valence bands. The bands originating from the antibonding levels are all empty, of which the s level lies at the lowest energy and forms the conduction band of the material.

In all III-V compounds, the top of the valence band occurs at the center of the Brillouin zone (Γ point), which for a f.c.c. lattice is a truncated octahedron. The sixfold degeneracy of the three valence bands at Γ is lifted by the spin-orbit coupling, yielding a quadruplet ($J = 3/2$) and a doublet ($J = 1/2$). This is illustrated in figure 2.1.

The devices studied in this thesis were grown on an InP substrate. However, the active regions comprise layers of ternary solid solutions between III-V binary compounds such as InGaAs or AlInAs. In the most strict sense, such alloys are not crystalline, as the atoms are randomly distributed in the lattice and therefore the potential felt by the electrons has no translational symmetry. However, it is possible to use an average periodic potential, according to the alloy volume fractions (virtual crystal approximation).

2.1.2 Dispersion relations and density of states

The stationary wavefunction for a free particle propagating in vacuum is a plane wave of the form $\exp(-i\mathbf{k}\cdot\mathbf{r})$, where the wavevector \mathbf{k} is related to the momentum of the particle according to the formula $\mathbf{p} = \hbar\mathbf{k}$. The energy of the particle is given by $E(k) = \hbar^2 k^2 / 2m_0$, m_0 being the particle mass.

In the case of electrons interacting with the atoms in a crystal, the problem is far more complex. The corresponding hamiltonian must, in principle, account for all the electron interactions, the motion of the nuclei, etc. However, it has been shown that many of those interactions can be represented by an averaged effective potential $U(\mathbf{r})$ which has the same periodicity as the lattice.

The band structure of the material is defined by the relationship between the electron energy (E) and its corresponding wavevector (k). Such dispersion relation is obtained by solving the Schrödinger equation for the potential $U(\mathbf{r})$. According to the Bloch theorem, due to the periodicity of the potential, the electronic wavefunctions can be expressed as

$$\psi_{\mathbf{k}}(\mathbf{r}) = u_{\mathbf{k}}(\mathbf{r}) \exp(-i\mathbf{k}\cdot\mathbf{r}) \quad (2.1)$$

The wavefunction of equation 2.1 resembles that of the free particle except for the term $u_{\mathbf{k}}(\mathbf{r})$, which has the periodicity of the lattice and modulates the fast oscillating exponential.

It is common practice in solid state physics, when dealing with an infinite medium, to pseudo-quantise the \mathbf{k} vector according to the Born-Von Karman cyclic boundary conditions. Conceiving the crystal as composed of identical blocks comprising N cells each, the lattice repeats itself at all positions $\mathbf{L}_i = N\mathbf{a}_i$ ($i = 1, 2, 3$), \mathbf{a}_i being the lattice fundamental vectors. As a result, the components of the wavevector \mathbf{k} must satisfy the following relations

$$k_i = n_i \frac{2\pi}{Na_i} \quad i = 1, 2, 3 \quad (2.2)$$

where n_i is an integer. For each k there is a family of Bloch-like solutions to the Schrödinger equation with eigenenergies $E_m(k)$, m being an integer. These families can be thought of as 'continuous' bands labelled by the index m .

One of the most striking consequences of the interaction of the electrons with the atoms in the crystal is the existence of forbidden energy gaps for the electrons. This can be understood in the light of different theoretical approaches (see, for example, references [2, 3]) such as the nearly free electron model, the tight binding model, or Kane's $\mathbf{k} \cdot \mathbf{p}$ method. There exist different types of forbidden gaps for the electrons, classified depending on the relative positions in reciprocal space of the extrema of conduction and valence bands. In this work, we will be concerned exclusively with compounds in which the bottom of the conduction band and the top of the valence bands occur at the same point in the Brillouin zone (same k), the so called direct bandgap materials.

For the purposes of the study presented here, we can restrict ourselves to the region in reciprocal space around the extrema of the conduction and valence bands. For the III-V compounds, this occurs at $k = 0$ (Γ point). For small values of k , the so called parabolic approximation applies and the dispersion relation for a given band can be expressed as

$$E(k) = E(k = 0) + \frac{\hbar^2 k^2}{2m^*} \quad (2.3)$$

Here, $E(k = 0)$ is the energy at the band extremum (minimum or maximum). The second term on the right hand side is similar to the energy of the free particle (note the quadratic dependence of the energy on the modulus of the wavevector k). In this case, however, m^* is the effective mass of the electron, resulting from the interaction with the

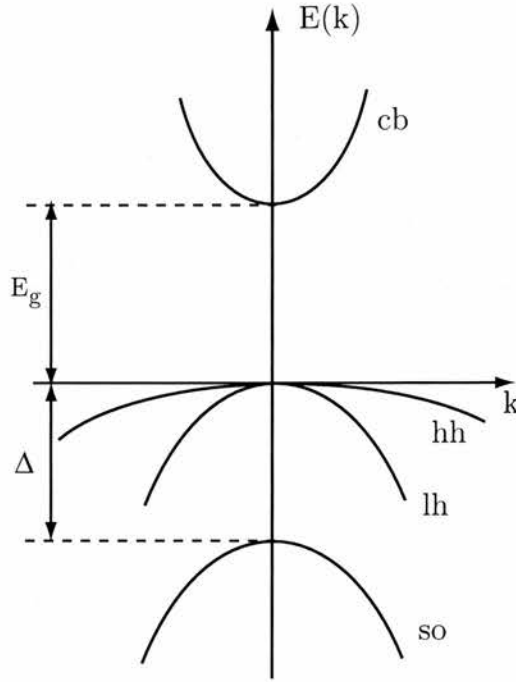


Figure 2.2: Band diagram of a semiconductor with direct bandgap in the parabolic approximation. The conduction band lies at the highest energies, separated from light and heavy hole bands at $k = 0$ by the gap energy E_g . The split-off band is also shown.

periodic potential of the crystal, and closely related to the band curvature (effective masses are positive/negative when the curvature of the band is directed upwards/downwards). The expression in equation 2.3 is a simplified version of the general case in which the effective mass is anisotropic and is represented by a tensor [3].

Although the physical interpretation of the negative effective masses is not trivial, the motion of valence electrons can be treated by considering fictitious particles with the same mass and electric charge (but of positive sign), referred to as holes, whose distribution is that of the unoccupied states in the band. This equivalent description facilitates the calculation of the semiconductor properties, as in the valence bands the density of holes is much smaller than that of the electrons.

Figure 2.2 illustrates the simplified case of four isotropic parabolic bands. These include the conduction band and the three valence bands, namely, heavy hole (hh), light hole (lh) and split-off (so). Light and heavy hole bands are degenerate at $k = 0$ and correspond to the $J = 3/2$ quadruplet discussed in section 2.1.1, while the split-off band is formed by the $J = 1/2$ doublet.

The electronic dispersion relations for the bands depicted in figure 2.2 are

$$E_c(k) = E_g + \frac{\hbar^2 k^2}{2m_e^*}, \quad (2.4a)$$

$$E_{hh}(k) = \frac{\hbar^2 k^2}{2m_{hh}^*}, \quad (2.4b)$$

$$E_{lh}(k) = \frac{\hbar^2 k^2}{2m_{lh}^*}. \quad (2.4c)$$

where the origin was taken at the top of the lh and hh valence bands. In these bands, thinking in terms of holes, energy would be measured downwards (consistent with the hole effective masses being positive, $m_{hh}^*, m_{lh}^* > 0$). m_e^* is the effective mass of the electrons in the conduction band. The split-off band lies at much lower energies and it is not so relevant to the work presented in this thesis.

To calculate the optical properties of semiconductors, the knowledge of both the available density of states and the occupation probability of the different states is essential. In a bulk semiconductor, the density of states in conduction and valence bands is given by

$$\rho_c(k) = \frac{1}{2\pi^2} \left(\frac{2m_e^*}{\hbar^2} \right)^{\frac{3}{2}} (E - E_g)^{\frac{1}{2}}, \quad (2.5a)$$

$$\rho_v(k) = \frac{1}{2\pi^2} \left(\frac{2m_h^*}{\hbar^2} \right)^{\frac{3}{2}} (-E)^{\frac{1}{2}}. \quad (2.5b)$$

Here, the effective mass m_h^* for the hole density of states in the valence band is taken to be $m_h^{*3/2} = m_{hh}^{*3/2} + m_{lh}^{*3/2}$ to include contributions from the light hole and heavy hole bands.

In thermodynamical equilibrium at a temperature T , the occupation probability of a given state by an electron or hole (both fermions) is dictated by the Fermi-Dirac distribution $f(E)$.

$$f(E) = \frac{1}{1 + \exp\left(\frac{E - E_F}{k_B T}\right)} \quad (2.6)$$

In equation 2.6, E_F is the Fermi energy, also known as chemical potential, and k_B is Boltzmann's constant.

The density of electrons in conduction band (n) and holes in valence band (p) can be

calculated as

$$n = \int_{E_g}^{\infty} \rho_c(E) f(E) dE, \quad (2.7a)$$

$$p = \int_0^{-\infty} \rho_v(E) [1 - f(E)] dE, \quad (2.7b)$$

where the carrier densities and occupation probability must be taken from equations 2.5 and 2.6. In the case of $E \gg E_F$, an approximate analytical expression for electron and hole densities can be obtained, which reads

$$n = N_C \exp\left(-\frac{E_g - E_F}{k_B T}\right), \quad (2.8a)$$

$$p = N_V \exp\left(-\frac{E_F}{k_B T}\right), \quad (2.8b)$$

where

$$N_C = \frac{1}{4} \left(\frac{2m_e^* k_B T}{\pi \hbar^2}\right)^{\frac{3}{2}} \quad N_V = \frac{1}{4} \left(\frac{2m_h^* k_B T}{\pi \hbar^2}\right)^{\frac{3}{2}}, \quad (2.9)$$

Within their limitations, the expressions in equations 2.8(a) and (b) are often used to calculate the position of the Fermi level, given the temperature and the carrier density.

2.2 Quantum wells and superlattices

Remarkable progress in epitaxy techniques over the past few decades currently allows the growth of semiconductor material with thicknesses of just a few atomic periods. By carefully choosing the material composition of the layers such that the strain due to the lattice mismatch is contained within some limits, the electrons can be tightly confined in a potential well in the direction of growth (z) resulting in quantum behaviour. Figure 2.3 shows the bandgap energy versus lattice constant for the InGaAs/AlInAs/InP material system.

In the plane of the layers, however, the electronic motion is unrestricted. As a result, the total electronic wavefunctions can be expressed as the product of an envelope function

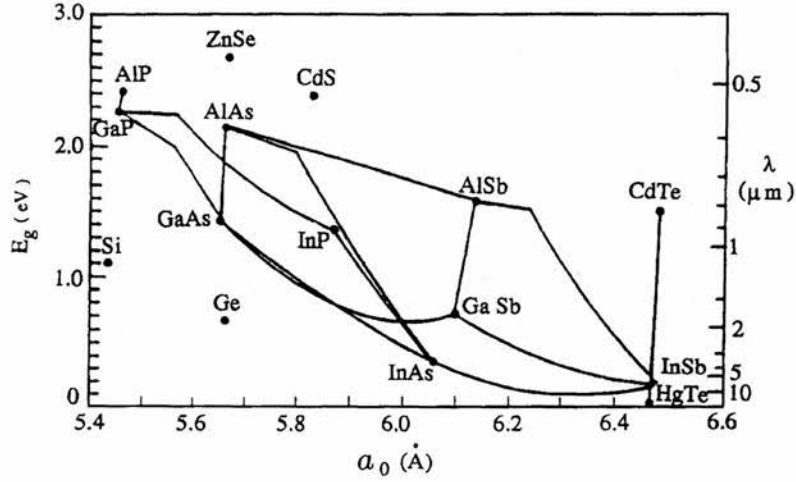


Figure 2.3: Plot of the bandgap energy versus lattice constant at room temperature for the III-V compounds relevant to the work presented here. Reproduced from reference [4].

$\zeta_N(z)$, solution to the one dimensional Schrödinger equation, with the Bloch function u_{n0} (accounting for the interaction with the periodic crystal), and the plane waves describing the motion parallel to the layers. Putting all these factors together, the electronic wavefunction reads [3]

$$\psi_n \cong \zeta_n(z)u_{n0}(\mathbf{r}) \exp(i\mathbf{K} \cdot \mathbf{R}), \quad (2.10)$$

where $\mathbf{K} = (k_x, k_y)$ and $\mathbf{R} = (x, y)$.

2.2.1 A single quantum well

Let us start by considering a single finite potential well of width L and depth V_0 , as depicted in figure 2.4. The envelope function of the electrons $\zeta_n(z)$ and the eigenenergies E_n associated with the motion in the direction of growth can be obtained by solving the time independent Schrödinger equation in 1-D, of the form

$$\left[-\frac{\hbar^2}{2m^*} \frac{\partial^2}{\partial z^2} + V(z) \right] \zeta_n(z) = E_n \zeta_n(z) \quad (2.11)$$

Note that the effective mass m^* will change from the well (m_w^*) to the barrier (m_b^*). The energy associated with the unrestricted in-plane motion (E_{xy}) is that of the bulk

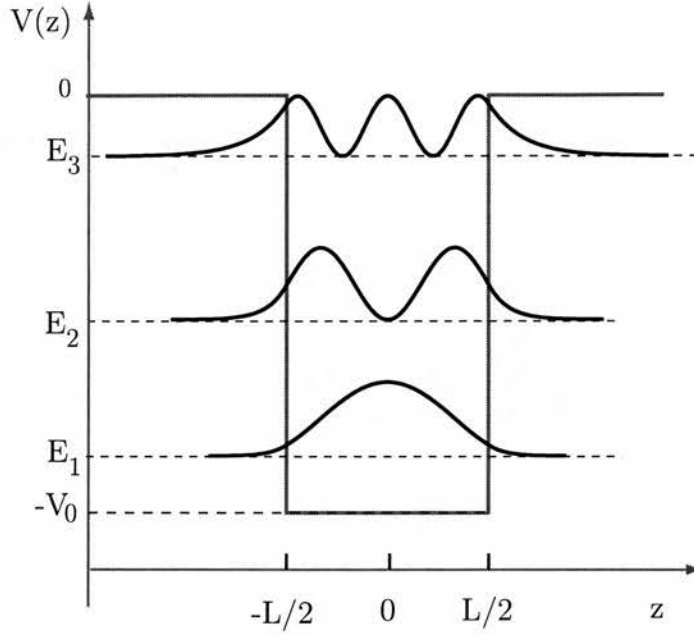


Figure 2.4: Diagram of the potential in a quantum well. The energy levels of the bound states are indicated, together with the moduli squared of the corresponding envelope wavefunctions.

semiconductor. Assuming parabolic bands

$$E_{xy} = \frac{\hbar^2 (k_x^2 + k_y^2)}{2m_w^*}. \quad (2.12)$$

Due to the symmetry of the potential, the solutions to equation 2.11 are either even or odd functions. The wavefunctions inside the well can be expressed as

$$\zeta(z) = A \cos(k_w z) \text{ for even states,} \quad (2.13a)$$

$$\zeta(z) = A \sin(k_w z) \text{ for odd states,} \quad (2.13b)$$

where $\pm k_w$ is the propagation constant of the waves, given by

$$k_w = \sqrt{\frac{2m_w^*}{\hbar^2} (E + V_0)} \quad (2.14)$$

In the barriers, the solutions to the Schrödinger equation are evanescent waves of the form

$$\zeta(z) = B \exp \left[-\kappa_b \left(z - \frac{L}{2} \right) \right]; \quad z \geq L/2 \quad (2.15a)$$

$$\zeta(z) = E \exp \left[\kappa_b \left(z + \frac{L}{2} \right) \right]; \quad z \leq -L/2, \quad (2.15b)$$

Here, for even states $B = E$, and for odd states $B = -E$. To obtain the solutions in equations 2.15(a) and (b), we have taken into account that the wavefunctions should not diverge for $z \rightarrow \pm\infty$. The resulting exponential decay is characterised by the constant κ_b .

$$\kappa_b = \sqrt{-\frac{2m_b^*}{\hbar^2}E}. \quad (2.16)$$

From equation 2.11, by applying boundary conditions (continuity of the wavefunction and also of its derivative divided by the effective mass), it can be shown that the energy satisfies the following transcendental equations

$$\frac{k_w}{m_w^*} \tan \left(k_w \frac{L}{2} \right) = \frac{\kappa_b}{m_b^*} \quad \text{for even states,} \quad (2.17a)$$

$$\frac{k_w}{m_w^*} \cot \left(k_w \frac{L}{2} \right) = -\frac{\kappa_b}{m_b^*}. \quad \text{for odd states} \quad (2.17b)$$

If the electron motion obeys equation 2.11, the number of bound states ($E < 0$) in the well is discrete, and the eigenenergies must be obtained from equations 2.17(a) and (b). These equations have analytical solutions only for the ideal case of an infinite well [3], and must otherwise be solved numerically.

One of the most remarkable conclusions of the solutions to the Schrödinger equation for the finite QW potential is the nonzero probability of finding the electron in the classically forbidden zone, as illustrated in figure 2.4 by the tails of the wavefunctions penetrating the barriers. This phenomenon, known as the tunnel effect, can only be explained in the light of quantum mechanics and is key to the operation of some devices, as we shall discuss later. The previous analysis can also be applied to holes in the valence bands.

The quantum confinement of the carriers in the growth direction is responsible for significant changes in the valence band structure, particularly, the mixing of light hole

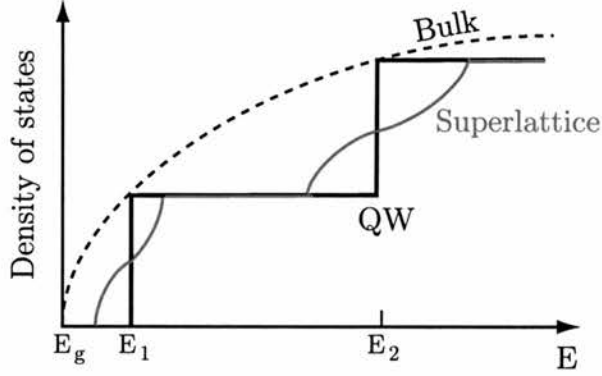


Figure 2.5: Sketch of the density of states of a quantum well (black solid line), compared to that of a bulk semiconductor (dashed line). The density of states of a superlattice, to be introduced in the next section, is plotted with a red line. The energy range starts at the bottom of the conduction band, arbitrarily chosen to be at E_g . Note that the QW density of states increases in steps of $m_w^*/\pi\hbar^2$ at the eigenenergies of the bound states in the well.

and heavy hole bands and the lifting of their degeneracy at $k = 0$. Also, when barrier and well materials are not perfectly lattice matched, strain (compressive or tensile) will play a significant role in dictating the band structure and, consequently, the optical properties of semiconductor devices.

A full treatment of the effects of strain is beyond the scope of this thesis. However, as it will become clear when describing the SOA subject of our study, it is relevant to point out that strained layers allow for the use of a wider range of materials and, to some extent, to 'engineer' the band structure [5]. In bulk materials, for example, strain can be used to balance the gain for TE and TM polarisations. When it comes to quantum wells, by intentionally introducing strain during growth, the relative position of the top of the light and heavy hole bands can be modified [2, 5] and even inverted (by virtue of tensile strain).

The quantisation of the energy levels of the carriers in the wells causes a drastic change in the available density of states, compared to the case of bulk materials (see equation 2.5). Mathematically, the QW two-dimensional density of states per unit area (in $eV^{-1}cm^{-2}$) reads

$$\rho_{QW}^{2D}(E) = \frac{m_w^*}{\pi\hbar^2} \sum_{n=1}^{\infty} H(E - E_n), \quad (2.18)$$

where $H(E - E_n)$ is the step function. Figure 2.5 compares bulk and QW density of states.

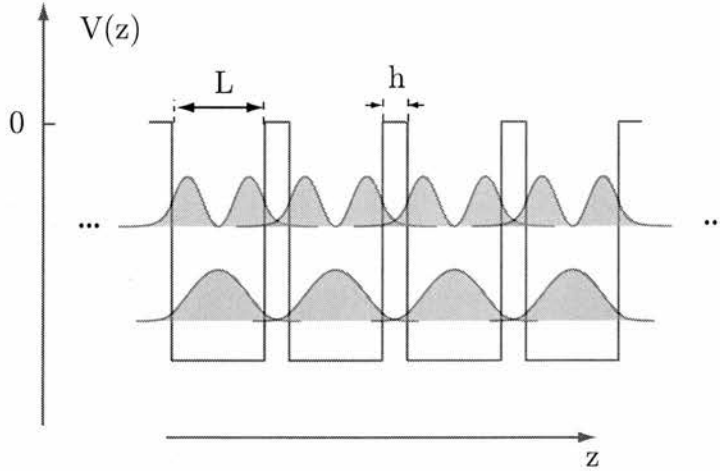


Figure 2.6: Diagram of the conduction band in a compositional superlattice. The energy levels and the moduli squared of the wavefunctions of the isolated quantum well bound states are also depicted. Note the overlap of the wavefunctions due to the thin barriers.

Note that, while the bulk density of states exhibits a quadratic dependence on the energy, ρ_{QW}^{2D} increases in steps of $m_w^*/\pi\hbar^2$, a constant of the material. The energies at which the steps occur are, however, those of the bound states in the well and thus depend on the confining potential.

2.2.2 Multiple quantum well structures and superlattices

So far, we have restricted our discussion to the physics of a single quantum well. However, the active region of devices such as lasers or amplifiers typically comprises several barrier/well pairs, either identical or with varying thicknesses. If the thickness of the barriers is large, the electronic wavefunctions of neighboring wells do not overlap significantly, and each of them can be treated separately as described in the previous section. Modern epitaxial techniques allow to grow wells separated by only a few atomic monolayers of barrier material. In this case, it is possible for the carriers to tunnel across the barrier [3]. This tunneling leads to drastically different optical properties and plays a fundamental role in the operation of a plethora of semiconductor devices, including QC lasers.

We will illustrate the implications of tunneling with the example of superlattices [6], structures comprising multiple periods of wells and ultrathin barriers, as they are relevant to the semiconductor devices studied in this work. Although the concept of the superlattice was introduced by Keyldish as early as 1962, it was the pioneering work by Esaki and Tsu

on compositional and doping superlattices [7] which attracted the attention of researchers.

Consider a finite sequence of quantum wells of length L , separated by barriers of thickness h , as depicted in figure 2.6. In the figure, the energy levels and the moduli squared of the electronic wavefunctions corresponding to the isolated quantum well bound states are also plotted. Note that, due to the small barrier width, the wavefunctions of neighboring wells overlap significantly. As a result of the subsequent tunneling across the thin barriers, the isolated quantum well bound states hybridise into minibands, separated by minigaps, just as in bulk semiconductors.

The superlattice potential alters the intrinsic E vs. k relationship of the semiconductor material in the growth direction, and the coupling of the wells leads to subband dispersion [3, 8]. An immediate consequence of the latter is that the characteristic steps in the QW density of states are smoothed out, as shown by the red line in figure 2.5.

2.2.3 Optical transitions in quantum wells

The optical properties of a semiconductor are determined by the different ways in which the carriers interact with light. In quantum wells, three types of optical transitions can occur, enumerated below.

- (i). An *interband* transition in which an electron from a valence subband is excited to a conduction subband.
- (ii). An *intersubband* transition in which an electron moves from one subband to another within the same band.
- (iii). An *intrasubband* transition in which an electron is promoted to a different k state within the same subband. In this case, interaction with a phonon or impurity is required to satisfy the momentum conservation.

Figure 2.7 illustrates interband and intersubband transitions (indicated with red and blue vertical arrows, respectively) in the case of a type I structure. The transition rates can be calculated within the framework of the envelope function approximation by using Fermi's Golden Rule [2]. We assume a dipole interaction between the optical field and the carriers $V(\mathbf{r}, t) = -e\mathbf{r} \cdot \mathbf{E}$, where \mathbf{E} is an electromagnetic wave of the form $\mathbf{E}(\mathbf{r}, t) =$

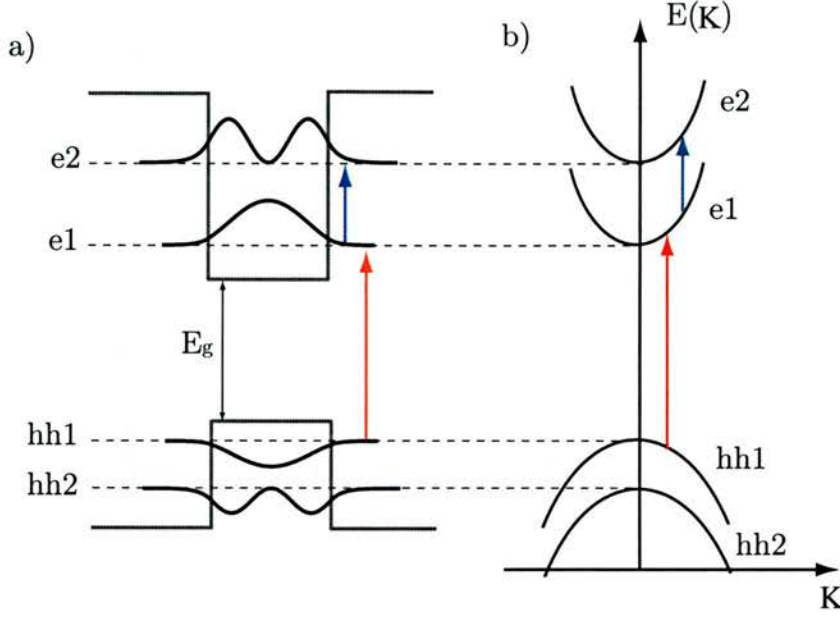


Figure 2.7: Sketch illustrating the interband (red arrows) and intersubband (blue arrows) transitions in a quantum well. (a) and (b) are the representations in real and reciprocal space, respectively. In (b), \mathbf{K} is the momentum in the plane of the layers.

$\frac{1}{2}\mathbf{E}_{\mathbf{q}} \exp[i(\mathbf{q} \cdot \mathbf{r} - \omega t)] + \text{c.c.}$. The following treatment is restricted to the simplified case of isotropic parabolic bands, as this is sufficient to analyse our results.

Interband transitions

For an interband transition between the state with in-plane momentum \mathbf{K} in the subband n and the state with momentum \mathbf{K}' in the subband m , the probability is given by

$$S(n\mathbf{K} \rightarrow m\mathbf{K}') = \frac{\pi e^2}{2\hbar} |\mathbf{E}_{\mathbf{q}} \cdot \mathbf{r}_{cv}|^2 |\langle m, c | n, v \rangle|^2 \delta(E_s - \hbar\omega) \Delta_{\mathbf{K}\mathbf{K}'}. \quad (2.19)$$

Here, \mathbf{r}_{cv} is the matrix element of \mathbf{r} between the Bloch functions of the bulk valence and conduction bands at $k = 0$. The second term in squared brackets is the overlap integral between the envelope functions of the states involved. The product of the latter two factors gives the effective dipolar matrix element of the interband transition (for example, in GaAs this effective dipole matrix element has a value of $\approx 0.6 nm$, if $\langle m, c | n, v \rangle = 1$). Since the wavevector of the photons \mathbf{q} is much smaller than \mathbf{K} and \mathbf{K}' , the conservation of momentum is approximately $\mathbf{K} \approx \mathbf{K}'$ and interband transitions are vertical in reciprocal space, hence the Kronecker delta $\Delta_{\mathbf{K}\mathbf{K}'}$ in equation 2.19.

The conservation of total energy is represented by the delta function $\delta(E_s - \hbar\omega)$, where E_s is the \mathbf{K} -dependent energy separation between initial and final states given by

$$E_s = E_g + E_m^c + \frac{\hbar^2 K^2}{2m_c^*} + E_n^v + \frac{\hbar^2 K^2}{2m_v^*}. \quad (2.20)$$

In equation 2.20, E_m^c and E_n^v are the quantum confinement energies of the states m (in conduction band) and n (in valence band), measured from the respective band extremum (in the latter case, energy is measured downwards, making $E_n^v, m_v^* > 0$). Note that the conservation condition sets an energy threshold of $E_g + E_m^c + E_n^v$ for a photon to induce the transition $n \rightarrow m$.

The overlap integral of the envelope functions $|\langle m, c | n, v \rangle|$ in equation 2.19 can introduce selection rules. In symmetric quantum wells, for example, transitions between subbands with different parity are forbidden. Furthermore, for subbands lying deep within the wells the envelope functions for electrons and holes are almost identical and only transitions between states with the same index ($m = n$) are allowed.

The term with the matrix element \mathbf{r}_{cv} imposes further restrictions. It can be shown that transitions between heavy hole subbands and electron subbands are forbidden for TM polarised light, while TE polarisation can induce transitions from both light and heavy hole subbands to an electron subband (see, for example, reference [2]). These selection rules, summarised in figure 2.8, contribute to the polarisation dependence of gain in SOAs, as we shall discuss in the next chapter.

Intersubband transitions

For intersubband transitions, carriers move between subbands which belong to the same band. This results in transition rates and, subsequently, selection rules being substantially different from those of interband transitions. To be more specific, we will consider the case of electrons in the conduction band. The electrons in the initial lower state must be created in the first place by, e. g., electrical injection or optical pumping. The transition rate between a state in subband n with transversal momentum \mathbf{K} and a state in subband m with transversal momentum \mathbf{K}' is given by

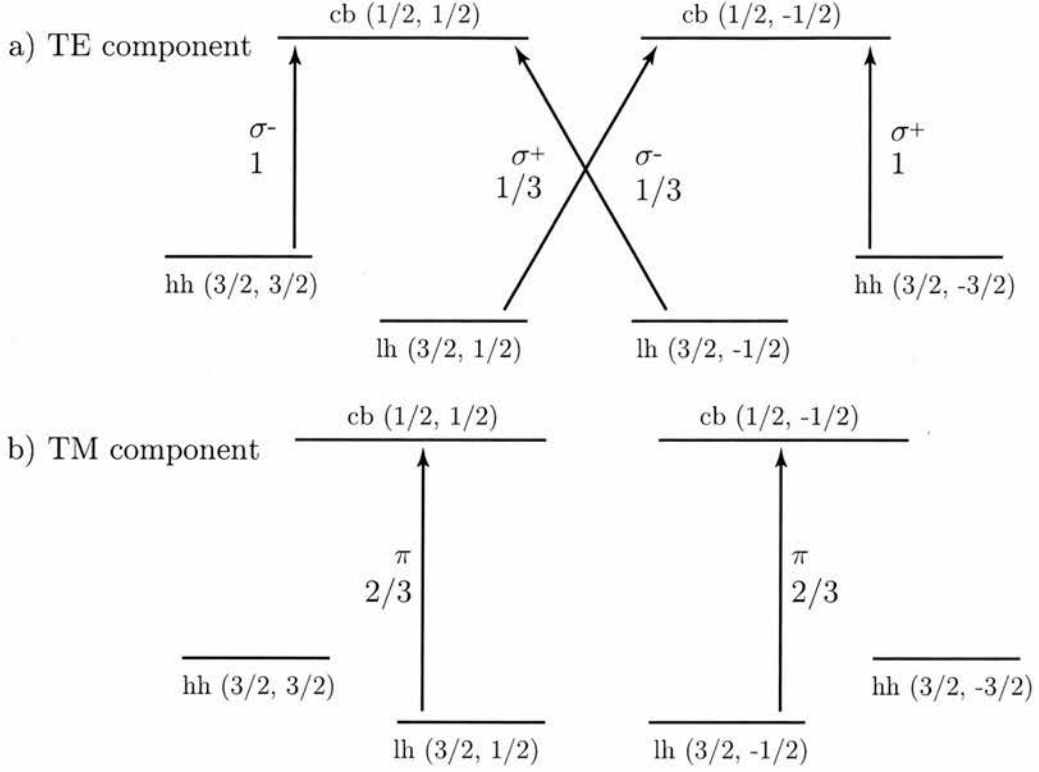


Figure 2.8: Summary of the different polarisation selection rules for GaAs QW, including the transition strengths. It is assumed that light propagates parallel to the layers, and both (a) TE and (b) TM polarisations are considered. π denotes light with linear polarisation and σ^+ and σ^- represent right and left circularly polarised light. Note that σ^+ and σ^- can be conceived as combinations of linear polarisations.

$$S(n\mathbf{K} \rightarrow m\mathbf{K}') = \frac{\pi e^2}{2\hbar} |E_{qz}|^2 |\langle m, c|z|n, v \rangle|^2 \delta(E_m - E_n - \hbar\omega) \Delta_{\mathbf{K}\mathbf{K}'}. \quad (2.21)$$

The last expression resembles to some extent equation 2.19, but also presents significant differences. Note that, in this case, the transition rate is proportional to the modulus squared of the component of the electric field in the direction of growth, implying that only light with TM polarisation can induce intersubband transitions. The latter dictates the polarisation of QC lasers. The dipole moment which determines the strength of the intersubband transitions depends exclusively on the envelope functions via the term $|\langle m, c|z|n, v \rangle|$. Therefore, for a given bulk semiconductor, the optical dipole matrix elements of intersubband transitions can be significantly larger than the interband analogues, up to a few nanometers. The δ function and Kronecker delta again represent

the conservation of total energy and momentum, respectively.

Note that the energy spacing between parallel subbands does not depend on \mathbf{K} . As a result, intersubband transitions lead to resonant absorption of photons at energies $\hbar\omega = E_m - E_n$, while interband absorption spectra present a staircase like appearance.

Line broadening

To obtain the optical transition rates we have followed a time-dependent perturbation approach. Unlike the density matrix formalism, this method does not take into account relaxation rates and other mechanisms that cause line broadening. As a result, the energy conservation in equations 2.19 and 2.21 is represented by a Dirac Delta function. A straightforward way of filling the gap between the two descriptions is by broadening the Dirac function into a lineshape function $g(\nu)$.

In quantum well lasers and amplifiers, the spectral broadening is caused mostly by intraband relaxation processes such as carrier-carrier and carrier-LO phonon scattering, characterised by a time constant τ_{in} [9]. The lineshape function is often approximated as Lorentzian function of the form

$$g(\nu) = \frac{(\Delta\nu/2\pi)}{(\nu - \nu_{mn})^2 + (\frac{\Delta\nu}{2})^2}. \quad (2.22)$$

Note that $g(\nu)$ is normalised so that $\int_{-\infty}^{\infty} g(\nu)d\nu = 1$. The function has its maximum at the resonant frequency of the transition ν_{mn} . $\Delta\nu$ is the full width at half the maximum (FWHM), related to the intraband relaxation time as

$$\tau_{in}^{-1} = \pi\Delta\nu, \quad (2.23)$$

Inhomogeneous broadening is treated by considering an ensemble of distinct systems characterised by different frequencies ν_{mn} . In low dimensional structures such as quantum wells or quantum dots, fluctuations in the growth parameters (e.g. variation of barrier/well widths) or interface roughness contribute significantly to the inhomogeneous line broadening.

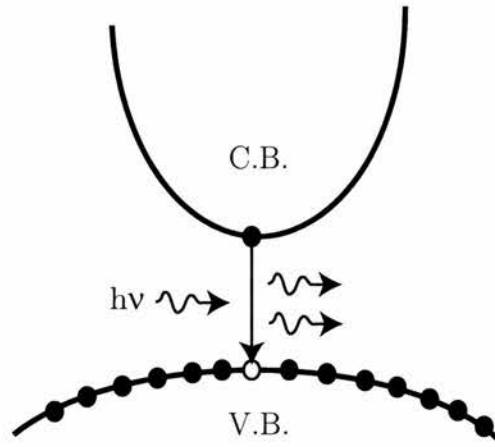


Figure 2.9: Simplified band diagram of a bulk semiconductor illustrating the concept of stimulated emission.

2.3 Semiconductor optical amplifiers

2.3.1 Principles of SOA operation

If light at the appropriate wavelength is incident upon a semiconductor, it can induce an electron in the conduction band to decay and occupy an empty state in the valence band, releasing the energy difference by emitting a photon. By virtue of such stimulated emission processes (illustrated in figure 2.9), provided that sufficient carrier population difference exists between conduction and valence bands, optical gain may be achieved. Although simplistic, this picture is useful to introduce the gain mechanism behind the operation of Semiconductor Optical Amplifiers (SOAs).

The required population difference is achieved by using a p-n junction. Impurities (or dopants) are added to the semiconductor material by substitution and create states just below the bottom of the conduction band (in the n-type region) or above the top of the valence band (in the p-type region), depending on whether the dopants are donors or acceptors. At room temperature, these states generate an excess of electrons in the conduction band (or holes in the valence band). In the absence of any applied bias across the p-n junction, as a result of the diffusion and subsequent recombination of these excess carriers, a depletion region is created in the vicinity of the junction. In this region, the ionised donors/acceptors generate the so called built-in potential V_{bi} , as illustrated in figure 2.10(a).

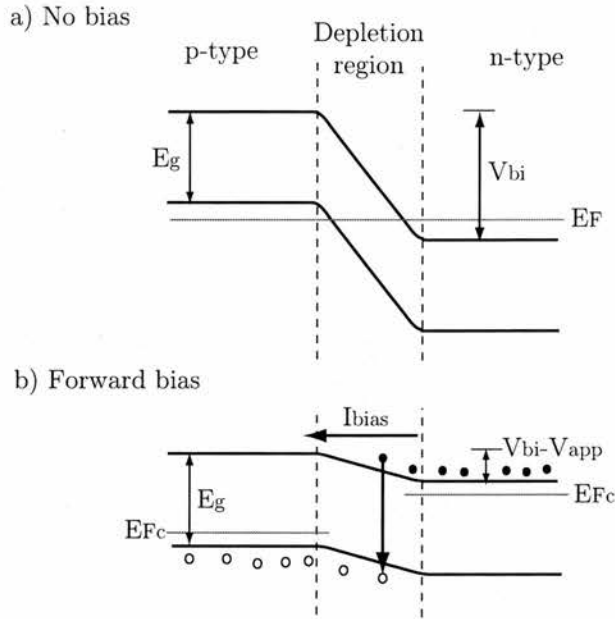


Figure 2.10: Sketch of the conduction and valence bands of a p-n homojunction (a) with no bias and (b) with forward applied bias. Electrons and holes are indicated with solid and empty circles, respectively.

Under forward bias, the applied potential V_{app} (more positive on the p side) counteracts V_{bi} , allowing a flow of majority carriers (see figure 2.10(b)). As the carriers within a band interact on much shorter timescales than those typical of interband processes, the populations in conduction and valence bands can be conceived as being in quasi-equilibrium and characterised by separate quasi-Fermi levels (E_{Fc} and E_{Fv}). As depicted in figure 2.10(b), electron and holes may recombine in the depletion region via radiative or non radiative processes (discussed in detail later).

2.3.2 Heterostructures

If the current is sufficient to achieve population inversion between conduction and valence bands, an incoming photon will be more likely to cause stimulated emission than absorption, and light is amplified. However, in a simple p-n homojunction, optical gain comes at the expense of large current densities.

Gain at lower currents can be achieved in heterostructures by reducing the active volume and by the confinement of the carriers. Optical confinement maximising interaction with the light. As discussed in section 2.2, epitaxial techniques allow the growth of layers of different materials (heterojunctions). By careful design, due the bandgap dependence

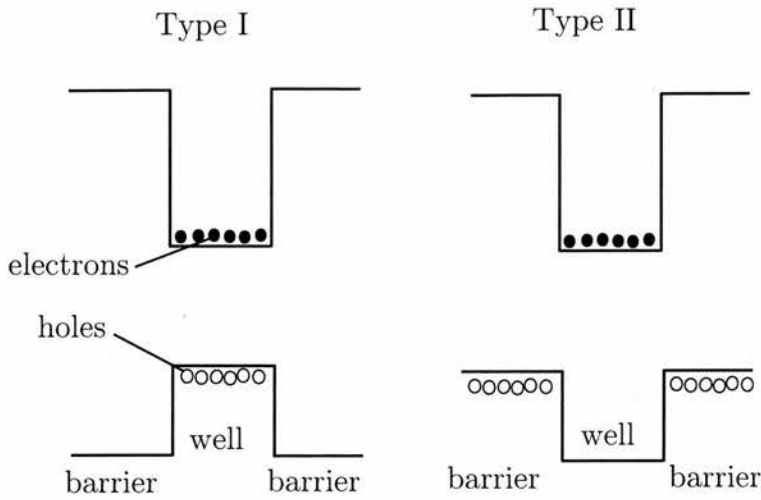


Figure 2.11: Diagram of two possible alignment of the bands in a heterojunction. In Type I, all carriers are localised in the wells, while in Type II electrons and holes are confined to the wells and barriers, respectively.

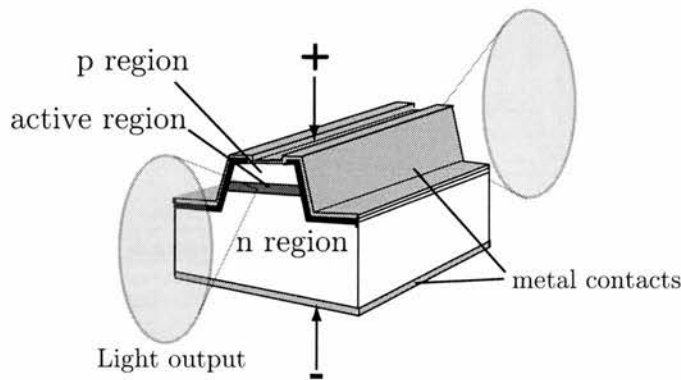


Figure 2.12: Sketch of the simplified structure of an SOA.

on material composition, these heterostructures provide confinement for the carriers in the direction of growth. Figure 2.11 illustrates two of the possible band alignments [6], resulting in the electrons and holes being localised in (a) the same or (b) different layers.

It is fortunate that, in most cases, refractive index and bandgap energy are inversely related. As a result, the cladding layers have lower refractive index than the active region and form a waveguide for the light in the growth direction. By etching deep ridges, carriers and optical modes are also confined in the transversal direction. To illustrate this, a sketch of a ridge waveguide SOA is shown in figure 2.12.

Under conditions of forward electrical bias, spontaneous emission of photons in the active region, due to the radiative recombination of electrons and holes, is amplified. This

is referred to as Amplified Spontaneous Emission (ASE), and is one of the main sources of noise in optical amplifiers. Furthermore, the reflection of the ASE at the facets of the device may cause lasing at the Fabry-Perot modes of the cavity above some threshold current. To be operated as an amplifier, device facets are typically anti-reflection (AR) coated and/or cleaved at a small angle to the waveguide. This way, optical feedback is minimised and lasing is prevented. As light undergoes a single pass along the active waveguide, SOAs are also referred to as travelling wave amplifiers (TWA).

The active region in an SOA can comprise bulk semiconductor material or lower dimensional structures such as quantum wells or dots. As discussed in section 2.2, the quantum confinement of the carriers will drastically influence the available density of states and therefore the optical gain. This will be the subject of the next section.

2.3.3 Optical gain and absorption

When light is incident upon a semiconductor, as a result of optical interband transitions, carriers can be generated when a photon is absorbed, or new photons may be emitted via stimulated emission, accompanied by carrier recombination. Whether the net effect on the incident light is absorption or amplification will be determined by the difference between the rates of upwards and downwards transitions.

The net absorption rate between states in the valence band and states in the conduction band can be obtained by treating the semiconductor as an inhomogeneously broadened ensemble of two level systems, and calculating the imaginary part of the corresponding optical susceptibility (see for example [2]). The resulting expression, for a bulk semiconductor, in units of $length^{-1}$ is

$$\alpha(\omega) = \frac{\pi e^2 x_{vc}^2 \omega}{\epsilon_0 \hbar n c} \rho_j(\omega) [f_v(\hbar\omega) - f_c(\hbar\omega)]. \quad (2.24)$$

Here, x_{vc} is the optical dipole matrix element of the transition, assumed to be independent of \mathbf{k} in this approximation. In obtaining the last expression, the Lorentzian lineshape function was approximated by a Dirac delta. $\rho_j(\omega)$ is the density of states joined by a photon of energy $\hbar\omega$, and is given by

$$\rho_j(\omega) = \frac{1}{2\pi^2} \left(\frac{2m_r^*}{\hbar} \right)^{\frac{3}{2}} (\hbar\omega - E_g)^{\frac{1}{2}} \quad (2.25)$$

where m_r^* is the reduced mass, $m_r^{*-1} = m_e^{*-1} + m_h^{*-1}$.

In equation 2.24, f_c and f_v are the probabilities of occupation of states $E_c(k)$ and $E_v(k)$. These are given by the quasi-equilibrium Fermi functions

$$f_c(E) = \frac{1}{1 + \exp \left[\frac{E_c(\hbar\omega) - E_{Fc}}{k_B T} \right]}, \quad (2.26a)$$

$$f_v(E) = \frac{1}{1 + \exp \left[\frac{E_v(\hbar\omega) - E_{Fv}}{k_B T} \right]} \quad (2.26b)$$

where $E_c(\hbar\omega) = E_g + \frac{m_r^*}{m_c^*}(\hbar\omega - E_g)$ and $E_v(\hbar\omega) = -\frac{m_r^*}{m_v^*}(\hbar\omega - E_g)$, taking into account the conservation of momentum in the interband transitions. E_{Fc} and E_{Fv} are the quasi-Fermi levels for conduction and valence bands, respectively.

The previous treatment can also be extended to quantum wells, keeping in mind the differences in the optical dipole matrix elements and density of states caused by the quantum confinement of carriers in one dimension. Recalling equations 2.18 and 2.19, the absorption spectra of quantum wells can be written as

$$\alpha_{QW}(\omega) = \sum_{n,m} \alpha_{QW}^{n \rightarrow m} H(\hbar\omega - E_g - E_m^c - E_n^v) [f_v(\hbar\omega) - f_c(\hbar\omega)], \quad (2.27)$$

where the summation includes the contributions of transitions between different pairs of subbands n (in valence band) and m (in conduction band). The absorption coefficient in each case is

$$\alpha_{QW}^{n \rightarrow m} = \frac{m_r^*}{\hbar^3} \hbar\omega \frac{(\mu_0/\epsilon_0)^{1/2}}{n(\omega)} |\eta_{\mathbf{q}} \cdot \mathbf{r}_{cv}|^2 |\langle m, c | n, v \rangle|^2 \quad (2.28)$$

where $\eta_{\mathbf{q}}$ is the vector indicating the polarisation of the optical field.

The differences in the optical dipole matrix element and density of states leads to very distinct absorption spectra for bulk semiconductors and quantum well structures, as illustrated in figure 2.13. However, in both cases, the condition for optical amplification (negative absorption) is $f_v(\hbar\omega) - f_c(\hbar\omega) < 0$. Taking into account equations 2.26a and b,

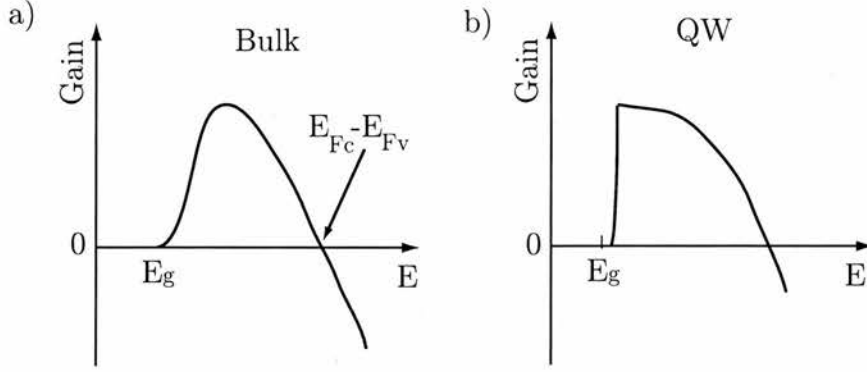


Figure 2.13: Sketch of the gain spectra of (a) Bulk and (b) QW laser structures.

this inequality can be rewritten as

$$E_{F_c} - E_{F_v} > \hbar\omega > E_g, \quad (2.29)$$

Equation 2.29 is known as the Bernard-Durrafourg condition, and states that only photons with energy smaller than the difference between the quasi-Fermi levels, but larger than the gap energy, will be amplified. For quantum wells, the lower limit is not E_g but the energy difference between the lowest conduction subband and highest valence subband. The latter allows for some bandgap engineering in QW lasers and amplifiers.

In real quantum well devices, the gain spectrum is not as sharp as depicted in figure 2.13(b). The causes for the latter include intraband relaxation [9], Coulomb effects such as carrier-carrier scattering, and fluctuations in the well widths. Also, the large carrier densities in amplifiers biased at gain may lead to bandgap shrinkage via Coulomb many-body effects (bandgap renormalisation), and subband mixing makes the picture more complicated. Due to the selection rules of interband transitions, the optical gain of quantum well devices is strongly dependent on the polarisation of light. In particular, depending on the device structure and material composition, distinct contributions due to transitions involving light or heavy holes may be distinguished in the gain spectrum for TE polarised light.

2.3.4 Optical nonlinearities

As described in the previous section, light at the appropriate wavelength may induce changes in the carrier populations of a semiconductor by virtue of interband transitions. In a SOA biased for gain, the probability of stimulated emission out-weights that of absorption and light is amplified with the subsequent depletion of the carrier density.

The total gain and phase change experienced by an optical beam upon propagation along the SOA waveguide depends drastically on the complex interplay between the optically induced processes and the relaxation dynamics of the carriers in the semiconductor.

This section is devoted to introducing the different carrier dynamics that dictate the SOA behaviour, particularly the nonlinearities arising from high optical excitation. First, we will focus our discussion on the gain changes. The nonlinear refraction, key to switching applications, is addressed later via the Kramers-Krönig relations [10].

For the general discussion of nonlinearities in semiconductors that follows, the dimensionality of the active region is not critically important. Nevertheless, some optical properties differ slightly in quantum confined structures. One relevant example is the stronger polarisation dependence compared to the bulk case, which may affect the polarisation of the pulses.

Interband dynamics

If a beam with a photon energy greater than the bandgap is incident upon a semiconductor, it will excite electrons from the valence band into the conduction band. Since the number of available states in either band is limited, according to Pauli's exclusion principle, the absorption will saturate if the beam is intense enough. This is referred to as the band-filling effect.

In a SOA, in an analogous fashion, the incident beam will be amplified via stimulated emission and, for large input powers, it will significantly deplete the available carrier density and thus saturate the gain. Along with this gain saturation, the refractive index of the material will change. The majority of switches employing SOAs, such as TOADs or Mach-Zehnder interferometers, rely on the phase change associated with this resonant band-filling nonlinearity.

The typical relaxation times in SOAs associated with interband dynamics are in the

order of hundreds of picoseconds (up to 1 ns depending on bias), while the carriers within a band are thought to reach a quasi-equilibrium via fast scattering processes on the order of a picosecond or less. Therefore, the amplification of CW beams or optical pulses with durations ($\tau_p > 10 ps$) is effectively dictated by interband dynamics and transport. This problem is well understood and has been extensively treated in the framework of rate equation models [11, 12]. In these, the carrier relaxation dynamics are accounted for via a recombination rate $R(N)$, which includes both radiative and nonradiative processes, namely

- (i). Electrons in the conduction band may decay spontaneously, emitting a photon, to occupy an empty state in the valence band. The rate at which spontaneous radiative recombination occurs is $B(N)N^2$, where $B(N)$ is the bimolecular recombination rate (note the dependence of B on the carrier density).
- (ii). Nonradiative recombination due to the presence of deep or surface defects, whose rate is $A_{nr}N$.
- (iii). Auger recombination [13], in which an electron recombines with a hole and transfers the excess energy to another electron (or hole) via a collision. Consequently, the auger recombination rate is proportional to the cube of the carrier density CN^3 .

The total recombination rate is $R(N) = A_{nr}N + BN^2 + CN^3$. In high quality materials, such as those employed in the active region of SOAs, the concentration of defects is small. It is therefore reasonable, for modelling purposes, to take $A_{nr} \approx 0$. Taking the latter into account, the total recombination rate can be rewritten as

$$R(N) = \frac{N}{\tau(N)}, \quad (2.30)$$

where $\tau(N)$ is a characteristic decay time, dependent on the carrier density, which accounts for both radiative and nonradiative processes.

$$\tau(N)^{-1} = B(N)N + CN^2 \quad (2.31)$$

The nonradiative Auger mechanism is of great importance in amplifiers biased at gain, as a result of the large carrier densities. Typical values of τ range from hundreds of

picoseconds to over 1 ns. Considerable efforts have been devoted to increase the recombination rate and, concomitantly, speed up the gain recovery. Different approaches include applying high biases (Manning *et al.* have reported upper state lifetimes as low as 20 ps [14]) or the use of a CW optical holding beam [15, 16] which, by inducing stimulated optical transitions between bands, yields an effective recovery time

$$\frac{1}{\tau_{eff}} = \frac{1}{\tau} + \frac{P_h}{E_h^{sat}}, \quad (2.32)$$

where P_h is the power of the CW holding beam and E_h^{sat} is the saturation energy [15].

The carrier density available for stimulated emission is limited, as dictated by the interplay of the current injection and the different recombination processes included in τ . As a result, the gain per unit of length g experienced by a single pulse or a CW beam propagating along the SOA waveguide is dependent on the incident power. From a simple rate equation model (similar to that described in section 4.2.1), the gain coefficient g can be expressed as

$$g = \frac{g_0}{1 + P/P_{sat}}, \quad (2.33)$$

for the case of a CW beam of power P . Here, g_0 is the small-signal gain (also referred to as *linear*) and P_{sat} is the power at which the gain coefficient is half of this unsaturated value.

$$P_{sat} = \frac{\hbar\omega\sigma}{\Gamma\tau a}, \quad (2.34)$$

where σ and Γ are the SOA active cross-sectional area and confinement factor, respectively. The differential gain $a = \partial g / \partial N$ relates the gain coefficient to the carrier density [5, 17].

The gain experienced by long optical pulses (with pulsewidths >10 ps) presents a similar power density-dependent saturation behaviour [11]. The saturation characteristics become quite different, however, when the duration of the pulses is comparable or shorter than the recovery times of ultrafast nonlinearities such as carrier heating. In this case, as a result of the ultrafast gain compression, the saturation behaviour of the SOA becomes pulsewidth dependent and saturation occurs at lower powers [18, 19, 20].

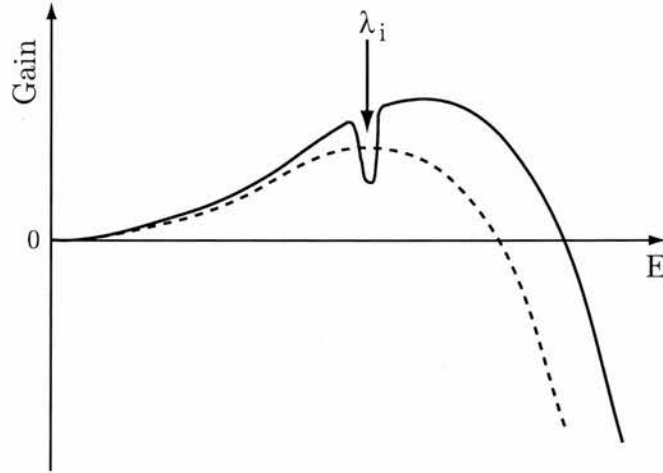


Figure 2.14: Sketch of the hole burnt in the gain curve by a beam centered at wavelength λ_i (solid line). The dashed line represents the gain curve after a new Fermi equilibrium is reached via carrier-carrier scattering. Note that the gain has been compressed and does not recover to the original value, since stimulated emission has reduced the total number of carriers.

SOA subpicosecond dynamics

The quest for faster switching speeds leads to the use of progressively shorter pulses. When entering the subpicosecond realm, various ultrafast effects come into play. These involve changes in the carrier energy distribution within a band. The most relevant to our work will be summarised next.

Spectral hole burning (SHB). In an inhomogeneously broadened gain material such as a semiconductor, an optical beam at a certain wavelength may induce transitions involving carriers from specific energy levels, thus burning a hole in the quasi-equilibrium Fermi distribution. In a very short time scale (~ 100 fs), carrier-carrier scattering yields a new distribution with a different total number of carriers.

In the gain region, light at wavelength λ_i will deplete the carrier density through stimulated emission, but only over a limited range of energies. This is depicted in figure 2.14, where the dashed line represents the gain profile after a new quasi-equilibrium has been reached. In an analogous fashion, if operating in absorption, the beam will create carriers only in a specific range thus digging a hole in the absorption curve. SHB does not occur at transparency, since no net stimulated transitions take place.

Carrier heating (CH). As mentioned previously the intraband quasi-equilibrium carrier

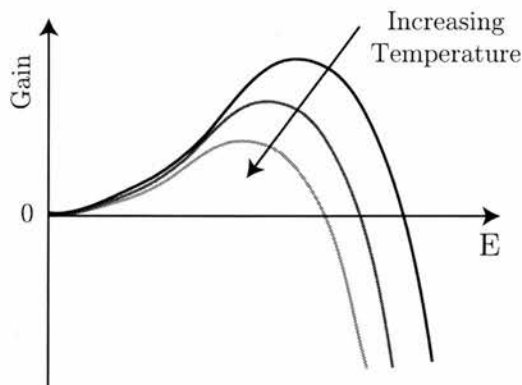


Figure 2.15: Sketch of the gain spectra for different temperatures of the carrier distribution. With increasing temperature, gain is compressed across the entire spectrum and the gain peak shifts towards longer wavelengths.

distribution is given by a Fermi-Dirac function, defined by the total carrier density and a temperature (T_c), which may not match that of the lattice (T_L). Raising the carrier temperature reduces the gain across all of the range of energies and shifts the gain peak towards longer wavelengths, the reason being the strong temperature dependence of the Fermi function [5]. Once the carrier distribution is heated, it will cool down to the lattice temperature via phonon emission. Non-equilibrium carrier heating has been found to play a fundamental role in the ultrafast dynamics of semiconductor gain media [21, 22]. Typical recovery times associated with this nonlinearity range between 500 fs and 1.5 ps [21].

Several mechanisms may contribute to carrier heating. Free Carrier Absorption (FCA) is one of them, as it creates highly energetic carriers in both bands. These carriers will share their energy with the rest via scattering, thus heating the distribution.

Carriers are said to be "hot" or "cold" depending on whether their energy is larger or smaller than the average energy of the distribution, defined as

$$\langle E \rangle = \frac{\int f(E)\rho(E)EdE}{\int f(E)\rho(E)dE}, \quad (2.35)$$

where $\rho(E)$ is the density of states and $f(E)$ the occupation probability, while $\int f(E)\rho(E)dE$ is simply the carrier density N . Another mechanism affecting the average temperature of the distribution is the addition or removal of carriers by the action of the optical beam (i.e. removing cold carriers or adding hot ones will heat the distribution, and vice versa). Stimulated emission is more likely to occur than FCA. However, it is not yet clear which

of the two processes will be dominant, as FCA causes larger changes in the carrier temperature. Higher order effects such as Two Photon Absorption (TPA) can also heat the distribution, though their influence is much less significant [23].

2.3.5 Nonlinear refraction

So far, we have described different ultrafast nonlinearities in SOAs from the gain point of view. However, it is the nonlinear refractive index change in SOAs that is the key factor for optical switching. In addition, it will influence the propagation of light through the device, introducing chirp and distorting the pulse spectrum [11, 24]. The connection between gain and refractive index is provided by the Kramers-Krönig relations [10]. Mathematically

$$n(\omega) = 1 + \frac{c}{\pi} P \int_0^{\infty} \frac{g_0(\Omega)}{\Omega^2 - \omega^2} d\Omega. \quad (2.36)$$

In equation 2.36, g_0 is the linear gain and P denotes the Cauchy principal value of the integral. The refractive index resulting from a change in gain can be predicted, according to [10],

$$\Delta n(\omega, \xi) = \frac{c}{\pi} P \int_0^{\infty} \frac{\Delta g_0(\Omega, \xi)}{\Omega^2 - \omega^2} d\Omega \quad (2.37)$$

where $\Delta g_0(\omega, \xi)$ is the change in linear gain due to some perturbation, labelled with ξ . This change can be written as $\Delta g_0(\omega, \xi) = g_0(\omega, \xi_1) - g_0(\omega, \xi_2)$, where $g_0(\omega, \xi_i)$ are the different gain curves. This formalism is very useful in the calculation of the dependence of refractive index on parameters such as carrier density ($\xi = N$) or temperature ($\xi = T$).

In general, the largest changes in the refractive index occur at energies around the band gap of the semiconductor [25]. For energies above, but near, the band-gap, decreasing the carrier density increases the refractive index and viceversa [26]. It must be pointed out that the changes in refractive index extend below the bandgap, allowing for gain-transparent interferometric switches in which the wavelength of the data channel is longer than the wavelength at the bandgap.

There may be additional contributions to the nonlinear refractive index arising from rapid electronic or virtual processes such as two photon absorption, the Stark effect [27] or the Kerr effect, which follow the profile of the pulse. However, regarding the duration

of the pulses employed in the experiments presented in this thesis, these contributions cannot be resolved and the heating of the carrier distribution is expected to be the most relevant nonlinearity dictating the SOA behaviour in the ultrafast regime.

The relations between changes in gain and refractive index are usually described via of the linewidth enhancement factor α [28]. In the case of changes related to the carrier density

$$\alpha_N = -\frac{\partial\chi_r/\partial N}{\partial\chi_i/\partial N} = -\frac{4\pi}{\lambda} \frac{\partial n/\partial N}{\partial g_0/\partial N}. \quad (2.38)$$

In equation 2.38, χ_r and χ_i are the real and imaginary parts of the complex susceptibility. α_N is also expressed in terms of the linear gain (g_0) and refractive index (n). Note that α_N is wavelength dependent.

In an analogous fashion, a temperature alpha-factor can also be defined

$$\alpha_T = -\frac{\partial\chi_r/\partial T}{\partial\chi_i/\partial T} = -\frac{4\pi}{\lambda} \frac{\partial n/\partial T}{\partial g_0/\partial T}. \quad (2.39)$$

Again, α_T depends on wavelength. It has been found that, near bandgap, heating of the carrier distribution causes an increase in the refractive index [26, 29].

2.3.6 Nonlinear effects on pulse propagation

As mentioned in chapter 1, strong optical pulses experience self-modulation when propagating along the SOA waveguide, caused by gain and refractive index nonlinearities. Additionally, these nonlinearities may also affect weaker pulses propagating in the same medium (cross-modulation). When the pulse duration is longer than ~ 10 ps, the resonant nonlinearities associated with interband transitions dictate the SOA behaviour and pulses undergo self-modulation, both in gain and in phase, due to changes in the carrier density [11]. As a result of this self-modulation, pulses with durations much shorter than the interband relaxation time experience significant spectral red-shifts and sharpening of the leading edge of the pulse. However, if the gain recovers partially within the pulse duration, the pulse spectrum broadens on both red and blue ends and the final pulse shape is more symmetric. These effects depend drastically on the shape and chirp of the initial pulse.

For subpicosecond pulses the picture is more complicated [30, 31], as intraband dy-

namics such as carrier heating (caused by FCA, stimulated emission and TPA) or spectral hole burning contribute significantly to the nonlinear gain and refractive index. The interplay of all these ultrafast nonlinearities depends drastically on pulse shape and duration. However, in general terms, dynamic changes in the refractive index and fast variations of the gain will cause the reshaping of the pulses. Additionally, due to the time dependent refractive index $n(t)$, the instantaneous frequency of the pulses varies as

$$\omega_{inst} = \omega_0 - \frac{\omega_0 L}{c} \left[\frac{\partial n(t)}{\partial t} \right], \quad (2.40)$$

where ω_0 is the pulse carrier frequency.

2.4 Quantum Cascade lasers

Quantum Cascade (QC) lasers [32] are semiconductor injection lasers based on optical and electronic intersubband transitions (ISTs) between the quantised states of multiple-quantum well structures. The emission characteristics of conventional diode lasers and the gain spectrum of SOAs are, to a large extent, determined by the device's material properties, notably the material's bandgap. Light emission from intersubband transitions in QC lasers, however, can be controlled via the well and barrier thicknesses (ranging from 0.5 to 10 nm) and the external applied electric field. Additionally, the unipolar nature of these lasers allows electrons to remain in the conduction band and undergo several ISTs, leading to a cascade effect and high output powers. The designed structures are grown by Molecular Beam Epitaxy (MBE) [33], well suited for such a demanding task.

A QC laser typically comprises several tens (20-30) of cascaded active region and injector pairs, each of them containing about 8 to 10 wells and barriers. Figure 2.16 shows an example of the conduction band diagram of two active regions with an intermediate injector. We assume a well depth of 520 meV, according to the low-temperature conduction band-offset usually associated with the materials' composition ($\text{In}_{0.53}\text{Ga}_{0.47}\text{As}$, $\text{Al}_{0.48}\text{In}_{0.52}\text{As}$), lattice matched to the InP substrate. The energy levels and the moduli squared of the electronic wavefunctions in the structure, some of which are plotted in figure 2.16, are obtained by solving numerically the Schrödinger equation. Figure 2.17 shows schematically the in-plane dispersion of the subbands localised in the active regions

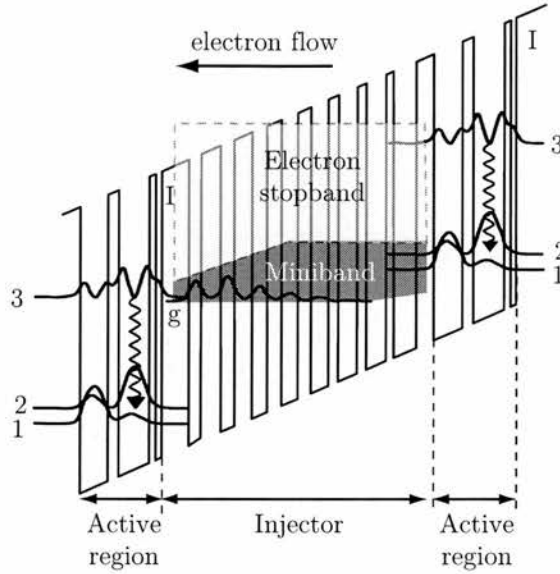


Figure 2.16: Conduction band diagram of two active regions and a injector in a QC laser stack. The energy levels and squared moduli of some relevant wavefunctions are also plotted. The laser transitions 3-2 are indicated with wavy arrows, while the dark and light shaded areas represent the miniband and electron stopband in the injector superlattice.

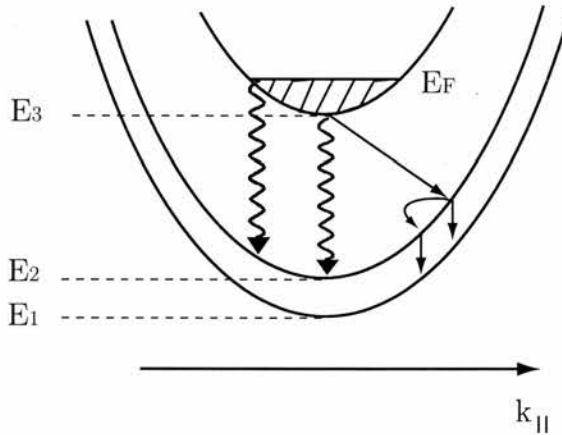


Figure 2.17: Schematic representation of the dispersion in the plane parallel to the layers of three subbands (labelled $n=1,2,3$) in the conduction band of a QC laser. The wavy arrows indicate the laser transition, and the straight lines represent the relaxation processes via electron-phonon scattering.

(labelled 1, 2 and 3).

The laser transitions 3-2 are indicated by wavy arrows in figures 2.16 and 2.17. Two types of active regions can be distinguished [34], depending on whether the wavefunctions of the laser states are mostly localised in adjacent wells (diagonal transition) or in the same well (vertical transition, as it is the case of figure 2.16). The former type was the first to be implemented [32], but designs with vertical transition have proven to perform

better in terms of operating temperature and output peak power. The injectors are superlattice structures designed to create a miniband across which electrons can be efficiently transported (dark shaded area in figure 2.16). Just above (light shaded area), lies the minigap of the superlattice which acts as a Bragg reflector and prevents the escape of electrons from the upper laser level (3). In addition, the innermost layers of the injector are doped with silicon (to typical sheet densities of $1 - 5 \times 10^{11} \text{ cm}^{-2}$ per period) thus providing extrinsic carriers.

A QCL can be conceived as a 4-level laser ($g \rightarrow 3 \Rightarrow 2 \rightarrow 1$). Under the appropriate electrical bias, state 3 and the ground level of the injector (g) line up. This results in the upper laser level being populated via resonant tunneling across the barrier labelled as I (see figure 2.16). The electrons in state 3 will scatter to the lower-lying levels, 2 and 1, via emission of longitudinal optical (LO) phonons. Despite these ultrafast relaxation mechanisms, the population inversion required for lasing may be achieved by tailoring fundamental properties such as energy levels, optical dipole matrix elements and, especially, scattering times. Electrons need only be injected into level 3 fast enough, and need to scatter from levels 2 and 1 into the following injector region at a high rate, again by tunneling. The fast depletion of the lower laser state (2) is usually achieved by choosing the layer thicknesses such that the energy separation between levels 2 and 1 is close to the longitudinal optical phonon resonance (37 meV) in the InGaAs/AlInAs active region materials. Once in the injector, the electrons thermalise and, if possible, relax via scattering with LO-phonons to the next level g of the following down-stream stage, hence the cascade effect.

2.4.1 Gain and loss in QC lasers

A quantitative expression for the gain in QC lasers can be obtained from a rate equation model, similar to those for conventional QW lasers. Including a phenomenological broadening of the transition ($2\gamma_{32}$), the gain coefficient g at cryogenic temperatures is given by [35]

$$g = \tau_3 \left(1 - \frac{\tau_2}{\tau_{32}} \right) \frac{4\pi e z_{32}^2}{\lambda_0 \epsilon_0 n_{eff} L_p} \frac{1}{2\gamma_{32}}, \quad (2.41)$$

and the material gain is thus obtained as $G_m = gJ$, where J is the current density.

In equation 2.41, z_{32} is the optical dipole matrix element of the laser transition and n_{eff} is the effective index of the optical mode. τ_{32} is the LO-phonon scattering time from level 3 to level 2, while τ_3 and τ_2 represent the total lifetimes of the electrons in levels 3 and 2, respectively. Note that the condition for population inversion is $\tau_2/\tau_{32} < 1$ and that, ideally, $\tau_{32} \gg \tau_2$. L_p is the length of a period, comprising one active region and one injector. Since the optical transitions occur only in a small portion of each period, this is equivalent to defining a distributed gain coefficient and facilitates the calculation of the laser threshold current.

To achieve lasing, the optical gain must out-weight the losses experienced by the light in the device waveguide, caused by three main sources. First, the laser samples are often cleaved leaving waveguides with parallel un-coated semiconductor facets. These provide a reflectivity of

$$R = [(n_{eff} - 1)/(n_{eff} + 1)]^2, \quad (2.42)$$

and consequently, a mirror loss coefficient of $\alpha_m = (1/L)\ln(R)$, L being the length of the optical cavity. These losses can be reduced by using high reflection/anti-reflection coatings at the facets. Additional losses may be caused by imperfections and roughness in the facets, which scatter the light output of the laser. These, however, cannot be easily quantified.

Due to the doping in the injector regions, the optical mode undergoes strong free carrier absorption. The corresponding loss coefficient α_w is estimated by means of a Drude model, as described in detail in section 5.2.2. Light propagating in the waveguide can also experience absorption due to resonant intersubband transitions. For example, transitions in the injector miniband can present large optical dipole matrix elements, which, together with the presence of extrinsic electrons, become potential sources of loss. It is one of the tasks during design to avoid such resonances.

Taking into account the different loss mechanisms described above, the threshold condition can be expressed as.

$$\Gamma g J_{th} = \alpha_m + \alpha_w \quad (2.43)$$

Here, the left hand side of the equation represents the gain experienced by the optical mode, while the right hand side includes the different loss coefficients. J_{th} is the threshold current density and the confinement factor (Γ) quantifies the overlap of the optical mode with the laser stack. Note that such confinement extends equally over active regions and injectors, and justifies the convenience of defining g as a distributed gain coefficient.

In the discussion so far, we have assumed operation at cryogenic temperatures. This applies to the work with QC lasers presented in this thesis, as laser samples are cooled with liquid nitrogen or helium. It must be noted, however, that QC laser performance is highly dependent on temperature. On the one hand, scattering rates are increased due to the large LO-phonon population at higher temperatures, and secondly, as the temperature is increased, thermally excited carriers in the injector are more likely to tunnel back into the lower laser state, thus spoiling the population inversion.

As with conventional lasers, the temperature dependence of the threshold current in QC lasers usually fits an exponential curve of the following form very well [35]

$$J_{th}(T) = J_0 \exp\left(\frac{T}{T_0}\right) \quad (2.44)$$

in the 100-300 K temperature range. T_0 is the so called characteristic temperature, which typically ranges between 100 and 200 K which is very large compared to conventional lasers. One reason for this is that Auger recombination is virtually non-existent for intersubband transitions, as long as the subbands are parallel as a function of the in-plane momentum (k_x, k_y) [2].

2.4.2 Carrier transport

Previously, when describing the gain mechanism in QC lasers, we referred to the transfer of carriers from injector into the upper laser level (3) via resonant tunneling. Later, in obtaining an expression for the gain coefficient, we assumed that this tunneling occurred at a sufficiently high rate and also that the lower laser level was promptly depleted. Carrier transport is a critical issue for laser operation and, as such, deserves a more in-depth discussion.

When the appropriate electric field is applied to the structure, the subbands corre-

sponding to injector ground state and the upper laser level line up. At perfect resonance, these two subbands fully anti-cross and become separated by an energy of $\Delta E = \hbar\Omega \approx 4 - 6 \text{ meV}$. A quantitative analysis based on a tight binding approximation [34] shows that in these circumstances, in the strong coupling regime, the tunneling time is

$$\tau_{\text{tunnel}} = \frac{\hbar}{e\Delta E}, \quad (2.45)$$

and the current density can be calculated as

$$J = \frac{eN_s}{2\tau_3}. \quad (2.46)$$

From equation 2.46, we see that the current density is limited by the lifetime of the upper laser level τ_3 . The doping concentration in the injectors must be chosen such that the sheet carrier density N_s allows for the required current, but keeping the losses due to free carrier absorption to a minimum.

Ideally, an electron injected into state 3 would undergo an optical transition to state 2 and then, on a very short time scale, scatter consecutively into state 1 and the next injector downstream. In real devices, however, additional paths for the carriers may exist, causing current leakage and yielding larger threshold current densities. Electrons in the upper laser level, for example, scatter to lower lying levels via the emission of LO-phonons, as accounted for by the state lifetime τ_3 . In short wavelength lasers, carriers may escape into the continuum by tunneling or, at high temperatures, due to thermal excitation. These different paths for carrier escape must be taken into account at the design stage, and will be discussed in further detail in chapter 5.

2.4.3 Intersubband optical nonlinearities in QC lasers

As discussed so far, the operation of QC lasers relies on band-gap engineering to achieve the required population inversion between subbands, maximise the optical dipole matrix element of the laser transition and facilitate the carrier transport.

Over the past few years, the large optical nonlinearities associated with intersubband transitions have provided one method of generating new wavelengths in QC lasers. The design flexibility of these lasers allows monolithic integration of such resonant nonlinearities

in the laser stack, achieving efficient intra-cavity wave mixing.

The research work presented in chapter 5 focuses on frequency upconversion in QC lasers via stimulated Anti-Stokes Raman scattering near resonance of ISTs. An in-depth discussion of this third order nonlinear process and the associated $\chi^{(3)}$ susceptibility, together with a thorough description of the device structure will be given in chapter 5, prior to the presentation of the experimental results.

2.5 Summary

In this chapter, first, fundamental concepts of semiconductor physics have been reviewed as a base on which to describe the operation of SOAs and QC lasers. These include the crystalline and electronic properties of III-V compounds, and the interaction of light with the carriers in a semiconductor. Particular stress was placed in discussing the implications of quantum confinement of the carriers in 2D structures and optical transitions (interband and intersubband) in quantum wells.

The gain and refractive index nonlinearities in SOAs have been discussed in the context of all-optical switching applications. On the longest timescales, the band-filling nonlinearity associated with interband transitions dictates the SOA behaviour. However, when using subpicosecond pulses, ultrafast intraband carrier dynamics such as spectral hole burning or carrier heating become important. The implications of these ultrafast nonlinearities in interferometric switching is not yet fully understood and is the subject of the experimental work presented in chapter 4.

Intersubband transitions in multiple quantum well structures can also sustain light amplification despite the ultrafast electron-LO phonon scattering, as demonstrated for the first time with the implementation of QC lasers. The principles of these novel injection semiconductor devices, designed by band-structure engineering, have been described. The topics covered include the gain mechanism, the sources of loss and the carrier transport across the structure, highlighting the role of resonant tunneling. This will serve as a base on which to address the nonlinear light generation via stimulated electronic Anti-Stokes Raman scattering in QC lasers.

References for Chapter 2

- [1] P Y Yu and M Cardona. *Fundamentals of Semiconductors*. Springer, 2nd edition, 1999.
- [2] E Rosencher and B Vinter. *Optoelectronics*. Cambridge University Press, Cambridge, 1st edition, 2002.
- [3] G Bastard. *Wave mechanics applied to semiconductor heterostructures*. John Wiley and sons, 1992.
- [4] V Mitin, V A Kochelap, and M A Stroschio. *Quantum heterostructures. Microelectronics and Optoelectronics*. Cambridge University Press, 1st edition, 1999.
- [5] W W Chow and S W Koch. *Semiconductor-laser fundamentals: physics of the gain materials*. Springer-Verlag, Berlin, 1999.
- [6] L Esaki. A Birds-Eye View on the Evolution of Semiconductor Superlattices and Quantum Wells. *IEEE J. Quantum Electron.*, 22(9), 1986.
- [7] L Esaki and R Tsu. Superlattice and negative differential conductivity in semiconductors. *IBM J. Res. Develop.*, 14:61–65, 1970.
- [8] P K Basu. *Theory of optical processes in semiconductors: bulk and microstructures*. Oxford University Press, New York, 1997.
- [9] M Asada. Intraband relaxation time in quantum-well lasers. *IEEE J. Quantum Electron.*, 25(9):2019–2026, 1989.
- [10] D C Hutchings, M Sheik-Bahae, D J Hagan, and E W Van Stryland. Kramers-krönig relations in nonlinear optics. *Opt. Quant. Electron.*, 24:1–30, 1992.
- [11] G P Agrawal and N A Olsson. Self-phase modulation and spectral broadening of optical pulses in semiconductor laser amplifiers. *IEEE J. Quantum Electron.*, 25(11):2297, 1989.
- [12] T Saitoh and T Mukai. Gain saturation characteristics of traveling-wave semiconductor laser amplifiers in short optical pulse amplification. *IEEE J. Quantum Electron.*, 26(12):2086–2094, 1990.
- [13] S Hausser, G Fuchs, A Hangleiter, K Streubel, and W T Tsang. Auger recombination in bulk and quantum well InGaAs. *Appl. Phys. Lett.*, 56(10):913–915, 1990.
- [14] R J Manning, D A O Davies, and J K Lucek. Recovery rates in semiconductor laser amplifiers: Optical and electrical bias dependencies. *Electron. Lett.*, 30(15):1233–1235, 1994.
- [15] R J Manning and D A O Davies. Three-wavelength device for all-optical signal processing. *Opt. Lett.*, 19(12):889–891, 1994.
- [16] R J Manning, D A O Davies, D Cotter, and J K Lucek. Enhanced recovery rates in semiconductor laser amplifiers using optical pumping. *Electron. Lett.*, 30(10):787–788, 1994.
- [17] G P Agrawal and N K Dutta. *Semiconductor lasers*. Van Nostrand Reinhold, New York, 2nd edition, 1993.
- [18] K L Hall, Y Lai, E P Ippen, G Eisenstein, and U Koren. Femtosecond gain dynamics and saturation behaviour in InGaAsP multiple quantum well optical amplifiers. *Appl. Phys. Lett.*, 57(27):2888, 1990.
- [19] S Nakamura, Y Ueno, and K Tajima. Femtosecond switching with semiconductor-optical-amplifier based symmetric Mach-Zehnder-type all-optical switch. *Appl. Phys. Lett.*, 78(25):3929–3931, 2001.
- [20] P Borri, S Scaffetti, J Mork, W Langbein, J M Hvam, A Mecozzi, and F Martelli. Measurement and calculation of the critical pulse width for gain saturation in semiconductor optical amplifiers. *Opt. Commun.*, 164:51–55, 1999.
- [21] M P Kesler and E P Ippen. Subpicosecond gain dynamics in GaAlAs laser diodes. *App. Phys. Lett.*, 51(22):1765–1767, 1987.

- [22] K L Hall, J Mark, E P Ippen, and G Eisenstein. Femtosecond gain dynamics in InGaAsP optical amplifiers. *Appl. Phys. Lett.*, 56(18):1740, 1990.
- [23] J Mork, J Mark, and C P Seltzer. Carrier heating in InGaAsP laser amplifiers due to two-photon absorption. *Appl. Phys. Lett.*, 64(17):2206, 1994.
- [24] R S Grant and W Sibbett. Observations of ultrafast refraction in an InGaAsP optical amplifier. *Appl. Phys. Lett.*, 58(11):1119–1121, 1991.
- [25] K L Hall, E R Thoen, and E P Ippen. *Semiconductors and Semimetals*, volume 59, chapter 2 Nonlinearities in Active Media. Academic Press, 1999.
- [26] C H Henry, R A Logan, and K A Bertness. Spectral dependence of the change in refractive index due to carrier injection in AlGaAs lasers. *J. Appl. Phys.*, 52(7):4457–4461, 1981.
- [27] M Sheik-Bahae and E W Van Stryland. Ultrafast nonlinearities in semiconductor laser amplifiers. *Phys. Rev. B*, 50(19):14171, 1994.
- [28] C H Henry. Theory of the linewidth enhancement factor. *IEEE J. Quantum Electron.*, 18(2):259–264, 1982.
- [29] C T Hultgren and E P Ippen. Ultrafast refractive index dynamics in AlGaAs diode laser amplifiers. *Appl. Phys. Lett.*, 59(6):635–637, 1991.
- [30] M Y Hong, Y H Chang, A Dienes, J P Heritage, P J Delfyett, S Dijaili, and F G Patterson. Femtosecond self- and cross-phase modulation in semiconductor laser amplifiers. *IEEE J. Sel. Top. Quantum Electron.*, 2(3):523–539, 1996.
- [31] R P Schrieck, M H Kwakernaak, H Jäckel, and H Melchior. All-optical switching at multi-100-Gb/s data rates with Mach-Zehnder interferometer switches. *IEEE J. Quantum Electron.*, 38(8):1053–1061, 2002.
- [32] J Faist, F Capasso, D L Sivco, C Sirtori, A Hutchinson, and A Y Cho. Quantum cascade laser. *Science*, 264(5158):553–556, 1994.
- [33] A Y Cho. *Molecular Beam Epitaxy*. AIP, Woodbury NY, 1994.
- [34] C Sirtori, F Capasso an J Faist, A L Hutchinson, D L Sivco, and A Y Cho. Resonant tunneling in quantum cascade lasers. *IEEE J. Quantum Electron.*, 34(9):1722–1729, 1998.
- [35] J Faist, F Capasso, C Sirtori, D L Sivco, J N Baillargeon, A L Hutchinson, S-N G Chu, and A Y Cho. High power mid-infrared ($\lambda \sim 5 \mu\text{m}$) quantum cascade lasers operating above room temperature. *App. Phys. Lett.*, 68(26):3680–3682, 1996.

Chapter 3

Device structure and experimental techniques

The aim of this chapter is to bring together the relevant information concerning the structure of the devices subject to our study. Practical issues such as the mounting of the samples or the temperature control are also discussed in detail. The remaining sections are devoted to describing the different experimental techniques and set-ups employed in the course of our work.

3.1 SOA structure and mounting of the device

The SOA subject of this study is a multiple quantum well (MQW) superlattice structure provided by R.J. Manning of Corning. It comprises 10 wells and 11 barriers of InGaAs on an InP substrate. The wells are 4 nm of unstrained material and the barriers are 6 nm with a tensile strain of -0.67% [1], resulting in strong gain for the TM mode, while retaining significant gain for the TE mode as well.

Figure 3.1 shows the schematics of the band structure of the superlattice forming the SOA active region, calculated by Jian Zhong Zhang and Ian Galbraith at Heriot-Watt University, Edinburgh [2]. The quantum confinement and the strain between wells and barriers causes the splitting of the light hole (lh) and heavy hole (hh) bands (otherwise degenerate at $k = 0$). This results, as indicated in the above mentioned figure, in a quasi-type II heterostructure for the light holes, although carriers are not tightly localised.

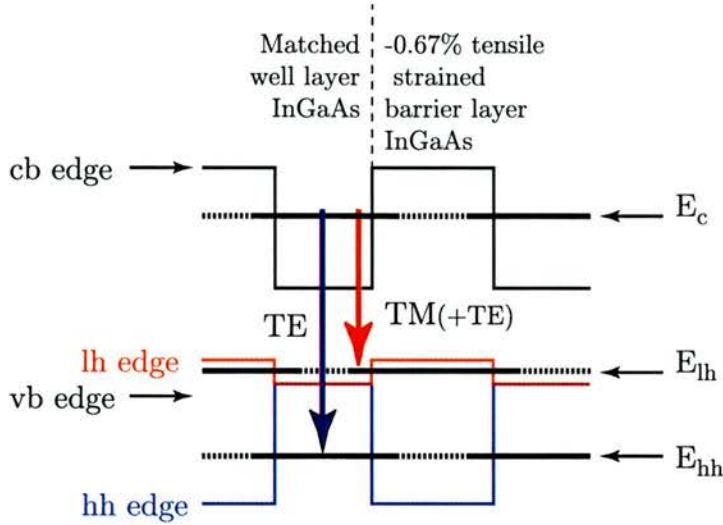


Figure 3.1: Sketch of the band structure in the active region of the SOA. Blue and red lines show, respectively, the valence bands for heavy holes and light holes. The horizontal black lines indicate the energy levels (the dashed portions illustrate the spreading of the wavefunctions in the classically forbidden zone) and the arrows show the allowed optical transitions.

Further calculations by J. Zhang and I. Galbraith [3] show that, for TM polarised light, only transitions between the conduction band and the lh band have strong optical dipole matrix elements in the vicinity of $k = 0$ (this is due to the overlap of the corresponding wavefunctions, and consistent with the polarisation selection rules of optical transitions in quantum confined structures, see section 2.2.3). TE polarised light, however, presents large optical dipole matrix elements for transitions to both the first lh and hh bands around $k = 0$ (even the transition to the second hh band appears to have a significant dipole strength).

The 1 mm long amplifier was grown at Corning as a buried structure by atmospheric pressure metallo-organic vapour phase deposition (MOVPE) [4] (see figure 3.2 for a detailed sketch). The regions with p -type and n -type doped material around the active region create a separate confinement heterostructure, which provides both optical and carrier confinement. Calculations show that the waveguide in figure 3.2 is single mode for light at $1.56 \mu\text{m}$ wavelength. In these calculations, performed by Michael Mazilu using *Femlab*, the effective refractive index of the active region was taken to be between 3.2 and 3.4, while the refractive index of the cladding was chosen within the range 3.5 and 3.65. To illustrate this, figure 3.2(b) shows the profile of the field E_z for the TM mode with indices of 3.2 and 3.6 for core and cladding, respectively.

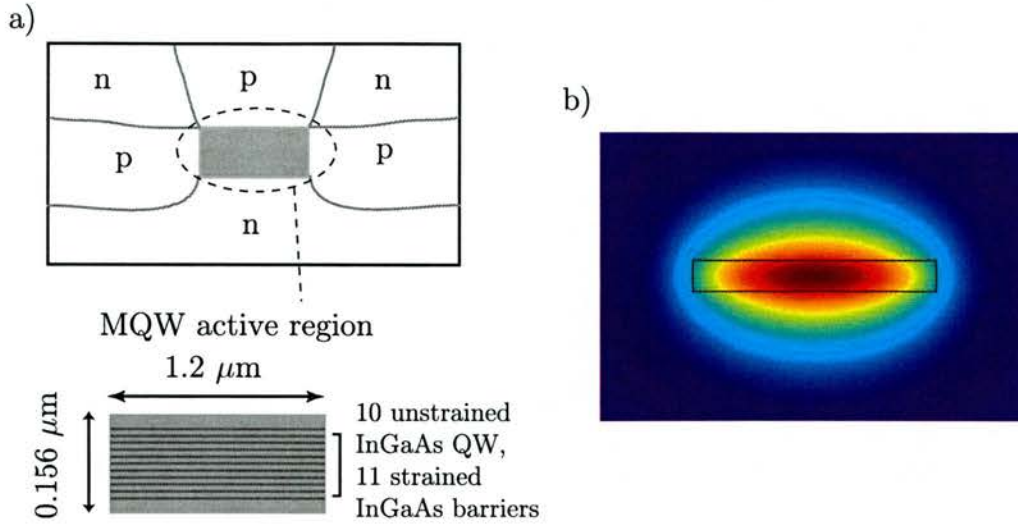


Figure 3.2: (a) Cross section of the SOA buried structure in the plane of the facets. (b) Contour plot of the E_z field corresponding to the fundamental TM mode in the waveguide at $1.56 \mu\text{m}$ wavelength.

To minimise feedback and prevent lasing when forward bias is applied, the waveguide end facets are tilted to 10° . In addition, a single antireflection coating was grown on both facets to improve the device performance as a travelling wave amplifier.

The SOA was pasted onto a *Kyocera* submount (see figure 3.3). To allow for the injection of current, a gold wire was bonded to the p-side of the SOA. The submount fits into a larger brass block (electrical earth) and is fixed with screws to ensure both good thermal and electrical contact. Just below the brass block, sandwiched between two electrically insulating layers, a peltier cooler driven by a temperature controller keeps the sink temperature constant at approximately $\sim 22^\circ\text{C}$ (monitored by a thermistor located very close to the device).

3.1.1 Device characterisation

The gain bandwidth and gain saturation of the SOA were thoroughly characterised as a function of electrical bias, optical power, wavelength and polarisation. These measurements were undertaken jointly with J. G. Fenn as part of her Ph.D. thesis [3]. The work reported in reference [3] also includes a study of the gain recovery on sub-picosecond time scales and its dependence on operating conditions such as electrical bias and optical power. These results will be used in setting modelling parameters and in the analysis of

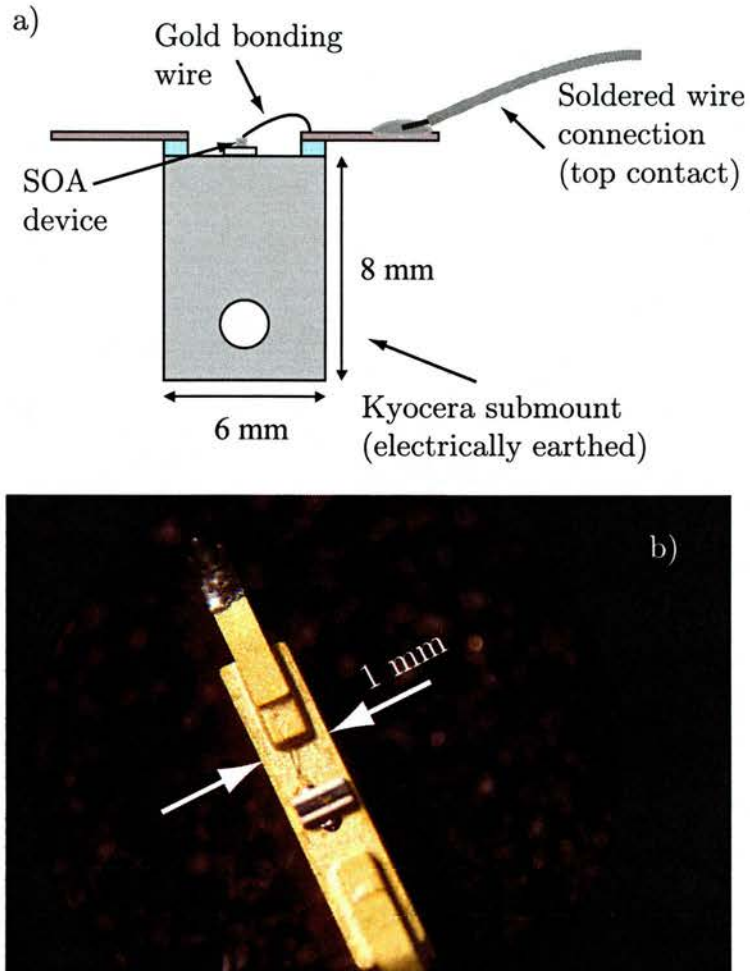


Figure 3.3: (a) Sketch of the SOA pasted on the *Kyocera* submount. (b) Top view of a different SOA mounted in identical fashion.

the experimental data of chapter 4.

Figure 3.4, for example, shows the small signal gain of the amplifier measured as a function of electrical bias at different wavelengths for both TE and TM polarised light. In connection with the band structure of the SOA superlattice discussed previously, it is worth pointing out that linear transmission measurements (see figure 3.5) reveal distinctive contributions to the TE gain attributed to transitions to hh and lh bands. On the other hand, as expected, TM gain was found to be solely due to transitions to the light hole band.

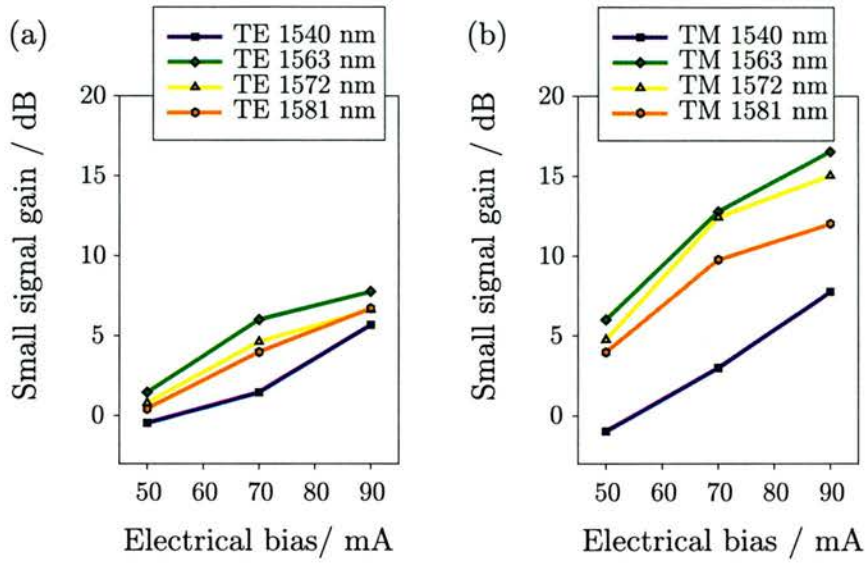


Figure 3.4: Small signal gain as a function of electrical bias at different wavelengths for both (a) TE and (b) TM polarisations.

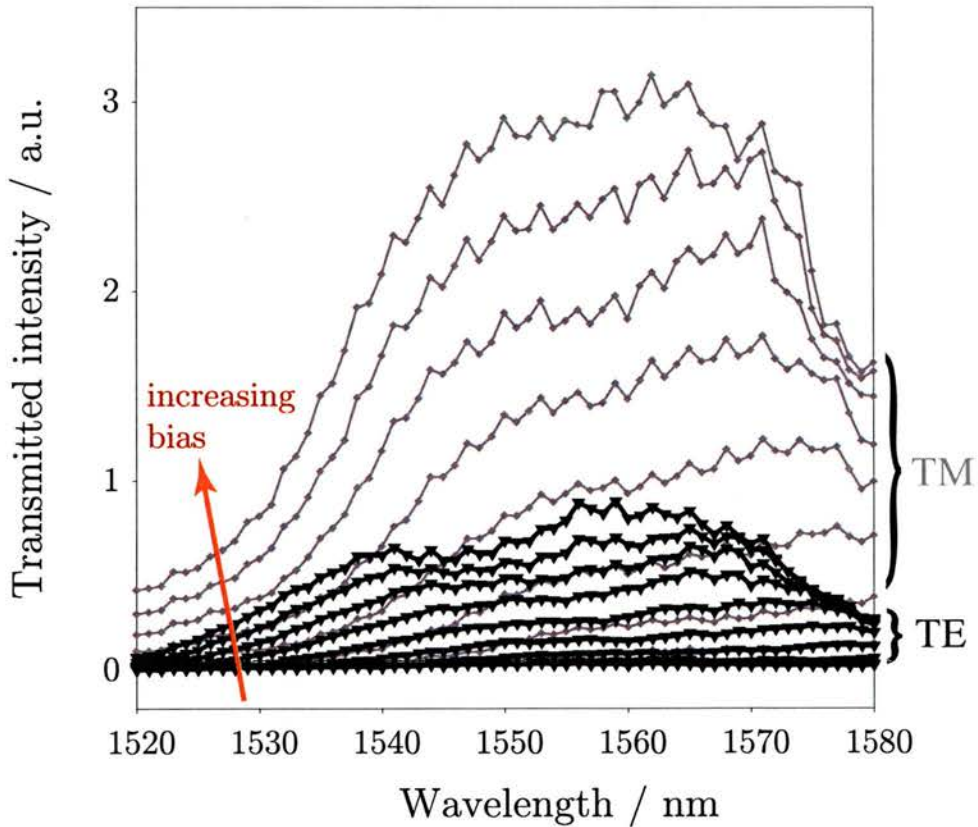


Figure 3.5: Intensity transmission of a CW beam measured at 35, 45, 55, 65, 75, 85, 95, 105 and 115 mA electrical bias as a function of wavelength for TE (grey lines and circles) and TM (black lines and triangles) polarisation.

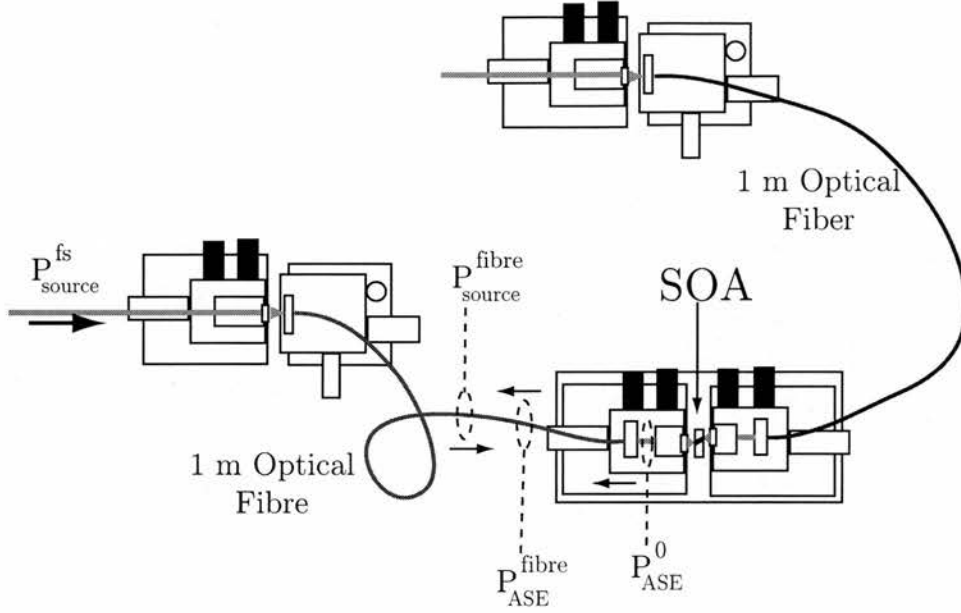


Figure 3.6: Schematics of the coupling of light into the SOA waveguide.

3.1.2 Coupling of light into the SOA waveguide

Our experiments require coupling light into the SOA waveguide from both sides. For that purpose, a factory aligned 3-block waveguide manipulator was used. As illustrated in figure 3.6, the brass block with the device is placed on the central block while adjacent microlenses collimate/focus the output/input light. On each side, the incoming beam is first coupled into a 1 m long section (with negligible dispersion [3]) of polarisation maintaining fibre by using mounts with FC fibre connectors. The latter was found to improve the stability in our measurements and greatly simplify the fine alignment of the setup, since the coupling of the light into the waveguide is isolated from changes in the direction of the source beam.

The device ASE power and the source beam are used to estimate, respectively, the device-to-fiber and free space-to-fibre coupling coefficients ($\eta_{device \rightarrow fibre}$ and $\eta_{fs \rightarrow fibre}$). The procedure outlined below was followed for the light coupled at both facets of the SOA.

In the first instance, we measure the collimated ASE power just after the microlens, P_{ASE}^0 (see figure 3.6). Detaching the fibre from the FC coupler on the far side, we also measure the power of the emerging ASE. The device to fibre coupling coefficient is then

given by

$$\eta_{device \rightarrow fibre} = \frac{P_{ASE}^{fibre}}{P_{ASE}^0}. \quad (3.1)$$

The coupling coefficient $\eta_{fs \rightarrow fibre}$ is defined as

$$\eta_{fs \rightarrow fibre} = \frac{P_{source}^{fibre}}{P_{source}^{fs}}, \quad (3.2)$$

where P_{source}^{fs} is the optical power of the incoming source beam. P_{source}^{fibre} is the power of the emerging light when detaching the fibre from the FC fibre coupler on the waveguide manipulator (see figure 3.6).

The total coupling coefficient is obtained as the product of $\eta_{device \rightarrow fibre}$ and $\eta_{fs \rightarrow fibre}$

$$\eta_{total} = \left(\frac{P_{ASE}^{fibre}}{P_{ASE}^0} \right) \times \left(\frac{P_{source}^{fibre}}{P_{source}^{fs}} \right). \quad (3.3)$$

Using a $\times 40$ microlens, typical values for the coefficients η_{output} and $\eta_{fs \rightarrow fibre}$ were found to be on the order of 10% and 25% respectively, yielding a total coupling coefficient of $\eta_{total} \approx 2.5\%$.

Similar methods to that previously described can be found in the literature [5]. In our case, the most significant source of uncertainty comes from the losses due to reflection at the device facets, which are not accounted for. These are, however, expected to be small due to the anti-reflection coatings.

3.2 Resolving the SOA ultrafast dynamics

3.2.1 The pump-probe technique

For the last twenty five years, pump-probe measurements [6] have been the standard tool to study material ultrafast dynamics. This is a time-domain technique in which a weak pulse (probe) experiences the material nonlinear response induced by a leading strong pulse (pump). The averaged probe transmission/phase shift is measured for different delays between the pump and probe pulses, thus obtaining a picture of how the pump induced changes in material gain/refractive index changes recover on ultrashort time scales.

One advantage of this technique is its simplicity. Furthermore, the resolution of the

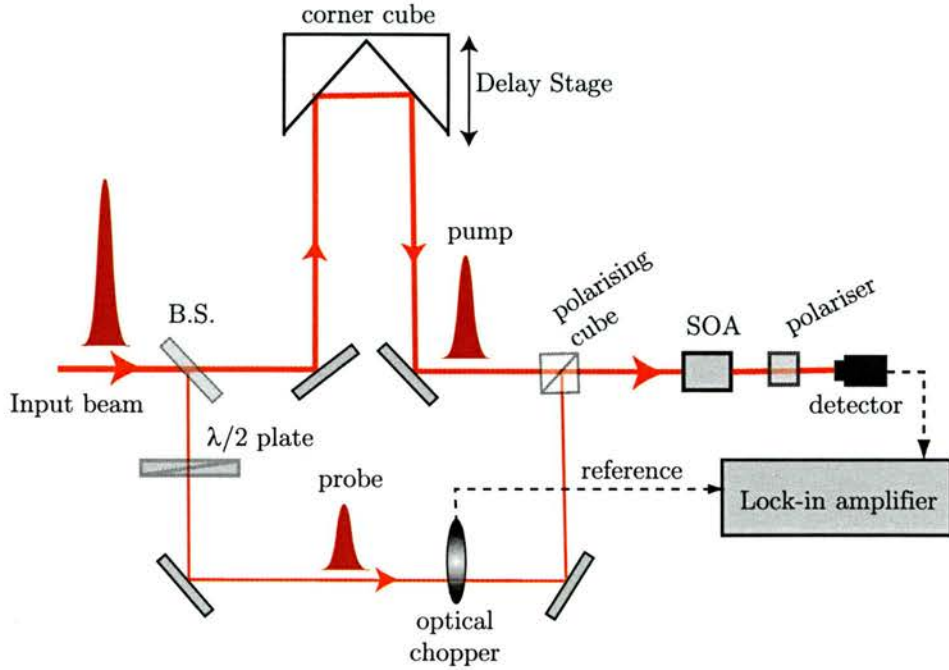


Figure 3.7: Pump-probe set-up for studying the gain dynamics. Pump and probe are orthogonally polarised and arrive to the SOA with a relative timing controlled by the delay stage. After propagating through the device, the polariser filters the probe, whose intensity is measured with a slow detector.

measurement depends on the temporal widths of pump and probe and subsequently does not require fast detection. Accurate control of the delay between pump and probe, of critical importance to this technique, can be easily achieved by means of a computer-controlled delay stage. Obviously, the next pump-probe pair must arrive once any effect due to the previous pump has disappeared.

To illustrate the principle of the pump-probe technique, figure 3.7 depicts one of the possible configurations, similar, although simpler, to those described in chapter 4. Note that pump and probe are degenerate (centered at the same wavelength), orthogonally polarised and that their relative timing is controlled by a delay stage.

In the set-up depicted in figure 3.7, the transmission of the probe is measured as a function of the delay with respect to the pump pulse. An optical chopper modulates the probe light. In the lock-in amplifier, the detected signal and the chopper reference are multiplied. As both signals are modulated with the same frequency, the filtered DC component of their product is proportional to the integrated power of the probe pulse. This coherent detection scheme greatly improves the sensitivity of the measurements, and

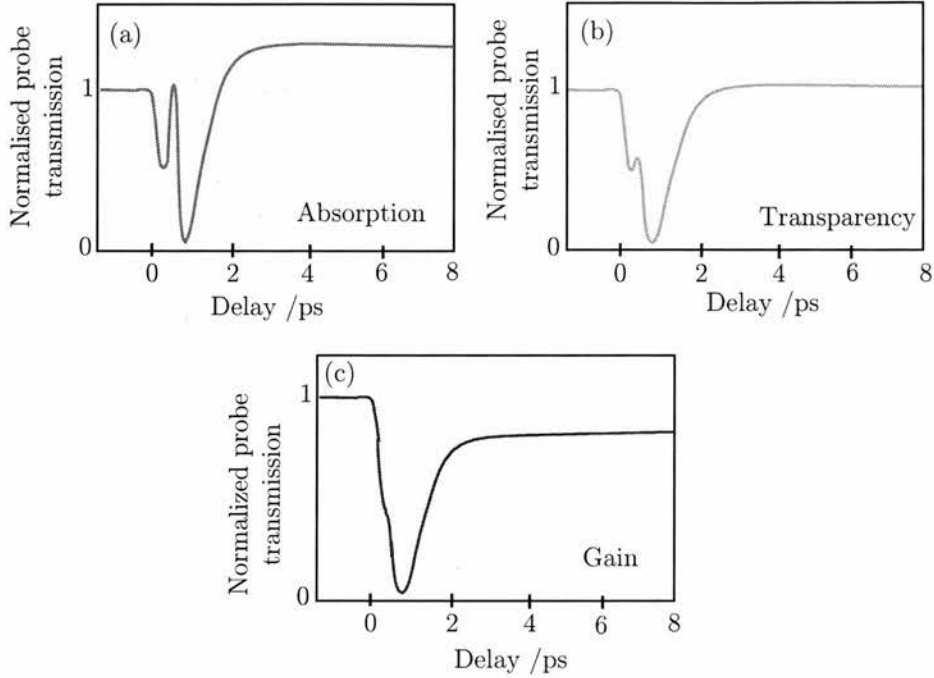


Figure 3.8: Example of typical pump-probe curves obtained for InGaAsP SOAs, in the three regimes of operation (a) absorption, (b) transparency and (c) gain.

minimises noise due to pump leakage in the polarisers.

Other pump-probe configurations have been proposed. The utilisation of a heterodyne detection technique [7] allows for co-polarised pump and probe, thus avoiding pulse walk-off in the sample due to group velocity mismatch and proves to be very useful in the study of devices whose gain is polarisation sensitive, such as compressively strained or unstrained multiple quantum wells. With some modifications and the use of an FM radio receiver, this technique allows measurement of the refractive index change as a function of the delay between pump and probe.

Our work is focused on the study of SOAs biased at gain, as needed for switching applications. However, SOAs can also be probed at transparency and absorption. Ultrafast nonlinearities such as SHB or carrier heating will have different signatures in the traces corresponding to these three regimes, as long as short enough pulses (typically less than 150 fs) are available to resolve them. Figure 3.8 shows a sketch of illustrative pump-probe traces in all regimes of operation. These are measurements of the changes in probe transmission, giving information on the gain dynamics. In an analogous fashion, changes in the refractive index can be measured and analysed. Henceforth, it should be kept in

mind that positive delays are defined by the pump preceding the probe.

In the figure, only a temporal range of 8 ps is pictured. Obviously, this is not enough to appreciate the long-lasting recovery associated with the band-filling nonlinearity which instead is observed as a change in level of the probe transmission. With the device under gain conditions, stimulated emission induced by the pump depletes the carriers in the conduction band thus reducing the probe transmission (note the negative step). In absorption, the optically stimulated creation of carriers increases the probe transmission, giving a positive step. At transparency, no net interband stimulated transitions occur so no long-lived change in transmission is observed.

Heading towards shorter time scale effects, we can see in all three regimes a probe transmission reduction recovering with a characteristic time on the order of hundreds of femtoseconds. This cannot be explained by spectral hole burning or any other effect involving interband transitions alone. It is due to the heating of carriers, which compresses the gain in all regimes of operation, and the subsequent cooling via coupling to the lattice vibrations.

Another remarkable feature is observed in absorption. It is a transient increase in probe transmission occurring in a time scale of 100-200 fs. In this case, the process responsible is SHB, which bleaches a hole in the absorption until fast carrier-carrier scattering drives the distribution into a new quasi-equilibrium. Under gain conditions, SHB causes a gain reduction and thus decreases probe transmission. In both absorption and gain, the SHB contribution is delayed regarding the zero delay point due to the finite carrier-carrier scattering times.

Finally, the fast transient decrease in probe transmission observed in the three cases has been attributed to two photon absorption (TPA). This is virtually instantaneous for the time resolution considered here, so the effect adiabatically follows the profile of the pulse. The small undulation observed at transparency near zero delay point cannot be attributed to SHB, since no net stimulated transitions take place. It is due mainly to the spectral artifact, this being the dynamic coupling between gain and refractive index [8]. A less significant contribution to this feature comes from the delay in the onset of carrier heating resulting from the finite carrier-carrier scattering times.

It is worth noting that alternative techniques, complementary to pump-probe, have

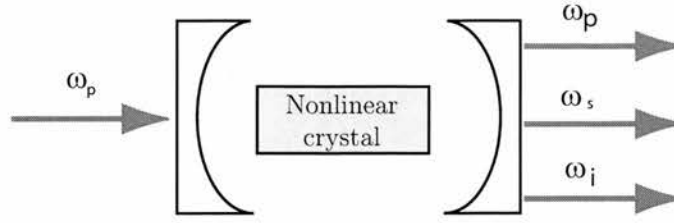


Figure 3.9: Schematics of an OPO.

been used to study the ultrafast response of SOAs. One remarkable example is Four Wave Mixing spectroscopy (FWM), belonging to the category of spectral domain measurements, which has attracted considerable attention since the late 1980's. In this case, a pump and a probe with carrier frequencies ω and $\omega + \Delta\omega$, respectively, are coupled into the SOA waveguide. Both will interfere and the beat frequency will drive the carriers in the material, modulating the gain/index profile of the device. As a result, via the third order susceptibility $\chi^{(3)}$, energy from the pump and the probe will be coherently transferred to a third field with carrier frequency $\omega - \Delta\omega$, known as the conjugate field, because its phase is the conjugate of the probe's. The energy of the conjugate signal is measured as a function of the delay between pump and probe. This provides useful information on excited state lifetimes and dephasing rates, since once the atomic states interacting with the fields have lost coherence between pump and probe arrivals, no FWM signal is observed.

3.2.2 Optical source: Optical Parametric Oscillator

In this subsection, the basic principles behind the Optical Parametric Oscillator (OPO) will be reviewed. It is not our aim to give a full description of the OPO theory, as it is a broad field in itself. We will concentrate on the OPO we use as the source of ultrashort pulses required for our measurements in SOAs.

An OPO consists basically of a nonlinear material within an optical resonator, to some degree resembling a conventional laser configuration. During the last decade, they have become established as versatile sources of ultrashort pulses in the near and mid-infrared range. As shown in figure 3.9 a strong beam (pump) enters the cavity and when crossing the crystal, it generates radiation at two lower energies. The higher frequency wave is called the signal (s) and the lower frequency wave is known as the idler (i). The coupling

and energy transfer between these waves takes place via a difference frequency mixing process [9] which exploits the material $\chi^{(2)}$ susceptibility of the crystal. As this is a parametric interaction, the three waves must meet the energy conservation condition.

$$\omega_p = \omega_s + \omega_i. \quad (3.4)$$

For the nonlinear interaction to be efficient, phase mismatch, given by equation 3.5, must be kept to a minimum, and ideally set to zero.

$$\Delta k = k_p - k_s - k_i, \quad (3.5)$$

where k_p , k_s , k_i are the pump, signal and idler wave vectors in the nonlinear crystal, respectively. Other factors such as crystal length and dispersion will be critical when high generated power and conversion efficiency are to be achieved.

The frequency of the signal and idler waves can be tuned in different ways. Since the refractive index in the nonlinear crystal depends on both wavelength and temperature, the operation of the OPO can be modified by changing the pump frequency or the crystal temperature. A third method relies on the crystal birefringence, rotating the angle at which the pump is incident upon the crystal.

In our OPO, crystal birefringence is not used to achieve phase matching, as it suffers from a number of limitations. We use quasi-phase matched conditions instead [10], whose principles are outlined in the next paragraph. However, pump wavelength and crystal temperature are still useful parameters to tune the OPO output.

If $\Delta k \neq 0$, waves still interact, though less efficiently, since they eventually slip out of phase when propagating through the crystal. This leads to an oscillating behaviour of the generated power and to poor overall conversion efficiency as the phase relation between the waves periodically changes from favouring forward conversion to back conversion. The concept is to reverse the sign of the nonlinear coefficient after propagation over the coherence length, this being the distance after which the gain is reduced by a half. This way the interaction is brought into phase and the conversion efficiency is substantially improved.

The nonlinear crystal used for our OPO was a 5 mm length of Periodically Poled

Litium Niobate (PPLN) divided into eight segments with grating periods ranging from 21.0 to 22.4 μm and antireflection coated at 1.55 μm . The crystal was mounted in an oven to allow temperature tuning.

So far we have described the nonlinear process taking place in the crystal and generating signal and idler waves from a strong pump. We shall now refer to the second key factor to OPO operation, namely, feedback. Our nonlinear crystal must be placed within an optical cavity for the signal and/or idler waves to resonate. Depending on whether only ω_s or both ω_s and ω_i resonate, we speak of Singly Resonant Oscillators (SRO) or Doubly Resonant Oscillators (DRO). Our OPO is synchronously pumped by a Ti:Sapphire mode locked laser and only the signal wave resonates in the cavity, thus providing greater stability at the cost of higher threshold power. The term "synchronously pumped" means that the OPO cavity length is matched to that of the Ti:Sapphire laser. This way, the resonating pulse meets the pump pulse at the crystal and is amplified in every round trip.

Our OPO, as shown in figure 3.10, is a three mirror synchronously pumped singly resonant standing wave cavity with a folded arm. Pumping is provided by a 82 MHz train of 1.8 ps pulses from a self-mode locked Ti:Sapphire laser (Spectra Physics Tsunami), pumped itself by a frequency doubled CW diode pumped $Nd : YVO_4$ (Spectra Physics Millennia X). Dispersion compensation within the cavity is achieved by means of two prisms. The mirrors in the set-up of figure 3.10(b) were chosen regarding their reflectivity to achieve optimum operation at 1.50 to 1.55 μm with a pump wavelength of 838 nm. The daily operation of the OPO required maintenance, which typically involved adjusting the length of the cavity to match that of the Ti:Sapphire laser.

Note that a repetition rate of 82 MHz (corresponding to a period of $\sim 12\text{ ns}$) allows the device to fully recover between the arrival of consecutive pump pulses in our experiments.

Monitoring system

The stability of the OPO as the ultrashort pulse source is critical to our pump-probe measurements. For this reason, a significant time was devoted to setting up a monitoring system using *Agilent VEE* software which keeps record of the OPO performance and other key factors, thus allowing us to check the validity of our measurements. A diagram of the monitoring system is sketched in figure 3.11, and figure 3.12 shows a screenshot of the

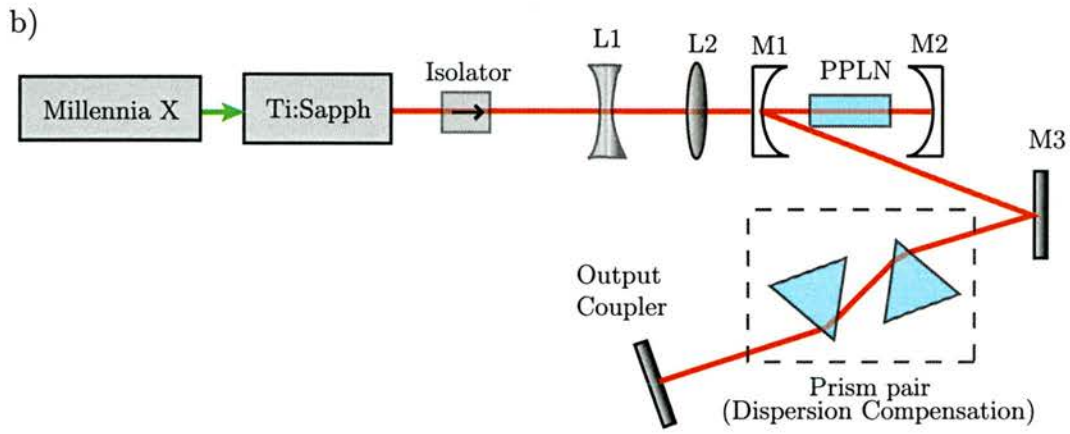
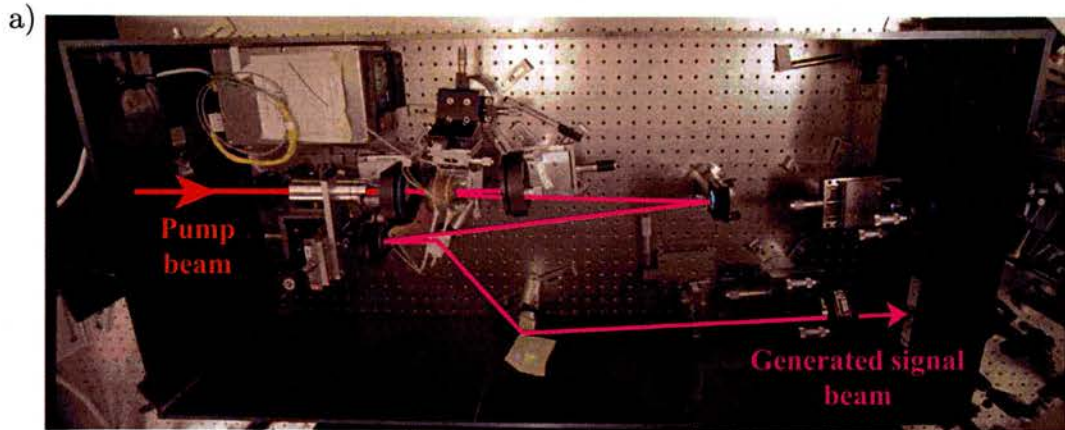


Figure 3.10: (a) Picture of the PPLN OPO set up (reproduced from [3]). (b) Diagram of the OPO. The mirror M3 is used to fold the cavity thus allowing the system to be compact.

monitoring software.

On the one hand, an internal photodiode samples the Ti:Sapphire laser power and this information is sent to a computer, which tracks the diode currents in the Millennia X as well.

The power spectrum of the OPO pulses was measured using a spectrometer (Rees Instruments, Laser λ meter, spectral range from 800 to 1600 nm) and stored. This allows a calculation of the pulse power, peak wavelength and spectral FWHM ($\Delta\nu$).

Since the nonlinear behaviour of semiconductor optical amplifiers is known to be drastically dependent on pulse width, it was therefore essential to our experiments to characterise the output of both the Ti:Sapphire laser and the optical parametric oscillator in the time domain.

On subpicosecond timescales, not even the fastest photodiodes currently available (with

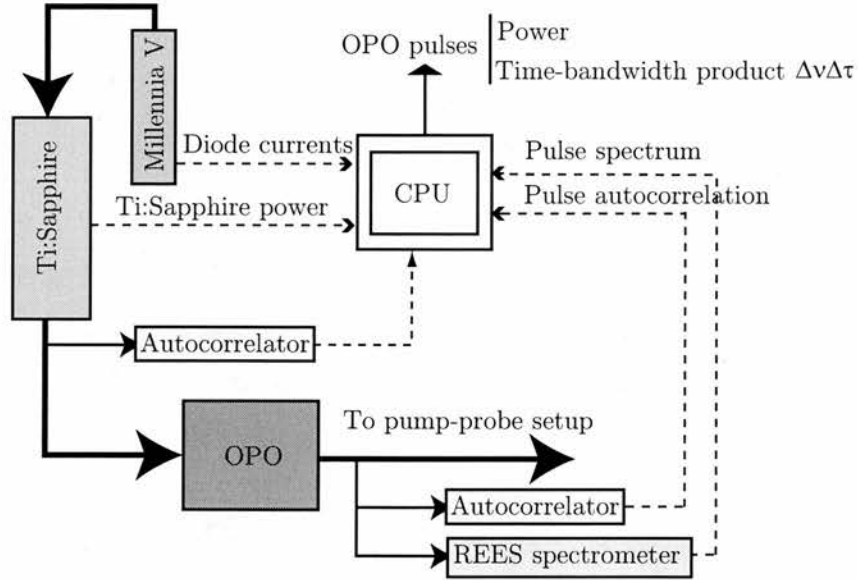


Figure 3.11: Diagram of the monitoring system.

rise times in the order of many hundreds of femtoseconds) allow for the direct measurement of the intensity profile of the pulses, $I(t)$, given by equation 3.6, or even to estimate their duration.

$$I(t) = |E(t)|^2 \quad (3.6)$$

In equation 3.6, $E(t)$ is the optical field, which can be expressed in terms of a complex envelope and the carrier frequency (ω_0).

$$E(t) = A(t) \exp [i\phi(t)] \exp (i\omega_0 t) + c.c. \quad (3.7)$$

In the monitoring set-up, the temporal characterisation of the pulses was carried out via the autocorrelation technique [11], illustrated in figure 3.13. The input pulse is split into two identical replicas which travel each along one arm of a Michelson interferometer. The path difference between the two pulses is varied by means of a moving mirror. When the two pulses meet again at the beam splitter, the total optical field is

$$E(t) + E(t - \tau), \quad (3.8)$$

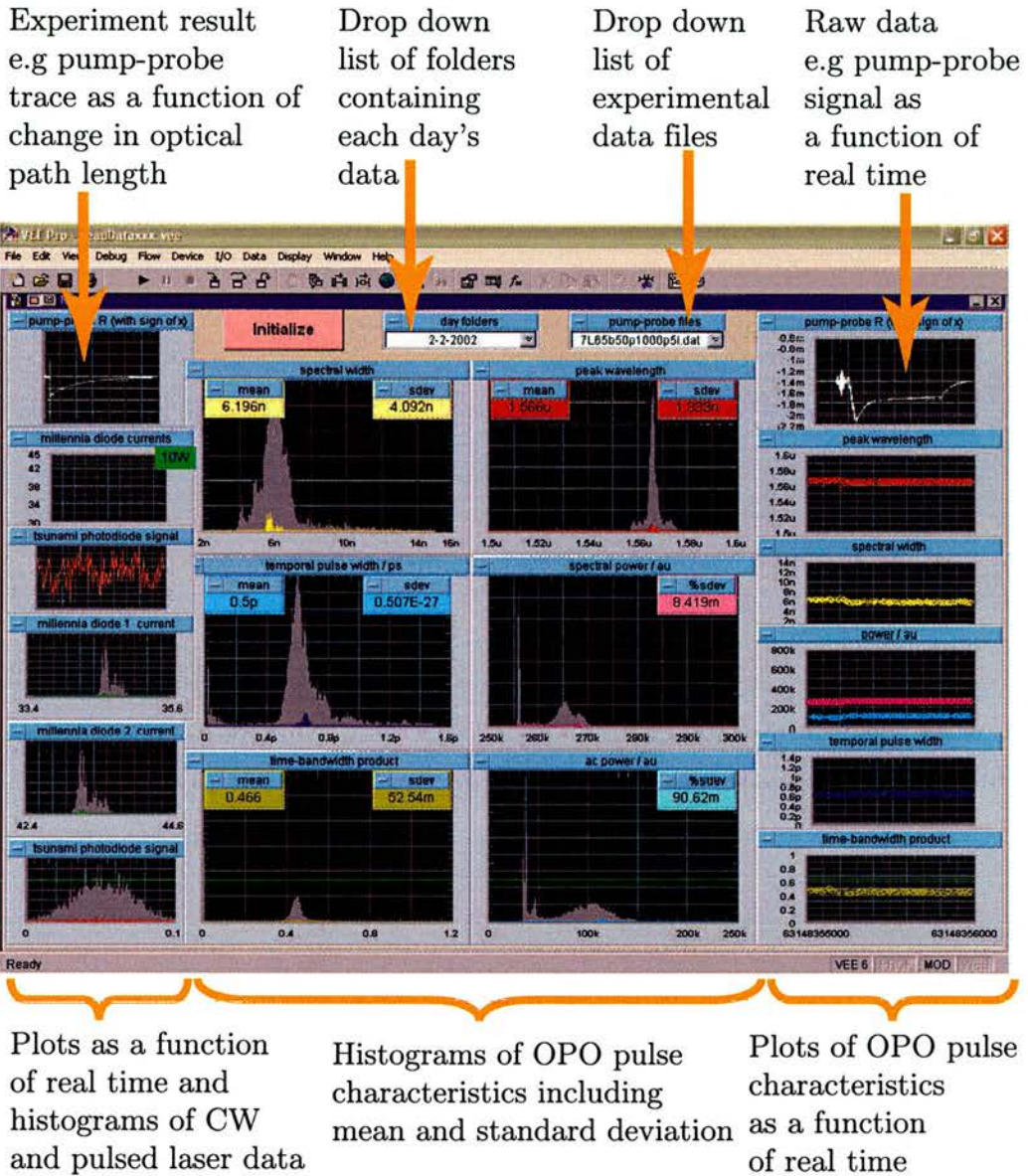


Figure 3.12: Screenshot of the monitoring software, reproduced from [3].

where τ is the delay between the pulses. The two pulses are made to interfere in a nonlinear detector, comprising a nonlinear crystal in which Second Harmonic Generation (SHG) occurs (KDP and BBO for pump pulse and OPO output wavelengths respectively) and a photomultiplier tube. The nonlinear signal generated by the overlap of the two pulses in the crystal can be expressed as

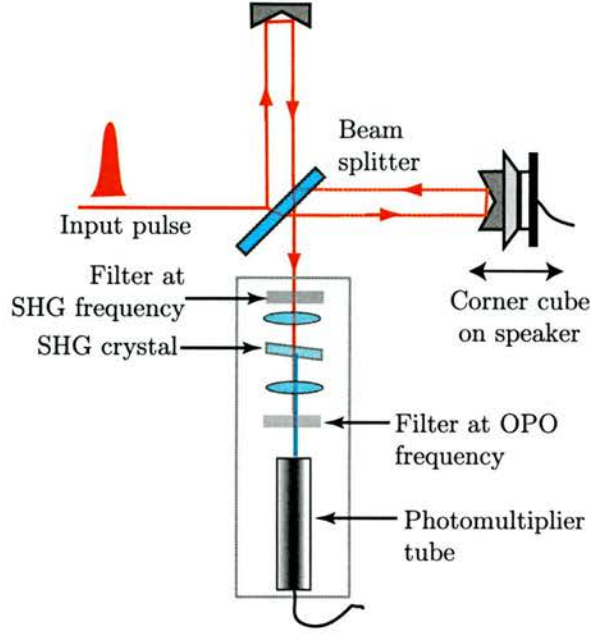


Figure 3.13: Schematics of the autocorrelator used to estimate the duration of the OPO pulses. A similar set-up was used with the pulses from the Ti:Sapphire laser.

$$G(\tau) = \frac{\int_{-\infty}^{\infty} |E(t) + E(t - \tau)|^2 dt}{2 \int_{-\infty}^{\infty} |E(t)|^2 dt} = \frac{\int_{-\infty}^{\infty} \left\{ A(t) \exp [i\phi(t) + i\omega_0 t] + A(t - \tau) \exp [i\phi(t - \tau) + i\omega_0(t - \tau)] + c.c. \right\}^2 dt}{2 \int_{-\infty}^{\infty} |E(t)|^2 dt} \quad (3.9)$$

The complex nature of the field envelopes in 3.9 will give interference terms, hence $G(\tau)$ being known as the interferometric autocorrelation. The latter is useful to detect the presence of chirp in the pulses, although it does not allow a determination the sign of the chirp unambiguously.

The detection system used in our set-up lacks of sufficient bandwidth to resolve the interference fringes, and the modified signal recorded is

$$g(\tau) = 1 + \frac{2 \int_{-\infty}^{\infty} I(t)I(t - \tau)dt}{\int_{-\infty}^{\infty} I(t)^2 dt}, \quad (3.10)$$

known as intensity autocorrelation. Note that equation 3.10 contains no phase information, so $g(\tau)$ is completely insensitive to the pulse temporal chirp. Regardless of the pulse shape,

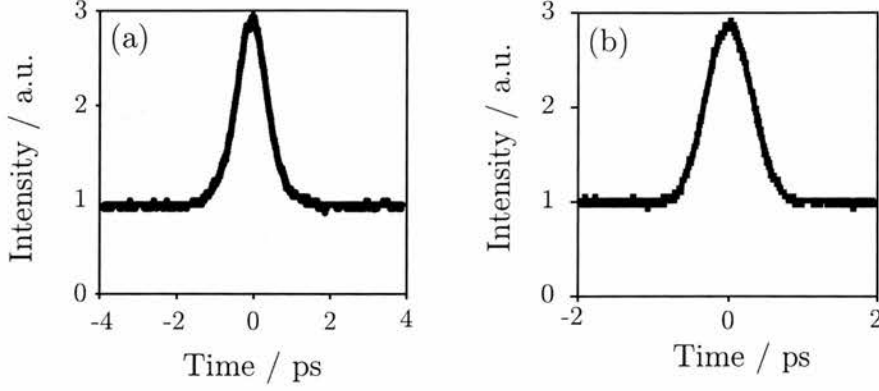


Figure 3.14: Autocorrelation traces of pulses (a) from the Tsunami Ti:Sapphire laser and (b) the OPO, measured by the monitoring system.

Field envelope	Intensity profile	k_i	$\Delta\tau_p \Delta\nu$
Gaussian	$\exp\left[-\left(\frac{t}{T}\right)^2\right]$	$\sqrt{2} \approx 1.414$	0.441
$sech^2$	$sech^2\left(\frac{t}{T}\right)$	1.543	0.315

Table 3.1: k_i constants, relating the autocorrelation width and pulse duration for gaussian and $sech^2$ intensity profiles.

the intensity autocorrelation is symmetric with respect to zero delay and ideally exhibits a peak to background ratio of 3:1.

Figure 3.14 displays an example of the autocorrelation traces measured in the monitoring set-up, both for pulses from the Ti:Sapphire laser and those generated by the OPO. The relation between the width of the intensity autocorrelation (Δt_i) and the full width at half the maximum (FWHM) pulse duration $\Delta\tau_p$, can be expressed as

$$\Delta\tau_p = \frac{\Delta t_i}{k_i} \quad (3.11)$$

where k_i is a constant which depends on the shape of the optical field envelope. Therefore, a certain intensity profile of the pulses must be assumed 'a priori' to estimate their duration. In our monitoring program, two different pulse profiles were considered, namely, gaussian and $sech^2$ (see table 3.1).

The last decade has seen significant developments in the characterisation of ultrashort pulses. Techniques such as FROG [12] and SPIDER [13] allow recovery of both the amplitude and phase profile of femtosecond pulses, however, the autocorrelation technique, within its limitations, was sufficient for our purposes.

The autocorrelation of the pulses generated in the OPO was sent, together with the

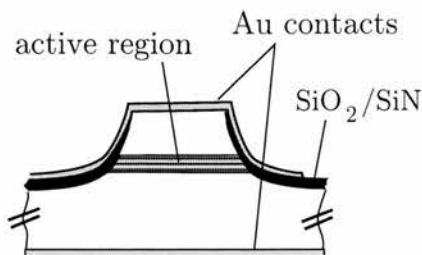


Figure 3.15: Cross section of a typical QCL in the plane of the facets.

corresponding spectrum, to the computer via a GPIB connection. Finally, the time-bandwidth product ($\Delta\tau_p\Delta\nu$) is calculated and stored, as it provides useful information on the chirp of the pulses (see figure 3.11).

3.3 Wafer processing and mounting of the QC lasers

The wafers of the QC laser reported in this thesis were grown by Molecular Beam Epitaxy (MBE) at Bell Labs (Lucent Technologies), following the design specifications developed at Princeton University (see section 5.2.1).

The processing of the wafers into lasers was carried out at Princeton University by Dr. D. Wasserman. This task involved etching deep ridge waveguides on the wafers using photolithography and deposition of an insulating layer of SiO_2/SiN . A second level of photolithography was used to open a window in the oxide and deposit a thin metal layer (100-200 μm thick) by evaporation. A metal layer was also evaporated on the back of the sample. The lasers were cleaved to 2-3 mm length and their facets left uncoated. We etched ridges 6 – 20 μm wide (waveguiding in the mid-IR wavelength range will be thoroughly discussed in chapter 5). The structure of a typical QC laser is depicted in figure 3.15.

Some samples were processed by etching circular mesas of a few hundred micrometers in diameter in the wafers, instead of waveguides. Metal contacts were evaporated on top of the mesas, and the samples were then cleaved to obtain maximum light output (see figure 3.16). These structures are well suited for luminescence measurements in the absence of optical feedback.

Once a portion of the wafer has been processed into lasers or mesas, robust packaging

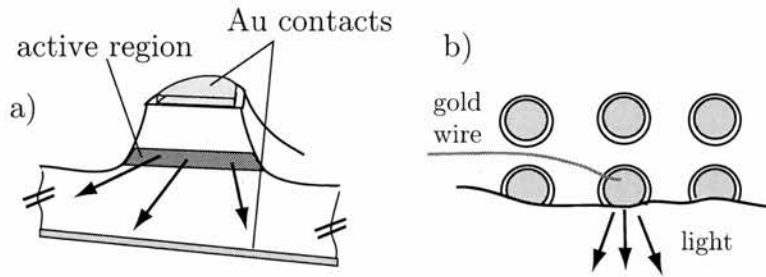


Figure 3.16: (a) Cross section of a sample comprising mesas. (b) top view of the sample. The black arrow indicates the emission of light.

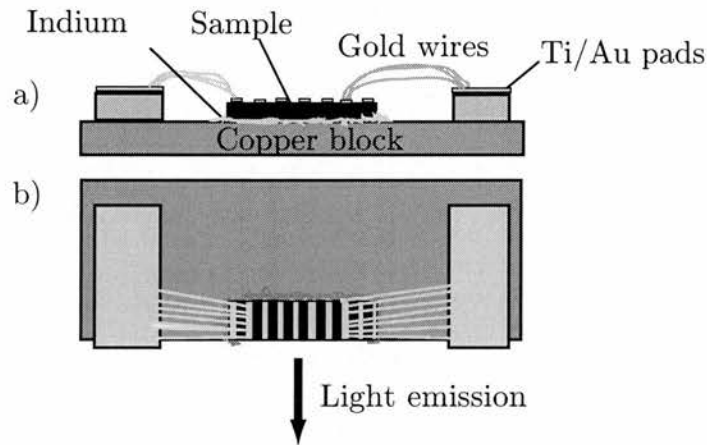


Figure 3.17: Sample mounting. (a) Facet view. (b) Top view.

is required to ease the handling and cooling of the samples.

A sample, typically comprising around 10 lasers grown n-side up, was pasted with indium onto a rectangular copper block (see figure 3.17). Titanium/Gold pads are glued on both sides and gold wires ($\sim 8 - 10$) are bonded from each pad onto one of the lasers. The copper block and the gold pads thus provide electrical contacts for two lasers in each sample.

To achieve low temperature operation of the lasers, the copper block is screwed onto a mount at the bottom end of a cold finger, as depicted in figure 3.18(a) and (c). According to their relative position in the set-up, the two lasers in the sample are labelled as 'top' and 'bottom'. The finger is introduced in a container (see figure 3.18(b)) and vacuum is created by means of a roughing pump. Finally, liquid nitrogen or liquid helium are fed into the finger to cool down the sample. At cryogenic temperatures, vacuum prevents atmospheric moisture from condensing on the samples.

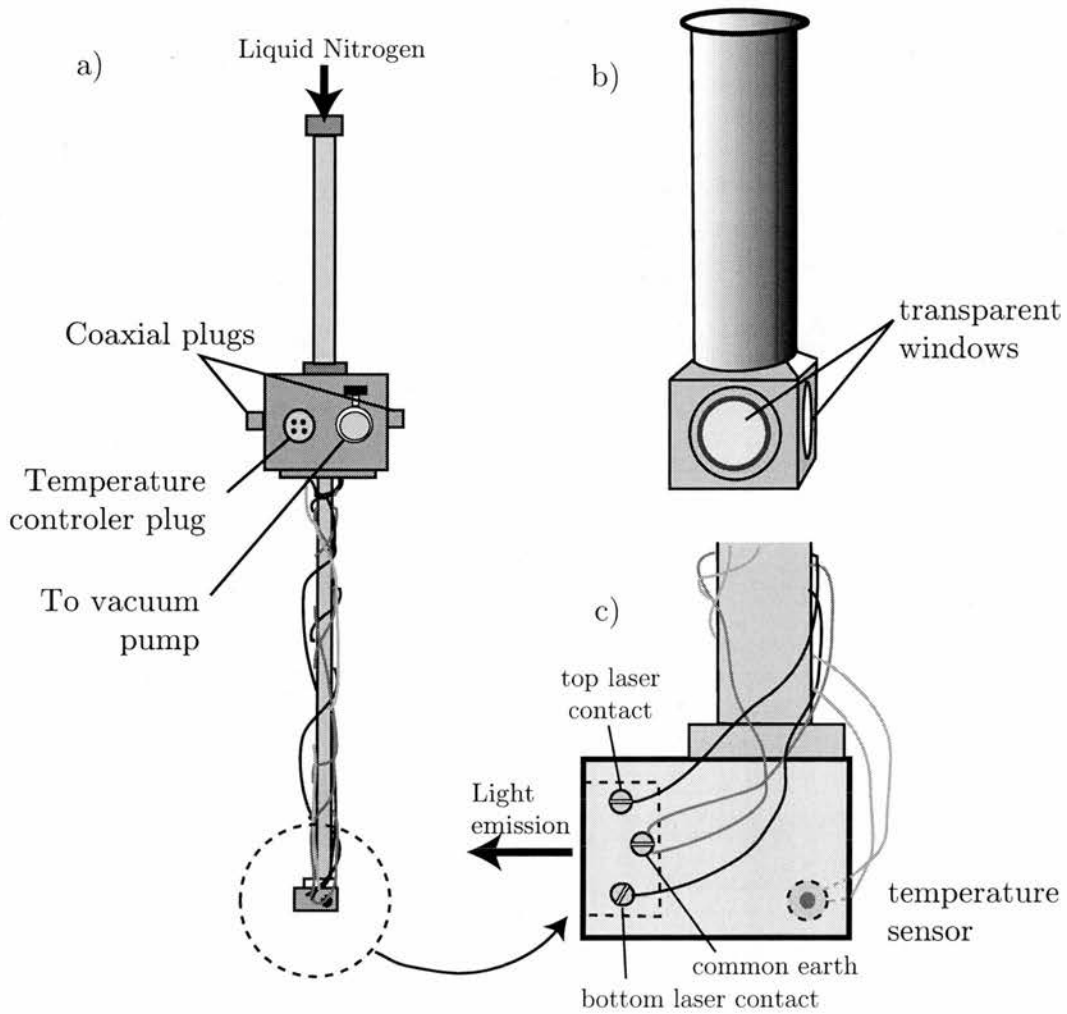


Figure 3.18: Schematics of the cryostat.

The finger is wired down to the bottom end to both inject current into the laser and to provide connection to a sensor monitoring the sink temperature.

3.4 QC laser characterisation

3.4.1 Spectral measurements

In the course of the work presented in chapter 5, Fourier Transform Infrared (FTIR) spectroscopy was used extensively to spectrally resolve the light output of QC lasers and

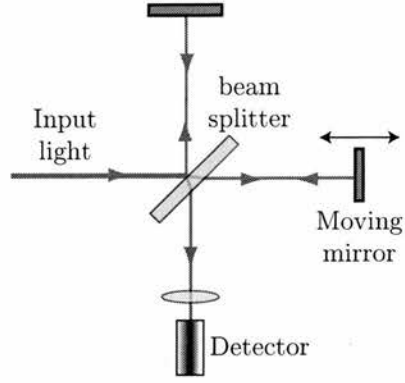


Figure 3.19: Schematics of the interferometer used in Fourier Transform spectroscopy. Note that one of the mirrors is moving back and forth around the position corresponding to zero path difference.

check that design expectations had been met. When lasing, spectral measurements directly characterise the devices, giving the operating wavelengths. Below threshold, the laser emission spectra provides useful information on the optical transitions and energy levels in the structure.

Fourier Transform spectroscopy is a well established analytical tool and is well described in the literature (see for example [14]). In this section, we will briefly discuss its basics and the particulars to our experimental setup.

In a FTIR spectrometer, light enters a Michelson interferometer in which one of the mirrors is moving back and forth from the constructive interference position (see figure 3.19). Let us start by considering an ideal beam splitter and plane waves. The signal in the detector would then be given by

$$I(x) = |\vec{E}|^2 = |E_{in}|^2 + |E_{in}|^2 \cos(kx) = |E_{in}|^2 [1 + \cos(kx)], \quad (3.12)$$

where E_{in} is the input field amplitude and x is the path difference. For non-monochromatic light with spectral power distribution $S(k)$, equation 3.12 would become

$$\begin{aligned} I(x) &= \int_0^\infty [1 + \cos kx] S(k) dk = \int_0^\infty S(k) dk + \int_0^\infty S(k) \frac{e^{ikx} + e^{-ikx}}{2} dk = \\ &= \frac{1}{2} I(0) + \frac{1}{2} \int_{-\infty}^\infty S(k) e^{ikx} dk, \end{aligned} \quad (3.13)$$

and, by rearranging the terms,

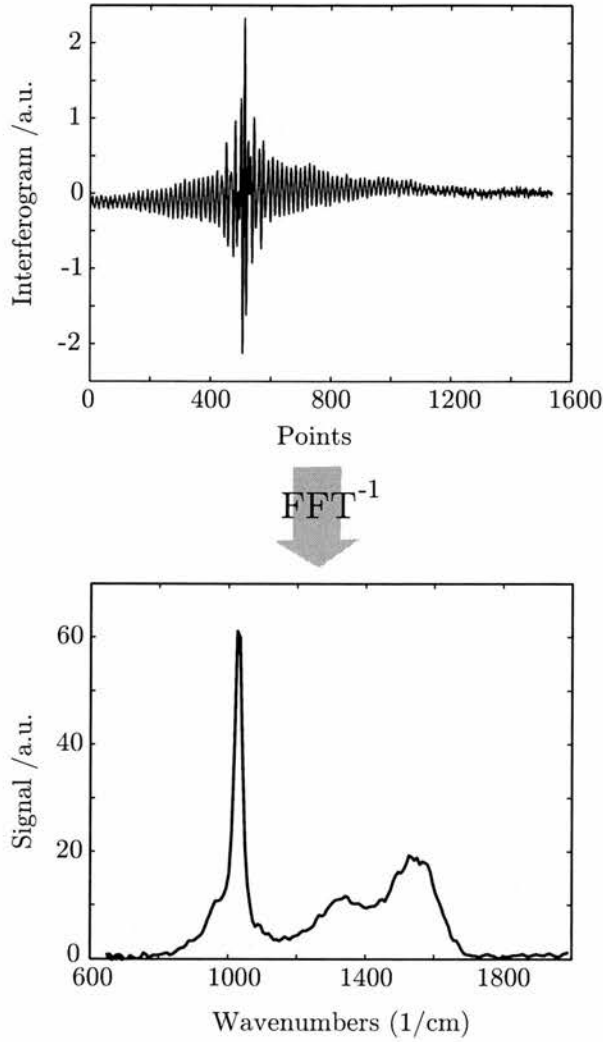


Figure 3.20: (a) Example of a measured interferogram. (b) Retrieved spectrum via Fourier calculations.

$$V(x) \equiv \frac{2I(x) - I(0)}{\sqrt{2\pi}} = \frac{1}{\sqrt{2\pi}} \int_{-\infty}^{\infty} S(k) e^{ikx} dk. \quad (3.14)$$

The last equation illustrates how the interferogram can be expressed as a Fourier transform of the spectral distribution of the input light. Therefore, $S(k)$ can be obtained from $I(x)$ via straightforward Fourier calculations. Figure 3.20 shows an example of a measured interferogram and the corresponding spectrum, retrieved by calculating the inverse Fourier transform.

In practice, the interferogram can only be measured for a discrete number of points within a limited range of x . As a result, the resolution is finite and proportional to

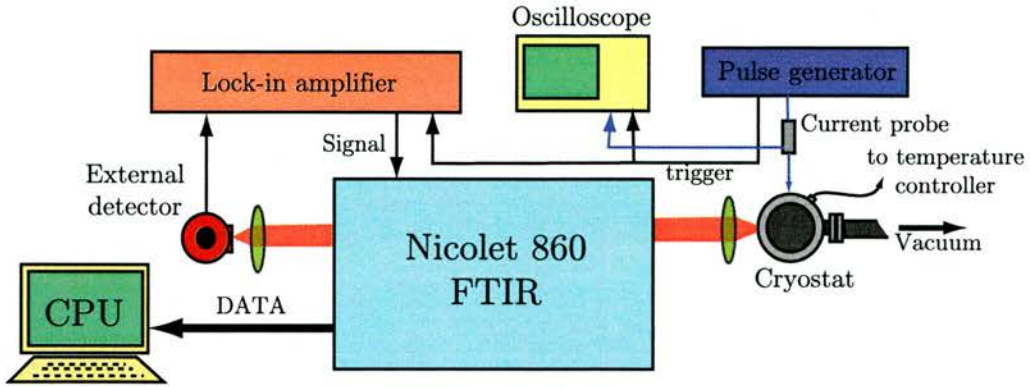


Figure 3.21: Sketch of the experimental set-up for spectral measurements.

$$(2\pi x_{max})^{-1}.$$

A FTIR spectrometer can be operated in two different modes, namely, fast-scan and step-scan. In the former, multiple interferograms are recorded and then averaged to yield the final result. This is useful when the lasers are above threshold and significant optical power is available. In the step-scan, the mirror is moved in steps and the interference signal is measured over some integration time for every position. Step-scan is much more time consuming and is best suited for low powers, such as those detected below threshold.

All the spectral measurements presented in chapter 5 were carried out using a Nicolet 860 FTIR spectrometer controlled by a lab computer. Apart from the interferometer, the Nicolet 860 includes two built-in detectors (a room temperature and a HgCdTe (Mercury Cadmium Telluride or MCT) detector, cooled externally with liquid nitrogen) and two internal sources (IR and white light), which can be arranged in different configurations via the computer. For wavelengths shorter than $6 \mu m$, external cooled InSb detectors were used, as they provide better sensitivity.

In our set-up, as sketched in figure 3.21, the QC laser is biased with current pulses of adjustable duration, usually within the 50-500 ns range, at a 82 kHz rate. The laser light was collimated with a lens (*Ge*, *CaF₂* or *ZnSe*, depending on the wavelengths to be measured) and sent to the spectrometer. The beam would then travel through the interferometer and across the sample compartment (not in use) to finally either reach the internal detector or leave the spectrometer to be detected externally. In step-scan measurements, the signal was sent to a lock-in amplifier for detection, and transmitted

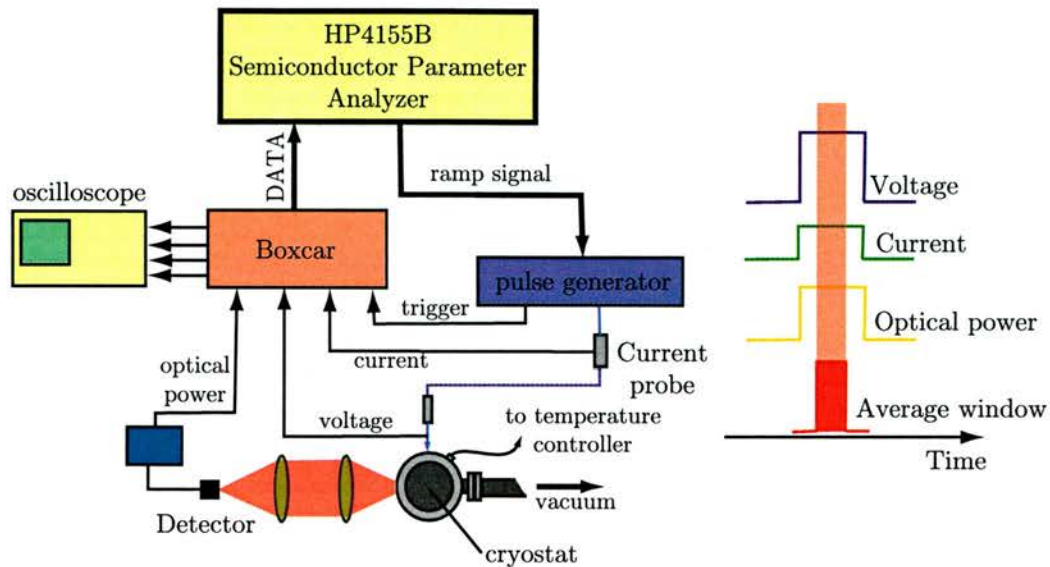


Figure 3.22: Diagram of the set-up to measure the light output and voltage versus current characteristics of QC lasers.

back to the spectrometer to be recorded.

3.4.2 Electrical measurements

The electrical response of QC lasers is a good indicator of performance and easily reveals current leakage or potential malfunctions. Voltage versus current measurements (I-V) were thus an everyday tool in the characterisation of our samples. By simultaneously measuring the output light power (henceforth referred to as light output and voltage versus current or I-V-L measurement), lasing thresholds were obtained.

In the experimental setup (figure 3.22), a HP4155B Semiconductor Parameter Analyser (SPA) sends a ramp signal to the pulse generator. As a result, the amplitude of the current pulses injected into the laser increases in small steps, typically up to 3 to 4 A. For every step, the boxcar averages voltage, current and peak optical power over some time window (as illustrated in the right inset of figure 3.22). These data are finally sent back to the SPA to be displayed and stored.

Figure 3.23 shows a typical example of the light output and voltage versus current characteristics of a QC laser, measured in the set-up of figure 3.22. Note that the L-I curve reveals that laser threshold is reached at approximately 1.3 A current.

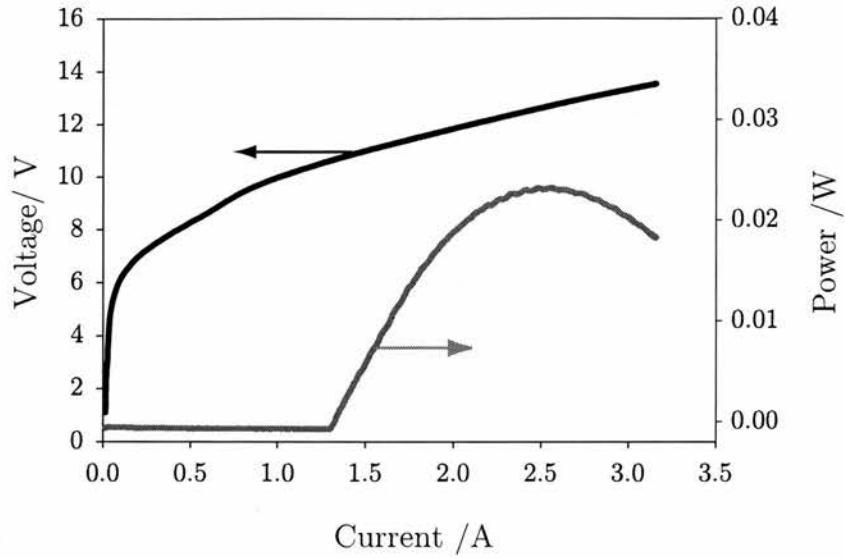


Figure 3.23: Example of typical IVL characteristics of a QC laser, showing the laser threshold at ≈ 1.3 A.

3.5 Summary

In the present chapter, we have described the structure and mounting of the semiconductor devices that are the subject of our study. In addition, the measurement techniques employed and experimental conditions under which this work was carried out have been explained in detail.

The principles of the pump-probe technique have been discussed as a means to study the ultrafast carrier dynamics in multiple quantum well semiconductor amplifiers. The source of ultrashort optical pulses used in our experiments, an optical parametric oscillator producing subpicosecond pulses and tunable around $1.5\ \mu\text{m}$ wavelength, was also described.

Following a description of the cryostat and vacuum systems employed to achieve low temperature operation, we introduced the techniques and experimental setups used in the characterisation of our QC lasers. These include Fourier Transform InfraRed (FTIR) spectroscopy and light output and voltage versus current measurements.

References for Chapter 3

- [1] R J Manning. Private communication. Corning, Ipswich, 2002.
- [2] J-Z Zhang and I Galbraith. Private communication. Heriot Watt University, Edinburgh, 2002.
- [3] J G Fenn. *Ultrafast dynamics in semiconductor optical amplifiers*. PhD thesis, School of Physics and Astronomy, University of St Andrews, May 2003.
- [4] C P Seltzer, A L Burness, M Stevenson, M J Harlow, D M Cooper, R M Redstall, and P C Spurdens. Reliable 1.5 μm buried hetrostructure, separate confinement, multiple quantum well (BH-SC-MQW) lasers entirely grown by MOCVD. *Electron. Lett.*, 25(21):1449–1451, 1989.
- [5] L F Tiemeijer, P J A Thijs, T van Dongen, J J M Binsma, and E J Jansen. Polarisation resolved, complete characterisation of 1310 nm fiber pigtailed multiple-quantum-well optical amplifiers. *IEEE J. Lightwave Technol.*, 14(6):1524–1533, 1996.
- [6] E P Ippen and C V Shank. *Ultrashort light pulses, picosecond techniques and applications*. Springer-Verlag, Berlin, 1977. Chapter: Techniques for measurement.
- [7] K L Hall, G Lenz, E P Ippen, and G Raybon. Heterodyne pump-probe technique for time-domain studies of optical nonlinearities in waveguides. *Opt. Lett.*, 17(12):874–879, 1992.
- [8] J Mork and A Mecozzi. Theory of the ultrafast optical response of active semiconductor waveguides. *J. Opt. Soc. Am. B*, 13(8):1803–1816, 1996.
- [9] R W Boyd. *Nonlinear Optics*. Academic Press, New York, 1992.
- [10] D T Reid, G T Kennedy, A Miller, W Sibbett, and M Ebrahimzadeh. Widely tunable, near-to mid-infrared femtosecond and picosecond optical parametric oscillators using periodically poled LiNbO_3 and RbTiOAsO_4 . *IEEE J. Sel. Top. Quantum Electron.*, 4(2):238–248, 1998.
- [11] J-C Diels and W Rudolph. *Ultrashort laser pulse phenomena*. Academic Press, London, 1996.
- [12] R Trebino and D J Kane. Using phase retrieval to measure the intensity and phase of ultrashort optical pulses: frequency resolved optical gating. *J. Opt. Soc. Am. A*, 10(5):1101–1111, 1993.
- [13] C Iaconis and I A Walmsley. Spectral phase interferometry for direct electric-field reconstruction of ultrashort optical pulses. *Opt. Lett.*, 23(10), 1998.
- [14] S Davis, M C Abrams, and J W Brault. *Fourier Transform Spectroscopy*. 2001.

Chapter 4

Ultrafast nonlinearities in semiconductor optical amplifiers

4.1 Introduction

In recent years, there has been considerable progress in the development of ultrafast optical signal processing applications using semiconductor optical amplifiers [1]. SOA-based interferometric switches, such as the Terahertz Optical Asymmetric Demultiplexer (TOAD) or the family of Mach-Zehnder interferometers (MZI), can be operated at rates faster than the interband gain recovery time of the material [2]. Particularly given the quality of fully integrated switches demonstrated recently [3], this approach provides an attractive solution to the demand for ultrafast, low energy optical switches. However, the implications of the refractive index changes associated with the subpicosecond gain dynamics in switching operation are not yet fully understood.

The first section of this chapter reviews different theoretical approaches to the study of the ultrafast dynamics of SOAs. In this context, we introduce a phenomenological model based on rate equations to be used in the analysis of our experimental results.

Following the description of the model, we present the results of interferometric three-beam pump-probe experiments on a SOA which can time-resolve the complex refractive index dynamics occurring during the onset of optical switching. These measurements reveal an ultrafast component on the edge of the switching window attributed to carrier heating, consistent with the numerical predictions.

In the experiments reported in the last section, counter-propagating sub-picosecond pulses are used to monitor gain saturation along the SOA waveguide. The functional form of the spatial dependence of gain saturation is found to be dependent on the pulse energy. The latter is analysed in the light of the model predictions, and the implications for all-optical switching applications are discussed.

4.2 Modelling the SOA dynamics

The propagation of light through a semiconductor optical amplifier is a highly complex problem, particularly in the case of sub-picosecond pulses. The carrier dynamics are dictated by a plethora of nonlinear phenomena which depend on a vast number of factors such as, amongst others, the material composition, the intensity of the optical beam or the electrical bias. Various approaches, differing in their level of complexity, have been taken to interpret the experimental results and theoretically understand the SOA behaviour.

Early models, such as that by Agrawal and Olsson [4], calculated the propagation of picosecond pulses (both amplitude and phase) in a SOA taking into account only the gain saturation due to band-filling. This model predicted strong self-phase modulation of the pulses, as they excite carriers and change the refractive index of the material, leading to spectral broadening and a frequency shift.

As temporal pulse widths were progressively shortened to a few picoseconds or even hundreds of femtoseconds, pump and probe experiments [5, 6] showed the signature of ultrafast phenomena not previously taken into account.

The first approach was purely phenomenological [7, 8], based on a rate equation model similar to that shown for interband nonlinearities. The equations are refined to take into account carrier heating and other ultrafast dynamics. This is done by means of "virtual populations" which change to reproduce the effects of those phenomena. This way, the gain compression due to carrier heating is modelled via a reduction in the virtual carrier density N_{ch} ; virtual because carrier heating does not change the actual carrier population.

The rate equation model allows interpreting the experimental results using an impulse response function h . This function consists of real and imaginary parts, $h = h_r + ih_i$, which respectively represent the refractive index and gain response of the SOA. h_r and

h_i are sums of exponentials with different characteristic times and weighted by constants. Each term is associated with a particular effect and the probe transmission is calculated as the convolution between the imaginary part of the impulse response function and the pulse autocorrelation. The relative amplitudes and time constants are finally obtained by fitting the experimental results. It is important to note that this approach assumes that the polarisation dephasing rates are fast compared to the width of the pulses (usually referred to as the adiabatic approximation).

Despite being simple and yielding very good fits of pump and probe traces, the results obtained should be considered with care, since spectral and coherent artifacts should be treated separately, the first being the dynamic coupling between gain and index and the latter the interference between pump and probe when they overlap. Besides, this model uses a large number of fitting parameters and does not lead to real insight into the nature of the different ultrafast processes involved.

At the opposite end of the complexity scale, efforts have been concentrated recently on modelling the SOA dynamics within the context of a first principles microscopic theory [9]. This implies treating the pulse propagation through the device as a Coulomb many-body problem. Therefore, physical insight is gained at the cost of mathematical complexity. In these models, the framework is the Semiconductor Bloch equations [10]. Apart from numerical differences in the estimates of gain and refractive index, and the inclusion of phenomena related to many body effects (band gap renormalisation, plasma screening, etc.), the main difference with respect to the previous approaches is the fact that the adiabatic approximation is not made here. The interplay between the different competing nonlinearities in SOAs taken into account in this model, lead to surprising predictions such as ultrashort pulse break-up in the time domain [11], later observed experimentally [12]. This suggested that coherent effects may play a more important role at room temperature than expected.

Standing in the middle ground, several rate equation models based in a semi-classical density matrix formulation [13, 14, 15, 16, 17] have provided good understanding of the SOA dynamics within a reasonably simple framework. The SOA is considered as an ensemble of inhomogeneously broadened two level systems. The concept of local carrier densities, being the density of carriers coupled by the electromagnetic field, is derived from

the diagonal elements of the density matrix, namely $\rho_c(k)$ and $\rho_v(k)$ (note the dependence in the vector number k). The non diagonal terms, accounting for polarisation, are usually adiabatically eliminated, assuming that the polarisation dephasing times (~ 50 fs) are much shorter than the length of the pulse. This allows for the use of concepts such as gain, but, as a counterpart, these models do not take coherent effects into account. Finally, to make the models consistent, the density matrix equations are coupled to the Maxwell equation for the propagating field.

However, these models remain phenomenological to some extent. Processes such as carrier-carrier scattering or the coupling to the lattice via phonon emission are still modelled by means of time constants representing the decay of the respective non-equilibrium distributions. The TPA coefficient is introduced as a fitting parameter as well. This is valid as long as the deviation from the Fermi distributions are not too large.

For the purposes of this thesis, a rate-equation based approach was adopted to assist in the analysis of the experimental results. The pump and probe pulses in the measurements presented here have orthogonal polarisations, rendering the coherent artifact negligible, and durations (500 fs $< \tau_p < 1$ ps) significantly longer than the typical dephasing times. The latter justifies the adiabatic approximation and allows for the use of the concept of gain.

However, solving the full set of density matrix equations was still beyond the scope of this thesis and further simplifications were made based on the experimental conditions. Since all the pulses are degenerate in wavelength, they interact with the same carrier population. Therefore, carrier densities can be obtained by summing the \mathbf{k} -dependent diagonal elements of the density matrix which correspond to transitions around the relevant photon energy.

It is also assumed that the gain and refractive index changes in the material are largely due to electron dynamics (equivalent to assuming that the electron and hole dynamics are the same). The equations describing carrier dynamics are therefore implemented only for conduction band electrons.

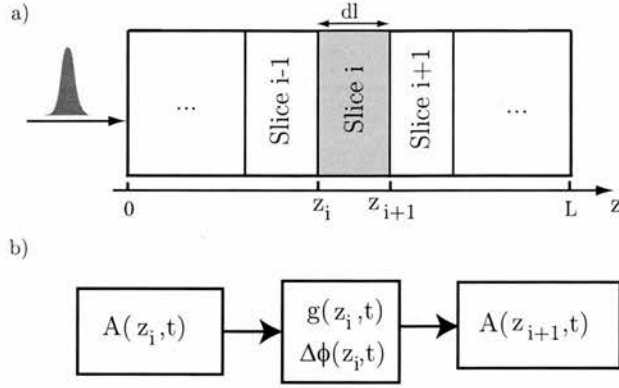


Figure 4.1: (a) Sketch of the SOA split in thin slices (b) Block diagram of the algorithm to calculate the propagation of the pump pulse in the device.

4.2.1 Our approach: a sliced propagation model

Basic equations: interband dynamics only

To explore our results, we use a model based on phenomenological rate equations originally developed in *Mathematica* by J. G. Fenn and M. Mazilu [18]. The SOA is split into thin slices of equal length having no internal variation of the carrier density. The temporal carrier dynamics induced by the incoming pump are solved for every slice, and the subsequent time dependent change in gain and refractive index is then used to simulate the probe propagation through consecutive slices. This is illustrated in figure 4.1.

Neglecting the ultrafast dynamics for the time being, the rate of change of the carrier density can be expressed as

$$\frac{\partial N(z_i, t)}{\partial t} = \frac{\mu J}{q\sigma L} - \frac{N(z_i, t)}{\tau_N} - g_m(z_i, t) \frac{\Gamma}{\hbar\omega\sigma} |A(z_i, t)|^2, \quad (4.1)$$

where $N(z_i, t)$ is the carrier density at position z_i (i^{th} slice) at time t . The first term on the right hand side of equation 4.1 accounts for the increase in carrier density due to the current injection J . μ is the injection efficiency, while q is the electron charge and σ and L are the SOA active cross-sectional area and length, respectively. The second term represents the carrier density decay (both radiative and non radiative) which is approximated by a single rate τ_N^{-1} , as discussed in section 2.3.4. Finally, the last term relates to stimulated emission, where A is the optical field with frequency ω . Γ is the confinement factor and g_m is the modal gain. As we are only considering the interband

dynamics, $g_m = g_N$, where g_N is the carrier density dependent gain, taken as

$$g_N = \left. \frac{\partial g}{\partial N} \right|_{N_{tr}} (N - N_{tr}) \quad (4.2)$$

Here, $\partial g/\partial N$ is the differential carrier density dependent gain and N_{tr} is the carrier density at transparency. It follows from equation 4.2 that when, by virtue of the injected current, the carrier density is larger than N_{tr} , g_N is positive. Under such conditions the carriers are depleted from conduction band via stimulated emission and the propagating pulse is amplified. It is said then that the device is being operated in gain. Note that, in the absence of optical field, the carrier density tends to an equilibrium value given by

$$N_0 = \frac{\mu J \tau_N}{q \sigma L} \quad (4.3)$$

Combining equations 4.1 and 4.2, the rate of change of the carrier density dependent gain can be expressed as follows,

$$\frac{\partial g_N}{\partial t} = \frac{g_0 - g_N}{\tau_N} - g_m \frac{|A|^2}{E_{satN}}, \quad (4.4)$$

where g_0 is the unperturbed gain, corresponding to the carrier density in equilibrium N_0 . E_{satN} is the saturation energy associated with interband processes, defined as

$$E_{satN} = \frac{\hbar \omega \sigma}{\Gamma \left. \frac{\partial g}{\partial N} \right|_{N_{tr}}} . \quad (4.5)$$

To describe the relationship between changes in refractive index, n and gain, g , α -parameters are used [19]. The linewidth enhancement factor for carrier density dependent gain changes is given by

$$\alpha_N = -\frac{4\pi}{\lambda} \left. \frac{\partial n/\partial N}{\partial g/\partial N} \right|_{N_{tr}} . \quad (4.6)$$

It is thereby possible to calculate the carrier density phase changes according to the formula

$$\frac{\partial \Delta \phi}{\partial z} = -\frac{1}{2} \alpha_N g_N . \quad (4.7)$$

The propagation of the optical field across a thin slice of thickness dl can be calculated as

$$A_{out} \approx A_{in} \exp \left\{ \left[\frac{1}{2} \Gamma g_m(z_i, t) - \frac{1}{2} \alpha_{int} + i \Gamma \Delta \phi(z_i, t) \right] dl \right\}, \quad (4.8)$$

where α_{int} describes the internal losses in the waveguide.

The calculations with this model are performed as follows. Initially, the gain in every slice is set to the unperturbed value g_0 . The pump pulse incident on the first slice is taken to have a gaussian intensity profile of width τ_p .

Solving equation 4.4 with this optical field and using equations 4.7 and 4.8, the amplitude of the optical field after propagating through the slice of thickness dl is obtained, and used as the input for the next slice. The propagation along the SOA waveguide is thus calculated iteratively across the consecutive slices. The complex gain at times after the pulse has left the SOA is calculated assuming that it recovers exponentially governed by the time constant τ_N .

This structure of model facilitates the calculation of the evolution of probe pulses propagating in both directions by adjusting the relative timing of the pulses with respect to the pump, as required for the TOAD configuration. For ease of evaluation, it is assumed that the probe pulses are too weak to significantly modify the carrier population; the only excitation is then due to the pump pulse.

The pulse energies are calculated by numerically integrating the moduli squared of the corresponding optical fields in the time range $[-7\tau_p, 5\tau_p]$ around the origin of the moving frame of reference. These integration limits were found to be sufficient, anticipating peak shifts caused by the gain and refractive index modulation.

Introducing the ultrafast dynamics

In the previous section, the structure of the rate equation model was explained. To do so, the simplest scenario was considered, where the only changes in gain and refractive index were those associated with the depletion of carriers in the conduction band. This level of simplicity is sufficient when working with pulse durations of tens of picoseconds or longer.

It is well known that when sub-picosecond pulses propagate through a SOA, new ul-

trafast dynamics come into play, namely, carrier heating, spectral hole-burning and two photon absorption. Previous pump-probe measurements with this amplifier [18], employing pulses of durations in the range 350 fs-1 ps, showed the slow gain recovery characteristic of interband processes and, on shorter timescales ($\sim 2 ps$), the signature of gain compression consistent with carrier heating. Spectral hole-burning and two photon absorption were not observed, as they occur in shorter time scales [8], beyond the temporal resolution of our experiments.

To accurately analyse our experimental results, the model must take into account the gain compression and subsequent index change caused by the heating of the carrier distribution. These ultrafast dynamics do not involve a real depletion of carriers from the conduction band. The pump causes an increase in the average energy of the carrier distribution, thus reducing the available electron population in the bottom of the band susceptible of undergoing stimulated emission. The resulting decrease in gain can be modelled by considering a 'virtual' population.

Including ultrafast carrier heating, the modal gain in the SOA may be defined as

$$g_m = g_N + g_T, \quad (4.9)$$

and the carrier temperature dependent gain is taken to be given by

$$g_T = \left. \frac{\partial g}{\partial T} \right|_{T_L} (T - T_L). \quad (4.10)$$

Here, T is the average temperature of the carrier distribution and T_L is the lattice temperature. The rate of change of the average carrier temperature can be calculated as

$$\frac{\partial T}{\partial T} = -\frac{T - T_L}{\tau_T} + \left(\frac{\partial T}{\partial U_c} \right) \left[\hbar\omega\sigma_{fca} + \left(\frac{\partial U_c}{\partial N} - E_c \right) g_m \right] \frac{\Gamma |A|^2}{\hbar\omega\sigma}. \quad (4.11)$$

where U_c is the energy of the carrier distribution [20]. The first term on the right hand side of equation 4.11 represents the cooling of the carrier distribution to the lattice temperature via carrier-phonon scattering (phenomenologically included via the time constant τ_T). The term in brackets accounts for the changes in temperature induced by the optical pulse via free carrier absorption (σ_{fca}), injection of hot carriers ($\partial U_c/\partial N$) and depletion of carriers

near the bottom of the band (E_c) by stimulated emission.

An expression for the rate of change of the temperature dependent gain can be obtained in a similar fashion to the carrier density analogue [20, 21, 22],

$$\frac{\partial g_T}{\partial t} = -\frac{g_T}{\tau_T} - g_m \frac{|A|^2}{E_{satT}}, \quad (4.12)$$

where a temperature saturation energy, E_{satT} is defined as

$$E_{satT} = \frac{\hbar\omega\sigma g_m}{\Gamma \left. \frac{\partial g_m}{\partial U_c} \right|_{U_c} [\sigma_{fca} N \hbar\omega + \left(\frac{\partial U_c}{\partial N} - E_c \right) g_m]} \quad (4.13)$$

The gain compression due to the heating of the carrier distribution will be accompanied by a change in the refractive index. In this case, a temperature linewidth enhancement factor, α_T , can be defined (see for example [7, 23])

$$\alpha_T = -\frac{4\pi}{\lambda} \left. \frac{\partial n / \partial T}{\partial g / \partial T} \right|_{T_L}. \quad (4.14)$$

The total phase change is $\Delta\phi = \Delta n 2\pi L / \lambda$, where the change in refractive index is given by the sum of contributions from carrier population and temperature changes. Substituting for Δn in terms of the gain factors and α -parameters, yields an expression for the phase change over distance as a function of the different gain changes

$$\frac{\partial \Delta\phi}{\partial z} = -\frac{1}{2} (\alpha_N g_N + \alpha_T g_T). \quad (4.15)$$

Regarding the pulse widths employed in our measurements (~ 700 fs), the inclusion of the carrier heating in the model is sufficient to interpret our results. However, in the framework of the phenomenological rate equations, dynamics taking place on shorter timescales, namely, spectral-hole burning and two photon absorption, can be taken into account straightforwardly in a similar fashion [18, 20].

Model parameters and calibration

For the model to be useful in the interpretation of the experimental results it is crucial to contrast the model calculations, drastically dependent on the chosen parameters, with the actual device behaviour.

	Value	Description
Γ	0.3	Confinement factor
L	1 mm	Device length
α_{int}	15 cm ⁻¹	Internal losses
τ_T	1.2 ps	Carrier cooling time
α_N	8	Carrier density alpha-factor
α_T	2	Temperature alpha-factor
E_{satN}	2 pJ	Carrier density saturation energy
E_{satT}	0.5 pJ	Temperature saturation energy

Table 4.1: Parameters for the phenomenological rate-equation model.

The amplifier used in the experiments described in this chapter had previously been the subject of a thorough study carried out by J. G. Fenn [18], as explained in section 3.1.1. The SOA was characterised by measurements of gain bandwidth, gain saturation, and gain recovery on sub-picosecond timescales, as a function of electrical bias, optical power and wavelength. To keep the numerical simulations as realistic as possible, the model parameters were estimated based on those early measurements, when available.

In reference [18], estimates of the recovery times τ_N and τ_T were obtained by fitting gain pump-probe traces. The slow recovery time τ_N in this amplifier was found to decrease significantly for larger applied electrical biases (faster than predicted for the case of Auger dominated recombination). Therefore, the value of τ_N in the model calculations was chosen accordingly with the experimental conditions to be reproduced. Pump-probe measurements also showed a bias dependence of the carrier cooling time (τ_T). However, the data was not conclusive and an average value of 1.2 ps was taken in all of our calculations.

The small signal gain g_0 at the appropriate wavelength and current injection was extracted from CW measurements.

Those model parameters which could not be measured were chosen within the range found in the literature (including [4, 20, 21, 24, 25, 26]). For example, the α -factors were set to $\alpha_N = 8$ and $\alpha_T = 2$. The confinement factor is $\Gamma = 0.3$ and the internal losses were taken to be $\alpha_{int} = 15 \text{ cm}^{-1}$.

The saturation of the gain with optical power is dictated by the energies E_{satN} and E_{satT} and exhibits a strong dependence on pulse width. The values for these parameters, namely, $E_{satN} = 2 \text{ pJ}$ and $E_{satT} = 0.5 \text{ pJ}$, were chosen within a reasonable range to achieve agreement with the measured energies at which gain dropped by 3dB (both in pulsed and CW experiments [18]).

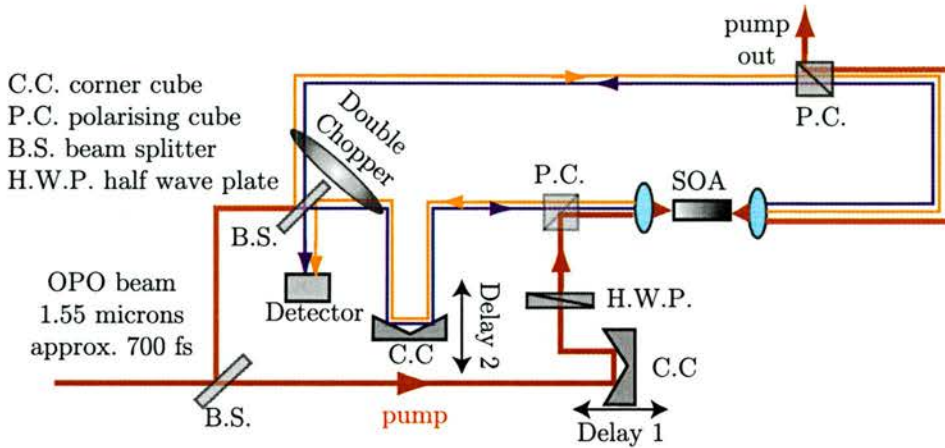


Figure 4.2: Sketch of the three beam pump-probe setup. Note the resemblance with a TOAD configuration. The thick red line indicates the pump beam, while the blue and yellow lines follow, respectively, the path of co- and counter-propagating probe pulses.

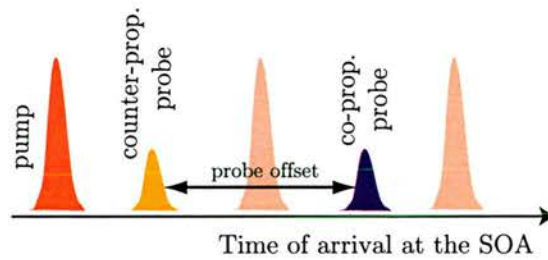


Figure 4.3: Diagram illustrating the timing in the arrival of the pulses at the SOA in the set-up of figure 4.2. Note the offset between co- and counter-propagating probes, which can be set by means of the delay stage 2 (see figure 4.2). In a typical measurement, the delay of the pump is varied by moving the delay stage 1, so as to map out the switching window.

The model parameters are summarised in table 4.1. Those parameters not listed there will be specified when appropriate, depending on the experimental conditions to be reproduced.

4.3 Ultrafast dynamics in SOA-based interferometric switches

4.3.1 Three beam pump-probe set-up

In this section, we present the results of interferometric three-beam pump-probe experiments on a SOA which can time-resolve the complex refractive index dynamics occurring during optical switching.

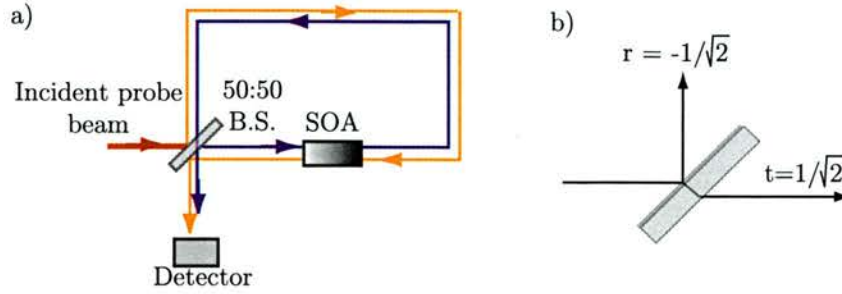


Figure 4.4: (a) Simplified diagram of the TOAD loop of figure 4.2.(b) Sketch illustrating the reflection and transmission of light in an ideal 50:50 beam splitter, including the corresponding coefficients for the optical field. Note that the reflection occurs from air to a higher index medium, hence the π phase shift.

The experimental configuration corresponds to the TOAD switch and is illustrated in figure 4.2. In this set-up, a weak input pulse is split into two TE polarised replicas (probes) which propagate around the loop in opposite directions, arriving at the SOA at different times (see figure 4.3), and finally interfering back at the beam splitter. A third strong TM polarised pulse (pump) is coupled into the loop to deplete some of the available carrier density in the SOA, therefore reducing the gain and, more importantly, causing a change in the refractive index.

Note that, as shown in figure 4.2, a double chopper is placed in the set-up such that, upon propagation along the loop, the co-propagating probe is modulated first with frequency $\frac{5}{6}f$ and later with frequency f . The counter-propagating replica undergoes identical modulation, although in the reverse sequence. By driving the local oscillator in the lock-in amplifier with a reference at the difference frequency ($\frac{1}{6}f$), only the signal corresponding to the probes after they travel along the entire loop is detected, and noise due to back reflections in the optical components or any unfiltered pump light is minimised.

Since the original probe beam is first incident upon the 50:50 beam splitter from a lower index medium (air), as illustrated in figure 4.4, the reflected optical field (counterpropagating probe, E_2) accumulates an extra π phase shift with respect to the transmitted light (co-propagating probe, E_1). After propagating along the loop, the counter-propagating probe is reflected again, this time inside the glass plate of the beam splitter, and no extra phase is accumulated. The total optical field incident upon the detector can thus be expressed as

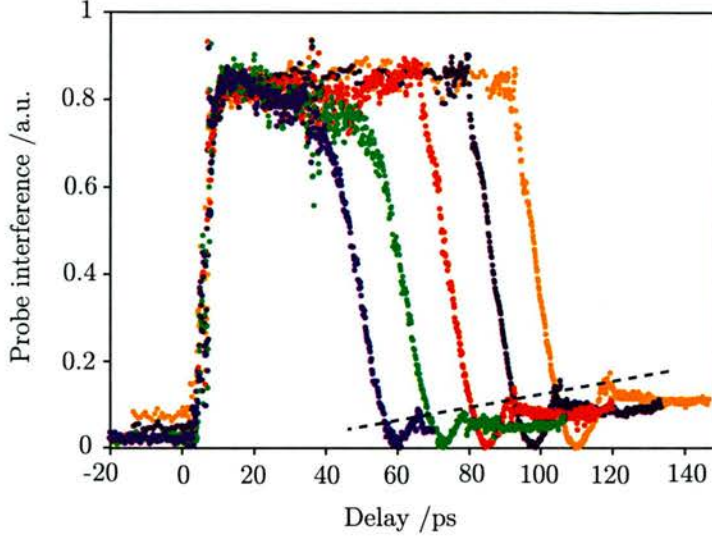


Figure 4.5: Interference of the probe pulses measured as a function of the delay with respect to the pump pulse. Starting with the narrowest switching window (blue dots), the path difference between the probes was increased in 2 mm for each measurement, resulting in an increase of ≈ 13 ps in the width of consecutive switching windows.

$$E_{TOT}(t) = E_1(t) - E_2(t), \quad (4.16)$$

and the interference of the two probes is given by

$$S(t) = |E_1(t)|^2 + |E_2(t)|^2 - 2|E_1(t)||E_2(t)| \cos[\Delta\phi(t)]. \quad (4.17)$$

If the pump arrives at the amplifier before or after both probes, these acquire the same phase when travelling through the SOA ($\Delta\phi = 0$) and interfere destructively at the detector. All the light is thus reflected back in the direction of the incoming probe beam. However, if the pump reaches the amplifier between the two probes, these will acquire a differential phase shift $\Delta\phi$ (ideally $\Delta\phi = \pi$) thus giving a transmitted pulse. By measuring the probe interference as a function of the delay of the pump, the switching window is mapped out.

In a real experiment, the beam splitter ratio depends on the angle of incidence, and the coupling of the light into the amplifier is not identical on both facets. As a result, one of the probes will be slightly stronger, giving a non zero interference signal outside the switching window.

Figure 4.5 shows a set of switching windows, measured employing ~ 650 fs pulses at

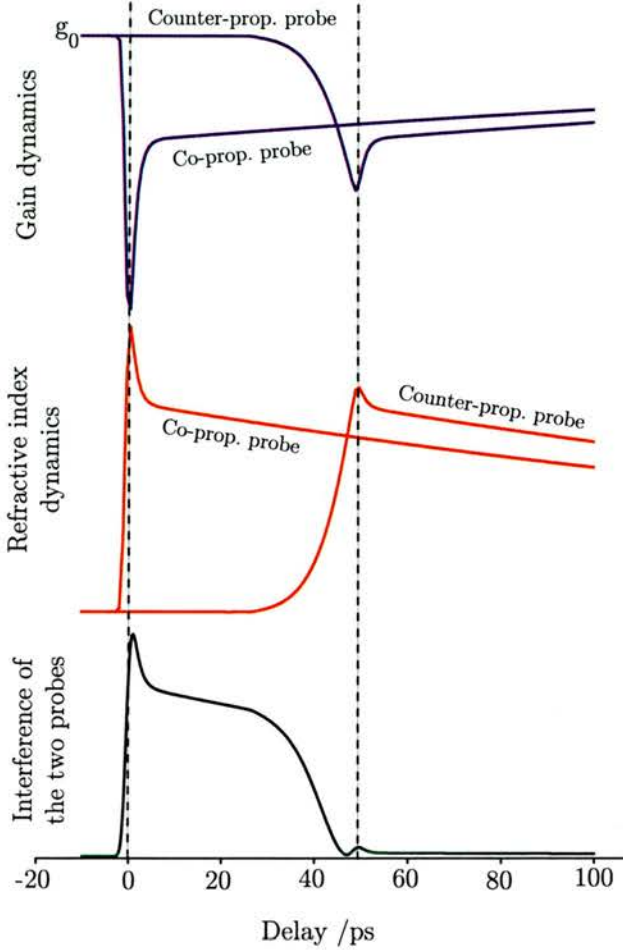


Figure 4.6: Sketch of a TOAD switching window (black line), as calculated with the model. The blue and red lines show the temporal evolution of the pump-induced changes in gain and refractive index, respectively, as seen by the co- and counter-propagating probes (note the delay between the two, due to the offset of the SOA in the loop).

1565 nm wavelength with an average energy per pump pulse of ~ 730 fJ. The electrical bias applied was 67 mA. For negative delays, both probes cross the SOA before the pump. Zero delay corresponds to the case in which the pump and the co-propagating probe pulses overlap in time. Starting from the narrowest window (light blue dots), the offset between the probes was increased in steps of 2 mm and, as a result, each window is ≈ 13 ps wider than the previous one.

The switching windows displayed in figure 4.5 present significant features other than those previously discussed. Most noticeable is the pedestal on the right of the switching windows, which increases with the window width. On the other hand, note that the on/off edge is far less sharp than its counterpart at zero delay. For the sake of clarity, figure 4.6

shows an example of switching window (black line) calculated with our model, together with the temporal evolution of the gain (blue line) and refractive index (red line) induced by the pump pulse. From figure 4.6, the origin of the pedestal located at a delay of ≈ 50 ps is clearly the mismatch in phase and gain between the two probes due to their offset, which tends to zero for larger delays. This mismatch is larger for wider windows, as both the gain and refractive index experienced by the co-propagating probe have more time to recover.

In a TOAD, pump and counter-propagating probe pulses meet at different points within the device as the delay is varied and different lengths of gain depleted waveguide are probed, so the sharpness of the on/off edge corresponds to $2T$, where T is the transit time of the pulses across the amplifier. The finite device length has been identified as one of the major limitation of switching configurations in which data and control pulses counter-propagate [27], and will be thoroughly discussed later in connection with the spatial dependence of nonlinearities.

Note that the switching window in figure 4.6 presents an ultrafast spike near zero delay due to the carrier heating dynamics. Such a feature is not observed in figure 4.5, due to the large range of delays considered, and measurements with higher resolution are required. This will be the subject of the next section.

4.3.2 Resolving the onset of all-optical switching

Interferometric switches based on gain depletion generally operate due to the refractive index change associated with the transfer of carriers from conduction to valence band. However, previous pump-probe experiments and some theoretical models stress the role of carrier heating and two photon absorption [28, 29] in the SOA response when subpicosecond pulses are involved. As discussed in section 3.2.1, the recovery of the gain/refractive index change induced by the pump will therefore be dictated by both the heated carrier distribution cooling down to the lattice temperature and the interband recovery. The former occurs via electron-phonon scattering within a time scale of a few picoseconds or less, while the latter may take up to a nanosecond depending on the current injection. As a result, the finite thermalisation time of the carriers and cooling to the lattice temperature will affect the shape of the switching window on the shortest timescales.

We have measured switching windows for a wide range of pump energies, focusing on

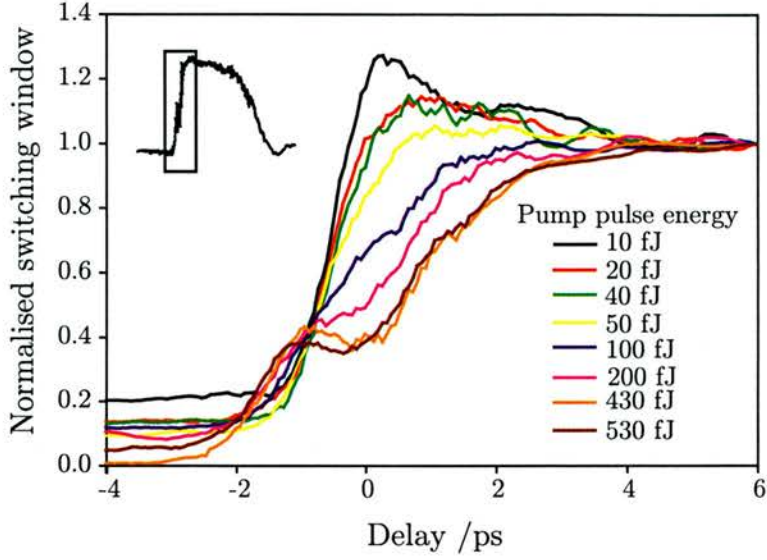


Figure 4.7: Off/On edge of different switching windows as a function of pump pulse energy. These windows have been normalised so that their amplitudes equal unity after the ultrafast component has decayed. The inset in the upper left corner depicts an example of a full switching window and, enclosed by the black box, the off/on edge subject of this study.

the shortest timescales around the onset of optical switching, as displayed in figure 4.7. We used 800 fs pulses at $1.57 \mu\text{m}$ and the SOA was biased at 65 mA. In the vicinity of zero delay, the computer-controlled stage was set to move in steps of $5 \mu\text{m}$ (corresponding to a change of $\sim 33 \text{ fs}$ in the delay between the pump and probe pulses).

For the sake of clarity, the switching windows in figure 4.7 have been normalised so that their amplitudes equal unity after the ultrafast component has decayed. Nevertheless, it must be kept in mind that the window amplitude increases at larger pump energies until a maximum is reached when $\Delta\phi = \pi$. For low pump powers, we observe a spike decaying in $\sim 2 \text{ ps}$ that gradually becomes a dip as the power is increased. This feature lasts longer than the duration of the pulse and cannot therefore be attributed to instantaneous processes following the pulse profile. Instead, this feature is caused by the change in refractive index related to carrier heating. For low pump pulse energies, the extra phase due to carrier heating adds constructively. However, for larger energies, when carrier density depletion alone gives a phase shift close to π , the extra phase due to carrier heating will lead to destructive interference, hence the dip. These observations are consistent with previous experiments on Mach-Zehnder interferometer switches [20, 30].

The background observed in figure 4.7 is due to a marginal imbalance of the TOAD

	Value	Description
g_0	130 cm^{-1}	Small-signal gain
τ_p	800 fs	Pulse duration
τ_N	284 ps	Slow interband recovery time

Table 4.2: Parameters of the phenomenological model used in the calculation of the switching windows of figure 4.8. The values of the parameters not listed here correspond to those in table 4.1.

setup. As discussed previously, this is caused by the non ideal beam splitter and the slightly different coupling efficiencies on both sides of the amplifier. Note that, in figure 4.7 this background is larger for smaller energies due to the normalisation.

Note that differential phase shifts of π and beyond have been measured at 65 mA for pump pulse energies below 0.6 pJ, in accordance with previous measurements on this amplifier [18]. The amplification of the pump beam via stimulated emission is the reason behind such low switching pulse energies, this being one of the main advantages of SOA-based switches.

So far, we have interpreted the experimental results exclusively in terms of the nonlinear phase shift induced by the pump beam. However, in these experiments, all pulses are degenerate in wavelength and therefore the probe pulses experience not only a nonlinear phase shift but also the gain compression in the amplifier induced by the pump, which can also influence the shape of the switching window.

4.3.3 Modelling of results and analysis

To explore the interplay of gain and refractive index dynamics in the shaping of the switching window, particularly on the shortest time scales, we use the phenomenological model. The SOA is perturbed by a high energy pulse and the propagation of two counter-propagating probes is modelled as a function of the delay with respect to the pump. The interference signal of the probes is then calculated by using equation 4.17 and integrated in time.

Figure 4.8 shows a set of switching windows (solid black lines) as a function of the pump energy (expressed in units of E_{3dB}), calculated with the model using the parameters detailed in table 4.2. E_{3dB} is the energy for which the total gain experienced by the pump pulse is half of the small signal value $\exp(\Gamma g_0 L)$, and was found to be 68 fJ. These windows have been normalised by the integrated power of a single probe pulse after propagating

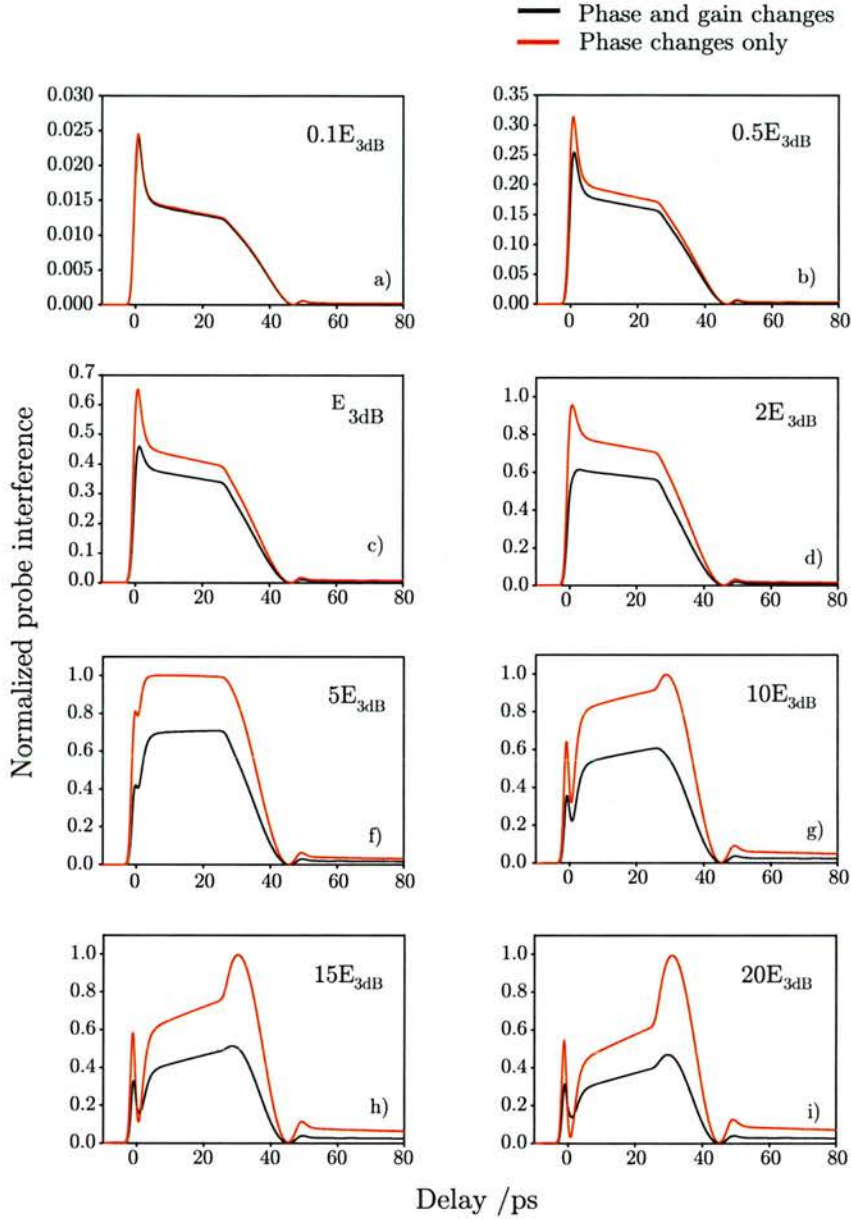


Figure 4.8: Switching windows calculated with the phenomenological model for a wide range of pump pulse energies, using the parameters of tables 4.1 and 4.2. E_{3dB} is the energy for which the total gain experienced by the pump pulse after crossing the SOA is half of the small signal value $\exp(\Gamma g_0 L)$. (Red) taking into account the phase dynamics alone, so the probes experience no gain compression induced by the pump. (Black) taking into account both gain and refractive index dynamics.

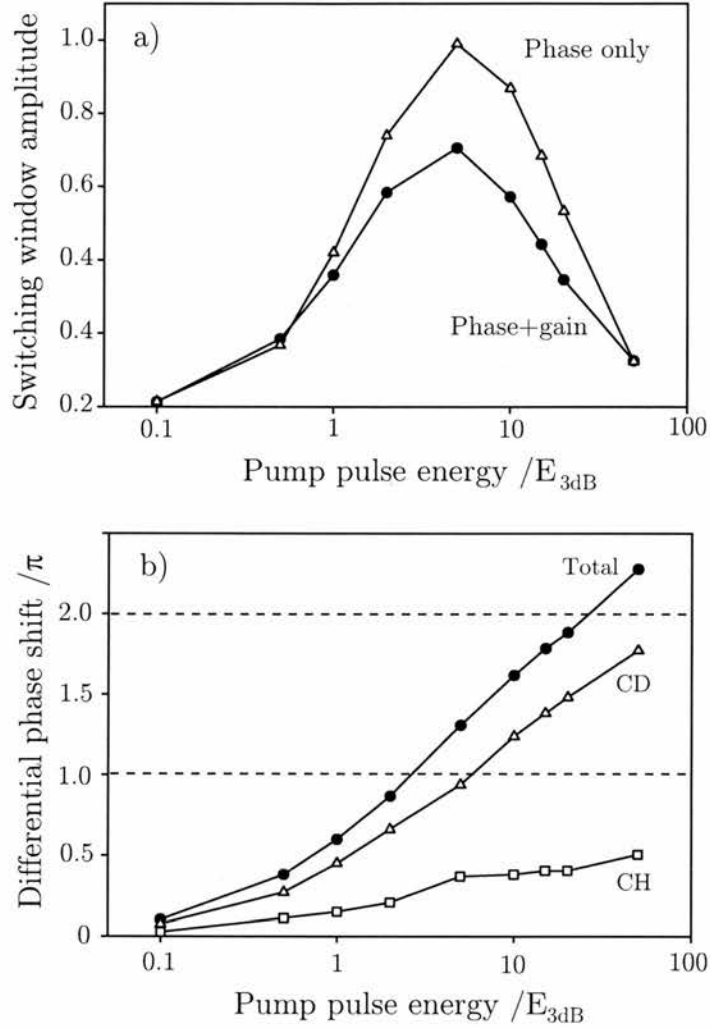


Figure 4.9: (a) Normalised amplitude and (b) nonlinear phase shift as a function of pump pulse energy, calculated from the switching windows of figure 4.8 (window corresponding to $50E_{3dB}$ not shown).

through the unperturbed SOA. This way, the amplitude of a switching window will be unity if the counter-propagating probes have experienced the same gain in the amplifier and have acquired a differential phase shift of π .

To illustrate the role of pump-induced gain compression, the same switching windows were calculated taking only into account the refractive index dynamics (red curves). The amplitude of the switching windows and the corresponding nonlinear phase shifts are displayed in figure 4.9 as a function of the pump pulse energy.

For the lowest pulse energy, figure 4.8(a), the nonlinear phase shift is small and the contributions of carrier density depletion and carrier heating add up constructively, causing

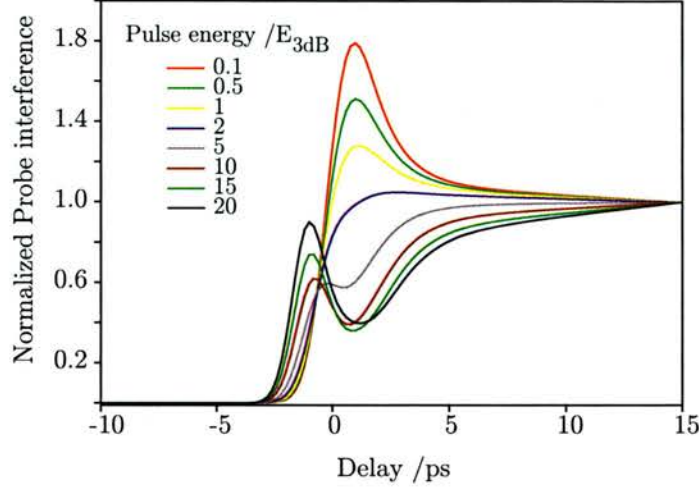


Figure 4.10: off/on edge of the switching windows of figure 4.8. For comparison with the experimental data, these windows have been normalised so that their amplitudes equal unity after the ultrafast component has decayed.

a spike around zero delay. The gain compression induced by the pump is negligible and both black and red switching windows are identical.

As the pulse energy is increased, see plots (a) to (d), so do the changes in refractive index due to carrier density depletion and carrier heating. This results in an improvement of the extinction ratio. Note, however, that the gain compression experienced by the co-propagating probe also increases with larger pump energies and reduces the amplitude of the switching window. In figure 4.8(d), the gain compression caused by the heating of the carrier distribution masks the spike.

When the pump pulse energy is such that the nonlinear shift due to carrier density depletion alone is close to π , the extra change in refractive index caused by carrier heating overshoots. The resulting destructive interference causes a dip, as observed in figure 4.8(f). In this case, the ultrafast gain compression enhances this feature. As the pulse energy is further increased, the dip becomes more pronounced and the switching ratio is degraded as a result of both the nonlinear shift being larger than π and the unbalancing of the TOAD due to the gain depletion in the amplifier. This eventually causes a strong reshaping of the window, as seen in figure 4.8(h).

For comparison with the experimental results, figure 4.10 shows the switching windows of 4.8 normalised so that their amplitudes equal unity after the ultrafast component has decayed. Note that the evolution of the ultrafast feature on the front edge of the

window is consistent with experimental data displayed in figure 4.7, starting as a spike and gradually becoming a dip as the pump energy is increased. However, we observe that the predicted ratio between peak transmission and the level reached after the ultrafast component has relaxed, is slightly larger than observed experimentally. This discrepancy is due to the choice of model parameters, particularly the α -factors α_N and α_T , and does not compromise the analysis presented.

The numerical results show that the gain compression in the amplifier not only degrades the extinction ratio but also tends to smooth the sharp features caused by the ultrafast changes in the refractive index change. This could be avoided by using a so called gain-transparent configuration [22, 30], in which the photon energy of the probe is smaller than the bandgap of the material so the pulse only experiences the changes in the refractive index.

In summary, we have reported for the first time, to the best of our knowledge, the experimental signature of a refractive ultrafast component in the switching windows of a TOAD setup. The nature and timescale (~ 2 ps) of this feature suggest carrier heating as responsible, consistent with the predictions of the phenomenological model. These results should also apply to other switching configurations using SOAs, such as Mach-Zehnder interferometers. It must be stressed that carrier heating has been found to distort significantly the edge of the switching windows for pump pulse energies well below 1 pJ. Since this effect is expected to be even more pronounced for shorter pulses, further understanding of the role of SOA ultrafast intraband dynamics on femtosecond timescales becomes essential if faster switching operation is to be achieved.

4.4 Spatial dependence of optical nonlinearities

Interferometric switches such as the TOAD, UNI or Mach-Zehnder interferometers exploit the large SOA resonant nonlinearities induced by an intense optical pulse. The self-modulation of the so called control pulse as it propagates results in a non-uniform gain/refractive index profile along the device waveguide. In configurations in which control and data pulses co-propagate, nonlinearities are averaged spatially across the entire SOA waveguide, and the sharpness of the switching window is only determined by the pulse

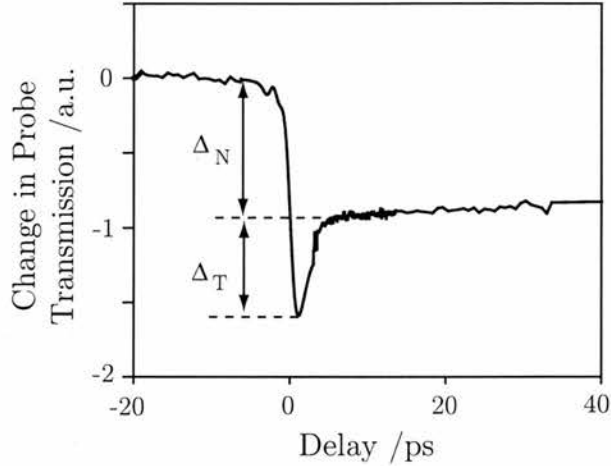


Figure 4.11: Example of a typical co-propagating pump-probe trace. Δ_N and Δ_T are the changes in probe transmission due to carrier density depletion and carrier heating, respectively.

duration. To illustrate this, figure 4.11 displays a typical example of a co-propagating pump-probe measurement, similar to that shown previously in figure 3.8(c).

The trace in figure 4.11 shows a sharp gain depletion around zero delay attributed to the band filling nonlinearity (there may also be a contribution from two photon absorption) and rapid partial gain recovery, Δ_T , associated with carrier cooling ($\sim 1 ps$) [8]. The full gain recovery due to the slower interband processes, Δ_N , takes hundreds of picoseconds and appears truncated in the figure.

In those configurations with counter-propagating geometries, control and data pulses meet at different points within the SOA as the delay is varied and therefore different lengths depleted by the control pulse are probed. In these circumstances, switching operation is thus not only dictated by the carrier temporal dynamics but also depends on spatial variables. The limitation imposed by the finite device length is widely acknowledged [27, 31]. However, little attention has been paid to the longitudinal effects [32] and, in particular, the spatial dependence of optical nonlinearities across the SOA waveguide due to self-modulation of the control pulse is usually overlooked. Instead, the gain depletion is often taken to be uniform [2, 33].

Here, we report pump-probe experiments with counter-propagating geometry to analyse the role of the gain depletion along the SOA waveguide, and the subsequent refractive index change, in switching operation. We use the phenomenological rate-equation model to clarify the device behavior.

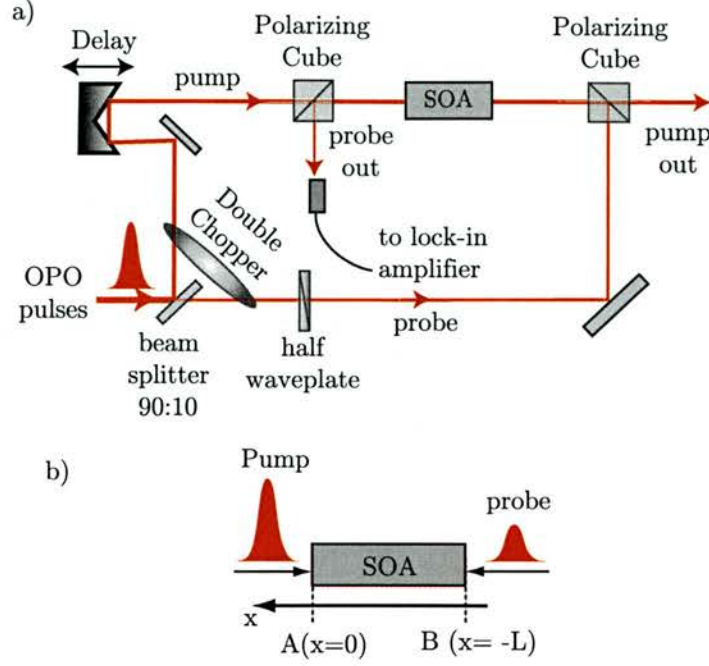


Figure 4.12: (a) Sketch of the experimental set-up for counter-propagating pump-probe measurements. (b) Diagram of the propagation of pump and probe pulses in opposite directions across the amplifier.

4.4.1 Experimental results

The experimental setup of figure 4.2 was modified by blocking the co-propagating probe beam. The schematics of this simplified configuration are displayed in figure 4.12. The input beam is split asymmetrically into pump (TM polarised) and probe (TE polarised) pulses, which propagate along the SOA in opposite directions.

In this set-up, the double chopper is positioned such that pump and probe are chopped with frequencies f and $\frac{5}{6}f$, respectively. The lock-in amplifier is then set to detect the difference frequency, so that only the changes on the probe signal induced by the pump are detected, because any pump leaks due to marginal polarisations are filtered electronically. This way, the change in probe transmission is measured in the lock-in amplifier as a function of the delay with respect to the pump. It must be noted that the detection arrangement using two different modulation frequencies was key to obtaining low noise pump-probe traces.

The counter-propagating pump-probe experiments reported here employed 700 fs pulses, with a bias of 70 mA applied to the SOA. The results shown in figure 4.13 correspond

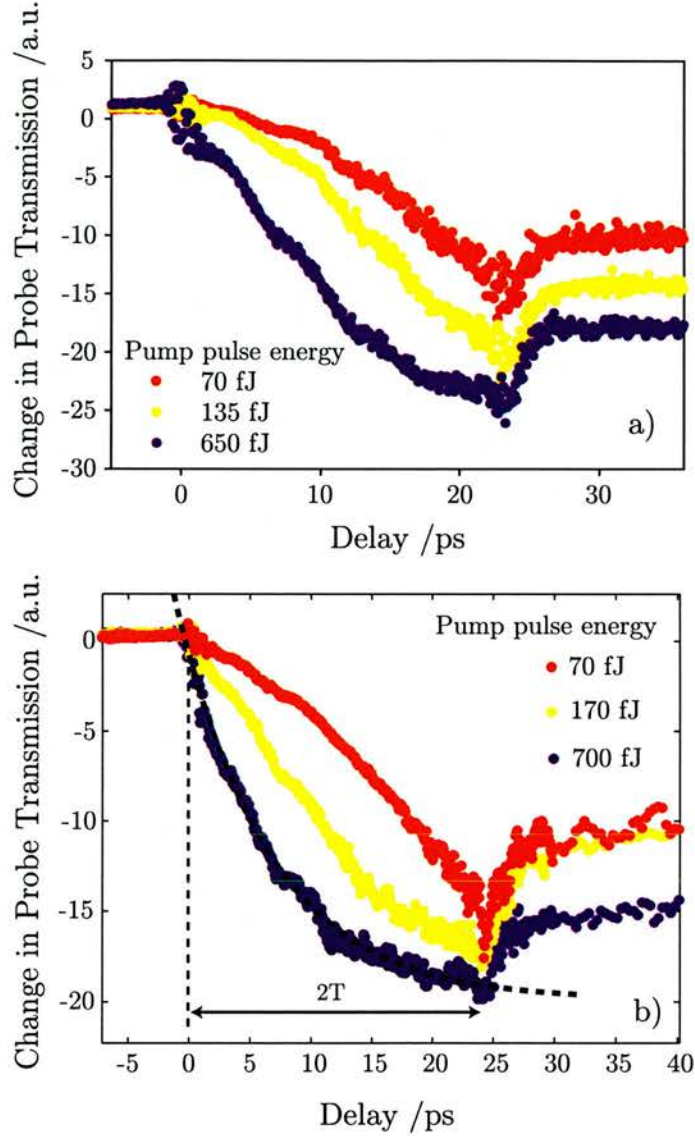


Figure 4.13: Counter-propagating pump probe traces measured at 70 mA electrical bias for a range of input pulse energies, using pulses of 700 fs duration centered at approximately (a) 1570 nm and (b) 1555 nm. The dashed line in (b) shows the fitting using equation 4.19.

to (a) 1570 nm and (b) 1555 nm wavelength, and differ substantially from those of typical co-propagating geometries (see figure 4.11). On the timescales considered, the slow interband dynamics appear as a negative step change in probe transmission. We observe a gradual gain depletion over 25 ps and only a "tail" of the fast carrier heating recovery.

To understand the slow pace of gain depletion, consider that for a delay $\tau = 0$, the probe meets the pump at facet "A" ($x = 0$). In this case the probe has propagated through the whole device before the pump has entered the facet and, therefore, no change in transmission is observed. As the probe delay is increased, the crossing point moves within

the SOA and, consequently, the probe travels through a progressively longer gain depleted portion of the amplifier. When the delay has been increased to $\tau = 2T (\approx 25 \text{ ps})$, where T is the transit time across the device, the two pulses meet at facet "B" ($x = -L$). It is then, in all cases, see figure 4.13, that the measured gain depletion is largest. The transmission as a function of probe delay shows a distinctly different characteristic depending on the pump pulse energy. At the lowest pump energies shown, red and yellow curves in (a) and red curve in (b), the gradient of the trace becomes more negative with increasing probe delay. However, the curves measured at higher input energies are steeper for small delays and their slope decreases as a function of probe delay.

4.4.2 Analysis and modelling results

To explore our results, we use the phenomenological model. The power of the pump through a small slice of the SOA of thickness Δl is calculated as

$$P_{out}(t) = P_{in}(t) \exp \{ [\Gamma g_m(z_i, t) - \alpha_{int}] \Delta l \} , \quad (4.18)$$

where $g_m(z_i, t)$ is the modal gain at position z_i (i^{th} slice) at time t , as obtained by solving equations 4.4 and 4.12. The input pulses have a gaussian intensity profile of width $\tau_p = 700 \text{ fs}$. As usual, Γ is the confinement factor and α_{int} accounts for the internal losses. The probe pulse energy is chosen to be small so that it does not modify the carrier population significantly.

In this case, the small-signal gain was taken to be $g_0 = 130 \text{ cm}^{-1}$ and the recovery times $\tau_N = 251 \text{ ps}$ and $\tau_T = 1.2 \text{ ps}$, were obtained from independent experiments made on this amplifier [18].

First, the gain experienced by a single pulse was calculated as the ratio of output and input pulse energies for a wide range of input energies. This is shown in figure 4.14, where the gain in dB includes the internal losses (α_{int}). The input energy for which the gain is half of the small-signal value $G_0 = \exp(\Gamma g_0 L)$ was found to be $E_{3dB} = 81 \text{ fJ}$, and is dictated mostly by E_{satN} , E_{satT} , the recovery times τ_N and τ_T , and the device length L .

Pump-probe traces are obtained by calculating the change in the integrated power of a probe pulse as a function of the delay with respect to the counter-propagating pump.

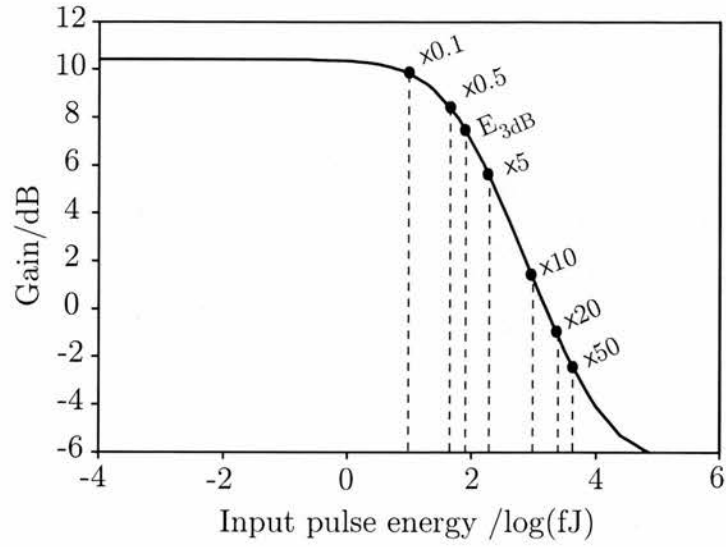


Figure 4.14: Device gain (including internal losses) as a function of input pulse energy, calculated by using the model of section 4.2.1.

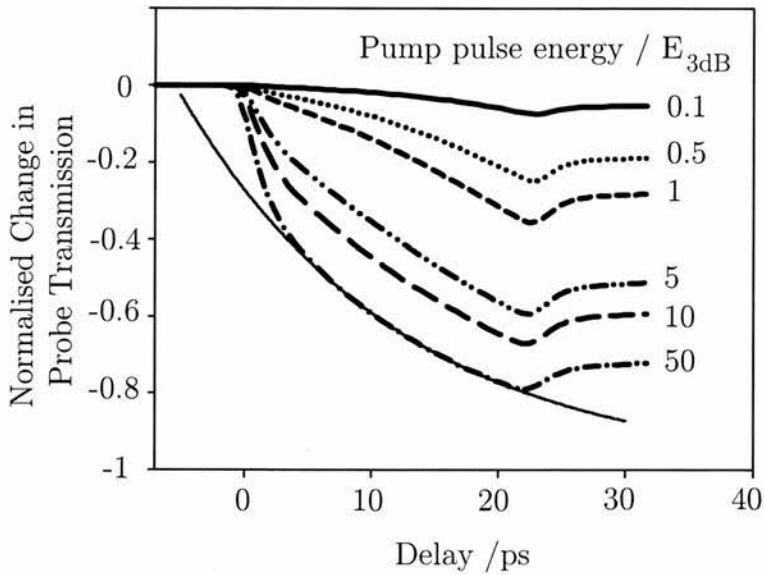


Figure 4.15: Calculated counter-propagating pump-probe traces for a range of different pump pulse energies using the model. E_{3dB} corresponds to the input pulse energy for which the device gain drops 3 dB with respect to its small-signal value. The thin solid line shows the fitting using equation 4.19.

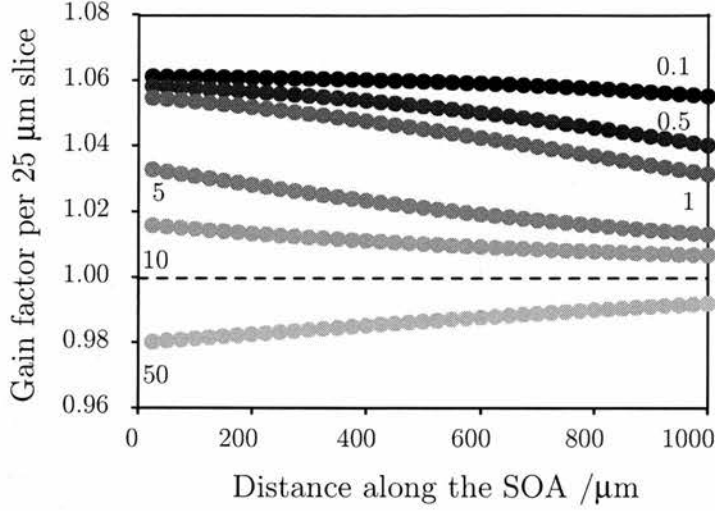


Figure 4.16: Gain per slice as the pump propagates along the length of the SOA, calculated for the same range of input pulse energies, expressed in units of E_{3dB} , as in figure 4.15.

Figure 4.15 shows traces for different pump pulse energies, normalised by the output energy of a probe pulse after propagating through the unperturbed SOA. The input pulse energies chosen are indicated in figure 4.14. As observed in figure 4.15, increasing the pump energy accelerates the gain depletion, consistently with the experimental results.

Figure 4.16 shows the gain available per slice as a function of position for different pump pulse energies as predicted by our model. The pump is amplified as it propagates along the device and, as a result, gain depletion increases. However, it is only at the highest input energies shown that the amplification of the pump is sufficient to saturate the gain in a portion of the device. Furthermore, a high energy pulse can heavily saturate the gain along the whole SOA length (see the $50E_{3dB}$ curve in figure 4.16. The gain is smaller than unity due to the internal loss, taken to be $\alpha_{int} = 15 \text{ cm}^{-1}$). Under these conditions, for a delay τ , the probe meets the pump at $x = -\tau L/2T$ and travels first through a small portion of the SOA of length L_T (dictated by τ_T) where the gain depletion is due both to changes in carrier density and carrier heating. However, in the rest of the waveguide, carriers had time to cool so the probe experiences a uniform gain due to carrier density depletion alone. As a result, the trace fits an exponential curve of the form

$$\Delta S(\tau) = S_0 \left\{ \exp \left[-\frac{\Gamma \Delta g_N^{sat} L}{2T} \tau - \delta_T \right] - 1 \right\} \quad (4.19)$$

remarkably well (see the black thin line in figure 4.15). Here, S_0 is the probe pulse energy

after propagating through the unperturbed SOA. Δg_N^{sat} is the initial step-like change in the local gain, uniform across the waveguide under full saturation conditions, due to carrier density depletion that later recovers as dictated by τ_N . The gain depletion due to carrier heating integrated along the length L_T is accounted for by the parameter δ_T . First, the validity of equation (4.19) was checked by fitting the trace calculated with the model for a pump pulse energy of $50E_{3dB}$ (see the black thin line in figure 4.15). This fit gives $\Delta g_N^{sat} = 46 \text{ cm}^{-1}$, in excellent agreement with the value of $45 \pm 1 \text{ cm}^{-1}$ predicted by the model across the entire SOA. As shown in figure 4.13(b), the trace measured at the highest pump pulse energy also fits to equation (4.19), yielding a value for $\Gamma \Delta g_N^{sat}$ of 31.4 cm^{-1} , and providing experimental evidence of gain saturation along the entire length of the amplifier.

In equation (4.19), we have neglected the slow gain recovery and pulse width, since $\tau_N \gg 2T \gg \tau_p$. For delays smaller than a few picoseconds such that $\tau L/2T < L_T$, the probe travels across a perturbed portion of the SOA shorter than L_T . As a result, the total gain compression experienced by the probe due to carrier heating is smaller than δ_T and equation (4.19) is no longer valid (note how the fit diverges from the data of figure 4.15 for $\tau < 3 \text{ ps}$).

The switching windows measured in section 4.3.2 clearly showed the signature of ultra-fast dynamics in the form of spikes or dips. Carrier heating reduces the saturation energy of the amplifier and plays a decisive role in dictating the propagation of the pump pulse and subsequent gain depletion across the device waveguide. Despite being determinant, the effects of carrier heating in counter-propagating pump-probe measurements are more subtle to distinguish, as they are only experienced by the probe in a small portion of the SOA.

4.4.3 Implications for all-optical switching

The experimental results presented so far indicate that the functional form of the spatial dependence of gain saturation is strongly dependent on pulse energy. On the other hand, gain changes in the SOA waveguide will be accompanied by changes in the refractive index, as expressed via the linewidth enhancement factors [19]. As a result of the cosine dependence of the interference signal on the differential phase shift between the two

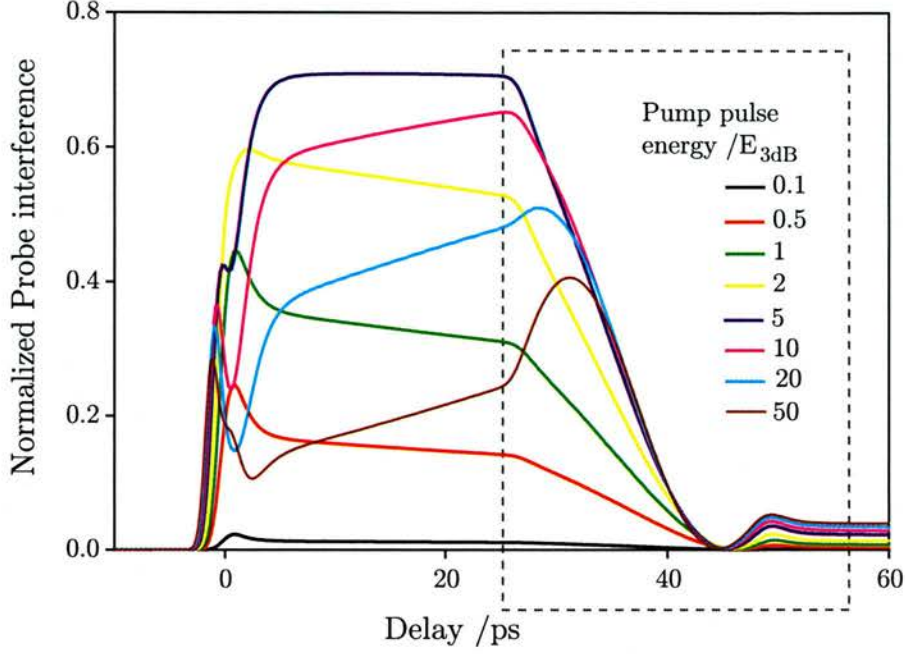


Figure 4.17: Normalised switching windows calculated with the model for the input pulse energies of figure 4.14. The dashed line encloses the on/off edge of the switching window.

counter-propagating probes ($\Delta\phi$), the energy of the control pulse plays a significant role in shaping the slow rising edge of the switching windows. To analyse this, the model of section 4.2.1 is used to calculate the switching windows corresponding to the input pulse energies of figure 4.14.

It can be seen in figure 4.17 that, as the pump pulse energy is increased, so does the switching window amplitude. For pulse energies larger than $5E_{3dB}$, the differential phase between the probes due to the depletion of the carrier density overshoots π , and the contrast ratio is degraded. Note that the shape of the on/off edge of the switching windows changes significantly with pulse energy.

More quantitative results can be extracted by estimating the fall time ($t_{1/2}$) of the switching windows. As illustrated in figure 4.18(a), $t_{1/2}$ is defined as the delay range over which the switching window amplitude is halved after pump and probe meet at facet A (see figure 4.13). Figure 4.18(b) displays the estimated $t_{1/2}$ as a function of pulse energy.

As the pulse energy is increased within the range $0.1E_{3dB} - 5E_{3dB}$, the edge of the switching window becomes sharper and $t_{1/2}$ decreases monotonically. The latter is consistent with the larger negative slopes in the corresponding counter-propagating pump-probe traces (see figure 4.15). For larger pulse energies, the amplification of the pump pulse is

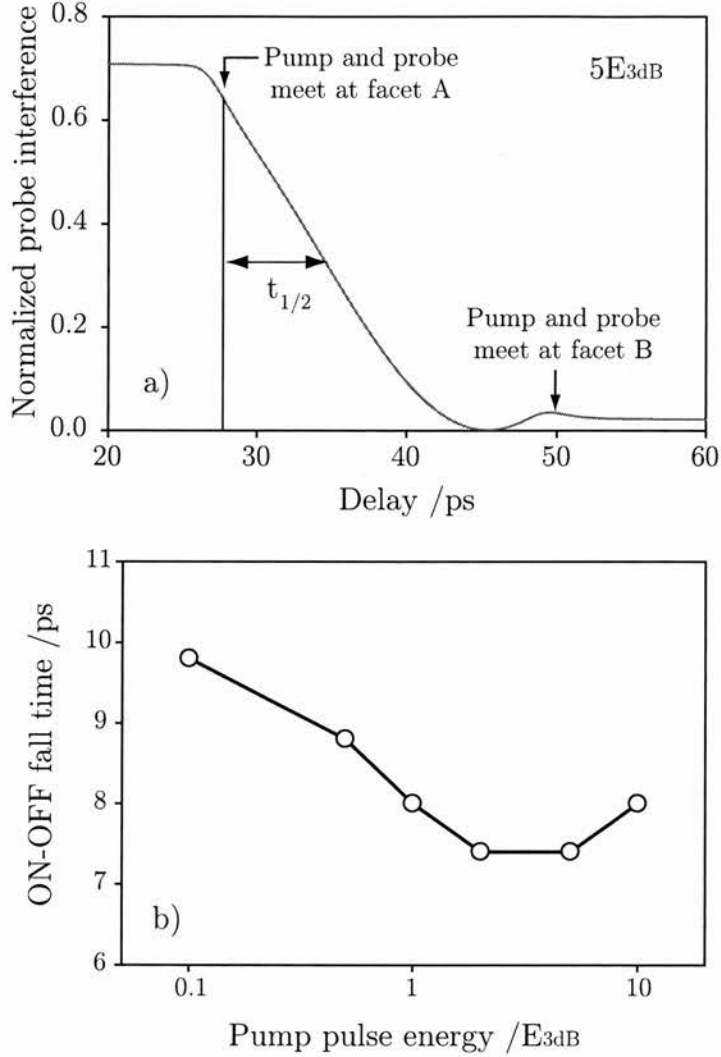


Figure 4.18: (a) Close up of the on/off edge of the switching window calculated for an input pulse energy of $5E_{3dB}$, illustrating the concept of the fall time $t_{1/2}$. (b) Fall time ($t_{1/2}$) of the on/off edge of the switching window as a function of the input pulse energy.

sufficient to saturate the gain in a significant portion of the amplifier, as discussed in connection with figure 4.16. At the same time, the subsequent differential phase shift due to carrier density depletion overshoots π and the cosinusoidal nature of the interference signal causes a significant reshaping of the switching window, rendering the former criteria for estimating the fall times inadequate. Note, however, the sharpness of the windows corresponding to $20E_{3dB}$ and $50E_{3dB}$ input pulse energies.

Numerical results show that the gain saturation across the whole device length induced by high energy pulses results in an effective narrowing of the switching windows.

The counter-propagating pump-probe measurements with subpicosecond pulses re-

ported in this section provide information on the spatial dependence of nonlinearities, namely, gain depletion and saturation, along the waveguide of a SOA. In switching configurations with co-propagating control and data pulses, only the control pulse duration dictates the sharpness of the switching window edge. However, counter-propagating schemes (e.g. TOAD or colliding pulse Mach-Zehnder) exhibit slow switch on/off, due to the device finite length. Although this limitation cannot be fully overcome, since the results in the counter-propagating geometry relate to the shape of the switching window in the above mentioned schemes, the measurements reported here demonstrate how systems could be optimised by adjusting parameters such as electrical bias and pump pulse energy. We show that the narrowest switching windows can be obtained in the limit when strong saturation is induced by the pump across the whole device length.

4.5 Summary

In this chapter, we report subpicosecond pump-probe measurements on an InGaAs multiple quantum well semiconductor optical amplifier to analyse the role of the ultrafast carrier dynamics in the operation of SOA-based interferometric all-optical switches.

First, we have reviewed different theoretical approaches to the study of carrier dynamics in semiconductor optical amplifiers, ranging from simple rate equations to first principles microscopic models. In this context, we have introduced a simple sliced propagation model based on rate equations. The ultrafast dynamics associated to the heating of the carrier distribution and subsequent cooling to the lattice temperature are taken into account via phenomenological parameters. Despite of its simplicity and within its limitations, this model proved very useful in the analysis of the experimental results.

We have presented experimental evidence of the signature of the carrier heating dynamics in the switching window of a TOAD-like interferometric setup. The dependence of this ultrafast feature on the pulse energy was analysed and found consistent with both the predictions of the model and measurements reported by other groups in switching configurations other than TOADs.

In the last section, we present experiments using subpicosecond pulses in a counter-propagating pump probe configuration to resolve the gain saturation along the SOA waveguide.

uide. The functional form of the spatial dependence of optical nonlinearities was found to depend strongly on pulse energy. In the light of the model calculations, we show that the effective width of the switching window decreases with larger pulse energies, parallel to the saturation of a longer portion of the amplifier. The narrowest switching windows can be obtained in the limit when strong saturation is induced by the pump across the whole device length.

We must stress that both the signature of ultrafast carrier dynamics at the onset of optical switching and strong saturation along the entire SOA waveguide have been observed for pulse energies below 1 pJ. These results thus highlight the relevance of such ultrafast nonlinearities in the context of all-optical switching with femtosecond pulses.

References for Chapter 4

- [1] D Cotter, R J Manning, K J Blow, A D Ellis, A E Kelly, D Nesses, I D Phillips, A J Poustie, and D C Rogers. Nonlinear optics for high-speed digital information processing. *Science*, 286(5444):1523–1528, 1999.
- [2] P Toliver, T Runser, I Glesk, and P R Prucnal. Comparison of three nonlinear interferometric optical switch geometries. *Opt. Commun.*, 175:365–373, 2000.
- [3] V M Menon, W Tong, C Li, F Xia, I Glesk, P R Prucnal, and S F Forrest. All optical wavelength conversion using a regrowth free monolithically integrated Sagnac interferometer. *IEEE Photon. Technol. Lett.*, 15(2):254–256, 2003.
- [4] G P Agrawal and N A Olsson. Self-phase modulation and spectral broadening of optical pulses in semiconductor laser amplifiers. *IEEE J. Quantum Electron.*, 25(11):2297, 1989.
- [5] C T Hultgren and E P Ippen. Ultrafast refractive index dynamics in AlGaAs diode laser amplifiers. *Appl. Phys. Lett.*, 59(6):635–637, 1991.
- [6] K L Hall, G Lenz, E P Ippen, U Koren, and G Raybon. Carrier heating and spectral hole burning in strained-layer quantum-well laser amplifiers at $1.5\mu\text{m}$. *Appl. Phys. Lett.*, 61(21):2512, 1992.
- [7] K L Hall, G Lenz, A M Darwish, and E P Ippen. Subpicosecond gain and index nonlinearities in InGaAsP diode lasers. *Opt. Commun.*, 111:589–612, 1994.
- [8] K L Hall, E R Thoen, and E P Ippen. *Semiconductors and Semimetals*, volume 59, chapter 2 Nonlinearities in Active Media. Academic Press, 1999.
- [9] S Huges. Carrier-carrier interaction and ultrashort pulse propagation in highly excited semiconductor laser amplifier beyond the rate equation limit. *Phys. Rev. A*, 58(3):2567–2576, 1996.
- [10] W W Chow and S W Koch. *Semiconductor-laser fundamentals: physics of the gain materials*. Springer-Verlag, Berlin, 1999.
- [11] S Huges. Microscopic theory of ultrashort pulse compression and break-up in a semiconductor optical amplifier. *IEEE Photon. Technol. Lett.*, 13(8), 2001.
- [12] F Romstad, P Borri, W Langbein, J Mørk, and J M Hvam. Measurement of pulse amplitude and phase distortion in a semiconductor optical amplifier: from pulse compression to breakup. *IEEE Photon. Technol. Lett.*, 12(12):1674–1676, 2000.
- [13] J Mork and A Mecozzi. Theory of the ultrafast optical response of active semiconductor waveguides. *J. Opt. Soc. Am. B*, 13(8):1803–1816, 1996.
- [14] J Mark and J Mork. Subpicosecond gain dynamics in InGaAsP optical amplifiers: Experiment and theory. *Appl. Phys. Lett.*, 61(19):2281, 1992.
- [15] A Mecozzi and J Mørk. Saturation induced by picosecond pulses in semiconductor optical amplifiers. *J. Opt. Soc. Am. B*, 14(4):761–770, 1997.
- [16] J M Tang, P S Spencer, and K A Shore. The influence of gain compression on picosecond optical pulses in semiconductor optical amplifiers. *J. Mod. Optic.*, 45(6):1211, 1998.
- [17] J M Tang and K A Shore. Strong picosecond optical pulse propagation in semiconductor optical amplifiers at transparency. *IEEE J. Quantum Electron.*, 34(7):1263, 1998.
- [18] J G Fenn. *Ultrafast dynamics in semiconductor optical amplifiers*. PhD thesis, School of Physics and Astronomy, University of St Andrews, May 2003.
- [19] C H Henry. Theory of the linewidth enhancement factor. *IEEE J. Quantum Electron.*, 18(2):259–264, 1982.
- [20] R P Schrieck, M H Kwakernaak, H Jäckel, and H Melchior. All-optical switching at multi-100-Gb/s data rates with Mach-Zehnder interferometer switches. *IEEE J. Quantum Electron.*, 38(8):1053–1061, 2002.

- [21] M Y Hong, Y H Chang, A Dienes, J P Heritage, P J Delfyett, S Djajili, and F G Patterson. Femtosecond self- and cross-phase modulation in semiconductor laser amplifiers. *IEEE J. Sel. Top. Quantum Electron.*, 2(3):523–539, 1996.
- [22] G Toptchiyski, S Kindt, K Petermann, E Hilliger, S Diez, and H G Weber. Time-domain modeling of semiconductor optical amplifiers for OTDM applications. *IEEE/OSA J. Lightwave Technol.*, 17(12):2577, 2000.
- [23] A Dienes, J P Heritage, M Y Hong, and Y H Chang. Time- and spectral-domain evolution of subpicosecond pulses in semiconductor optical amplifiers. *Opt. Lett.*, 17(22):1602–1604, 1992.
- [24] R J Manning, A D Ellis, A J Poustie, and K J Blow. Semiconductor laser amplifiers for ultrafast all-optical signal processing. *J. Opt. Soc. Am. B*, 14(11):3204–3216, 1997.
- [25] M Eiselt. Optical loop mirror with semiconductor laser amplifier. *Electron. Lett.*, 28(16):1505–1507, 1992.
- [26] K J Blow, R J Manning, and A J Poustie. Nonlinear optical loop mirrors with feedback and a slow nonlinearity. *Opt. Commun.*, 134:43–48, 1997.
- [27] M Eiselt, W Peiper, and H G Weber. All-optical high speed demultiplexing with a semiconductor laser amplifier in a loop mirror configuration. *Electron. Lett.*, 29(13):1167–1168, 1993.
- [28] A Mecozzi and J Mørk. Saturation effects in nondegenerate four-wave mixing between short pulses in semiconductor laser amplifiers. *IEEE J. Sel. Top. Quantum Electron.*, 13(5):1190–1207, 1997.
- [29] H J S Dorren, X Yang, D Lenstra, G D Khoe, T Simoyama, H Ishikawa, H Kawashima, and T Hasama. Ultrafast refractive-index dynamics in a multiquantum-well semiconductor optical amplifier. *IEEE Photon. Technol. Lett.*, 15(6):792–794, 2003.
- [30] S Nakamura, Y Ueno, and K Tajima. Femtosecond switching with semiconductor-optical-amplifier based symmetric Mach-Zehnder-type all-optical switch. *Appl. Phys. Lett.*, 78(25):3929–3931, 2001.
- [31] J P Sokoloff, P R Prucnal, I Glesk, and M Kane. A terahertz optical asymmetric demultiplexer (TOAD). *IEEE Photon. Technol. Lett.*, 5(7):787, 1993.
- [32] K J Blow, R J Manning, and A J Poustie. Model of longitudinal effects in semiconductor optical amplifiers in a nonlinear loop mirror configuration. *Opt. Commun.*, 148:31–35, 1998.
- [33] K I Kang, T G Chang, I Glesk, and P R Prucnal. Comparison of Sagnac and Mach-Zehnder ultrafast all-optical interferometric switches based on semiconductor resonant optical nonlinearity. *Appl. Optics*, 35(3):471–426, 1996.

Chapter 5

Stimulated electronic Anti-Stokes Raman emission in QC lasers

5.1 Nonlinear generation of light in QC lasers

Over the last decade, QC lasers have rapidly become compact and reliable high-power sources covering the mid- to far-infrared wavelength range ($3.5\text{--}24\ \mu\text{m}$). Intensive research is currently being undertaken aiming to expand the spectral range available with this technology. Laser emission in the Terahertz regime ($\lambda > 50\ \mu\text{m}$), with photon energies smaller than one LO-phonon, is one subject of study [1]. At the opposite end of the spectrum, research has diversified covering material systems other than InGaAs/AlInAs with larger band offset, such as GaN/AlGaN [2] or Sb-based heterostructures [3].

It is well known that intersubband transitions (ISTs) in asymmetric coupled quantum wells can display giant nonlinear optical susceptibilities [4, 5, 6], and thus be exploited to generate new wavelengths. To this contribute both the large optical dipole matrix elements of ISTs and the enhancement of nonlinearities occurring near resonance of these transitions [7].

Schemes in which asymmetric coupled quantum wells are pumped by an external optical field have several drawbacks. The coupling of the pump light into such structures is inefficient, since only transitions involving TM polarisation are allowed by the selection rules, and large pump powers are required. In addition, beam overlap can also be an issue.

With QC lasers, it is possible to selectively replace active regions/injectors with non-

linear elements or to integrate nonlinear transitions directly into the active regions themselves, thus allowing for efficient intra-cavity wave mixing [8]. This was recently demonstrated for sum frequency, second harmonic and third harmonic generation [9, 10, 11].

The monolithic integration of resonant optical nonlinearities based on intersubband transitions and QC lasers has several advantages. First, QC lasers can provide high optical power densities thus being very effective pump sources. Unlike in other schemes, the emission of pump photons and nonlinear processes occur in every stage of the cascade. Therefore, the entire waveguide core contributes to the nonlinear generation of light. In addition, good overlap between pump modes and the nonlinear region is obtained.

Keeping in mind the multitude of known nonlinear phenomena, we are just beginning to scratch the surface of the potential arising from the combination of nonlinear optics and QC lasers. In this context, stimulated Raman scattering has been one subject of research, having the added advantage that no phase-matching is required. Chapter 5 describes the work carried out at Princeton University, whose goal is achieving a QC electronic Anti-Stokes Raman laser. Here we report, to the best of our knowledge, the first observation of stimulated electronic Anti-Stokes (AS) Raman emission in a QC laser and discuss the feasibility of AS lasing.

5.1.1 Stimulated Raman scattering

Raman scattering [7, 12] is a two-photon process in which a photon at ω_1 is absorbed and a photon with frequency ω_2 is emitted, as illustrated in figure 5.1. As this occurs, the material evolves from initial state $|i\rangle$ to a final state $|f\rangle$. When $\omega_1 > \omega_2$, we speak of Stokes Raman scattering while the case $\omega_2 > \omega_1$ is referred to as Anti-Stokes (AS) Raman scattering (labelled as a) and b), respectively, in figure 5.1). To fulfill energy conservation requirements, $\hbar(\omega_1 - \omega_2) = E_{fi}$ for Stokes Raman scattering and $\hbar(\omega_1 - \omega_2) = E_{if}$ for the Anti-Stokes case, where $E_{fi} (= -E_{if})$ is the energy between final and initial state.

In stimulated Raman scattering, the frequency shift between incident and generated light corresponds to the frequency of some internal oscillation of the material, typically molecular vibrations¹ or optical phonons. This nonlinear process has found multiple applications as the basis for high resolution spectroscopic techniques, and also in the

¹Stimulated Raman scattering was first observed by Woodbury and Ng in the nitrobenzene molecule in 1962 [13].

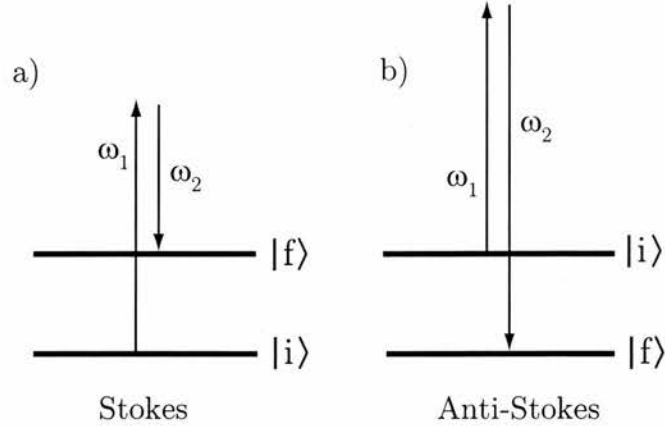


Figure 5.1: Diagram of the Raman process for a) Stokes and b) Anti-Stokes Raman scattering.

development of new light sources known as Raman lasers (see [12] and references therein). In this respect, the recently reported first continuous wave all-silicon laser, employing stimulated Raman scattering as the gain mechanism [14], is an outstanding example.

Typically, as depicted in figure 5.1, the detuning of both ω_1 and ω_2 from any resonances with higher-lying levels in the material is much larger than the broadening of such levels. The Raman transition then takes place mediated by a virtual level and the one-photon absorption is minimised [7]. However, in asymmetric quantum well structures such as QC lasers, the Raman nonlinearity can be greatly enhanced near resonance with intersubband transitions. As ISTs take place between the quantised states of the electrons, we speak of *electronic* stimulated Raman scattering.

Raman lasing based on ISTs has been theoretically discussed [15] in comparison with conventional optically pumped intersubband lasers. However, to date, only Stokes Raman lasing has been demonstrated experimentally. Liu *et al.* used *GaAs/AlGaAs* double quantum well structures pumped externally by a CO_2 laser in a side-pumping cleaved-facet geometry [16, 17]. In this case, the Stokes Raman shift was tailored to match the energy of a LO phonon mode, thus enhancing the nonlinearity.

More recently, Troccoli *et al.* have reported a QC laser where the electronic Stokes Raman process occurs in the active region [18]. The difference between pump and Raman laser frequencies was of the order of 40-50 meV. Unlike other nonlinear phenomena such as second harmonic or third harmonic generation, Raman scattering has the added advantage that no phase matching is required [12], which greatly simplifies the waveguide design [10].

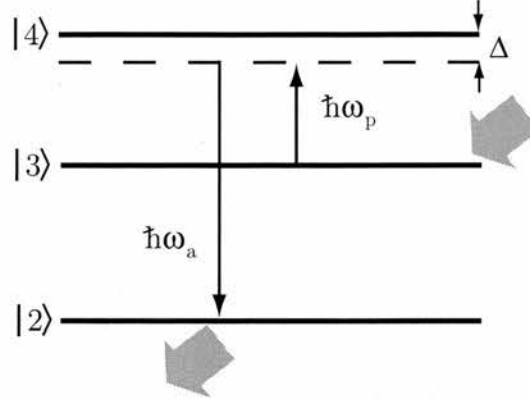


Figure 5.2: Sketch of the Anti-Stokes nonlinear region in a QC laser. The right gray arrow indicates the injection of carriers into state 3, while the left arrow shows the depletion of carriers in state 2.

The aim of this research at Princeton University is to achieve lasing using stimulated Anti-Stokes Raman scattering between electronic levels in the active region of a QC laser. This is sketched in figure 5.2, which shows the energy diagram corresponding to the conduction band of one period of the nonlinear stack. The conventional notation for the electronic states is used.

Electrons populating level 3 would undergo AS Raman scattering stimulated by the pump light, emitting photons with energy $\hbar\omega_a = \delta E_{42} + \Delta$, where δE_{42} is the energy separation between levels 4 and 2 and Δ is the detuning, defined as $\Delta = \hbar\omega_p - \delta E_{43}$. Lasing occurs via the excitation of the coherent nonlinear polarisation of the IST between states 4 and 2. The right gray arrow in figure 5.2 indicates the injection of carriers into state 3, while the left arrow illustrates the scattering of electrons from level 2 into the injector of the next stage.

As an aid in the design of the nonlinear active regions, a quantitative expression of the AS Raman gain is needed. The resonant nonlinear response of our effective three level system 2-3-4 is calculated by solving the coupled electronic density-matrix equations and electromagnetic Maxwell equations for pump and AS fields [19] following a similar derivation to that outlined in references [8, 20]. We will restrict ourselves to the case of purely homogeneous broadening, which is justified by the largely lorentzian lineshape that ISTs display in absorption experiments.

The density matrix equations have the general form [21]

$$\frac{d\rho_{mn}}{dt} + (\gamma_{mn} + i\omega_0^{mn}) = \frac{ie}{\hbar} \mathbf{E} \sum_q (z_{mq}\rho_{qn} - z_{qn}\rho_{mq}), \quad (5.1)$$

$$\frac{d\rho_{mm}}{dt} + \hat{R}_m = \frac{ie}{\hbar} \mathbf{E} \sum_q (z_{mq}\rho_{qm} - z_{qm}\rho_{mq}). \quad (5.2)$$

Here, \mathbf{E} is the total electric field interacting with our system. The dephasing of the off-diagonal terms (ρ_{mn}) is accounted for via phenomenological \mathbf{k} -independent relaxation rates, γ_{mn} . In doing so, we are neglecting many-body effects [8]. On the other hand, ω_0^{mn} and $d_{mn} = ez_{mn}$ are the transition frequency and optical dipole matrix element of the transition m-n, respectively. In the equations for the diagonal elements of the density matrix ρ_{mm} (equation 5.2), the pumping and relaxation rates affecting the population of the different levels are grouped in the terms \hat{R}_m .

We introduce slowly varying amplitudes for the off-diagonal elements in equations 5.1 as follows

$$\rho_{32}(t) = \sigma_{32}(t)e^{-i\omega_{32}t}, \quad (5.3a)$$

$$\rho_{42}(t) = \sigma_{42}(t)e^{-i\omega_a t}, \quad (5.3b)$$

$$\rho_{43}(t) = \sigma_{43}(t)e^{-i\omega_p t}. \quad (5.3c)$$

Note that, as depicted in figure 5.2, $\omega_{32} = \omega_a - \omega_p$. The electric field interacting with our system is the sum of the pump E_p and the Anti-Stokes E_a fields, both detuned from resonance by Δ . We also introduce slowly varying complex amplitudes of the electrical fields, as done previously with the coherence elements of the density matrix.

$$E_a(z, t) = \frac{1}{2}\varepsilon_a(z, t)\exp(-i\omega_a t + ik_a z) + c.c. \quad (5.4)$$

For each field, we define the complex Rabi frequency $e_a(z, t) = d_{24}\varepsilon_a(z, t)/2\hbar$ and $e_p(z, t) = d_{34}\varepsilon_p(z, t)/2\hbar$. Neglecting second derivatives of the amplitudes, the propagation of the Anti-Stokes field along the z direction will be dictated by the following wave equation,

$$\frac{\partial e_a}{\partial z} + \frac{n_a}{c} \frac{\partial e_a}{\partial t} + \kappa_a e_a = \frac{2\pi i \omega_a d_{24}^2 N_e \varsigma_a}{\hbar c n_a} \sigma_{42}, \quad (5.5)$$

where $n_a = k_a c / \omega_a$ is the effective refractive index of the mode, κ_a accounts for the nonresonant losses and ς_a is the nonlinear optical confinement factor of the AS mode. N_e is the total density of electron states in the active region. An analogous expression can be written for the pump field,

$$\frac{\partial e_p}{\partial z} + \frac{n_p}{c} \frac{\partial e_p}{\partial t} + \kappa_p e_p = \frac{2\pi i \omega_p d_{34}^2 N_e \varsigma_p}{\hbar c n_p} \sigma_{43}. \quad (5.6)$$

Substituting the definitions of equations 5.3 and the Rabi frequencies in the expressions for the off-diagonal density matrix elements, we obtain

$$\frac{d\sigma_{32}}{dt} + \Gamma_{32}\sigma_{32} = -ie_a\sigma_{43}^* + ie_p^*\sigma_{42}, \quad (5.7a)$$

$$\frac{d\sigma_{42}}{dt} + \Gamma_{42}\sigma_{42} = ie_a n_{24} + ie_p\sigma_{32}, \quad (5.7b)$$

$$\frac{d\sigma_{43}}{dt} + \Gamma_{43}\sigma_{43} = ie_p n_{34} + ie_a\sigma_{32}^*, \quad (5.7c)$$

In deriving these equations, the so called rotating-wave approximation has been used, only valid for small detunings of the pump and Anti-Stokes fields from the relevant transitions. On the other hand,

$$\Gamma_{32} = \gamma_{32}, \quad (5.8a)$$

$$\Gamma_{42} = \gamma_{42} + i(\omega_{42} - \omega_a) = \gamma_{42} + i\Delta, \quad (5.8b)$$

$$\Gamma_{43} = \gamma_{43} + i(\omega_{43} - \omega_p) = \gamma_{43} + i\Delta. \quad (5.8c)$$

In equations 5.7, note that $\sigma_{mn} = \sigma_{nm}^*$. The terms $n_{ij} = \rho_{ii} - \rho_{jj}$ are the normalised population differences, governed according to the following expressions

$$\frac{dn_2}{dt} = -2Im[e_a^* \sigma_{42}] + r_{42}n_4 + r_{32}n_3 - r_2n_2, \quad (5.9a)$$

$$\frac{dn_3}{dt} = -2Im[e_p^* \sigma_{43}] + r_{43}n_4 - r_{32}n_3 + R, \quad (5.9b)$$

$$\frac{dn_4}{dt} = -2Im[e_a^* \sigma_{42}] - 2Im[e_p^* \sigma_{43}] - (r_{42} + r_{43})n_4, \quad (5.9c)$$

as derived from equation 5.2. Here, r_{ij} is the decay rate from level i to j and R accounts for the injection of carriers into level 3. Assuming very fast scattering of electrons from level 2 into the level 3 in the next period, $r_2n_2 + r_{32}n_3 = R$, i.e., a closed system.

The generation threshold to the first order in the AS field amplitude ($|e_a|^2 \ll \gamma_{23}\gamma_{24}$) can be found assuming a constant pump-field intensity. Solving equations 5.7 under steady-state conditions, we find

$$\sigma_{42} = \frac{-i}{\Gamma_{42} + \frac{|e_p|^2}{\gamma_{32}}} \left[\frac{|e_p|^2 n_{34}}{\gamma_{32}\Gamma_{43}^*} - n_{24} \right] e_a. \quad (5.10)$$

Substituting the latter expression in equation 5.5

$$\frac{\partial e_a}{\partial z} + \left\{ \kappa_a - \frac{2\pi\omega_a d_{42}^2 N_e \varsigma_a}{\hbar c n_a} \frac{1}{\Gamma_{42} + \frac{|e_p|^2}{\gamma_{32}}} \left[\frac{|e_p|^2 n_{34}}{\gamma_{32}\Gamma_{43}^*} - n_{24} \right] \right\} e_a = 0, \quad (5.11)$$

and assuming $e_a \propto \exp(\frac{1}{2}gz)$, it is straightforward to find the complex small-signal gain associated with processes near resonance

$$g_r = \eta_a Re \left\{ \frac{1}{\Gamma_{24} + \frac{|e_p|^2}{\gamma_{23}}} \left[\frac{|e_p|^2 n_{34}}{\gamma_{23}\Gamma_{34}^*} - n_{24} \right] \right\}, \quad (5.12)$$

where

$$\eta_a = \frac{4\pi\omega_a d_{24}^2 N_e}{\hbar c n_a}. \quad (5.13)$$

The inner brackets in equation 5.12 enclose two terms. The first one corresponds to the two-photon process of AS Raman scattering, while the second term accounts for the resonant one-photon absorption of the Anti-Stokes radiation. After taking the real part of equation 5.12, we obtain

$$g_r = \eta_a \left[\frac{(\tilde{\gamma}_{24}\gamma_{34} + \Delta^2) |e_p|^2 n_{34}}{\gamma_{23} (\tilde{\gamma}_{24}^2 + \Delta^2) (\gamma_{34}^2 + \Delta^2)} - \frac{\tilde{\gamma}_{24}^2 n_{24}}{(\tilde{\gamma}_{24}^2 + \Delta^2)} \right], \quad (5.14)$$

where $\tilde{\gamma}_{24} = \gamma_{24} + |e_p|^2/\gamma_{23}$ is the "power-broadened" linewidth of the transition 2-4. The generation condition is given by

$$g_r > \alpha_a, \quad (5.15)$$

that is, the resonant gain overcoming the non-resonant losses α_a at the Anti-Stokes frequency, which include waveguide loss and transmission in the facets. Equation 5.14 indicates that the AS Raman gain depends linearly on the population difference n_{34} , the pump intensity, and the product of the optical dipole matrix elements of transitions 2-4 and 3-4 squared ($d_{24}^2 d_{34}^2$). The population differences are themselves function of the detuning, which makes the dependence of the AS Raman gain on Δ not trivial.

In the limit $\Delta \rightarrow \infty$, the expression in curly brackets in equation 5.14 reduces to

$$\frac{|e_p|^2 n_{32}}{\gamma_{23} \Delta^2} - \frac{n_{24} \gamma_{24}}{\Delta^2}, \quad (5.16)$$

the first term corresponding to the standard AS Raman gain far from any resonance, which can be obtained via second order perturbation calculations [22]. The second term again accounts for the linear absorption of the AS photons.

5.2 Laser design

5.2.1 Different designs of active regions

The design of one of our QC lasers involves, in a first stage, choosing the appropriate well and barrier widths in the active regions to both maximise the pump optical power and enhance the AS Raman nonlinearity.

In principle, it is convenient to integrate both pump laser and nonlinearity in the same active region [9, 18]. This increases the mode overlap and allows for more periods to be grown. However, we decided to have a 2-stack active waveguide core, as illustrated in figure 5.3, so we could design the more complex nonlinear region independently and then tailor the pump stack to lase at the required wavelength. Although this comes at the

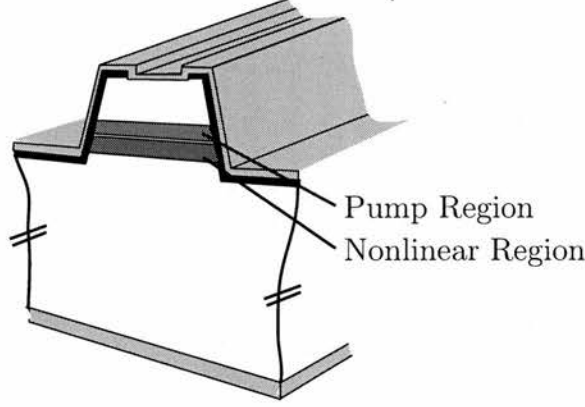


Figure 5.3: Sketch of a QC laser in which the pump laser is monolithically integrated with the nonlinear region in a 2-stack active waveguide core.

expense of a larger combined period length ($L_p = L_{NL} + L_{pump}$), we obtain better optical dipole matrix elements and scattering times.

The thicknesses of the different layers and the external applied field were input into a QBasic program. We assumed a well depth of 520 meV, according to the low-temperature conduction band-offset usually associated with the materials' composition ($\text{In}_{0.53}\text{Ga}_{0.47}\text{As}$, $\text{Al}_{0.48}\text{In}_{0.52}\text{As}$), lattice matched to the InP substrate. The potential for the electrons in the conduction band was simulated and then the Schrödinger equation was solved numerically. This way, we obtained the energy levels and the squared moduli of the corresponding electronic wavefunctions. The low doping in our structures (typical sheet densities of the order of 10^{11}cm^{-2}) allows us to neglect the extra potential created by the ionised donors (key in some types of superlattice active regions [23]). A separate program took the calculated wavefunctions and estimated the electron-LO phonon scattering times using a Fröhlich interaction model [24].

The design process involves trying different combinations of well and barrier widths iteratively, checking for improvements of the relevant figures of merit. When it comes to the nonlinear stack, the main goal is to maximise the AS Raman gain. By rewriting equation 5.14 in a more convenient fashion,

$$g_r = \frac{4\pi\omega_a N_e}{\hbar c n_a} \left[\frac{(\tilde{\gamma}_{24}\gamma_{34} + \Delta^2) d_{24}^2 d_{34}^2 \left| \frac{\epsilon_p}{2\hbar} \right|^2 n_{34}}{\gamma_{23} (\tilde{\gamma}_{24}^2 + \Delta^2) (\gamma_{34}^2 + \Delta^2)} - \frac{\tilde{\gamma}_{24}^2 n_{24}}{(\tilde{\gamma}_{24}^2 + \Delta^2)} \right], \quad (5.17)$$

some design guidelines can be inferred. First, maximise the product of the optical dipole

matrix elements corresponding to transitions 4-2 and 4-3. Level 2 must be depleted as fast as possible (small τ_2) and the scattering rate $r_4 = \tau_4^{-1}$ should be large to reduce n_{24} (Note that under such conditions, population inversion between states 4-2 may also be possible). On the other hand, $r_3 = \tau_3^{-1}$ should also be kept small to maximise n_{34} ($= n_3 - n_4$).

Larger doping concentrations in the injectors would increase the available carrier density N_e and, subsequently, the nonlinear gain. However, as we will soon discuss, light propagating in the waveguide would then undergo strong attenuation due to free carrier absorption.

According to equation 5.17, the AS Raman gain increases with the pump intensity. The pump region is thus designed to provide maximum optical power at the required wavelength. The gain coefficient of a QC laser at low temperature is given by

$$g = \tau_3 \left(1 - \frac{\tau_2}{\tau_{32}} \right) \frac{4\pi e z_{32}^2}{\lambda_0 \varepsilon_0 n_{eff} L_p} \frac{1}{2\gamma_{32}}, \quad (5.18)$$

where 3 and 2 are the upper and lower laser levels, respectively, as explained earlier (see section 2.4.1). Since we do not have much control over γ_{32} and L_p does not change significantly during design, a more compact expression can be used as a figure of merit

$$\tau_3 \left(1 - \frac{\tau_2}{\tau_{32}} \right) z_{32}^2 h\nu_{32} \quad (5.19)$$

Henceforth, we will express times in picoseconds, energies in milli-electron volts and optical dipole matrix elements in nanometers. Again, it is clear from equation 5.19 that maximizing the optical dipole matrix element of the transition 3-2 (z_{32}) is crucial. On the other hand, the scattering rate (r_3) of carriers from the upper laser level into lower energy levels must be small and the lower laser state must be readily depleted (small τ_2) to maximise the population inversion.

Next, the different designs of active regions developed as a part of my work in Princeton are described in detail and compared.

Design I: wafer D2924

The work described here followed some previous research carried out at Bell Labs (Lucent Technologies). An early design, D2924, had been developed by C. Gmachl and

co-workers and a batch of lasers was already available. The barrier/well widths in one of the 30 periods of the nonlinear stack, given in units of nanometers, are 4.0/ **2.6**/2.9/ **2.9**/2.6/ 2.7/2.3/ 2.7/2.0/ **2.7**/1.7/ **3.8**/2.5/ **4.2**/1.8/ **7.1**, where the wells are shown in bold face and the barriers in plain face; the underlined layers are doped to $2 \times 10^{17} \text{ cm}^{-3}$. This notation will be kept consistently throughout the present chapter.

The pump is a conventional 30-period QC-laser emitting at $\lambda \sim 10.5 \mu\text{m}$. Each of these periods comprises the following layers 3.5/ **4.1**/2.4/ 4.2/2.3/ 4.3/2.2/ **4.2**/2.2/ **4.2**/2.5/ **5.5**/1.2/ **6.6**/1.1/ **7.7**/1.1/ **8.8**, with the underlined layers doped to $1.5 \times 10^{17} \text{ cm}^{-3}$. Figure 5.4 shows the conduction band of both regions, as well as the moduli squared of the electronic wavefunctions. The blue arrows in (a) indicate the AS Raman transition. To avoid confusion, unless indicated otherwise, the electronic states involved in the AS Raman process will henceforth be labelled with arabic numbers (2, 3, 4) and the upper and lower laser levels in the pump stages will be referred to as U and L, respectively. In all cases, the letter g identifies the ground level of the injector.

Starting with figure 5.4(a), note how the ground level of the injector, g, is anticrossed with the second level of the widest well of the active region (3), thus allowing the tunneling [25] of electrons. Approximately 137 meV above, and mostly localised in the two adjacent wells, we find state 4. The two anticrossed levels contribute to the optical dipole matrix element z_{43} , giving $z_{43} \approx (1.5^2 + 0.9^2)^{1/2} \approx 1.8 \text{ nm}$.

Level 2 is the lowest energy state involved in the AS Raman process, located 296 meV below state 4. The optical dipole matrix element z_{42} is estimated to be 0.6 nm and carriers are swept out of level 2 with a characteristic time of $\tau_2 = 0.4 \text{ ps}$. Apart from 2, the states labelled $|a\rangle$ and $|b\rangle$ in figure 5.4(a) are also good candidates for being the lower level in the Anti-Stokes emission. Of these two, level $|a\rangle$ stands out, as it presents the strongest optical dipole matrix element $z_{4a} = 1.3 \text{ nm}$ and it is depleted very fast via scattering into lower energy levels ($\tau_a = 0.36 \text{ ps}$).

The main drawback of this design are the significant optical dipole matrix elements corresponding to the transitions from the highly populated state 3 in the nonlinear active region into lower energy levels. Since the total oscillator strength is fixed, according to the Thomas-Reiche-Kuhn rule [6], the large optical dipole matrix elements of transitions such as 3-1, 3-b and 3-2 (0.7, 0.7 and 1.0 nm respectively), will lead to a reduced z_{34} and

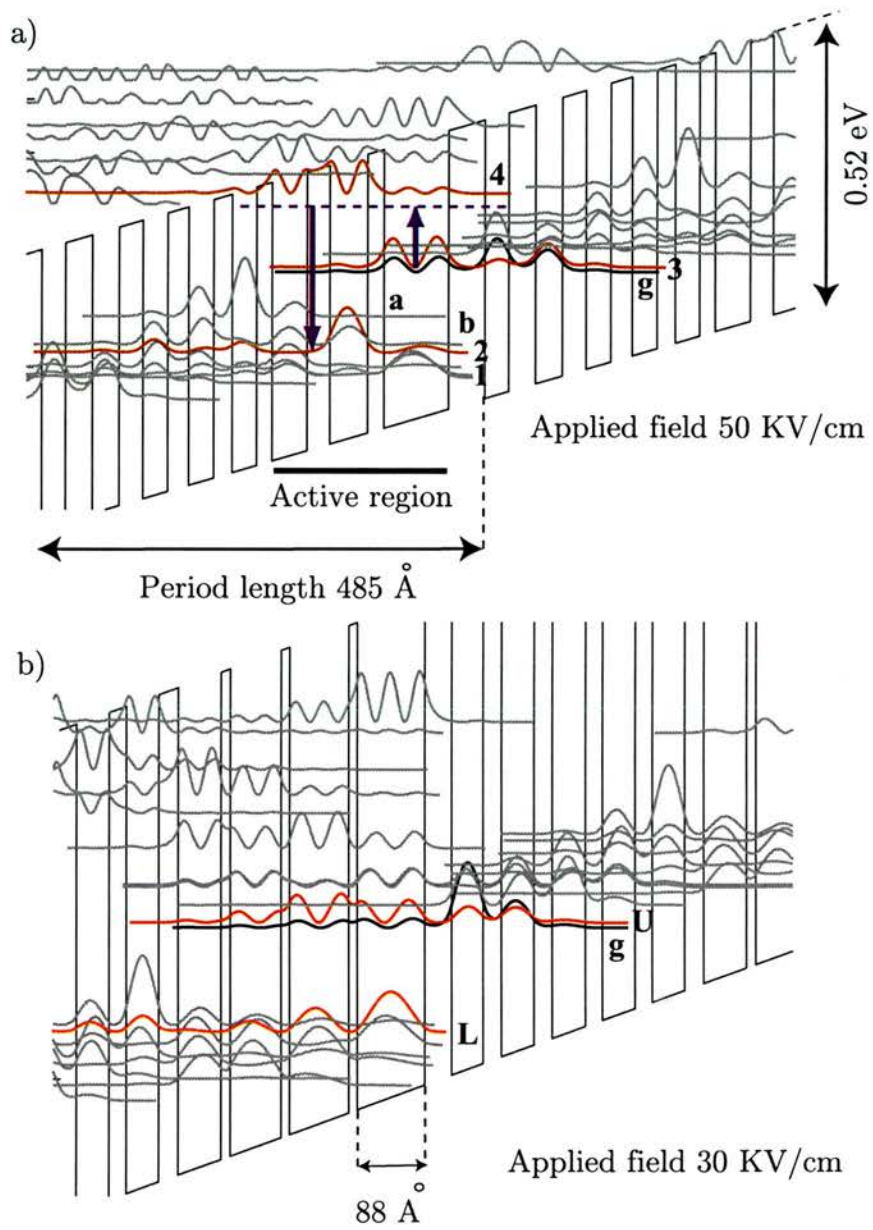


Figure 5.4: Sketch of the conduction band of D2924, for both a) the nonlinear region and b) the pump stack, together with the moduli squared of the electron wavefunctions. In a) the AS Raman process is indicated by the blue arrows, and the states involved are highlighted in red.

thus to a decrease in the nonlinear gain.

On the other hand, the presence of state 1 localised mostly in the same well as state 3 gives carriers an extra scape route via fast scattering with the LO-phonons. As a result, τ_3 is short, only 1.5 ps, and the nonlinear gain is reduced.

The pump stack (see figure 5.4(b)) was designed to lase with photon energy 117 meV and thus pump the nonlinear region below resonance. The widths of wells and barriers were carefully chosen so as to maximise the spatial spread of both upper and lower laser levels, increasing the optical dipole matrix element $z_{UL} = 2.4 \text{ nm}$. The relevant scattering times are $\tau_U = 1 \text{ ps}$, $\tau_{UL} = 4.3 \text{ ps}$, and $\tau_L = 0.4 \text{ ps}$. Substituting these parameters in equation 5.19, a figure of merit of $\approx 611 \text{ ps.nm}^2.\text{meV}$ is obtained.

Design II: wafers D3008 and D3036

The first design I developed at Princeton University shared the basic ideas of D2924. However, some modifications were introduced to optimise the relevant optical dipole matrix elements and scattering times. The layer thicknesses of one of the 20 periods comprised in the nonlinear stack are 4.6/ **2.8**/2.9/ **2.8**/1.7/ **2.6**/3.0/ **2.9**/2.1/ **3.2**/2.0/ **3.4**/1.5/ **3.6**/1.8/ **4.6**/2.2/ **7.3**, using the same notation as with the previous design. The doping concentration in the underlined layers is $2.5 \times 10^{17} \text{ cm}^{-3}$.

In an analogous fashion, the barrier/well widths in one period of the pump region are 3.4/ **3.8**/2.4/ 4.2/2.3/ 4.3/2.2/ **4.2**/2.2/ **4.3**/2.2/ **5.5**/1.2/ **6.2**/1.1/ **7.1**/1.1/ **8.2**. The pump stack comprises 20 periods and the doping in the underlined layers is $1.5 \times 10^{17} \text{ cm}^{-3}$. A detailed diagram of the conduction band of both nonlinear and pump regions is shown in figure 5.5.

In the nonlinear active regions, we aimed to increase z_{42} and z_{43} by tailoring the overlap of the relevant wavefunctions. We obtained $z_{42} = 1.8 \text{ nm}$ and $z_{43} = 1.8 \text{ nm}$, a significant improvement compared to the previous design, with energy separations of $\delta E_{43} = 123 \text{ meV}$ and $\delta E_{42} = 231 \text{ meV}$.

To speed up the depletion of level 2, the energy difference with level 1 is tailored to be almost resonant with the LO-phonon (36 meV), resulting in $\tau_2 = 0.2 \text{ ps}$. The lifetime of state 3 is 1.6 ps, mostly dictated by the LO-phonon scattering into the first level of the widest well of the nonlinear active region.

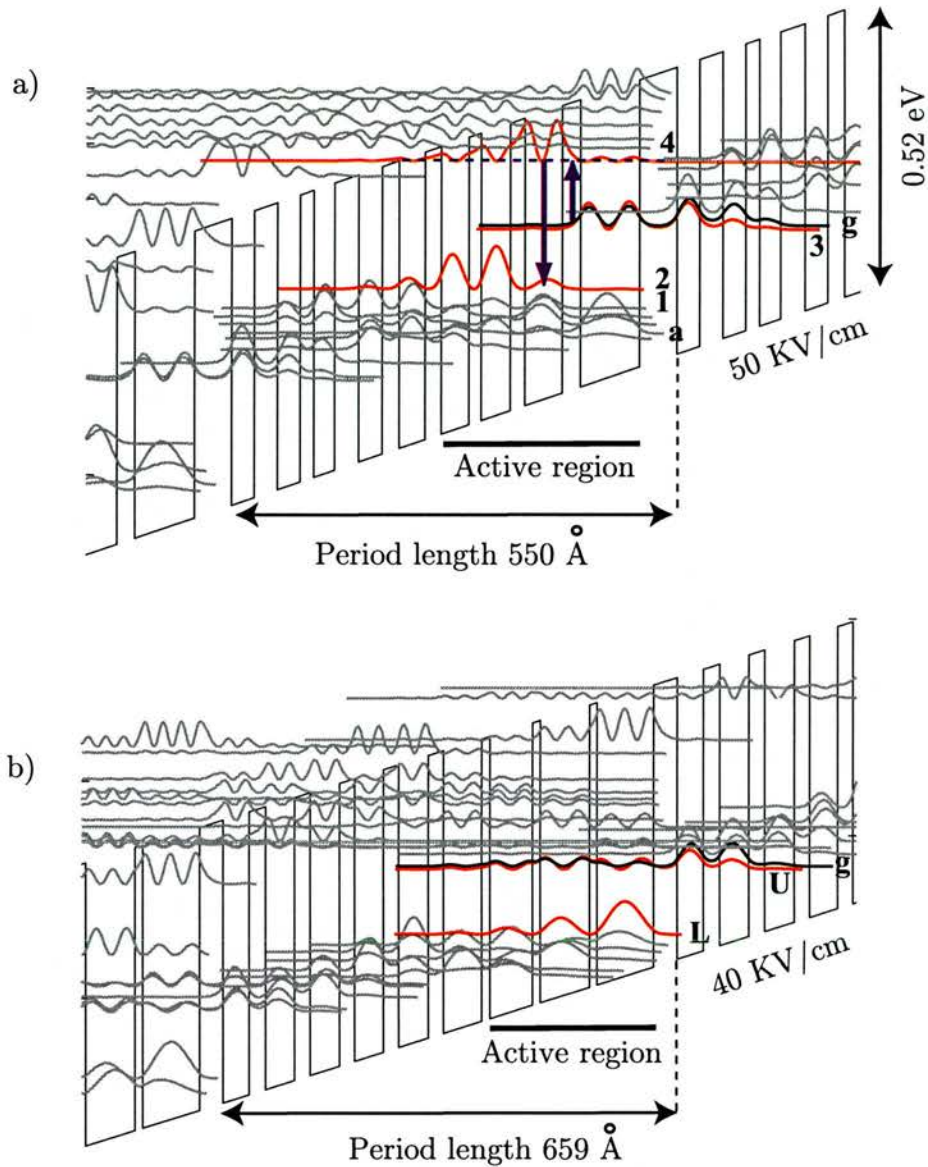


Figure 5.5: Conduction band of D3008/D3036 for both (a) nonlinear and (b) pump stacks indicating the external applied field. The moduli squared of the electron wavefunctions are also plotted, highlighting in red those involved in the AS Raman process (indicated by the blue arrows).

As in D2924, the transition from the highly populated state 3 into the first level of the widest well presents a significant optical dipole matrix element (1.0 nm). This is a major drawback, as it was found to cause unwanted lasing in some samples (see section 5.3.2).

In this case, we designed the pump stack, figure 5.5(b), to pump the nonlinear structure very close to resonance ($\hbar\omega_p = 120 \text{ meV}$). Keeping the lasing energy approximately constant as required, the well and barrier widths had to be varied to maximise the gain. The estimated optical matrix element of the pump laser transition U-L is $z_{UL} = 2.7 \text{ nm}$,

and the relevant scattering times $\tau_U = 1.2 ps$, $\tau_{UL} = 4.3 ps$ and $\tau_L = 0.4 ps$. Using equation 5.19, we find that the figure of merit of this pump design is $\approx 952 ps.nm^2.meV$, that is, larger to that of D2924 by a factor of 1.5.

During the growth of wafer D3008 at Bell Labs (Lucent Technologies), some problems concerning one of the dopant cells was reported. To confirm that the doping concentrations still matched the design specifications, another wafer was ordered and labelled D3036.

Design III: wafers D3015 and D3037

Compared with the two previous designs, wafers D3015 and D3037 present a major modification: the last well in each period of the nonlinear stack, which is also the first well in each active region, was narrowed so as to anticross its first bound state with the ground level of the adjacent injector. Since no lower energy states overlap significantly with state 3 anymore, unwanted lasing is prevented and τ_3 is substantially longer.

The detailed well and barrier widths in each of the 26 periods comprised in the nonlinear region are as follows, 4.5/ **3.1**/2.9/3.1/2.5/ **3.2**/3.0/ **3.3**/1.5/ **3.7**/1.5/ **4.2**/1.5/ **4.8**/1.5/ **2.7**, using the conventional notation. The underlined wells and barriers are doped to $2 \times 10^{17} cm^{-3}$. As sketched in figure 5.6(a), the energies of the transitions 4-3 and 4-2 are $\delta E_{43} = 137 meV$ and $\delta E_{42} = 225 meV$. The corresponding optical dipole matrix elements are estimated to be $z_{43} = 1.8 nm$ and $z_{42} = 2.0 nm$, and the relevant scattering times $\tau_4 = 0.9 ps$, $\tau_3 = 2.9 ps$, and $\tau_2 = 0.2 ps$. Note that τ_3 is almost twice the value obtained in previous designs.

In this case, the pump was designed to emit photons with energy 136 meV, resonant with the energy separation between levels 4 and 3. This stack comprised 20 periods with the following layer thicknesses, 3.4/ **3.3**/2.4/ 3.8/2.3/ 4.3/2.2/ **4.2**/2.2/ **4.3**/2.2/ **5.2**/1.2/ **5.6**/1.3/ **6.6**/1.3/ **7.9**. The underlined wells and barriers were doped to $1.5 \times 10^{17} cm^{-3}$.

Numerical calculations yield $z_{UL} = 2.4 nm$, $\tau_U = 1.3 ps$, $\tau_{UL} = 4.2 ps$ and $\tau_L = 0.4 ps$. This gives a figure of merit of $\approx 921 ps.nm^2.meV$, as calculated using equation 5.19, very close to that of D3008.

D3015 was the first wafer corresponding to design III to be grown. However, for similar reasons to D3008, a second wafer with identical specifications was ordered and labelled

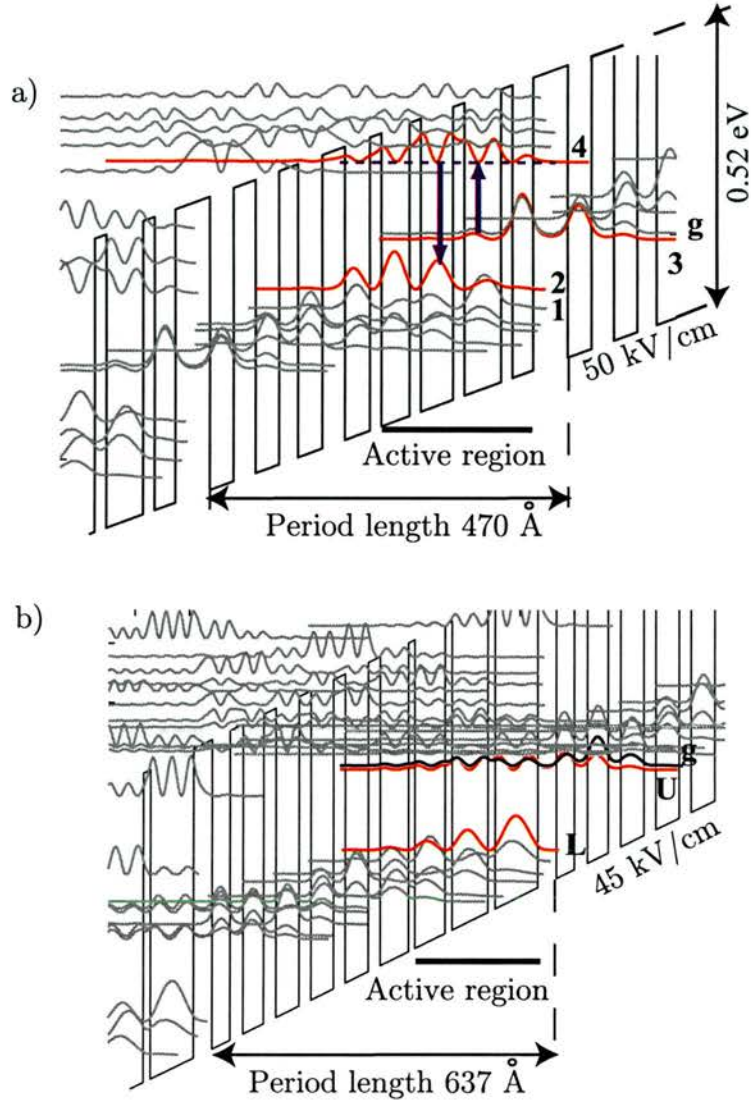


Figure 5.6: Diagram of the conduction band of D3015/D3037, for both (a) the nonlinear region and (b) the pump stack, together with the moduli of the electron wavefunctions. In a) the AS Raman process is indicated by the blue arrows, and the states involved are highlighted in red.

D3037.

Design IV: wafer D3018

Using the same nonlinear region as in design III, the pump region in wafer D3018 was redesigned to lase with $\hbar\omega_p = 115 \text{ meV}$, that is, with a detuning of approximately $\Delta = -20 \text{ meV}$ below resonance. Our aim was to establish whether the subsequent reduction in the linear absorption of the pump light would lower the AS Raman lasing threshold.

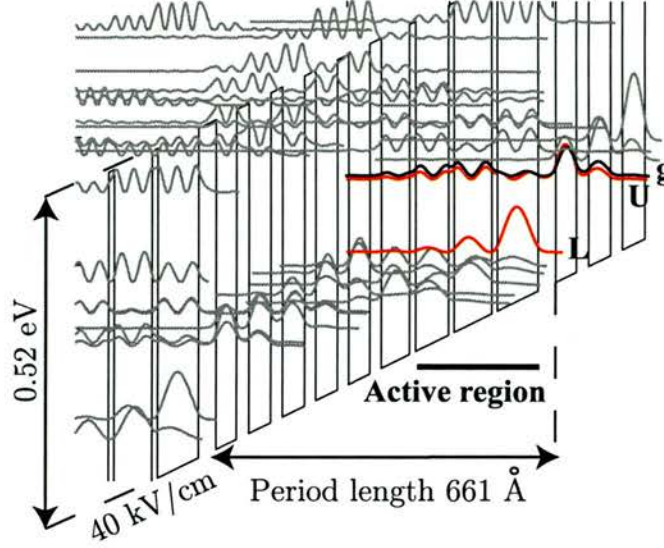


Figure 5.7: Sketch of the conduction band of the pump region in D3018. The nonlinear region is identical to that of D3015 (see figure 5.6(a)).

The barrier/well widths in a period of the pump stack are 3.4/ 4.0/2.4/ 4.2/2.3/ 4.3/2.2/ 4.2/2.2/ 4.2/2.2/ 5.5/1.2/ 6.4/1.1/ 7.3/1.1/ 7.9, with a doping concentration of $1.5 \times 10^{17} \text{ cm}^{-3}$ in the underlined layers. Figure 5.7 shows a diagram of the conduction band in the pump region.

The optical dipole matrix element of the laser transition was estimated to be $z_{UL} = 2.3 \text{ nm}$, while the scattering times are $\tau_U = 1.6 \text{ ps}$, $\tau_{UL} = 6.19 \text{ ps}$ and $\tau_L = 0.4 \text{ ps}$. These combine to give a figure of merit $\approx 910 \text{ ps.nm}^2.\text{meV}$, of the same order of magnitude as those of designs II and III.

5.2.2 Mid-IR Waveguides

Lasing occurs when gain out-weighs loss in the device waveguide. So far, while gain mechanisms have already been discussed in detail, the waveguide loss was simply introduced as a factor, α_w , in the threshold equation (2.43). In this section, we will describe the waveguide design used in our lasers, pointing out some key issues to applications in the mid-IR.

To efficiently confine light in a dielectric waveguide, a high refractive index contrast between core and cladding is required. This way, the overlap (Γ) of the optical mode and the active region is maximised, lowering the laser threshold.

When it comes to QC lasers in our material system and at wavelengths $\sim 2 - 15 \mu m$, dielectric waveguides are the common choice. In this case, the core is formed by hundreds of GaInAs/AlInAs wells/barriers. For our purposes, the refractive index of the active regions and injectors is calculated as the average of $n_{GaInAs} \sim 3.49$ and $n_{AlInAs} \sim 3.20$, weighted with the respective volume fractions. As this usually gives $n_{core} \sim 3.35$, the InP substrate ($n_{InP} \sim 3.10$) makes for a convenient bottom cladding, saving MBE time. The top cladding was grown with AlInAs (if available, InP is also a very good alternative).

Significant portions of a QC laser are n-doped with Silicon for carrier transport. This results in a decrease of the refractive index that must be taken into account and, eventually, can be used to our advantage. However, at the same time, light in the mid-IR range undergoes strong free carrier absorption, which increases the loss and ultimately determines α_w .

To design our waveguides, first we calculate the refractive index of the different regions. Using a Drude model for free carrier absorption [26], the real and imaginary parts of the dielectric function can be expressed as

$$\varepsilon_r(\omega) = \varepsilon_\infty \left(1 - \frac{\omega_p^2}{\omega^2 + \gamma^2} \right), \quad (5.20a)$$

$$\varepsilon_i(\omega) = \frac{\varepsilon_\infty \omega_p^2 \gamma}{\omega (\omega^2 + \gamma^2)}, \quad (5.20b)$$

where ε_∞ is the high frequency dielectric constant and γ is a phenomenological rate related to the scattering of carriers with phonons and impurities; ω_p is the plasma frequency, defined as

$$\omega_p = \sqrt{\frac{4\pi N_d e^2}{m^* \varepsilon_\infty}}. \quad (5.21)$$

Here, N_d and m^* are the doping concentration and the electron effective mass, respectively. For typical dopings ($\leq 10^{17} cm^{-3}$), the plasma frequency lies in the mid to far-IR range. The values of ε_∞ and m^* for the different materials used in our calculations are summarised in table 5.1. The carrier scattering time, $\tau = \gamma^{-1}$, was taken to be 0.1 ps.

From equations 5.20(a) and (b), the complex refractive index can be easily calculated

	m^*/m_0	$\epsilon_\infty/\epsilon_0$
InP	0.080	9.6
AlInAs	0.076	10.23
GaInAs	0.043	12.14

Table 5.1: Values of the high-frequency dielectric constant (ϵ_∞) and the electron effective mass (m^*) used in our Drude model calculations.

as

$$\bar{n} = \frac{\sqrt{\epsilon_r^2 + i\epsilon_i^2}}{\epsilon_0} \quad (5.22)$$

Once the refractive index of the different layers is known for both pump and Anti-Stokes wavelengths, we can obtain the intensity profile of the TM modes by solving the 1D waveguide equations in the direction of growth. The absorption coefficient for a given mode is then calculated from the corresponding effective index, \bar{n}_{eff} , as

$$\alpha_w = \frac{4\pi \text{Im}(\bar{n}_{eff})}{\lambda_0} \quad (5.23)$$

where λ_0 is the wavelength in the vacuum. The fact that the Anti-Stokes Raman nonlinear process is automatically phase matched [12] greatly simplifies the design.

By varying the layer thicknesses and doping concentrations in the cladding, we look for maximum overlap of the pump and AS modes with the active regions while keeping absorption as low as possible. In principle, single mode waveguides are preferred. However, even if higher order modes do exist, they are unlikely to be excited due to their much larger absorption coefficients and poor confinement factors.

For the sake of clarity, a detailed waveguide cross-section of wafer D3015, including layer thicknesses and doping concentrations, is displayed in figure 5.8. As seen in this figure, doped GaAlInAs graded regions are grown to ease the carrier transport across the structure, otherwise hindered by the band discontinuities between the different layers.

Figure 5.9 shows the normalised intensity profiles of the pump ($9.1 \mu m$) and AS ($5.5 \mu m$) fundamental modes, together with the profiles of the real part of the refractive index, calculated for the cross-section of figure 5.8.

Even though the light in our lasers is mostly confined in the core, the optical mode interacts with the claddings and may even reach the metal of the top contact. The coupling

Material	Doping (n-type)	Thickness		
GaInAs	$1 \times 10^{20} \text{ cm}^{-3}$	200 Å	Cladding	
GaInAs	$3 \times 10^{18} \text{ cm}^{-3}$	8000 Å		
Ga _{0.5x} Al _{0.5(1-x)} InAs graded region	$1 \times 10^{17} \text{ cm}^{-3}$	250 Å	Cladding	
AlInAs	$2 \times 10^{17} \text{ cm}^{-3}$	4000 Å		
AlInAs	$1 \times 10^{17} \text{ cm}^{-3}$	21000 Å	Cladding	
Ga _{0.5x} Al _{0.5(1-x)} InAs graded region	$1 \times 10^{17} \text{ cm}^{-3}$	250 Å		
GaInAs	$1 \times 10^{17} \text{ cm}^{-3}$	2000 Å	Cladding	
Ga _{0.5x} Al _{0.5(1-x)} InAs graded region	$1 \times 10^{17} \text{ cm}^{-3}$	250 Å		
Ga_{0.5x}Al_{0.5(1-x)}InAs Pump stack	$1.5 \times 10^{17} \text{ cm}^{-3}$	637 Å 20×	Waveguide core	
Ga _{0.5x} Al _{0.5(1-x)} InAs graded region	$1 \times 10^{17} \text{ cm}^{-3}$	324 Å		
GaInAs	$1 \times 10^{17} \text{ cm}^{-3}$	200 Å		
Ga _{0.5x} Al _{0.5(1-x)} InAs graded region	$1 \times 10^{17} \text{ cm}^{-3}$	250 Å		
Ga_{0.5x}Al_{0.5(1-x)}InAs Nonlinear stack	$2 \times 10^{17} \text{ cm}^{-3}$	470 Å 26×		
Ga _{0.5x} Al _{0.5(1-x)} InAs graded region	$1 \times 10^{17} \text{ cm}^{-3}$	308 Å		
GaInAs	$1 \times 10^{17} \text{ cm}^{-3}$	6000 Å		
Ga _{0.5x} Al _{0.5(1-x)} InAs graded region	$1 \times 10^{17} \text{ cm}^{-3}$	250 Å		
Low doped n-InP substrate ($1-4 \times 10^{17} \text{ cm}^{-3}$)				Cladding

Figure 5.8: Waveguide cross-section of D3015. For every layer, material composition, doping concentration and thickness are given.

of the light to the surface plasmon in the semiconductor-metal interface substantially increases the loss. While this can be avoided by growing thicker claddings and thus keeping the mode far from the contacts, it comes at the expense of longer MBE times. Our approach is inspired to some extent in the proposal by Sirtori *et al.* [27], known as 'plasmon-enhanced' waveguides, but limited by the difficulty of having to work simultaneously with two different wavelengths.

As seen in both figures 5.9(a) and (b), the bottom cladding is the low doped InP substrate. The top cladding consists mostly of a thick low-doped AlInAs layer to provide low-loss optical confinement.

The refinement comes with the highly-doped ($3 \times 10^{18} \text{ cm}^{-3}$) GaInAs layer grown just before the top contact layer. This doping concentration is such that both pump and Anti-Stokes wavelengths are shorter than the plasma wavelength ($\approx 14 \mu\text{m}$). This

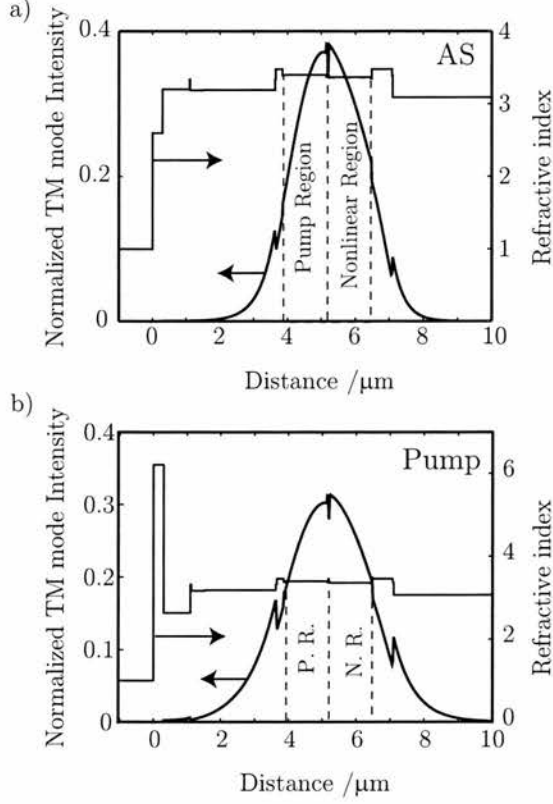


Figure 5.9: Normalised intensity mode profile and profile of the real part of the refractive index in the (reverse) growth direction for both Anti-Stokes and pump fundamental modes in D3015.

leads to a significant decrease of the refractive index, specially for the pump wavelength ($n_{GaInAs}(9.1 \mu m) \sim 2.63$), much closer to the plasma resonance, as illustrated in figure 5.10. As a result, the higher index contrast provides better confinement and reduces the coupling to the surface plasmons. Figure 5.10 illustrates how choosing a doping concentration involves a trade-off between lower refractive index and larger absorption.

For wafer D3015, our calculations estimated α_w at pump and AS wavelengths to be 10.6 cm^{-1} and 3.0 cm^{-1} , respectively. The difference between them is explained by the Drude model, which predicts a λ^2 dependence of α . The overlap of the pump mode with the Anti-Stokes and pump active regions is 0.32 and 0.33 respectively. On the other hand, the confinement factor of the Anti-Stokes light is 0.38, as only the nonlinear region is considered. The waveguide specifications, including both layer thicknesses and doping concentrations change slightly from one design to another. However, absorption coefficients and confinement factors are of the same order of magnitude.

Apart from waveguiding in the growth direction, achieving both good optical and

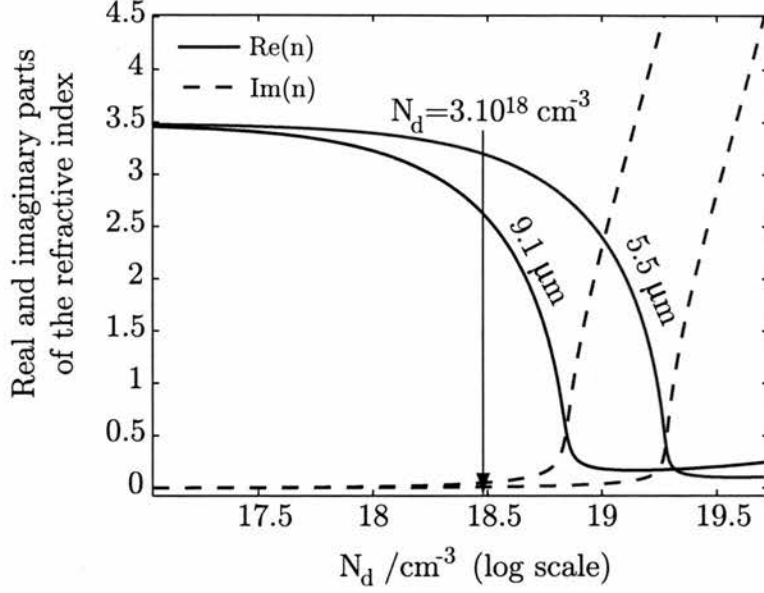


Figure 5.10: Calculation of the real and imaginary parts of the refractive index of GaInAs as a function of doping concentration, using a Drude model. Results for both pump and Anti-Stokes wavelengths of D3015 are shown.

current transversal confinement is also crucial. This is achieved by etching deep ridges in our wafers (as described in section 3.3). This way, heat is more efficiently removed, as the surface to volume ratio is larger when compared to planar structures. In addition, the in-plane resistance is much smaller than the resistance across the long stack causing significant lateral current spreading if no current confinement is applied. We etched ridges $6 - 20 \mu\text{m}$ wide. Although wider ridges generally allow for more power, higher order transversal modes may be excited. The lasers are cleaved to 2-3 mm length and the facets are left uncoated.

5.3 Experimental results

In the section that follows, we present the experimental results which make the case, to our knowledge, for the first observation of stimulated electronic Anti-Stokes emission in QC lasers.

Different samples were processed out of each wafer, labelled accordingly and then characterised by means of spectral and electrical measurements, as explained in chapter 3. In each sample, the two bonded lasers are identified as 'top' and 'bottom' according

	Peak 1	Peak 2	Peak 3
0.50 A	23.6/ 118 /11	27.2/ 154 /27	46.0/ 178 /20
0.75 A	85.6/ 118 /7	56.2/ 155 /22	71.8/ 181 /20
1.00 A	411.4/ 117 /4	88.1/ 155 /18	98.6/ 183 /21

Table 5.2: Values of $a/c/w$ obtained fitting the spectra of figure 5.11 to three lorentzian curves. The peak amplitude (a) is given in arbitrary units, while the energy at the maximum (c) and FWHM (w) are both expressed in milli-electron volts.

to their position in the experimental set-up. First, results corresponding to the different designs are reported separately, often referring to details described previously in section 5.2.1. In the final part, we compare the results from different designs and discuss the feasibility of AS lasing.

5.3.1 Wafer D2924

With sample D2924A1 mounted and cooled down to liquid helium temperatures ($\sim 7 K$), we first carried out luminescence measurements.

Below threshold, light is emitted when electrons decay spontaneously from highly populated states. In the nonlinear stack, these are the anticrossed pair formed by the levels 3 and g. In the pump region, carriers will decay from the anticrossed upper laser level (U) and injector ground level. The emission spectra of laser D2924A1(bottom) was measured at three different peak currents in pulse mode (100 ns pulse duration at 84 KHz repetition rate, corresponding to a duty cycle of $\approx 0.8\%$). These measurements employed the internal MCT detector of the Nicolet FTIR spectrometer, and the results are displayed in figure 5.11.

The emission spectra of QC lasers, plotted as a function of photon energy (E), usually fit very well to Lorentzian curves of the form

$$L(E) = \frac{a}{4 \left(\frac{E-c}{w} \right)^2 + 1}, \quad (5.24)$$

where a , c and w are, respectively, the peak height, center and full width at half the maximum (FWHM). The results of fitting our spectra to three lorentzian peaks are displayed in table 5.2.

The main peak at $10.5 \mu m$ (118 meV) observed in figure 5.11 corresponds to the pump laser transition (designed to be 117 meV). The fast growing peak intensity and charac-

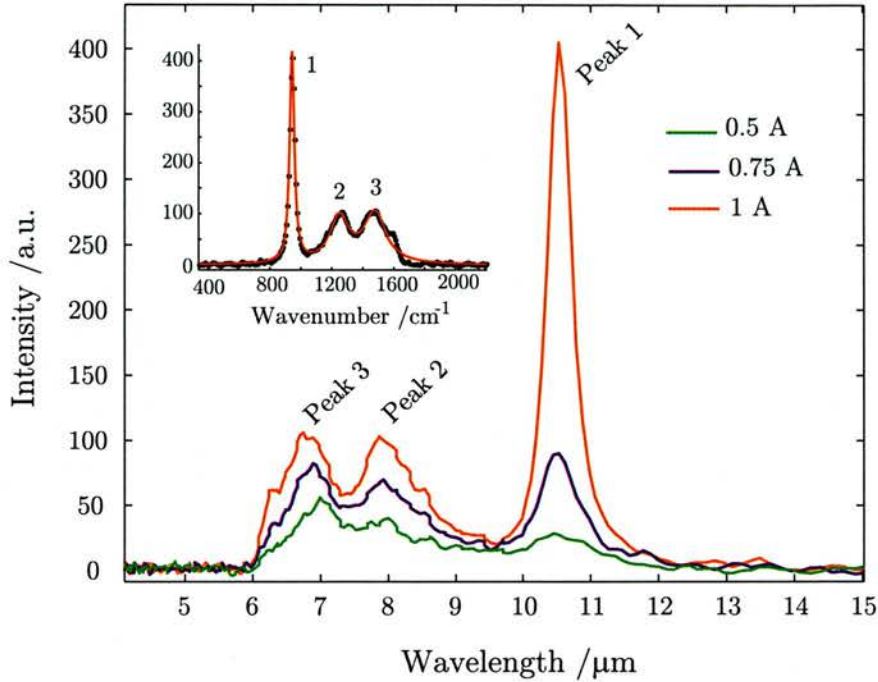


Figure 5.11: Emission spectra below threshold of laser D2924A1(bottom) at peak currents 0.5, 0.75 and 1 A. These measurements were carried out at liquid helium temperatures in current pulsed mode ($\sim 7 K$). The inset in the upper left corner shows the fitting of the 1 A spectrum, plotted versus wavenumber ($1/\lambda$).

teristic narrowing when the current is increased, suggest the proximity of the pump laser threshold. Also in the pump region, significant emission due to the spontaneous decay into the state just above L is expected (see figure 5.4(b)), since the transition presents a large optical dipole matrix element ($1.7 nm$). However, such luminescence cannot be observed as it is too close in energy to the pump laser transition.

The signature of spontaneous emission from the nonlinear region is also observed in the measured spectra. The broad peak at 155 meV ($8.0 \mu m$), labelled as 2 in figure 5.11 is most likely formed by the contribution of two different transitions, namely, 3-b ($145 meV$) and 3-2 ($159 meV$) (see figure 5.12). On the other hand, peak 3 can be attributed to the decay of electrons from level 3 into the pair of anticrossed states labelled as 1 (located $202 meV$ and $207 meV$ below level 3, respectively).

The light output and voltage versus current characteristics of sample D2924A1 were measured at liquid nitrogen temperatures ($\sim 77 K$), as shown in figure 5.13. The pump laser threshold of D2924A1(bottom) was reached at a peak current of 1.1 A (see black dashed line). For comparison, the light output and voltage versus current characteristics

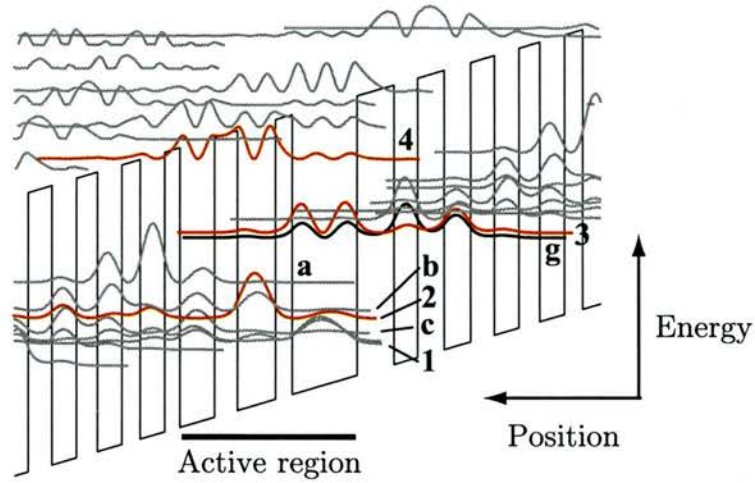


Figure 5.12: Conduction band diagram of one period of the nonlinear stack of D2924.

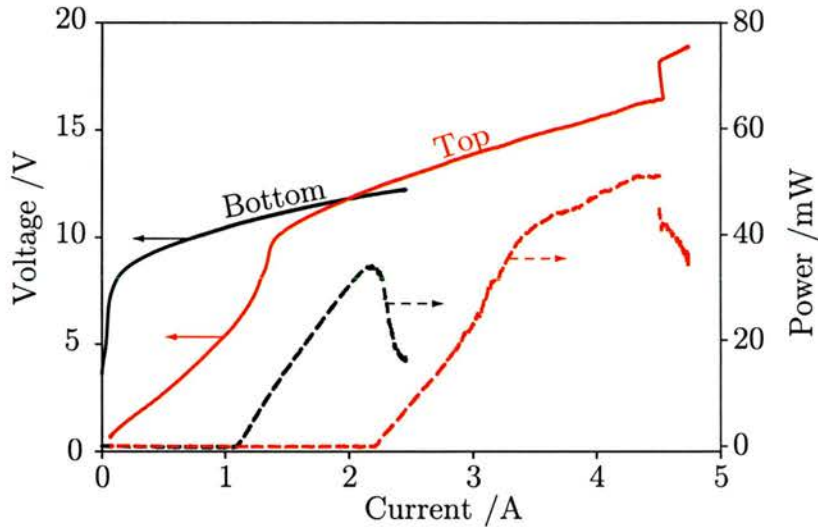


Figure 5.13: Light output and voltage versus current characteristics of bottom (black) and top (red) lasers in sample D2924A1. The voltage-current curves are plotted with straight lines, while the dashed lines correspond to optical power versus current.

of the top laser in the sample are also plotted. The latter reveal significant losses (leakage current), resulting in a larger threshold current. On the other hand, the discontinuity observed around 4.5 A suggests some problem with the contacts.

The emission of laser D2924A1(bottom) at short wavelengths was measured at a heat sink temperature of $\sim 7 K$, in pulsed current mode (100 ns pulse duration), using an InSb detector cooled with liquid nitrogen. Figure 5.14 shows the spectra measured at 1.8, 2, 2.25 and 2.5 A peak currents. No light was detected below the pump laser threshold.

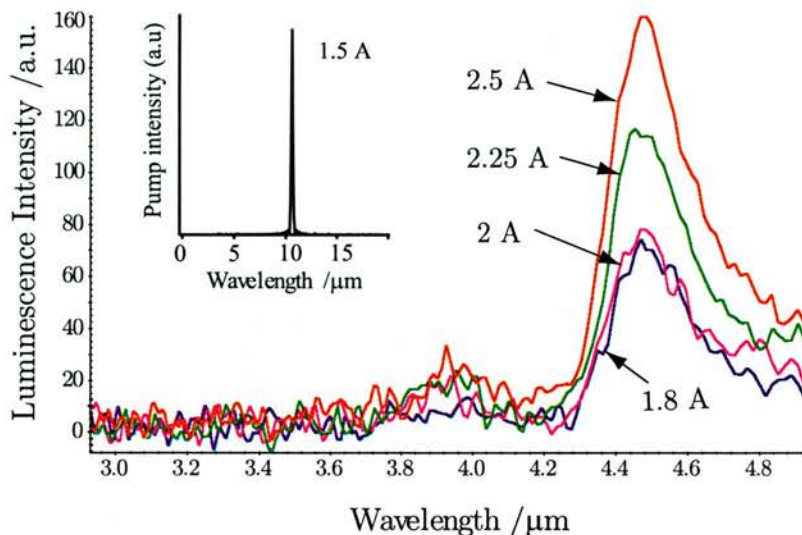


Figure 5.14: Short wavelength emission spectra of D2924A1 (bottom) above threshold. The main peak at $4.5 \mu\text{m}$ is attributed to stimulated Anti-Stokes emission. The inset shows the pump spectrum measured at $\sim 90 \text{ K}$ for a peak current of 1.5 A.

	Peak Amplitude /a.u.	Center Energy /meV	FWHM /meV
1.8 A	76	276	12
2 A	82	277	12
2.25 A	122	278	10
2.5 A	167	277	12

Table 5.3: Amplitude, center energy and FWHM of the peak in the spectra of figure 5.14 as obtained from a Lorentzian fit. Due to the peak's asymmetry, only the half corresponding to higher energies was considered.

The main feature in the measured emission spectra is an asymmetric peak at approximately $4.5 \mu\text{m}$ wavelength (276 meV). The peak's high energy side was fitted to a Lorentzian curve, and the results are displayed in table 5.3.

This peak can be attributed to Anti-Stokes Raman Scattering. Since the pump photon energy is $\hbar\omega_p = 118 \text{ meV}$ and $\delta E_{32} \approx 155 \text{ meV}$, as estimated from the long wavelength luminescence spectra in figure 5.11, we would expect $\lambda_a = 4.5 \mu\text{m}$.

In the nonlinear region of D2924 several transitions from state 4 to lower energy states other than 2 present large optical dipole matrix elements (figure 5.12). As a result, it is possible to have Anti-Stokes emission at various wavelengths. This is the case of level b, 145 meV below level 3 by design, which would give Anti-Stokes emission at around $4.7 \mu\text{m}$, thus explaining the main peak's asymmetry. On the other hand, the small peak observed at approximately $3.9 \mu\text{m}$ (318 meV) can be explained by Anti-Stokes emission

	Peak 1	Peak 2	Peak 3
3.0 A	47/ 129 /17	16/ 164 /28	41/ 188 /21
3.6 A	87/ 129 /14	29/ 170 /33	52/ 190 /16
4.0 A	132/ 129 /14	45/ 169 /29	81/ 190 /17

Table 5.4: Values of a/c/w obtained fitting the spectra of figure 5.15 to three lorentzian curves. The peak amplitude (a) is given in arbitrary units, while the energy at the maximum (c) and FWHM (w) are both expressed in meV.

involving the pair of anticrossed states labelled as 1 (found to be approximately 183 meV below state 3 in luminescence measurements below threshold).

Electrons in state 3 can be excited by the pump light into the level 4 and then decay spontaneously to the lower state (2), emitting a photon of energy δE_{42} . However, in this case, we are pumping the nonlinear region well below resonance, with a detuning of $\Delta = \hbar\omega_p - \delta E_{43} = (118 - 137)\text{ meV} = -19\text{ meV}$, which makes the real transfer of electrons to state 4 less likely. Consequently, the spectra in figure 5.14 show no trace of such incoherent upconversion, i.e., no emission is observed at $\lambda = 4.2\ \mu\text{m}$ (corresponding to $\delta E_{42} \approx 137\text{ meV} + 155\text{ meV}$).

5.3.2 Wafers D3008 and D3036

The first sample processed at Princeton University was D3008A1, consisting of deep-etched mesas, not waveguides, a few hundred microns in diameter. Metal contacts were evaporated on top of the mesas. The sample was then cleaved to obtain maximum light output and two of the mesas were bonded in the usual fashion.

Samples processed as mesas are very well suited for luminescence measurements. We measured the spectra of the light emitted by D3008A1(bottom) for a range of currents with the sample cooled to liquid nitrogen temperatures. The results are displayed in figure 5.15.

The main feature in figure 5.15 is a peak centered at around 129 meV . For higher photon energies, emission corresponding to different transitions overlap and distinguishing individual contributions becomes difficult. However, experimental data fit very well to a set of lorentzian curves, labelled from 1 to 3 in figure 5.15. The results of the fitting are detailed in table 5.4.

While the peak centered at 129 meV is due to the emission of pump photons (120

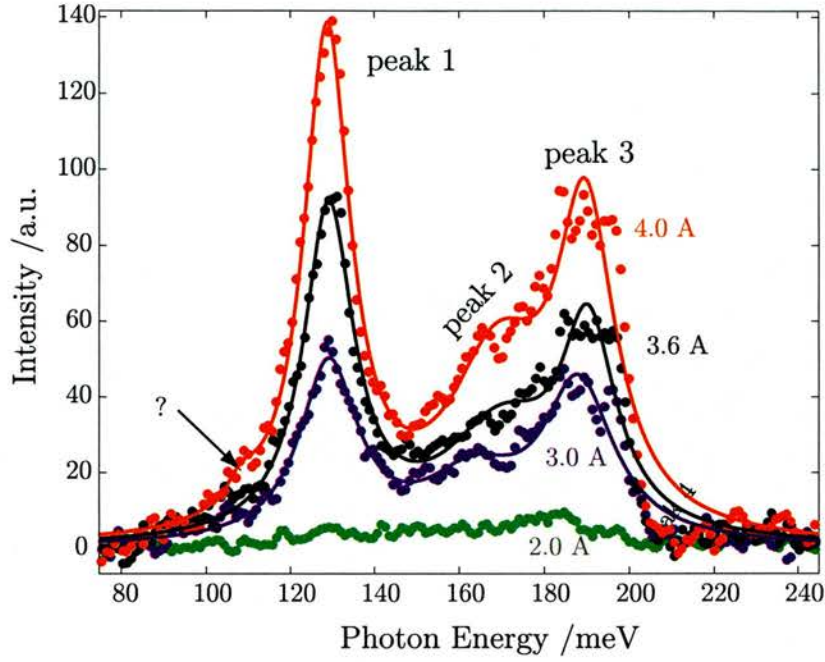


Figure 5.15: Emission spectra of D3008A1(bottom) measured at liquid nitrogen temperatures for a range of peak currents.

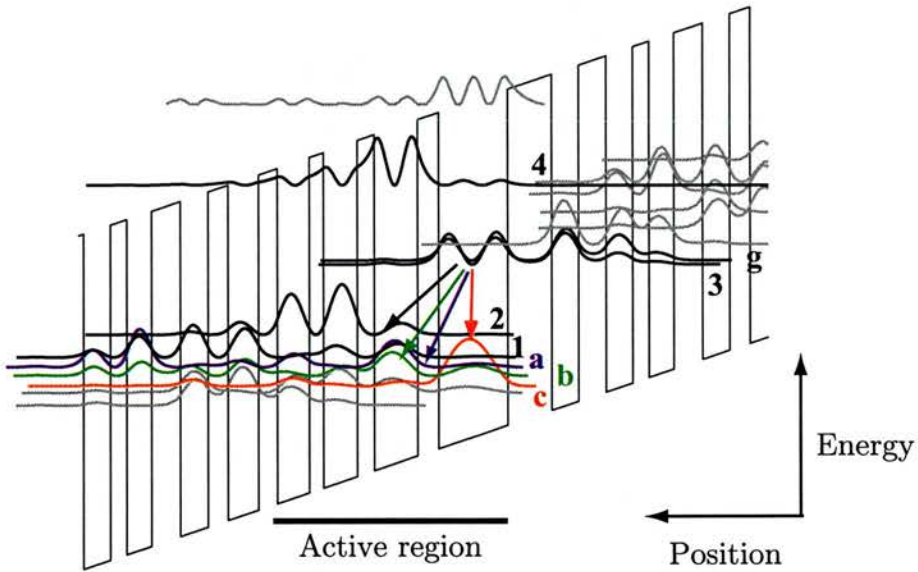


Figure 5.16: Sketch of one period of the nonlinear stack in wafer D3008. The transitions contributing to the measured spontaneous emission are highlighted.

meV by design), the light detected with higher photon energies originates in the nonlinear stack when electrons decay spontaneously from state 3 (see figure 5.16). This way, photons with energy 164 meV are emitted in the transition 3-a (by design, $z_{3a} = 0.6 \text{ nm}$, and the photon energy is estimated to be 160 meV and the optical dipole matrix element 0.6 nm).

Across the 180-200 meV range, all three fitted spectra are remarkably flat, indicating the presence of at least two nearby peaks. However, these contributions cannot be resolved accurately and were thus fitted to a single peak, labelled as 3. This peak, centered at around 190 meV, can be attributed to transitions from state 3-b and 3-c (with energies 173 and 189 meV by design, and optical dipole matrix elements 0.7 and 1.1 nm, respectively).

In figure 5.15, the spectrum measured for a current of 4 A reveals a small peak almost masked by the pump emission. A lorentzian fit estimates the peak center energy to be 109 meV with a FWHM of 9 meV, matching the predicted energy separation of 108 meV between levels 3 and 2.

Following these preliminary measurements on D3008A1, different samples of wafers D3008 and D3036 were processed by etching deep-ridge waveguides, thus providing optical confinement for the laser modes. Some of these devices did not lase and only spectral measurements below threshold were carried out, yielding similar results to those obtained with D3008A1.

Laser D3008A3a(bottom) presented good voltage and light output power versus current characteristics, measured at liquid nitrogen temperatures. The voltage-current curve in figure 5.17 indicates that approximately 0.5 A are being lost due to current leakage, therefore increasing the pump laser threshold ($\approx 2.6 A$). The light output versus current curve presents an abrupt slope change at around 4 A, whose origin will be discussed in detail later.

The emission spectra of D3008A3a(bottom) above threshold was measured 3, 4 and 5 A electrical bias using the MCT detector, as displayed in figure 5.18. These measurements were taken in pulsed mode (100 ns current pulses) at heat sink temperatures $\sim 77 K$.

Figure 5.18 shows that pump photons are emitted with an energy of $\sim 132 meV$. The peak centered at exactly twice that energy, observed in all three spectra, is a spurious nonlinear electrical signal often originated in the detector electronics due to the high optical power of the pump and saturation of the detector.

Unexpectedly, the spectrum measured at 5 A reveals lasing with around 200 meV photon energy, thus explaining the change in slope of the light output versus current curve in figure 5.17. Lasing occurs in the nonlinear stack between states 3 and $|c\rangle$ ($\delta E_{3c} = 189 meV$ according to design, see figure 5.16), due to the high population of the former

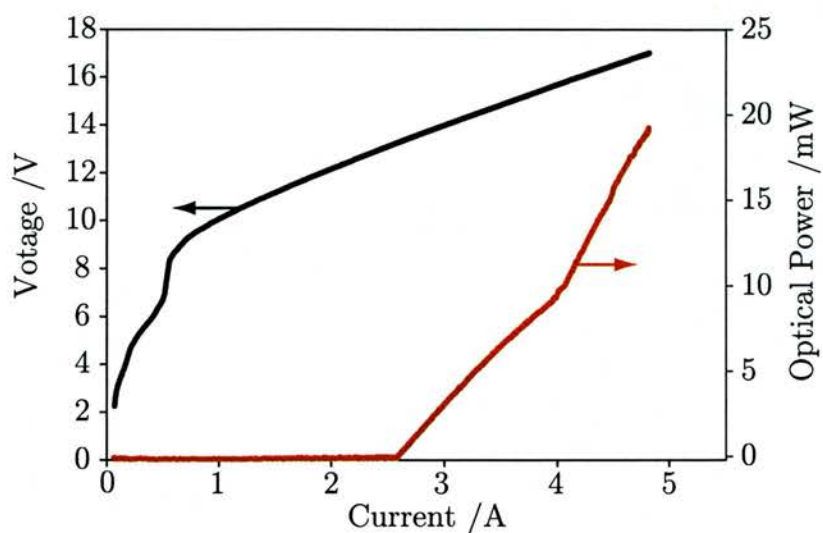


Figure 5.17: Voltage (black curve) and light output (red curve) versus current characteristics of D3008A3a(bottom) measured at liquid nitrogen temperatures.

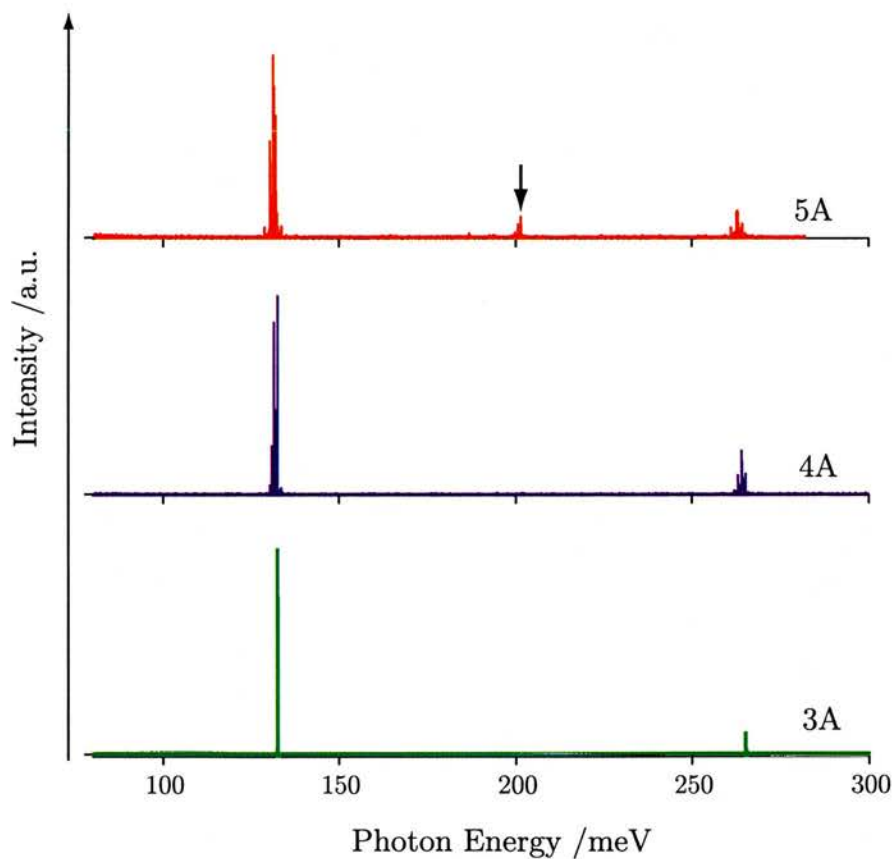


Figure 5.18: Emission spectra of laser D3008A3a(bottom) measured for 3, 4, and 5 A peak currents. The black arrow indicates an extra laser line observed at 5 A electrical bias.

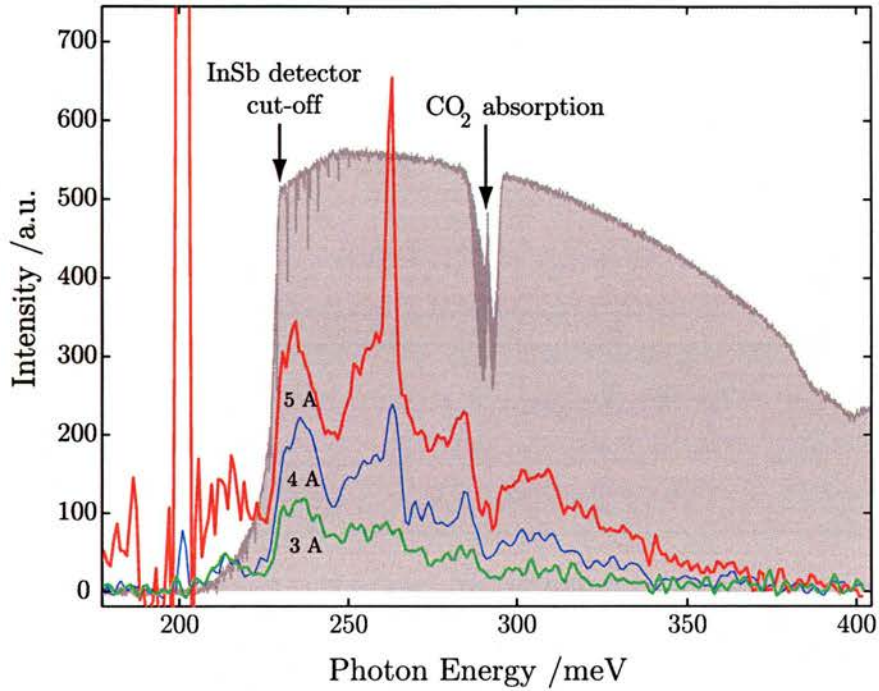


Figure 5.19: Emission spectra of laser D3008A3a(bottom) measured for 3 4 and 5 A peak currents. These measurements were taken at liquid nitrogen temperatures in pulsed mode (100 ns pulse duration) using a cooled InSb detector. The spectrum of the broad IR source in the Nicolet 860 was also measured to illustrate the InSb detector's cut-off and is plotted as a grey shaded area.

and the large optical dipole matrix element of the transition (1.0 nm).

Spectral measurements were carried out with D3008A3a(bottom) above threshold using a cooled InSb detector (see figure 5.19). The spectrum of the broad IR source in the Nicolet 860 was also measured to show the cut-off of the InSb detector and is plotted as a grey shaded area.

Figure 5.19 shows that emission increases as current is ramped up. The curves corresponding to 4 and 5 A reveal two peaks centered at approximately 235 and 255 meV. Although below the InSb detector cut-off, the spectrum measured for 5 A shows the lasing with 200 meV photon energy previously discussed, due to the large optical power emitted.

In this case, the AS Raman photon energy is expected to be approximately 241 meV ($\lambda_{AS} = 4.7 \mu m$), since $h\nu_p = 132 meV$ and $\delta E_{32} \approx 109 meV$ -from previous luminescence measurements with D3008A1 (see figure 5.15)-. Therefore, the peak at 255 meV can be attributed to AS Raman emission within a 6% error.

Note that the pump photon energy, 132 meV, is 12 meV (10%) larger than designed for. As a result, pumping is detuned above resonance with the transition 4-3 and electrons

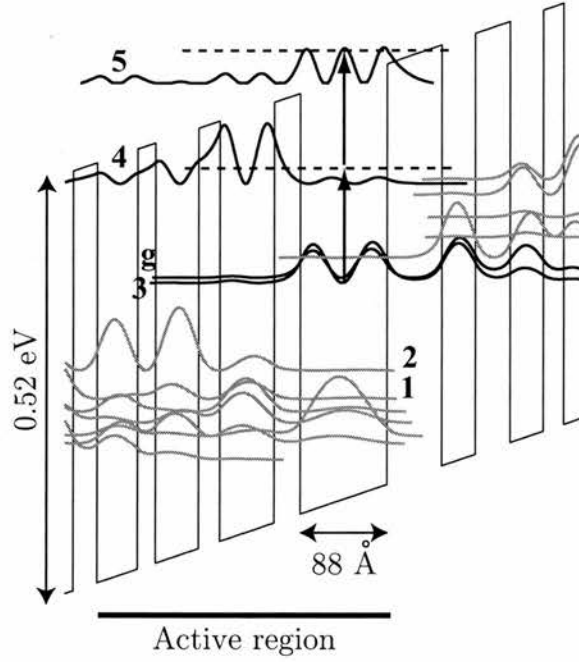


Figure 5.20: Conduction band diagram of the active region in a period of the nonlinear stack of D3008.

can be excited by pump photons directly into the upper level (4) and decay spontaneously into level 2. This incoherent upconversion process is the cause for the peak observed at 235 meV ($\delta E_{42} = 231 \text{ meV}$ by design), also taking into account the sharp cut-off ($\sim 230 \text{ meV}$) of the InSb detector used in these measurements.

The spectrum corresponding to an injected peak current of 5 A also reveals a spike at exactly twice the pump photon energy. This cannot be explained by a spurious nonlinear electrical signal, since the pump photon energy is well below the cut-off of the InSb detector and does not appear in the measured spectra. We believe that this peak can be attributed to second harmonic generation in the nonlinear stack involving a triplet of states localised mostly in the widest well of the active region (see figure 5.20). According to design $\delta E_{54} = 110 \text{ meV}$, $\delta E_{43} = 123 \text{ meV}$ with the optical dipole matrix elements $z_{54} = 1.2 \text{ nm}$, $z_{43} = 1.3 \text{ nm}$ and $z_{53} = 0.6 \text{ nm}$.

5.3.3 Wafers D3015 and D3037

The first lasers processed out of D3015 and D3037 showed anomalous voltage versus current characteristics behavior because the oxide had not been completely etched away of the top of the ridge. After introducing changes in the processing, sample D3015D2a was

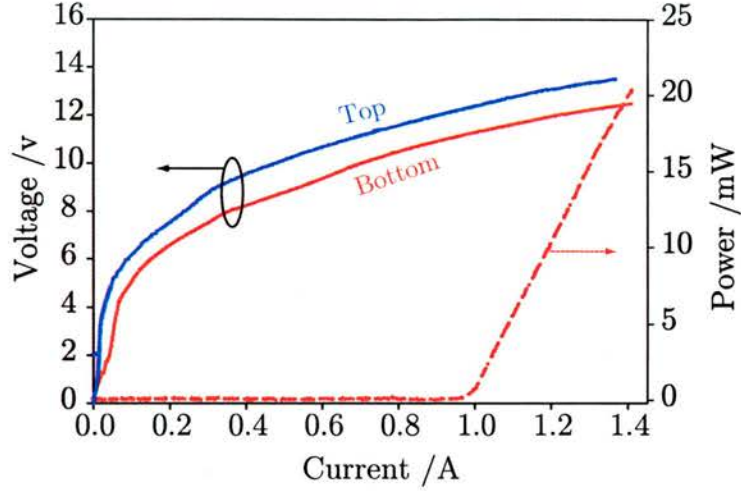


Figure 5.21: IVL characteristics of sample D3015D2a. The voltage (solid) and optical power (dashed) versus current for the bottom laser are plotted in red. The blue line is the Voltage-Current curve of the top laser.

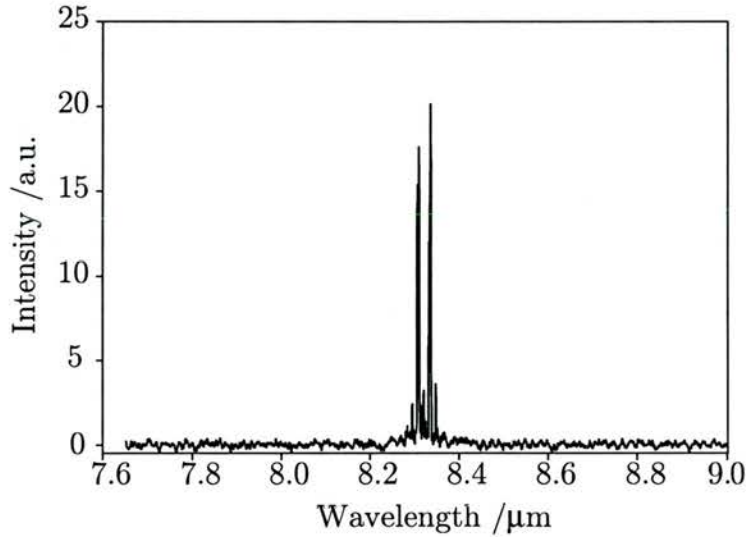


Figure 5.22: Fast-scan spectrum of D3015D2a(bottom) showing the pump lasing wavelength at $8.3 \mu\text{m}$ (150 meV). This measurement was carried out at 90K with the MCT detector, injecting pulses with 2 A peak current and 100 ns duration.

found to present good light output and voltage versus current characteristics at heat sink temperatures $\sim 77 \text{ K}$, as depicted in figure 5.21.

The pump in D3015D2a(bottom) reached laser threshold at a peak current of 1 A , emitting at $\lambda \approx 8.3 \mu\text{m}$ (150 meV), as measured at cryogenic temperatures (see figure 5.22). Note that this pump photon energy is approximately 9% larger than designed for (137 meV).

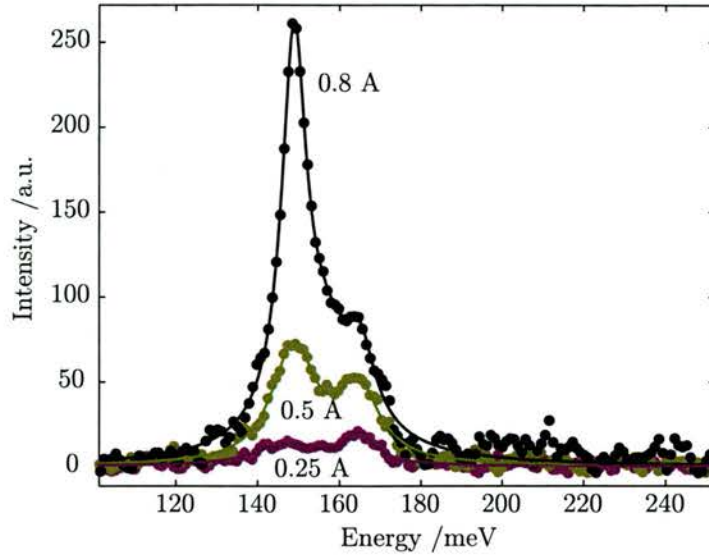


Figure 5.23: Emission spectra of D3015D2a(bottom) below threshold.

The emission of D3015D2a(bottom) below threshold was also measured. Step-scans using the MCT detector were carried out for 0.25, 0.5 and 0.8 A and the results are shown in figure 5.23. The solid lines in this figure show the fitting of the data. In the spectra measured at 0.25 and 0.5 A electrical bias, only two peaks can be distinguished (at 149 meV and 165 meV). Of these, the former clearly corresponds to the pump laser transition. Photons emitted with 165 meV can be attributed to the spontaneous decay of electrons to the state immediately below the lower lasing level in the pump region. Note that no luminescence originated in the nonlinear region is observed in the spectra, probably due to the low peak currents used in the measurement.

The shape of the 0.8 A spectrum hints a third peak in between the two previously reported. The spectrum was thus fitted to three Lorentzian curves and the extra peak was found at 156 meV, although the signal is too weak to be conclusive.

The top device in sample D3015D2a, whose voltage-current characteristics are displayed in figure 5.21 with a blue curve, did not lase. However, it proved very useful for measuring the emission spectra below threshold, since the spontaneous emission was not masked by the pump laser light when injecting large currents. These spectra are shown in figure 5.24.

The most prominent feature in figure 5.24 is due to the spontaneous emission of pump photons with 150 meV energy, and is consistent with the luminescence observed for the

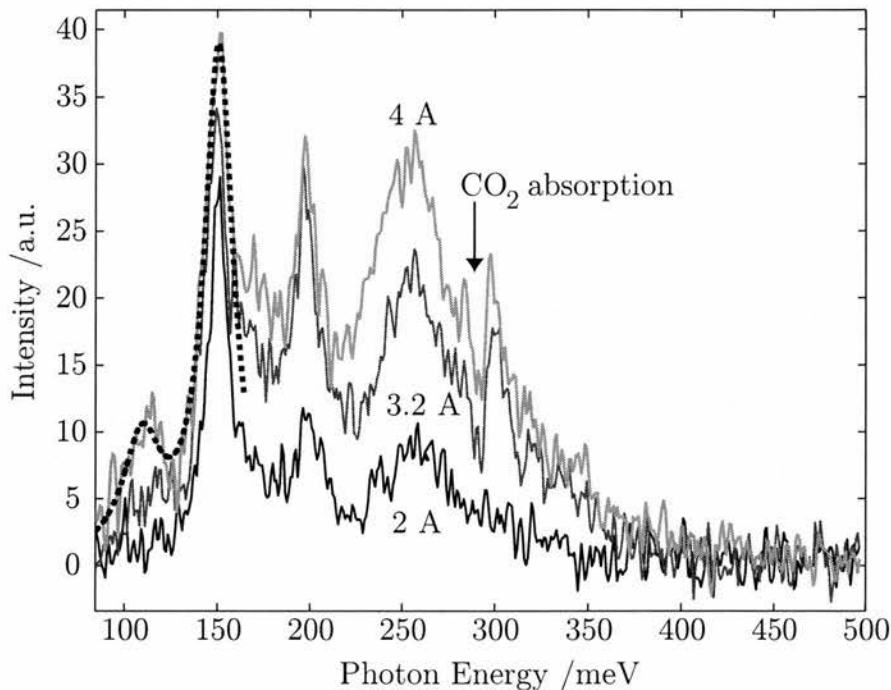


Figure 5.24: Emission spectra of D3015D2a(top) measured at 85 K for 2, 3.2 and 4 A. The dashed line shows a Lorentzian fit for the 4 A data, cropped above 160 meV.

bottom laser, analysed previously. Note, however, that no significant increase of the peak amplitude or narrowing occurs as the current is ramped up.

The spectrum measured with 4 A reveals an small peak at 110 meV, according to a Lorentzian fit (dashed line). Such emission can only be attributed the transition 3-2 in the nonlinear region (with an estimated energy of 88 meV, according to design). The energy of this transition strongly depends on the applied field, since the states involved are localised in different wells. Therefore, the difference between the measured photon energy and our expectations, layer thickness fluctuations during growth aside, is most likely due to the applied field being larger than the 45 kV.cm^{-1} originally used in our design.

A rough estimate of the electrical field can be obtained using the voltage versus current characteristics displayed in figure 5.21. With D3015D2a(top), a voltage of 13.5 V was measured for the highest current available at the time, 1.4 A. Assuming an uniform field across both the nonlinear and pump regions, and a voltage drop of 0.5 V in the contacts, we obtain

$$E = \frac{(13.5 - 0.5) \times 10^{-3} \text{ kV}}{(20 \times 637 \text{ \AA} + 26 \times 470 \text{ \AA}) \times 10^{-8} \text{ cm.}\text{\AA}^{-1}} = 50 \text{ kV.cm}^{-1}, \quad (5.25)$$

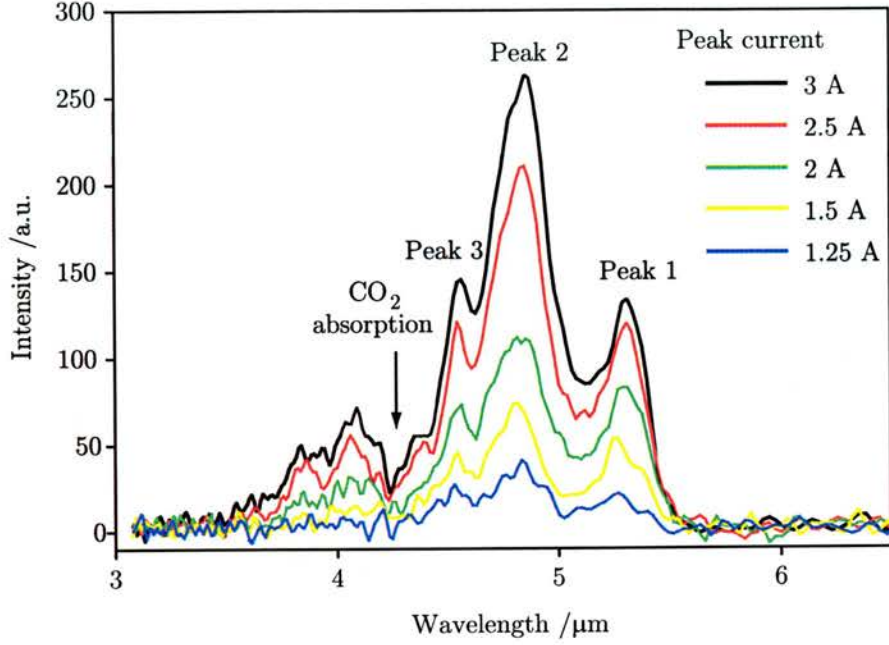


Figure 5.25: Short wavelength emission spectra of D3015D2a(bottom) for a range of peak currents. These measurements were carried out in pulsed current mode at liquid nitrogen temperatures using a cooled InSb detector.

which is correct for the nonlinear region, but higher than intended for the pump. On the other hand, the spectra in figure 5.24 were measured for currents larger than 1.4 A, and the applied fields are probably higher.

Back in figure 5.24, we see a peak at 200 meV and broad emission centered around 260 meV. This luminescence was not observed in measurements with D3015D2a(bottom) and such high energy photons cannot be originated in the nonlinear region. To check this, a wafer comprising only periods of the nonlinear structure was ordered and luminescence measurements will soon be carried out by D. Wasserman. Although at this point this phenomenon is not fully understood, we believe that, with large applied fields, electrons tunnel from the injector into the states above the pump upper laser level and decay spontaneously into lower-laying energy levels.

Using a cooled InSb detector we measured the emission spectra of D3015D2a (bottom) at liquid nitrogen temperatures (77 K) (see figure 5.25). The results of fitting the peaks in these spectra to lorentzian curves are shown in table 5.5.

In figure 5.25, the main peak at $4.8 \mu m$ can be attributed to stimulated AS Raman scattering ($h\nu_p = 150 meV$ and $\delta E_{32} = 110 meV$ -from luminescence measurements below

	Peak 1	Peak 2	Peak 3
1.25 A	18/ 236 /7	35/ 257 /13	18/ 274 /12
1.5 A	47/ 235 /8	67/ 258 /12	29/ 274 /16
2 A	76/ 234 /8	108/ 257 /17	43/ 274 /11
2.5 A	104/ 234 /7	201/ 257 /15	71/ 273 /13
3 A	112/ 234 /6	254/ 256 /16	89/ 273 /12

Table 5.5: Values of $a/c/w$ obtained fitting the spectra of figure 5.25 to three lorentzian curves. The peak amplitude (a) is given in arbitrary units, while the energy at the maximum (c) and FWHM (w) are both expressed in milli-electronvolts.

threshold-, giving an expected $\lambda_a = 4.7 \mu m$). Pumping in sample D3015 is taking place above resonance, and electrons in level 3 excited by the pump photons can easily scatter into subband 4, and decay spontaneously into level 2. Such incoherent up-conversion process is the cause of the peak observed at $5.3 \mu m$ (235 meV), which is truncated by the wavelength cut-off at $\sim 5.4 \mu m$ of the InSb detector. This measured photon energy of 235 meV is larger than expected by design ($\delta E_{42} = 225 meV$). The detuning, obtained from the shift between the lines corresponding to AS Raman scattering and incoherent up-conversion, is $\Delta = 258 meV - 235 meV = +23 meV$.

5.3.4 Wafer D3018

D3018 was the last wafer to be grown during my stay at Princeton, and only preliminary results are available at this time. Sample D3018E3 was processed by etching mesas (a few hundred micrometer in diameter), well suited for luminescence measurements, instead of waveguides. Metal contacts were evaporated on top of the mesas. The sample was then cleaved to obtain maximum light output and two of the mesas were bonded in the usual fashion.

The emission from sample D3018E3 was measured for a range of peak currents, using the MCT detector cooled with liquid nitrogen. As both top and bottom mesas yielded analogous results, only the data corresponding to D3018E3(bottom) are displayed in figure 5.26.

The spectra in figure 5.26 show that most of the light is emitted with photon energies below 200 meV. Beyond that, only broad emission centered around 250 meV is detected. The latter is very similar, if much less pronounced, to that observed with D3015D2a (see figure 5.24). Designs III and IV differ only slightly in the design of the pump. There-

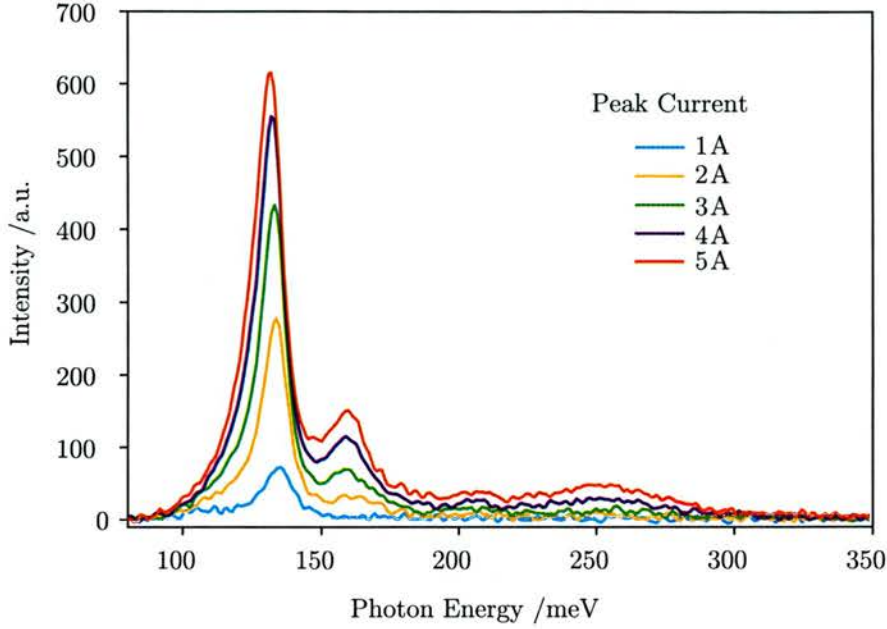


Figure 5.26: Emission spectra of D3018E3(bottom) for a range of peak currents. These measurements were carried out at 82 K using a cooled MCT detector.

	Peak 1	Peak 2	Peak 3
2 A	36/ 123 /22	263/ 133 /10	23/ 164 /15
3 A	79/ 125 /20	396/ 133 /9	49/ 162 /20
4 A	148/ 125 /16	477/ 132 /9	94/ 161 /17
5 A	220/ 126 /16	476/ 132 /9	125/ 160 /18

Table 5.6: Values of a/c/w obtained fitting the spectra of figure 5.26 below 180 meV to three lorentzian curves. The peak amplitude (a) is given in arbitrary units, while the energy at the maximum (c) and FWHM (w) are both expressed in milli-electronvolts.

fore, we believe the origin of this high energy photons to be the same, namely, electrons scattering from the injector into states above the pump’s upper laser level and decaying spontaneously.

A closer examination of the emission spectra, as displayed in figure 5.27(a), reveals two peaks centered at around 130 meV and 160 meV. The asymmetry of the largest peak suggests that it is formed by the contribution of two different transitions. Figure 5.27(b) shows the fitting of the spectrum measured at 5 A electrical bias to a set of two (blue line) and three (red line) Lorentzian functions. Note that the third peak at approximately 126 meV explains the observed asymmetry, while just two Lorentzian curves do not give a satisfactory fit of the experimental data. The other spectra were fitted in a similar fashion, as shown by the solid lines in figure 5.27(a), and the results are summarised in table 5.6.

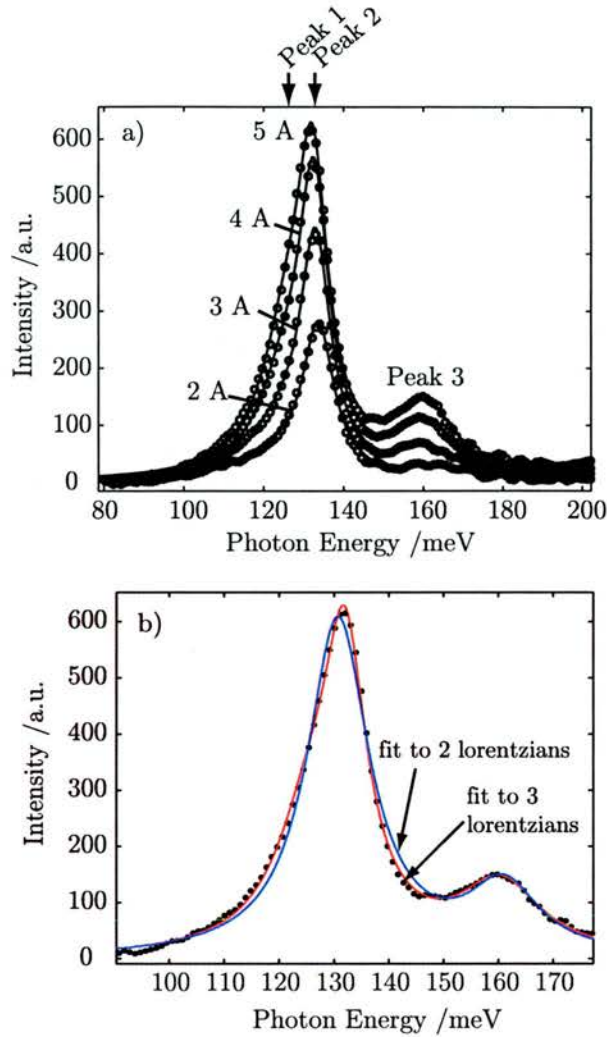


Figure 5.27: (a) Emission spectra of D3018E3 (bottom) measured at different electrical biases with the sample cooled to ~ 82 K. The solid lines show the fitting of the data to three Lorentzian peaks. (b) Spectrum measured at 5 A peak current (black dots), illustrating the difference between the fittings to 2 (blue line) and 3 (red line) Lorentzian functions. Note that peak 1 centered at ≈ 126 meV, attributed to the transition 3-1 in the nonlinear region (see figure 5.6(a)), explains the observed asymmetry, while just two Lorentzian curves do not give a satisfactory fit of the experimental data.

Photons emitted in the nonlinear region have small energies. Peak 1 can be attributed to the decay of electrons from state 3 to the state immediately below 2 in the nonlinear region (the energy associated with this transition is 124 meV by design with an estimated optical dipole matrix element of 0.8 nm).

The peak centered around 133 meV is due to the pump photons (designed for 115 meV). The small FWHM (9 meV) is most likely due to the difficulty of fitting such two nearby peaks (1 and 2), and must therefore be taken with reserve. Peak 3 can be attributed to the spontaneous decay of electrons from the pump's upper laser state into the state just

below L (137 meV according to design, with an estimated optical dipole matrix element of 1.0 nm).

5.4 Comparative analysis

In the previous section, we have presented experimental evidence of electronic stimulated Anti-Stokes Raman emission in QC laser samples of three different designs. However, in all cases, no narrowing of the AS emission peak, which would indicate AS Raman gain in our samples, has been observed so far.

In lasers from wafer D2924 (design I), the pump photon energy is well below resonance with the transition 4-3 in the nonlinear stack ($\Delta = -20 \text{ meV}$) and AS Raman light is emitted at $4.5 \mu\text{m}$ wavelength, in good agreement with the predictions. However, Raman lasing was not accomplished due to both the low pump power and large detuning from resonance.

In both designs II (wafers D3008 and D3036) and III (wafers D3015 and D3037), the pump wavelength was tailored to be quasi-resonant with the 4-3 transition and thus enhance the Raman nonlinearity. AS Raman emission was observed in samples from wafers D3008 and D3015. However, in both cases, spectral measurements showed that pumping was taking place above resonance. In these circumstances, electrons in level 3 excited by the pump photons can easily scatter into subband 4, and decay spontaneously into level 2. This incoherent upconversion process, observed in samples of both designs II and III, reduces the available population inversion. The latter, combined with the low optical power densities of the pump (below 100 mW) rendered the nonlinear gain insufficient to overcome the losses.

A fourth design was developed (wafer D3018), keeping the nonlinear stack of design III but modifying the pump region to achieve negative detuning. Preliminary emission spectra show the pump photon energy to be larger than designed for, but still below resonance with the 4-3 transition.

Taking into consideration the research undertaken to date, some suggestions for improvement can be made. We believe that, by virtue of an optimised detuning (2-3 linewidths below resonance), the Raman nonlinearity would be enhanced, keeping the

linear absorption of the pump light low. Additionally, an increase in the pump power can be accomplished via improved active region design and/or by coating the laser facets to maximise the reflectivity at the pump wavelength. Further work in these lines should lead to achieving electronic Anti-Stokes Raman lasing.

5.5 Summary

In this chapter, the first observation of Anti-Stokes Raman emission in a Quantum Cascade laser is reported. This work was carried out during a nine month stay as a visiting student at Princeton University.

First, we have addressed the topic of nonlinear light generation as a means to spread the wavelength range available with QC lasers. In this context, regarding the enormous potential of the integration of optical nonlinearities in these devices, stimulated Raman scattering was introduced as the subject of this research.

Following preliminary work by C. Gmachl at Bell Labs (design I), three different designs of active regions to achieve AS Raman lasing were developed as a part of my work. In all four, the pump laser is monolithically integrated with the Anti-Stokes nonlinear region in a 2-stack active waveguide core. Key issues to mid-IR waveguides, such as free carrier absorption, have also been addressed and thoroughly discussed.

Stimulated electronic AS Raman emission has been observed in separate samples utilising distinct nonlinear (and pump laser) active region designs. This is the first step towards AS Raman lasing, which holds promise to extend straightforward operation of unstrained InP QC lasers to wavelengths below $4\mu m$. The frequency shifts between AS Raman and pump photons were measured to be over 100 meV, significantly larger than those reported with intersubband Stokes Raman lasers. In addition, some samples in which the nonlinear region is pumped very close or above resonance of the 4-3 transition (D3008 and D3015) were found to emit light via incoherent upconversion processes. At this time, only preliminary emission measurements below threshold are available with samples of wafer D3018 (Design IV).

In our measurements, no narrowing of the AS emission peak, which would indicate AS Raman gain in our samples, has been observed so far. However, we believe that further

optimisation of the nonlinear region, especially in the light of an optimised (smaller) detuning Δ , and an increase in the pump power should lead to achieving electronic Anti-Stokes Raman lasing.

References for Chapter 5

- [1] M Rochat, J Faist, M Beck, U Oesterle, and M Ilegems. Far-infrared ($\lambda = 88 \mu\text{m}$) electroluminescence in a quantum cascade structure. *App. Phys. Lett.*, 73(25):3724–3726, 1998.
- [2] C Gmachl, H M Ng, S N G Chu, and A Y Cho. Intersubband absorption at $\lambda \sim 1.55 \mu\text{m}$ in well- and modulation-doped GaN/AlGaIn multiple quantum wells with superlattice barriers. *App. Phys. Lett.*, 77(23):3722–3724, 2000.
- [3] C Becker, I Prevot, X Marcadet, B Vinter, and C Sirtori. InAs/AlSb quantum-cascade light-emitting devices in the $35 \mu\text{m}$ wavelength region. *App. Phys. Lett.*, 78:1029–1031, 2001.
- [4] M K Gurnick and T A DeTemple. Synthetic nonlinear semiconductors. *IEEE J. Quantum Electron.*, 19(5):791–794, 1983.
- [5] M M Fejer, S J B Yoo, R L Byer, A Harwit, and J S Harris. Observation of extremely large quadratic susceptibility at $9.6 - 10.8 \mu\text{m}$ in electric-field-biased AlGaAs quantum wells. *Phys. Rev. Lett.*, 62(9):1041–1044, 1989.
- [6] E Rosencher, A Fiore, B Vinter, V Berger, Ph Bois, and J Nagle. Quantum Engineering of Optical Nonlinearities. *Science*, 271:168–173, 1996.
- [7] R W Boyd. *Nonlinear Optics*. Academic Press, New York, 1992.
- [8] A Belyanin, F Capasso, V V Kocharovskiy, VI V Kocharovskiy, and M O Scully. Infrared generation in low-dimensional semiconductor heterostructures via quantum coherence. *Phys. Rev. A*, 63(053803), 2001.
- [9] N Owschimikow, C Gmachl, A Belyanin, V Kocharovskiy, D L Sivco, R Colombelli, F Capasso, and A Y Cho. Resonant second-order nonlinear optical processes in quantum cascade lasers. *Phys. Rev. Lett.*, 90(4):043902, 2003.
- [10] O Malis, A Belyanin, C Gmachl, D L Sivco, M L Peabody, A M Sergent, and A Y Cho. Improvement of second-harmonic generation in quantum-cascade lasers with true phase matching. *App. Phys. Lett.*, 84(15):2721–2723, 2004.
- [11] T S Mosely, A Belyanin, C Gmachl, D L Sivco, M L Peabody, and A Y Cho. Third harmonic generation in a Quantum Cascade laser with monolithically integrated resonant optical nonlinearity. *Opt. Express*, 12(13):2972–2976, 2004.
- [12] Y R Shen. *The Principles of Nonlinear Optics*. Wiley, New York, 1984.
- [13] E J Woodbury and W K Ng. Ruby laser operation in the near ir. In *I.R.E. Proceedings*, volume 500, page 2367, 1962.
- [14] H Rong, R Jones, A Liu, O Cohen, D Hak, A Fang, and M Paniccia. A continuous-wave Raman silicon laser. *Nature*, 433:725–728, 2005.
- [15] J B Khurgin, G Sun, L R Friedman, and R A Soref. Comparative analysis of optically pumped intersubband lasers and intersubband Raman oscillators. *J. App. Phys.*, 78(12):7398–7400, 1995.
- [16] H C Liu, I W Cheung, A J SpringThorpe, C Dharma-wardana, Z R Wasilewski, D J Lockwood, and G C Aers. Intersubband Raman laser. *App. Phys. Lett.*, 78(23):3580–3582, 2001.
- [17] H C Liu, C Y Song, Z R Wasilewski, A J SpringThorpe, J C Cao, C Dharma-wardana, G C Aers, D J Lockwood, and J A Gupta. Coupled electron-phonon modes in optically pumped resonant intersubband lasers. *Phys. Rev. Lett.*, 90(7), 2003.
- [18] M Troccoli, A Belyanin, F Capasso E Cubukcu, D L Sivco, and A Cho. Raman Injection Laser. *Nature*, 433:845–848, 2005.
- [19] A Belyanin. Private communication. Texas A&M University, College Station, TX, 2003.
- [20] O Kocharovskaya, Y V Rostovtsev, and A Imamoglu. Inversionless amplification in the three-level atoms with and without a hidden inversion in reservoir. *Phys. Rev. A*, 58(1):649–654.

- [21] J T Verdeyen. *Laser Electronics*. Prentice Hall, Cambridge, 1st edition, 1995.
- [22] A Yariv. *Quantum Electronics*. Wiley, New York, 3rd edition, 1989.
- [23] G Scamarcio, F Capasso, C Sirtori, J Faist, A L Hutchinson, D L Sivco, and A Y Cho. High-power infrared (8-micrometer wavelength) superlattice lasers. *Science*, 276:773–776, 1997.
- [24] E Rosencher and B Vinter. *Optoelectronics*. Cambridge University Press, Cambridge, 1st edition, 2002.
- [25] C Sirtori, F Capasso an J Faist, A L Hutchinson, D L Sivco, and A Y Cho. Resonant tunneling in quantum cascade lasers. *IEEE J. Quantum Electron.*, 34(9):1722–1729, 1998.
- [26] P Y Yu and M Cardona. *Fundamentals of Semiconductors*. Springer, 2nd edition, 1999.
- [27] C Sirtori, J Faist, F Capasso, D L Sivco, A L Hutchinson, and A Y Cho. Quantum cascade laser with plasmon-enhanced waveguide operating at 8.4 μm wavelength. *Appl. Phys. Lett.*, 66(24):3242–3244, 1995.

Chapter 6

Summary and Conclusions

6.1 Summary of thesis

Over the past decades, the field of optoelectronics has undergone remarkable progress. This has been in part fuelled by the needs of lightwave communications, novel optical sources or all-optical alternatives for switching and logic applications. Amongst the plethora of existing optoelectronic devices, the work presented in this thesis focuses on two particular examples, namely, semiconductor optical amplifiers and Quantum Cascade lasers. The former have become promising candidates for all-optical switching, while QC lasers are appealing compact high-power optical sources for applications in the mid- to far-IR wavelength range, such as trace gas sensing. **Chapter 1** introduces the motivations for our work in the context of the present challenges and research trends.

The operation of both SOAs and QC lasers is dictated by the way in which light interacts with electrons and the carrier dynamics. The gain/refractive index experienced by subpicosecond pulses propagating across a SOA is determined by the complex interplay between interband transitions and intraband processes. In QC lasers, however, the relevant intersubband dynamics and carrier transport are dominated almost solely by the LO-phonon scattering. These and other fundamental concepts of semiconductor physics are covered in **chapter 2** and serve as the base on which present and analyse our experimental work.

Chapter 3 brings together the relevant information concerning the structure of the

devices subject of our study and practical issues (mounting of the samples, temperature control, etc.). The different experimental techniques and set-ups employed in the course of our work are also detailed here.

Chapter 4 studies the implications of the SOA ultrafast carrier dynamics in interferometric switching applications using subpicosecond optical pulses. This was done experimentally by means of the pump-probe technique and a simple sliced propagation rate equation model was developed to explore the result. First, we present the results of interferometric three-beam pump-probe experiments on a SOA using a TOAD-like configuration and pulses with duration ~ 700 fs. This arrangement allows to time-resolve the complex refractive index dynamics occurring during optical switching.

By fully mapping out the switching windows we observe that

- The top of the switching windows is not flat, following the slow recovery of the refractive index change associated with the band-filling nonlinearity.
- A pedestal is observed on one side of the switching windows, increasing in amplitude for wider windows. This is caused by the mismatch in phase and gain between the two probes when they arrive at the SOA after the pump, which slowly tends to zero. This mismatch is larger for wider windows, as both the gain and refractive index experienced by the co-propagating probe have more time to recover.
- One of the edges of the switching windows is much less sharp, corresponding to twice the transit time across the amplifier. This is a common feature of those configurations in which the control and data pulses propagate in opposite directions.

Measurements with higher temporal resolution focusing on the onset of all-optical switching reveal that

- An ultrafast feature (~ 2 ps) can be distinguished on the edge of the switching windows, evolving from a spike to become a dip as the pump pulse energy is increased in the 10-530 fJ range. The nature and time scale of this feature point at carrier heating as responsible, consistent with previous co-propagating pump-probe measurements carried out under similar conditions on the same amplifier.

- Carrier heating was found to influence significantly the shape of the switching window edge, and a more pronounced effect is to be expected for shorter pulses (possibly together with spectral hole burning, not resolved in our experiments).

The measurements were found consistent with the predictions of the model, which showed that

- To optimise the switching ratio in a degenerate arrangement (pump and probe have the same wavelength) such as the one studied here, a trade-off must be reached between the nonlinear phase shift and the gain compression experienced by one of the probes.
- Gain compression also influences the shape of the switching window and tends to smooth the sharp features caused by the nonlinear refractive index.

Ultrafast dynamics such as carrier heating play a significant role in dictating the onset of optical switching, resulting in slower switching speeds of SOA-based interferometric configurations than those achieved with passive semiconductor nonlinear waveguides [1]. However, ultrafast switching with SOAs is still possible [2], with the critical advantage of switching pulse energies lower by several orders of magnitude, well below 1 pJ.

The second part of chapter 4 is devoted to studying the spatial dependence of nonlinearities in SOAs, caused by the self-modulation of the pump pulse, and its implications for all-optical switching.

Two-beam counter-propagating pump-probe measurements showed that

- The functional form of the spatial dependence of gain saturation depends drastically on pulse energy. At energies below 1 pJ, the amplification of the pump was found to saturate the gain in a portion of the device.
- At sufficiently high input energies (still below 1 pJ for the given experimental conditions), the pump saturates the whole length of the SOA and the counter-propagating pump-probe trace resembles an exponential curve. A simple analytical expression, function of the device parameters, was derived for this case and used to fit the experimental results.

The model was used to contrast the results and to explore how this effect translates when it comes to the shape of the slow edge of the switching window. Numerical calculations show a substantial decrease in the effective fall time of the switching window edge for increasing pump pulse energies.

The experimental work on nonlinear light generation in QC lasers is presented in **chapter 5**. The goal of this research, carried out at Princeton University, was to achieve an Anti-Stokes Raman QC laser by using the $\chi^{(3)}$ nonlinearity associated with intersubband transitions. In the light of this investigation, we can conclude that

- Stimulated electronic AS Raman emission has been observed in samples of three different designs (both nonlinear region and pump laser). This is the first step towards AS Raman lasing, which holds promise to extend straightforward operation of unstrained InP QC lasers to wavelengths below $4\ \mu\text{m}$.
- The frequency shifts between AS Raman and pump photons were measured to be over 100 meV, significantly larger than those reported with intersubband Stokes Raman lasers.
- Some samples in which the nonlinear region is pumped very close or above resonance of the 4-3 transition (D3008 and D3015) were found to emit light via incoherent upconversion processes.
- AS Raman lasing in QC lasers is feasible, provided an optimised negative detuning and an increase in the pump power.

6.2 Further work

Our study of the SOA ultrafast dynamics relevant to all-optical switching was conducted on a single device. This particular amplifier had been the subject of an extensive characterisation [3], which proved very useful in the interpretation of the experimental results. However, it would be desirable to carry out similar measurements on other SOAs to compare these observations and extend our analysis.

Longitudinal effects, for example, could be further explored by comparing a set of

devices differing only in their length. This would also allow an investigation of the dependence on this parameter of recovery times, saturation energies and other crucial magnitudes.

Investigating the ultrafast dynamics in Quantum Dot amplifiers would be especially appealing, as these present distinct features compared to bulk and QW active material. Ultrafast gain recovery has been reported in these devices. However, quantitative measurements of the associated refractive index changes are scarce and the feasibility of large nonlinear phase shifts, as needed for interferometric switching, is still subject to discussion. Due to the strong polarisation dependence of gain in QD SOAs, co-polarised TE pump and probe pulses are best suited for this task. This would require modifications in our current set-up (using, for example, an heterodyne pump-probe technique would be appropriate in this case).

In the line of investigating alternative material families, devices grown with dilute nitrides such as GaInNAs on GaAs substrates are one interesting subject of study. The latter have recently been attracting considerable attention amongst researchers due to their radically distinctive optical and electronic properties, which are not yet fully understood.

The different mechanisms dictating the carrier dynamics on subpicosecond timescales are drastically dependent on pulse width. Although the signature of carrier heating has been observed with pulse durations of ~ 700 fs, as reported in this thesis, working with shorter pulses would be advantageous in several ways. These include the enhancement of the ultrafast nonlinearities and higher temporal resolution in pump-probe measurements (thus allowing to distinguish the contributions of different ultrafast dynamics, e.g., spectral hole burning). Unfortunately, the duration of the pulses generated by our OPO is not easily tunable, and a different nonlinear crystal would be required to obtain pulse widths below 300 fs.

Despite its simplicity, the sliced propagation rate-equation model proved very useful in the interpretation of our experimental results, particularly in understanding the interplay of the ultrafast gain and refractive index dynamics in SOA-based interferometric switches such as the TOAD or illustrating the spatial profile of gain depletion induced by the pump pulses across the amplifier. Further sophistication could be accomplished by including spectral effects such as gain or waveguide dispersion (especially relevant if shorter pulses

are to be considered), or by taking into account the effects of amplified spontaneous emission (ASE).

In the light of the work on QC lasers presented in this thesis, some lines for improvement can be drawn in the pursuit of AS-Raman lasing.

The AS-Raman gain can be enhanced, on one hand, by an optimised design of the nonlinear and pump regions. Further work in choosing the appropriate barrier/well widths of the QC stack should lead to obtaining larger optical dipole matrix elements of the relevant intersubband transitions and more convenient scattering rates. The pump optical power could also be increased, subsequently enhancing the Raman gain, by coating the laser facets for high reflectivity at the pump wavelength.

Our measurements show that it is also crucial to pump the nonlinear regions with an optimum detuning from resonance of the transition 4-3. The detuning Δ should be negative (to avoid direct scattering of electrons to the upper level and the resulting incoherent upconversion emission) and 2-3 times larger than the linewidth to minimise the linear absorption of the pump photons.

From the structural point of view, a 2-stack waveguide core approach (as adopted in the work presented here) is not the only choice. By alternating pump and nonlinear periods in a single stack, the overlap of the Anti-Stokes optical mode with the active region could be significantly increased (at the expense of a more complex design).

References for Chapter 6

- [1] K Tajima, S Nakamura, and Y Ueno. Ultrafast all-optical signal processing with symmetric Mach-Zehnder type all-optical switches. *Opt. Quant. Electron.*, 33:875–897, 2001.
- [2] S Nakamura, Y Ueno, and K Tajima. Femtosecond switching with semiconductor-optical-amplifier based symmetric Mach-Zehnder-type all-optical switch. *Appl. Phys. Lett.*, 78(25):3929–3931, 2001.
- [3] J G Fenn. *Ultrafast dynamics in semiconductor optical amplifiers*. PhD thesis, School of Physics and Astronomy, University of St Andrews, May 2003.

Publications

"Spatial dependence of gain nonlinearities in InGaAs Semiconductor Optical Amplifier". A. Gomez-Iglesias, J. G. Fenn, M. Mazilu, and A. Miller. (Accepted for publication in *App. Phys. Lett.*).

"Stimulated Electronic Anti-Stokes Raman Emission in Quantum Cascade Lasers". A. Gomez-Iglesias, D. Wasserman, C. Gmachl, A. Belyanin, and D.L. Sivco. (submitted to *App. Phys. Lett.*).

Conferences

"Stimulated Electronic Anti-Stokes Raman Emission in Quantum Cascade Lasers". A. Gomez-Iglesias, D. Wasserman, C. Gmachl, A. Belyanin, D.L. Sivco. Oral presentation MoB-2-2. 17th International Conference on Indium Phosphide and Related Materials. Glasgow, May, 2005.

"Intraband carrier dynamics in semiconductor optical amplifier-based ultrafast switch". A. Gomez-Iglesias, J.G. Fenn, M. Mazilu, A. Miller and R.J. Manning. Contributed poster H5.169. 27th International Conference on the Physics of Semiconductors. Flagstaff, July 2004. AIP Conference Proceedings CP772.

"Carrier heating in a Terahertz Optical Asymmetric Demultiplexer". A. Gomez-Iglesias, J.G. Fenn, M. Mazilu, A. Miller and R.J. Manning. Oral presentation CFC5. Conference on Lasers and Electro-Optics. San Francisco, May 2004.

"Spatial dependence of SOA nonlinearities relevant to all-optical switching". A. Gomez-Iglesias, J. G. Fenn, M. Mazilu and A. Miller. Oral presentation TuAA5. 16th LEOS Annual Meeting. Tucson, October 2003.

"Counter-propagating pump-probe measurements in multiple quantum well semiconductor optical amplifier". A. Gomez-Iglesias, J. G. Fenn and Alan Miller. Oral presentation. EQUONT-2 Quantum State Engineering and Ultrafast Optical Interactions in Semiconductors. Toledo (Spain), June 2003.

"Ultrafast dynamics in semiconductor optical amplifiers with implications for interferometric switching". J. G. Fenn, M. Mazilu, A. Gomez Iglesias, A. Miller. 15th LEOS Annual Meeting. Glasgow, November 2002.

Acknowledgements

I am indebted to many friends and colleagues who have contributed, in many ways, to make this thesis happen.

I would like to thank especially Professor Alan Miller for his confidence, guidance and support all the way. I am also grateful to the Ultrafast Photonics Collaboration (EPSRC) and the Nicol Trust for funding my studentship.

To the members of the A-Team, past and present...

Julia, for getting me started in the lab and introducing me to the social life of St Andrews.

Steve, for wise advice both on work and healthy living (if I only followed it...)

Michael, for his help with the theory and model calculations.

Andy, always up for a laugh, for assistance with my computer problems.

Charis, Matt, Jonathan, and Dave, for the time shared, endless coffee breaks and deep chat (fighting my little-Spain prejudices).

Jean-François, fellow continental cast-away, for showing me the dark side of Dundee and controversial political discussions.

Thanks to the guys in the W-squad for the good times and Friday football.

I want to express my deep gratitude to Professor Claire Gmachl for giving me the opportunity to work in her group at Princeton University. Also for her availability, many helpful discussions and mentoring during my stay. Thanks to Afusat, Gary, Scott, Zhijun, Jian-Zhang and Khandaker for making me feel part of the group. I am especially indebted to Daniel Wasserman for processing my samples.

Thanks to Bob Manning for supplying the amplifier, and Debbie Sivco at Lucent Technologies for growing the wafers used in my work at Princeton.

To Alejandro, Belen, Cristinota & Cristinita, Jesus... for their friendship and for putting up with my endless chatting and pre-submission paranoia. Also to my friends at home, Alex, Rafa, Jorge, Alejandro, David, Anton, Abraham... for staying in touch and making the most of my short visits.

To Sandra, for giving me so much and being always there for me (and for keeping me and my mind away from the lab, sometimes).

Finally, to my parents, grandparents and the rest of the family, always encouraging, for supporting me all these years and making me feel not so far away.